SAPIENZA
UNIVERSITÀ DI ROMA

Sapienza University of Rome

Department of Mechanical and Aerospace Engineering
PhD in in Aeronautics and Space Engineering

Thesis For The Degree Of Doctor of Philosophy

Integrated Aeroservoelastic Modeling for Preliminary Aircraft Design with Multi-Objective Optimization

Advisor
Prof. Franco Mastroddi

Co-advisor
Fabio Vetrano PhD

PhD Candidate
Marta Colella

Academic Year MMXXIII-MMXXIV (XXXVI cycle)

A tutti gli abbastanza di cui mi sono sentita meno.
Ai vuoti non colmati, ridimensionati con il tempo.

Abstract

The next few years present new and fascinating challenges in the aeronautic field with the proposal of innovative designs that aim to improve the performance of the aircraft and to reduce its environmental impact. These requirements involves rethinking the sizing of the aircraft from the preliminary design stages. In order to have wisely sizing that optimizes the aircraft performance and respects all the design constraints, it is essential to use a Multi-disciplinary Design Optimization procedure, considering all the involved disciplines simultaneously. Each discipline requires the adoption of an appropriate engineering model to describe its physics with a given level of accuracy. Moreover, through the optimization process, the involved disciplines interact through conflicting goals and constraints in the search for the optimal design that meets all the requirements. This thesis proposes a rapid and effective Multi-Disciplinary Design Optimization methodology for sizing the wing, tail and ailerons in the preliminary design of an aircraft, with particular emphasis on explicit Multi-Objective approach, incorporating the controller optimization into the framework. More specifically, it comprises a structural model generator and reduced-order models with a good balance of accuracy and computational time. The reduced-order models used for optimization involve the integration of flight and control dynamics and aeroservoelasticity. Hence, it is necessary to define: a structural finite-element model for wing and tail, with relative simplifications on fuselage and control surfaces; an analytical aerodynamic model using the modified Strip theory and Theodorsen approximation with finite wing for compressible flow; and finally a control law model for the usage of aileron in Load Alleviation or Active Flutter Suppression. The developed procedure, starting from a mission and a target payload, calculates the optimal cruise performance by maximizing the cruise speed and the aircraft range, thus minimizing the weight of the aircraft. Moreover, the constraints applied in the optimization process are selected based on potential critical conditions within the flight envelope and the aircraft's mass. This selection considers both typical constraints relevant in the preliminary stage from academic perspectives and those prevalent in industry practices. Therefore, through the imposition of geometric, aeroelastic and aeroservoelastic constraints, the optimiser sizes the aircraft's wing, tail, aileron and the control laws. The optimisation methodology is validated through three different strategies with an increasing number of disciplines, to demonstrate how the inclusion of each discipline changes the optimal design. In particular, the strategy involving all disciplines gives the best optimum design in terms of target space and validity, and it underscores that the inclusion of the controller enhances the overall performance.

Keywords: Multi-Disciplinary Design Optimization, Multi-Objective Design Optimization, Reduced-Order Models, Finite Element Model, Load Alleviation, Active Flutter Suppression

Author's email marta.colella@uniroma1.it

Contents

List of Figures

List of Tables

Nomenclature

AR_e Equivalent Aspect Ratio

AR_w, AR_t Aspect Ratio of the wing and tail

C_L, C_{L_w}, C_{L_t} Total Lift coefficient, Lift coefficient of the wing and tail

$C_{m_{\delta_e}}$ Elevator Static Controllability Factor

D_0, D_i Shape and Induced Drag

M Mach number

S_w, S_t Aerodynamic surface of the wing and tail

U_D Dive speed

U_f^{CL} Flutter speed in Closed Loop System

U_f^{OL} Flutter speed in Open Loop System

U_r Reversal speed

α Attack Angle

δ_e Elevator Angle

δ_t Tail Angle

ϕ_w,ϕ_q,ϕ_{M_w},ϕ_{M_q} Lift and moment indicial functions associated to the downwash w and the pitch rate q

ρ_∞,q_D Air density and dynamic pressure

σ_{max} Von Mises max stress

a Dimensionless elastic axis position measured from the middle-chord, positive aft

b,c Semi-chord and chord length

e Oswald factor

h,α Plunging and pitching displacements

k Reduced frequency

t,τ Time variable and its dimensionless counterpart

t_r Rolling Time

w,q Downwash velocity and the pitch rate

x_G Position of aircraft mass center

x_w, x_t Position of the aerodynamic center of the wing and tail

Acronyms

AFS Active Flutter Suppression

CL Closed Loop

DOE Design of Experiments

FEM Finite Element Model

GLA Gust Load Alleviation

MAC Mean Aerodynamic Chord

MDO Multi-Disciplinary Design Optimization

MIMO Multi-Inputs,Multi-Outputs

MLA Maneuver Load Alleviation

MOO Multi-Objective Optimization

MTOW Maximum Take Off Weight

MZFW Maximum Zero Fuel Weight

OL Open Loop

PI Proportional–integral controller

ROM Reduced-Order Model

SAH Semi Aeroelastic Hinge

SISO Single-Input,Single-Output

SOO Single-Objective Optimization

SVD Singular Value Decomposition

TSFC Thrust-specific fuel consumption

ULH Uniform Latin Hypercube

XDSM Extended Design Structure Matrix

Summary of the thesis

Research motivation, problems and objectives

The aviation industry is going through a crucial phase of innovation-focused research aimed at balancing the growing requirements for efficiency, sustainability, and performance in aircraft design. As the demand for air travel continues to grow, there is an increasingly urgent need for innovative solutions, that look at fuel efficiency, environmental impact, and operational capabilities. In this context, the *Multi-Disciplinary Design Optimization (MDO)* turns out to be the most suitable methodology during the preliminary design stage, providing a comprehensive approach to balancing all the conflicting design objectives.

One of the main challenges in modern aircraft design is to achieve optimal fuel efficiency without compromising the performance (as explained in Fig. 1 with the historical improvements on fuel consumption). The aircraft fuel consumption is not only a critical economic factor, but also a key factor in environmental sustainability. In addition to the fuel efficiency and environmental considerations, the aircraft must satisfy rigorous performance requirements, including speed and mileage range. Reaching the balance between speed, range and operational efficiency is a complex task that requires a global approach. By considering the interdependences between all the disciplines, the *MDO* enables the identification of the design configurations that optimize both fuel efficiency and operational capabilities, ensuring that the resulting aircraft meets the different requirements of the aviation industry. More specifiacally, the *MDO* represents a promising way to explore the complex trade-offs and interplays between all the disciplines involved as aerodynamics, propulsion, and structural design.

There are several interesting examples of innovative design proposal, like the Blended Wing Body (Ref.[2]) and the ZEROe Aircraft concept (Ref. [3]), and many *MDO*'s researches have been carried out on aircraft design (Refs. [4–7]). The goal of the *MDO* is to effectively coordinate all the disciplines involved, enabling them to work collaboratively in order to achieve a global optimal solution, through valid and specific architectures for the problem to be solved (Ref. [8]). Different types of architectures for *MDO* problem solving have been proposed in the literature, as in Refs. [9, 10]. More specifically, the *MDO* approach involves a constant exchange of information among the disciplines involved, so any changes made in one discipline can be evaluated for their impact on the others. This collaborative approach is critical to balancing the trade-offs between the different aircraft needs and requirements, helping to achieve complex and optimal solutions. Furthermore to achieve a congruent collaboration across all disciplines, the level of accuracy used needs to be consistent for all disciplines involved (see Ref. [11] for details on the usage of multiple fidelity levels in the same optimization process).

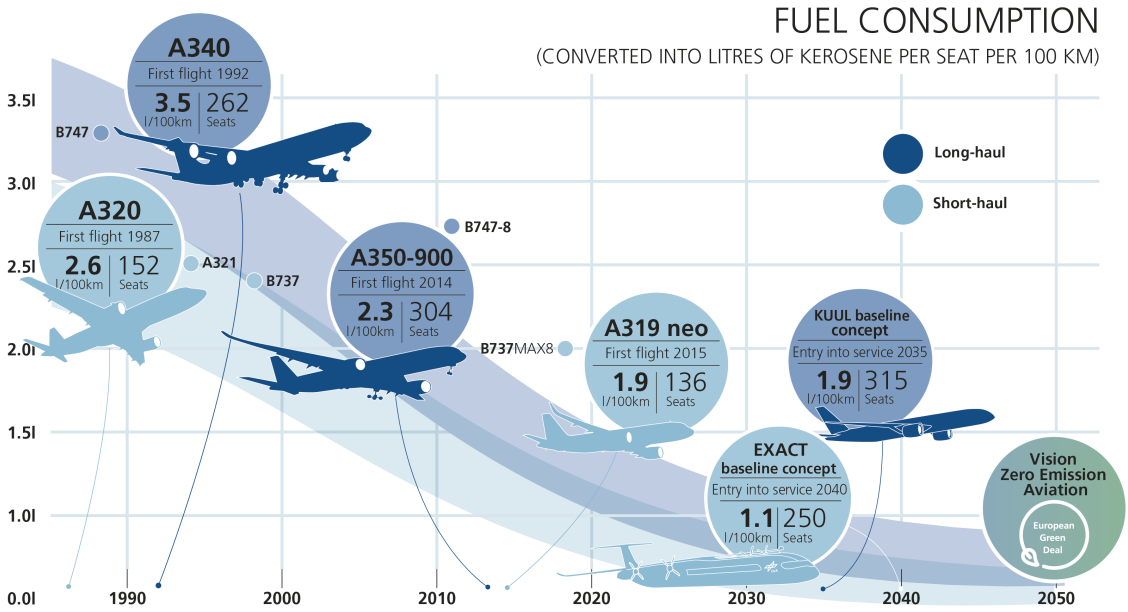

Figure 1: Reduction in fuel consumption in time (Ref. [1])

An additional aspect to bear in mind in the optimization process is the computational time and cost, which are closely related to the type of models involved in the procedure. Adopting more detailed and complex models, such as those based on high-fidelity numerical analysis, can result in longer computational times and higher computational costs because of the need to solve complex and detailed equations. On the other hand, the use of simplified models or approximation approaches can significantly reduce the computational time, inevitably leading to solutions that are less accurate. These faster models can be particularly useful in the early stages of the design process, allowing rapid exploration of possible solutions. Therefore, it is essential to balance model accuracy with the need for acceptable computational time. In addition, the integration of parallel computing techniques and the use of advanced computational resources can help to optimize the run times, allowing faster convergence to optimal solutions in the complex *MDO* context.

The research conducted and this thesis work are inspired by the aviation industry's need to develop innovative aircraft for a modern era emphasizing efficiency, sustainability, and performance. The goal is to use the capabilities of the Multidisciplinary Design Optimization to address this need. With a specific focus on critical performance such as fuel consumption, environmental impact, and speed/mileage range, this study attempts to play a role in the progress of the aeronautical engineering and to encourage the emergence of a more sustainable and competitive aviation industry. The innovation suggested in this thesis involves incorporating, in the initial design phase, not only the wing optimization but also the tail and the control surface optimization, taking into account a specific mission and fuselage configuration. Furthermore, the early integration of the

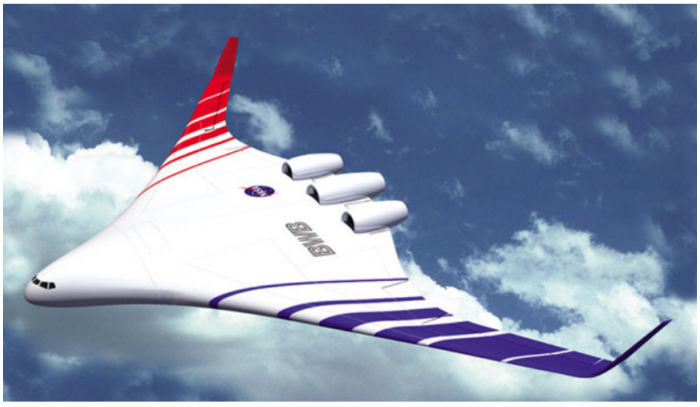

Figure 2: The new concept of aircraft by NASA: The Blended Wing Body, Ref. [2]

control discipline represents an unconventional approach, and the objective of this inclusion is to highlight the positive advantages derived from adopting such a methodology. The disciplines involved are integrated into the optimization process sequentially, using a genetic optimization algorithm (Ref. [12]), and considering as initial population the Design of Experiments computed using the Uniform Latin Hypercube (ULH) Algorithm (Ref. [13]). More soecifically, for each design of the optimization, the aerodynamic and structural numerical models and the control law synthesis are generated. The analyses performed exploit the Finite Element Model and the Reduced Order Models for the aeroelastic representation of the aircraft, taking the advantage of the analytical modeling for the aerodynamic definition, in order to speed up the dynamic analyses (generally at high computational time and cost). The proposed optimization methodology carefully considers a wide range of constraints, including those commonly found in the academic literature and those encountered in industrial optimization during the preliminary design phase.

Multi-disciplinary design optimization: a literature review

Current challenges in aeronautics are to achieve increasingly innovative, efficient, and environmentally friendly designs. This implies the need to improve existing design solutions, and to redefine the aircraft sizing searching the optimum solution for cost, fuel use and noise reduction. Therefore, in this scenario, the most powerful engineering tool currently used is the *MDO*. This procedure involves simultaneously all the disciplines useful for the design, considering the possible couplings and conflicts of their objectives and constraints. Generally, the optimization of a single discipline presents relatively low difficulties, in fact a proper choice of the design parameters to which the discipline is sensitive would be enough to improve its performance. Of course, such design parameters could negatively affect the performance of other disciplines. For this reason, it is necessary to take a global view of the problem, considering all the relevant disciplinary behaviors and their requirements. In addition, the usage of this procedure in the early stages of the design process can significantly reduce the time and cost of the design cycle. Finally, this approach allows the usage of more combinations of design parameters and greater exploration of the design space, and thus leads to finding unconventional configurations. The Multidisciplinary optimisation technologies have reached a level of maturity that allows their widespread implementation and use in both industry and research (Refs. [14–20]). In fact, they encompass an ever-expanding set of optimisa-

Figure 3: The ZEROe concept of Aircraft by AIRBUS Ref. [3]

tion algorithms and automation frameworks (Refs. [21–23]), increasing the number of disciplines and design objectives over time, and improving the capabilities for high-fidelity aerostructure optimisation (Refs. [24, 25]). To develop new designs that perform better than those currently used, accurate modeling is necessary, taking into account the multidisciplinary nature of the problem. Industries and research centers are putting forward a number of new aircraft concepts to cut down on the energy consumption of civil aircraft. The Blended Wing Body (Fig. 2) is an example of *MDO* application, created through a collaboration between Boeing and NASA, and it is still studied by various research centers and universities (Ref. [26]). The advantage of this unconventional configuration is improved performance, noise, and emission reduction. However, its disadvantage lies in the difficult structural design due to the absence of a circular/elliptical body representing the fuselage. Other innovative designs have been proposed by Airbus, through the zero emission project (Ref [3]). Airbus' ambition is to bring to market the world's first commercial aircraft powered by hydrogen by 2035. This involves a rethinking of the position and shapes of the tanks. The propellant will no longer necessarily be stowed on the wings but, depending on the aircraft configurations, will have to be stowed in different places including portions of the fuselage. This involves a total rethink of the aircraft to be able to use hydrogen tanks and hybrid engines. The *MDO* technique is becoming increasingly effective in addressing the current challenges in the aerospace field, including the detailed design of the subsystem, the aero-structural coupling, and a number of critical analyses from different disciplines. For this reason, presently most aerospace companies, research centers and universities are developing multidisciplinary tools for the conceptual and the preliminary vehicle design (Refs. [21, 27]). Some examples of such tools for the aerospace problems can be get from the literature, as $NeoCASS$ (Next generation Conceptual Aero Structural Sizing) Ref. [11], which is a Matlab® toolbox developed by the Politecnico di Milano for the structural sizing and the aeroelastic analysis of aircraft. An open-source framework called $OpenMDAO$ is being developed by the NASA Glenn Research Center to analyze and optimize multidisciplinary designs (Ref. [28, 29]). It can be adapted to include different disciplines at multiple levels of fidelity and manage their interaction. While, a parametric modeler for structural and aerodynamic meshes is being developed by The University of Michigan, in order to be coupled with $OpenMDAO$ (Ref [30]). Many applications in the literature exploit the integrated frameworks for the *MDO*. In addition to promoting integrated codes for multidisciplinary analysis, the *MDO* community is dedicating

significant efforts to various aspects. These include developing efficient mathematical formulations for the optimization problems, implementing new optimization algorithms, and exploring efficient architectures for the process (Refs. [31, 32]). These efforts are driven by the search for an optimal balance between achieving high-quality results and maintaining acceptable computation times. The initial task is to select objectives, constraints and design variables. The proper formulation of the optimization problem is critical, as it includes key factors that can profoundly affect the entire process.

Methodology proposed and activities description

In the context of aircraft design, considering the growing demand for aviation services and exploiting the expanding computational resources, this thesis is guided by the following objectives:

- creation of a tool to perform the aircraft *MDO*, exploiting the adoption of Finite Element Models and Reduced Order Models
- understanding the complex interaction between disciplines in the field of aircraft system engineering
- practical use of the tool, specialization of the analyses to reduce the time and the cost of development of new design of aircraft

Therefore, the thesis focuses on two main aspects: aircraft design and optimization. The first aspect involves the incorporation of appropriate engineering models for each discipline involved, while the second aspect involves the integration of these disciplines within an appropriate multidisciplinary design optimization (*MDO*) architecture. To achieve these goals, the activities undertaken include:

- the bibliography research on aircraft design and on *MDO*
- the implementation and the validation of a mathematical, physical and numerical model for each discipline involved in the aircraft design. In particular, in the Matlab ® environment the aeroservoelastic model is developed as a black box with the usage of input-output files. More specifically, the model has the capability of:
  - define the vehicle *geometry sizing*, considering a specific mission to accomplish, and estimate the *Maximum Take Off Weight* of the aircraft.
  - give the formulation of the *Finite Element Model* for both the structural and the aerodynamic aspects of the aircraft. The definition of the input files compatible with the Nastran® solver, and the implementation of the output readout file have been carried out. Two aircraft models are taken into account, the first one is the aircraft in the *Maximum Take Off* configuration, while the second one is the aircraft in the *Maximum Zero Fuel Weight* configuration.
  - define the *aerodynamic Reduced Order Model*, based on the analytical indicial functions (The model has been validated using comparisons between the analytical model and the finite element model).
  - define the *integrated model of aeroelasticity and flight dynamics*

  - run the *static and the dynamic analyses*, choosing the worst conditions for each analysis in the flight envelope and focusing on the sizing output
  - use of *Active Flutter Suppression* and *Gust Load Alleviation* control law model, based on specific synthesis criterion
  - calculate the *aircraft best performance* parameters at cruise condition.

- the building of the optimization workflow by integrating the black boxes linked between each others (in a sequential way). The chosen architecture is the sequential one, including an internal optimization for the control law synthesis.

- the choice of the design variables of the optimization process taking into account their range bounded by lower and upper limits. A trade-off between the speed and the exploration of the objective space of solution is considered. Moreover, the physical and manufacturing feasibility are taken into account.

- the test of different optimization algorithms, and the choice of the algorithms to use (the *SimpleGADriver* and *NSGA-II* from *OpenMDAO* Ref. [28]

- perform the Multi Objectives Disciplinary Design Optimization of the aircraft design. Results are discussed from engineering, mathematical, and computational perspectives.

Outline of the thesis

The present Ph.D. thesis is divided into three parts. In the first part, the theoretical background of the *MDO* theory and the *MDO* methodology proposed are described. The second part is devoted to the Aircraft Design and to the description of the Aeroservoelastic modelling developed. Finally, the last part shows the application cases and the validation of the methodology proposed. In addiction, there are two supporting appendices.

The Chapter 1

This section delves into the theoretical background of the Multidisciplinary Design Optimization, with a focus on its mathematical aspects. The discussion includes the distinction between the single-objective and the multi-objective *MDO*, describing the primary architectural framework and presenting various optimization algorithms. The chapter concludes by outlining the methodology presented in this thesis, providing a comprehensive overview that includes the disciplinary considerations, the motivations behind the choice of performance objectives, and the integration of specialized constraints adapted to each project's own flight envelope.

The Chapter 2

This section is dedicated to the complete descriptions of all the engineering models necessary to design an aicraft model and its mission. First the integrated modelling of aeroelasticity and flight dynamics is described. Secondly, the models of mass estimation, structure, aerodynamic and control law are described. Moreover, the validation process for the analytical aerodynamic model and for the control law synthesis are supported by examples, using benchmark configurations.

The Chapter 3

This section describes the application cases and the results of the optimization process. More specifically, the validation process of the optimization methodology proposed is shown through the

comparison of the best designs obtained from the different optimizations specialized with different number of disciplines involved.

In Appendix A.1 the lifting line theory is described

In Appendix A.2 the calculations for the Equivalent Aspect Ratio definition are shown.

Chapter 1

Multi-Disciplinary Design Optimization theoretical issues

Generally, engineering is in charge of solving complex problems, in which the inclusion of a large number of disciplines is essential. Particularly in the early stages of design, it is essential to involve all design parameters and considerations simultaneously in order to take into account the complexity of the problem. Moreover, all disciplines involved in the problem are generally strongly coupled and influenced by most of the design parameters. Therefore, in order to obtain a design that takes into account all the interactions between the involved disciplines and design parameters, the use of a *MDO* methodology is necessary. In this chapter first an overview of the theoretical issues related to *MDO* is presented, and then the optimization methodology used in this activity is described.

1.1 MDO

The Multidisciplinary optimization (MDO) is basically about identifying the most effective design solution that meets specific objectives and respects specific constraints. Such goals can be related to improving performance, such as efficiency, or minimizing weight, always meeting different design constraints, such as stress limits or manufacturing feasibility. Specifically, the MDO takes a comprehensive and optimized approach to engineering design by considering these factors simultaneously. The current state of MDO includes advanced algorithms, optimization techniques and computational tools, which make it easier to manage the intricate interactions between different disciplines efficiently using mathematical models and simulation techniques. The field of MDO is dynamic and continually adapting to the evolving needs of complex engineering systems, with significant potential to improve design outcomes and promote innovation in all areas.

1.1.1 Level of disciplinary modeling

During the optimization process, the disciplines involved are defined by representative engineering models. The fidelity of these descriptive models can vary; the greater the descriptive ability, the better the simulation results. Therefore, increasingly accurate numerical models allow for better and better simulation of the disciplinary behaviors. Unfortunately, improving the descriptive accuracy of the high-fidelity models leads to an increase in the problem size and in the computational cost

of the objective functions. Generally, the fidelity level of the descriptive models involved in the optimization is chosen according to the following characteristics:

- the representative model must be *effective* in estimating the response parameters involved in the MDO for calculating constraints and targets
- the multidisciplinary description must be *homogeneous,* in order to avoid the optimization being handled only by the most accurately described discipline. In fact, a descriptive difference among the level of accuracy used for disciplines would lead to an unreliable solution, influenced only by one discipline and not caring for the others.
- simulation burden must be *affordable* during an iterative process
- the generation of the model and the execution of the analysis must be fully *automated* as part of the optimization process, without the need for human intervention.

Due to the cost and the time constraints, it is challenging to incorporate high-fidelity models into the optimization process. One possible solution to this problem is to use *multiple fidelity* levels in the same optimization process. A commonly used method is to create multiple models for the same discipline and then analyze them by solvers with different approximation (Ref. [11]). Moreover, the optimization algorithm is also capable of implementing a multi-fidelity approach (Ref. [33, 34]). There are two types of multi-fidelity optimization methods available: convergent methods utilizing high-fidelity gradient or high-fidelity pattern-search, and heuristic model calibration approaches, which may involve interpolating high-fidelity data or adding a Kriging error model to a lower fidelity function.

1.1.2 Single and Multi Objective Optimization

Usually, the optimization problems are defined as the conventional search for the stationary points of a function. Specifically, the process involves the constrained minimization or maximization of one or more functions representing the objectives to be optimized, subject to specific constraints. The mathematical formulation of the problem could be summarized as

$$\begin{aligned}
\underset{\mathbf{x}}{minimize}: \quad & \Psi(\mathbf{x}) = [f_1(\mathbf{x}), f_2(\mathbf{x}), \ldots, f_N(\mathbf{x})] \\
inequality\ \ constraints: \quad & g_j(\mathbf{x}) \leq 0 \qquad\qquad j = 1, 2, \ldots, m_1 \\
equality\ \ constraints: \quad & h_k(\mathbf{x}) = 0 \qquad\qquad k = 1, 2, \ldots, m_2 \\
lower\ \ and\ \ upper\ \ bounds: \quad & x_i^{LB} \leq x_i \leq x_i^{UB} \qquad i = 1, 2, \ldots, m
\end{aligned} \tag{1.1}$$

where $\mathbf{x}$ is the design variable set to be defined, $\Psi(\mathbf{x})$ collects the objective functions, $h_k(\mathbf{x})$ are the equality constraints, and $g_j(\mathbf{x})$ are the inequality constraints. Moreover, every design variable x_i must be inside an appropriate range, which is delimited by lower x_i^{LB} and upper x_i^{UB} bounds. This process defines the feasible set, denoted as $x_i^{LB} \leq x_i \leq x_i^{UB}$. The crucial initial considerations in the analysis of an optimization problem concern the exploration of design space and goal space. These spaces include potential design solutions and their corresponding results, calculated through the objective functions. The feasible set represents a subset of the overall design space, typically constrained by a combination of side constraints and equality/inequality constraints. All

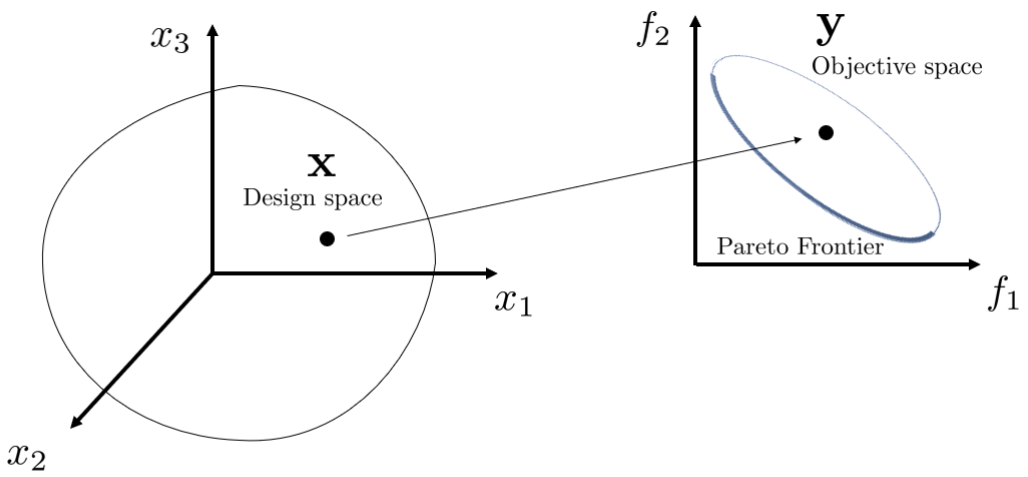

Figure 1.1: Design and objective spaces with the Pareto frontier

the acceptable solutions are in the feasible objective space. The optimal design depends on the definition of the problem; if it is *Single-Objective Optimization (SOO)* ($\Psi(\mathbf{x}) = f_1(\mathbf{x})$), the optimal solution is unique, while if it is *Multi-Objective Optimization (MOO)* with two objectives functions ($\Psi(\mathbf{x}) = [f_1(\mathbf{x}), f_2(\mathbf{x})]$), the best solutions lie on a 1D curve called the Pareto frontier (Ref. [35], see Fig.1.1), as with three objectives, the best designs are located on a 2D surface. Therefore, the Pareto frontier has a dimension of $n-1$. The design parameters may take on continuous or discrete values. The discrete values can be further classified as either ordered or unordered. For instance, an example of a discrete ordered design parameter is the count of reinforcements, which can only assume natural numbers. On the other hand, an example of a discrete unordered design parameter is the type of reinforcements, where a natural number is associated to a specific shape (e.g., 1 for circular, 2 for rectangular).

1.1.3 Algorithms for the Single and Multi Objective Optimization

An optimization algorithm provides a numerical approach to obtain advanced design solutions from an initial condition. Several optimization algorithms are designed to handle optimization problems, each of which is suitable for particular features of the problem. The literature presents a wide range of optimization algorithms, each focusing on specific aspects such as determinism, gradient reliability, stochastic nature, unbounded or bounded conditions, single-objective or multi-objective, local or global optimization, convexity, and more. The classification of optimization algorithms can be based on several principles (see Ref. [36–41]). Strategies for solving the *MOO* problems are discussed here, since the solution of the *SOO* problems can be derived as a special case of *MOO* by imposing $N = 1$. These methods can be classified into two categories: deterministic methods, also known as gradient-based, and stochastic methods, often referred to as population-based (Refs. [42, 43]).

Traditionally, the deterministic methods have been the main choice for solving the *SOO* problems. These methods are based on a set of necessary and sufficient conditions that the solution must

satisfy, focusing on the location of the stationary points of the objective and constraint functions. The gradient based algorithm finds the minimum of a function starting by a point inside the domain and moving in the opposite direction of the gradient (as described in Ref. [44]), the application of this algorithm is also studied in non-linear optimization problems (Ref. [45]). Within deterministic methods, a subdivision based on how they handle the objectives and the constraints exists; the direct methods employ a hill climbing in the objective space, adjusting its direction according to the local gradient, while indirect methods solve a set of equations derived from setting the objective function's gradient equal to zero. The gradient-based methods are inherently local and presume the existence of the derivatives. Consequently, their application is limited to the problems characterized by smooth and regular functions. Despite this limitation, the gradient-based search method (using techniques such as the Simplex Method, Steepest Descendant, and Newton Ref. [46]) prove to be very efficient for the local optimizations and the solution refinement. One of the most used method is the classical Broyden-Fletcher-Goldfarb-Shanno (BFGS) optimization algorithm, which is a variable metric method [47–50]. In contrast, the most recent class of optimization methods, the stochastic methods, adopts the guided random search techniques. These methods introduce the randomness into the design space and exploit additional information about the target space to guide the search to the potentially favorable regions. Moreover, the stochastic methods can be further categorized into single-point search and multiple-point search. The first one involves searching one point at a time during each iteration, while the latter explores several points (a population) simultaneously. All the stochastic methods are based on behaviors observable in the nature, and they can be classified in: the Evolutionary Algorithms (EA) (Ref. [51]), the Genetic Algorithms (GA) (Ref. [12]), the Particle Swarm Optimization (PSO), the Simulated Annealing (SA) (Ref. [52]), and the Game Theory-based optimization (GT) (Ref. [53]). The stochastic methods are robust schemes useful for solving problems where the design space is huge and discontinuous. One of the advantages of the stochastic methods is the lower mathematical complexity of the search procedure due to the use of randomness instead of gradient calculation. Randomness is why these methods can be considered global, they are not limited by the gradient path and they can more likely find the global optimum even if the objective function is not smooth and continuous. Moreover, these methods can be implemented easily for solving *MOO* problems, since the optimization process does not require analytical/numerical calculations on the objective functions, only the evaluation of the objective functions. However, the main disadvantage of the stochastic methods is in the necessity of evaluating the output functions for each design, which can cause much slower convergence than deterministic optimization methods. The Genetic algorithms (GA) is used in this thesis, so more details about it will be provided in the following Subsection.

These multitude of approaches can be also classified into aggregating, non-Pareto population-based, and Pareto-based techniques. Aggregating techniques, also known as scalarization, are used for problems with multiple objectives using deterministic algorithms that are intrinsically single objective. In such instances, one option is to combine the various objectives into a composite objective function. This can be achieved through methods like weighted combination or goal-based approaches. The Weighted Sum Method ([54]) is the most common methodology for combining objectives into one composite functional Φ by using weight coefficients w_n in order to assign to each

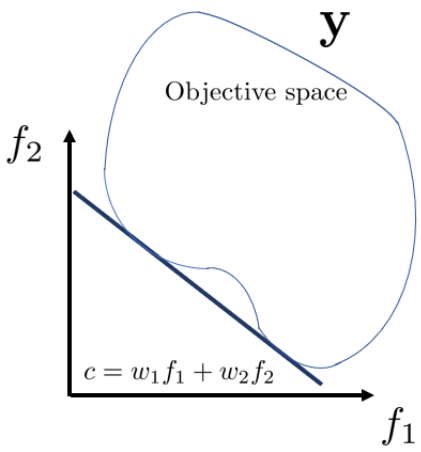

Figure 1.2: Pareto front using *Weighted Sum Method*

objective a relative weight.

$$\begin{aligned} \underset{\mathbf{x}}{minimize}: \quad \Phi(\mathbf{x}) \quad &= \quad \sum_{n=1}^{N} w_n f_n(\mathbf{x}) \\ with \quad \sum_{n=1}^{N} w_n &\stackrel{!}{=} 1 \end{aligned} \tag{1.2}$$

The main limitation of this approach is that, when it is used to generate the Pareto frontier, it is unable to capture the points located in non convex sections of the Pareto frontier within the objective space as in Fig. 1.2. Furthermore varying the weights consistently and continuously could be difficult and may not necessarily results in a regular distribution of Pareto optimal points. In order to overcome these difficulties, other scalarized functions such as the Weighet Glocal Criterion (WGC) method can be used (several formulations are referred to in the literature [39]). Specifically, in addition to the weights w_n an exponential parameter p is introduced for emphasizing the minimization of the objective function with the worst relative value. An example of common weighted global criterion method is

$$\underset{\mathbf{x}}{minimize}: \quad \Phi(\mathbf{x}) \quad = \quad \left\{ \sum_{n=1}^{N} w_n [f_n(\mathbf{x}) - f_n^{ut}(\mathbf{x})]^p \right\}^{1/p} \tag{1.3}$$

As a general rule, changing w_n allows the global Pareto frontier to be evaluated, while changing p allows a local area of the Pareto frontier to be better refined (Ref. [55]). In the non-Pareto population-based approaches, distinct sub-populations are employed for different objectives. On the other hand, the Pareto population-based techniques include algorithms such as Multiple Objective Genetic Algorithm (MOGA)), Non-Dominated Sorting GA (NSGA), and Niched Pareto GA.

Genetic Algorithms (GA)

The Genetic Algorithms (GA) are typical examples of evolutionary algorithms, in which a population of individuals evolves according to the logic of the natural selection, where the cumulative selection

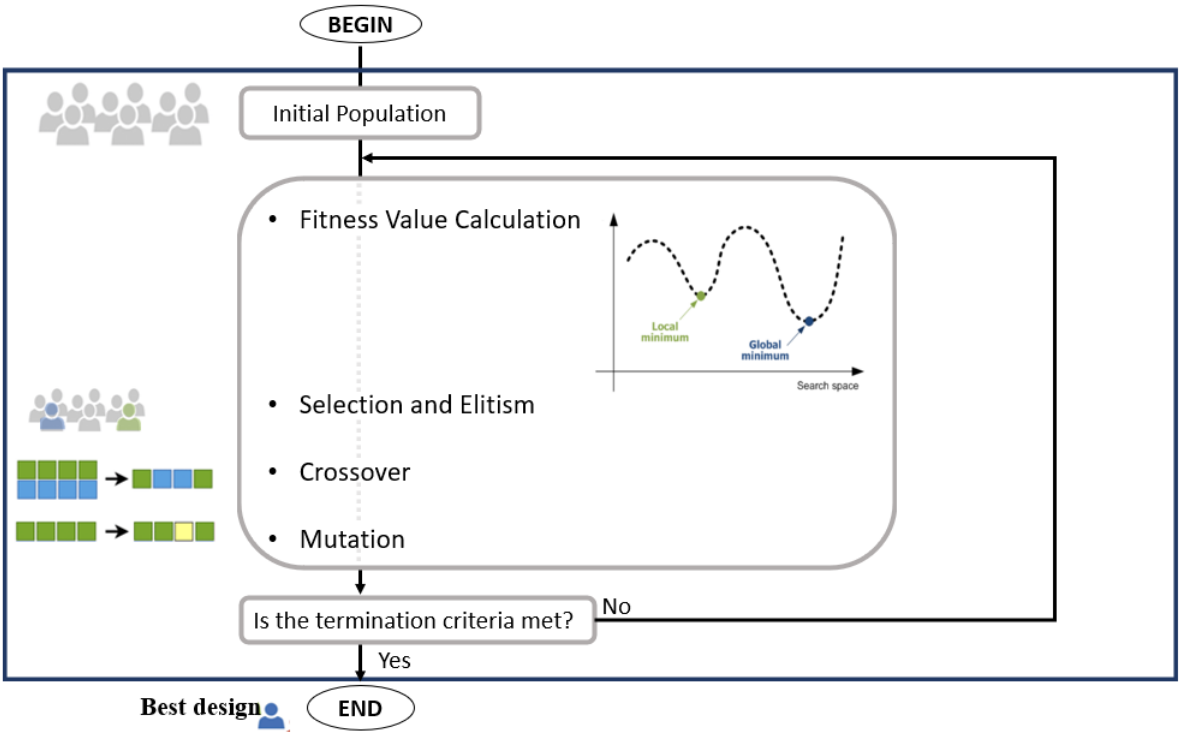

Figure 1.3: GA flowchart

of the most adapted genes over time has led to the development of the new species Ref. [56]. Originally, the algorithm, developed by Holland (Ref. [57]) and Goldberg (Ref. [12]) reproduces the genetic operations on the design variable, associated with the natural gene entity. Therefore, in that view of natural entities, if every design variable is seen as a gene, a vector of design variables is like a chromosome (or individual), and a group of individuals represent a population, which change at each generation through the genetic operators. Taking into account the stages of the evolutionary path, an initial population is generated (using random and statistical principles, see Sub. 1.5), and the cost function and constraints are calculated for each individual; individuals with the best fitness values are selected to survive as relatives in the new generation. Specifically, their genetic material (design variables) is exchanged through the crossover mechanism to produce a certain percentage of individuals of the next generation (see Fig. 1.4(a)). To ensure the genetic diversity, another percentage of the new generation is created with the mutation operator (see Fig. 1.4(b)), which involves a random change in one or more genes on the chromosome of the existing individuals; this mechanism prevents the algorithm from remaining fixed in a local minimum. The flowchart of the genetic algorithm is shown in Fig. 1.3 (see Refs. [40, 58] for more details).

1.1.4 Design of Experiments

To initiate a stochastic method, it is essential to generate an initial population comprising a set of design variables known as *Design of Experiments (DOE)*. Within the DOE, each design variable is subjected to systematic changes according to a defined pattern. The goal is to comprehensively cover the design space, ensuring a thorough exploration of potential solutions. The DOE technique, originally introduced by R. Fisher in Ref. [59], is used as a method to maximize system knowledge using a minimum number of experiments.

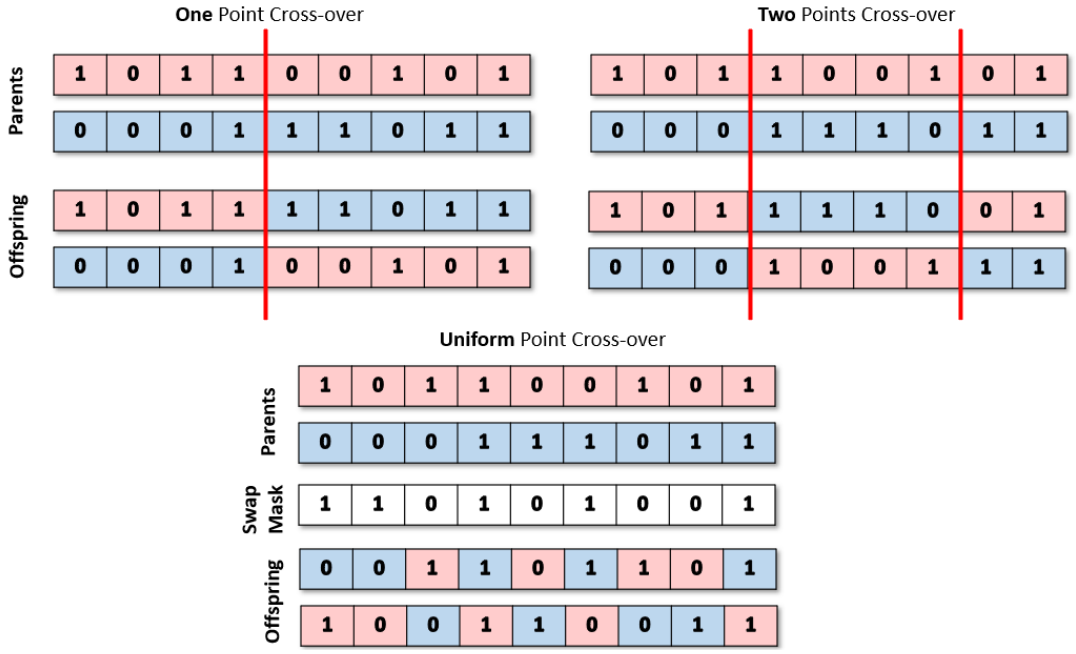

(a) Cross-over operation

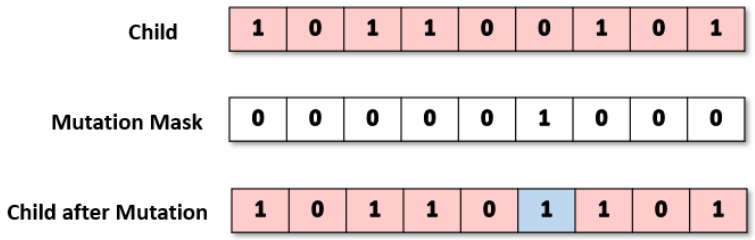

(b) Mutation operation

Figure 1.4: Genetic operations

The most used algorithm for computing the DOE are: the random, the *Uniform Latin Hypercube (ULH)*, the Sobol, the Incremental Space Filler (ISF), the full factorial and the orthogonal. The random scheme relies on the principles of mathematical random number generation, as illustrated in the methodology described in Ref. [60]. However, a disadvantage of this approach is the potential for sample clustering due to inherent randomness. To address this limitation, the Sobol scheme (refer to Ref. [61]) aim to create a quasi-random distribution of samples that are maximally spaced apart. Nonetheless, this algorithm may still present clustering problems along the diagonal direction. The Incremental Space Filler (ISF) algorithm introduces new points by starting from the midpoint of each design variable. Each point is strategically added to maximize the minimum distance between existing points. The Greedy algorithm offers a methodology for constructing an ISF Design of Experiments (DOE) in Ref. [62]. Uniform Latin Hypercube (*ULH*), as described in Ref. [13],

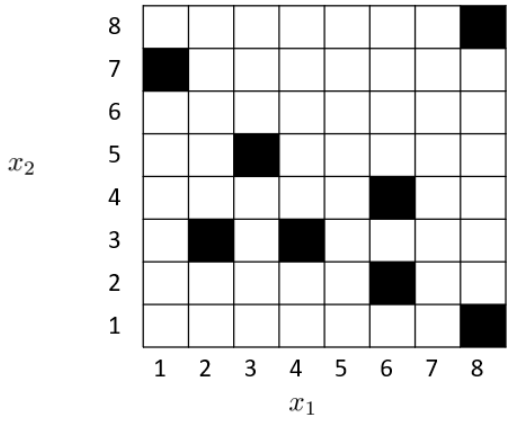

(a) Random Scheme

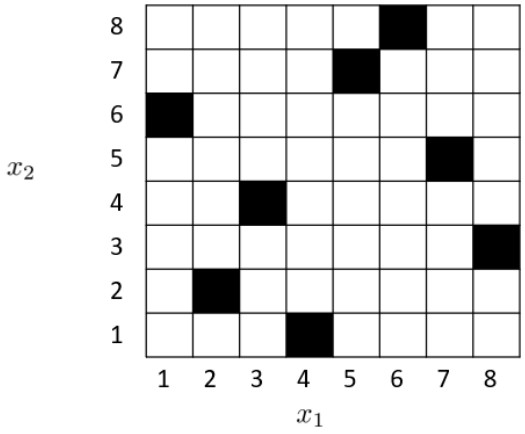

(b) ULH Scheme

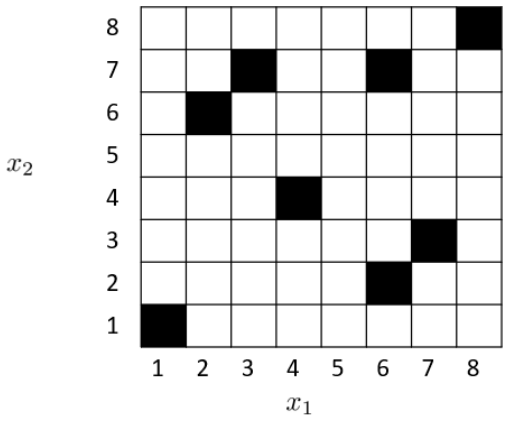

(c) Sobol Scheme

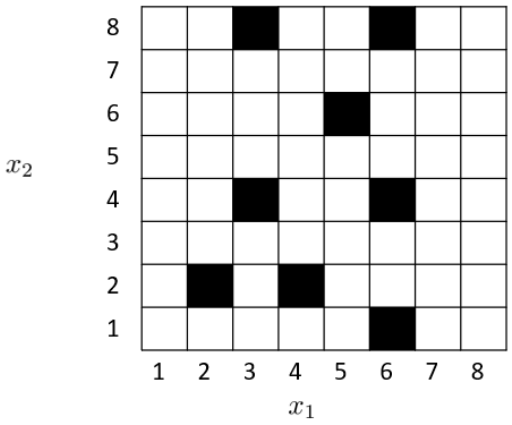

(d) ISF Scheme

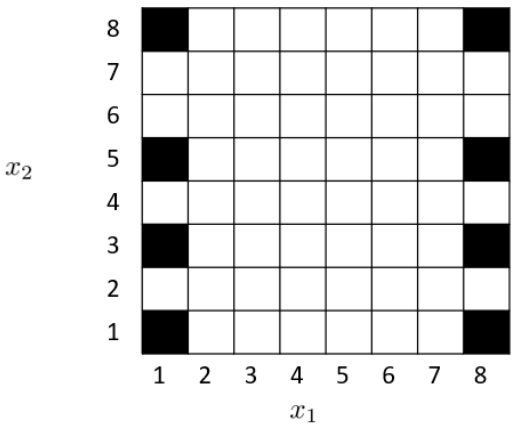

(e) Full Factorial Scheme

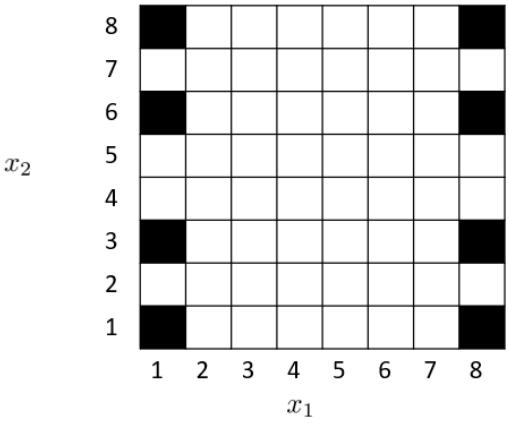

(f) Taguchi Orthogonal scheme

Figure 1.5: Comparison between different DOE schemes

constitutes an advanced Monte Carlo sampling technique. It divides each design variable range into n intervals and selects a random value from each interval. This approach ensures a uniform coverage of the design space, even with a limited number of points. Another DOE algorithm is the full factorial method Ref. [63], which divides the design variable ranges into levels and explores all possible combinations of factors. However, this approach can be time-consuming, particularly when the number of levels is low. A modified version of the full factorial is the orthogonal DOE, developed in Ref. [64]. The difference between the various algorithms is shown in Figure 1.5. Specifically, a design space with 64 points is provided, including 2 variables (x_1 and x_2), in which 8 samples are chosen based on the different DOE algorithms described above. It can be seen that the best algorithm that can uniformly cover the design space is the *ULH*.

1.1.5 Architectures for MDO process

There are different ways to solve the same optimization problems, considering that it is possible to have different inter-connections between the disciplines or a different logic flow order, as explained in Ref. [65] in which the optimization architecture is cataloged and described in detail. Selecting an *MDO* architecture implies deciding a strategy for coupling the different disciplinary models in order to solve the overall optimization problem. The *MDO* architectures can be classified into monolithic and distributed approaches, depending on if the overall problem is solved all together or if it is broken up into multiple sub-problems.

The first generation of *MDO* architectures defined the solution involving the integration of various analyses with a single optimizer in a single-level approach, which worked well only for small problems. A second generation of *MDO* architectures has been defined, using distributed analysis and optimization with parallel computations on multiple computers, with modular analysis, interdisciplinary communication, and database management. Examples of this second generation include iSight, Boeing Access Manager, and Langley FIDO. Finally, a third generation, defined as strategies for distributed design optimization, has improved efficiency in managing the complexity of large-scale applications.

The timing of system or discipline analyses is another important aspect of the *MDO* architecture, with two different approaches: Nested Analysis And Design (NAND) and Simultaneous Analysis And Design (SAND) (see Ref. [66]). These can be used at both the system and discipline levels. The NAND approach includes the determination of independent variables, followed by an internal loop to find the coupling and state variables. In contrast, the SAND determines simultaneously the independent and dependent variables to avoid internal loops, introducing copies of variables for each sub-problem in the discipline and consistency constraints. The Figures 1.6 show the gradual parallelization of a Multidisciplinary design at the discipline level, from the full nested to the full simultaneous scheme, through the introduction of consistency constraints and copies of the design variables. Over time, different architectures have developed, including monolithic and distributed approaches, as well as concurrent or nested analyses. The literature on Multidisciplinary Design Optimization (MDO) presents several studies, with notable contributions such as Hafka et al. Ref. [67] and Balling and Sobieski Ref. [66] providing early insights into the MDO approaches. Alexandrov and Hussaini Ref. [68] edited a comprehensive collection of papers that discussed in depth the state of the art of MDO, while Martins Ref. [65] presented a survey highlighting the most recent developments in MDO architectures.

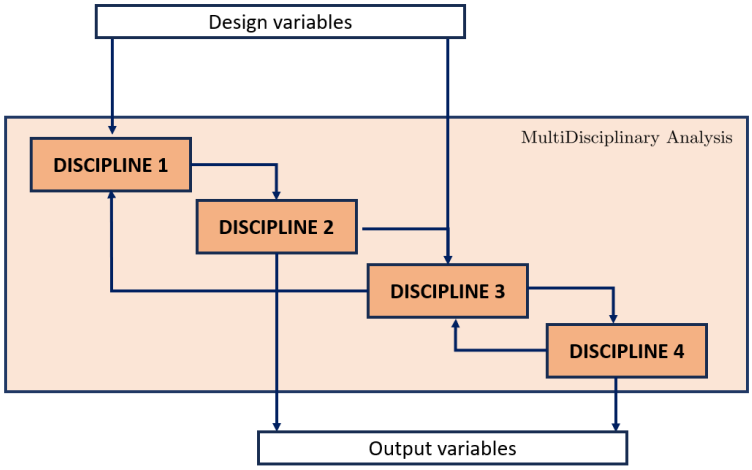

(a) Full nested

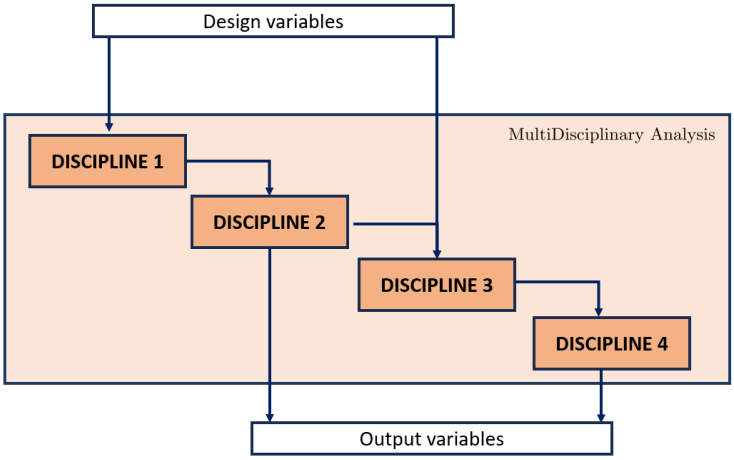

(b) Introduction of consistency constraints

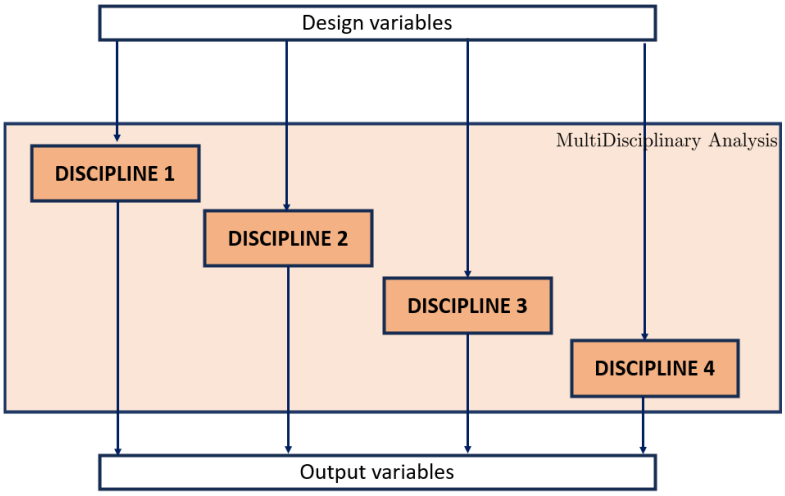

(c) Full-simultaneous

Figure 1.6: The gradual parallelization of a Multidisciplinary design at the discipline level, starting from a full-nested analysis and ending in a full-simultaneous analysis

The simplest way to implement a multidisciplinary optimization problem is to handle it as a single optimization problem while ensuring the multidisciplinary feasibility. The Multidisciplinarity arises from the fact that several elements, such as design variables, objectives, and constraint functions, may affect or be affected by multiple disciplinary behaviors. This optimizer regulates the set of design variables based on the values of the objectives and constraints, established by performing disciplinary analyses at each iteration. These analyses can range from detailed physical simulations performed by disciplinary software to database interrogation, of varying complexity. In this context, some of the most widely used monolithic architectures include the MultiDisciplinary Feasible (MDF) and the Individual Design Feasible (IDF), subdivided according to the kind of feasibility of the architecture (see Ref. [69]). The achievement of disciplinary autonomy in complex and large *MDO* problems involves the decomposition of the optimization problem into sub-problems, whose aim is to produce the same solution at reassembly. Large-scale systems are typically designed using a distributed design approach, in which each design group is responsible for optimizing a specific discipline or subsystem by adjusting its own subset of design variables. Decomposing a problem with strongly coupled components is a challenging task that requires careful consideration. Several methods have been developed to efficiently decompose such problems, as Collaborative Optimization (CO) and Bi-Level Integrated System Synthesis (BLISS).

MultiDisciplinary Feasible (MDF) and Individual Design Feasible (IDF)

The MultiDisciplinary Feasible (MDF) architecture is a simple and fully integrated optimization approach, it is based on a monolithic NAND-NAND (Necessary AND Necessary Nonconflicting) structure in which all disciplines are interconnected and a multi-disciplinary analysis is conducted to calculate the complete set of output variables. This process extends the single-discipline optimization concept to multiple disciplines. The MDF uses a single optimizer to manage the entire optimization process. The optimizer provides a vector of design variables to the design process, and all discipline analyses are carried out to obtain the system output variables, used to evaluate the objective and constraint functions in the optimization process (see Fig.1.7). The main advantage of MDF is that it returns a design that always satisfies the consistency of the process, while the main disadvantage is that the architecture requires the full multidisciplinary analysis at each iteration. A set of common variables must be computed and returned to the optimizer each time to evaluate the goals and the constraints. Until a consistent set of variables is found, disciplinary analyses must be performed multiple times, so this procedure requires an iterative process, in addition to the main optimization, to be developed.

Like MDF, the Individual Design Feasible (IDF) does not change the optimization problem formulation and can be related to a monolithic SAND-NAND procedure. In the IDF approach, direct communication between disciplines is eliminated, so each discipline can be solved in isolation (see Fig. 1.8). Moreover, this architecture is based on a system-level SAND approach, which allows parallel computation for each discipline. Coupling variable targets are used to share information between disciplines, specifically coupling variables copies and consistency constraint are introduced. In the original formulation, the IDF adds the equality constraint per set of coupling variables, in order to ensure that the coupled system is consistent. The main disadvantage of IDF is the increase in the size of the optimization problem, because an equality constraint is added for each coupling variable. Moreover, another problem can arise when using a gradient-based algorithm for

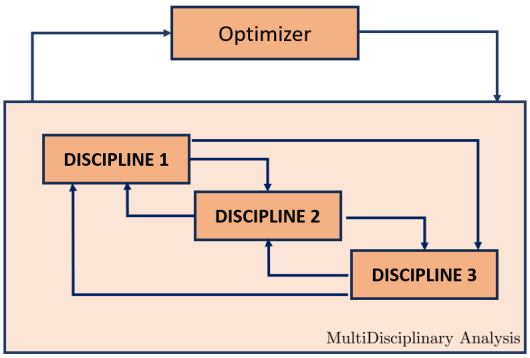

Figure 1.7: Simple scheme of MultiDisciplinary Feasible (MDF)

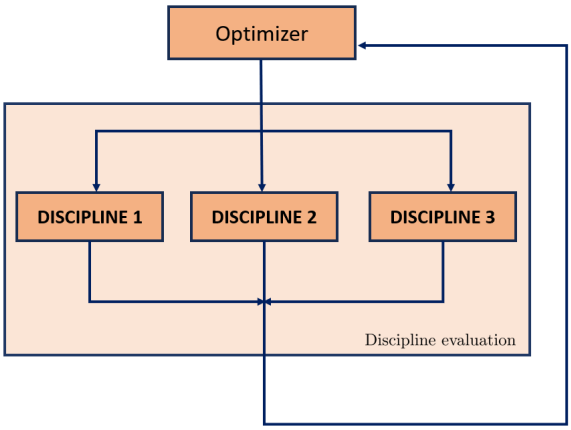

Figure 1.8: Simple scheme of Individual Design Feasible (IDF)

optimization, disciplinary analysis being very expensive.

Collaborative Optimization (CO) and Bi-Level Integrated System Synthesis (BLISS)

The Collaborative Optimization (CO, Ref. [9]) and the Bi-Level Integrated System Synthesis (BLISS, Ref. [10]) are two more recent distributed architectures. The CO and BLISS architectures allocate the constraint satisfaction to the disciplinary sub-optimizations, which are closely associated with such constraints (see Fig. 1.9). Another level of decomposition is introduced, local objective functions to be optimized are assigned to individual disciplinary subsystems, each of which manages its own design variables (which can be local degrees of freedom or duplicates of global variables). Here, the global variables are optimized at the system level, while their duplicates are used by sub-spaces, and at the system level the consistency is ensured. The use of these architectures has several advantages, such as the possibility of using a more suitable software for each subspace, or such as the reduction in the number of shared constraints and the real independence in design sub-optimizations due to the use of local variables that allow the creation of disciplinary groups, which leads to making design decisions based on local problems. In the CO system, the optimizer maximizes the global objective function and it handles the global design variables, the copies of these global variables are given only to the sub-optimization problems influenced by them, and finally the sub-optimizers manipulate them to satisfy the local constraints. The measure of interdisciplinary consistency could be defined in different ways, by using linear or quadratic functions (Ref. [70]). On

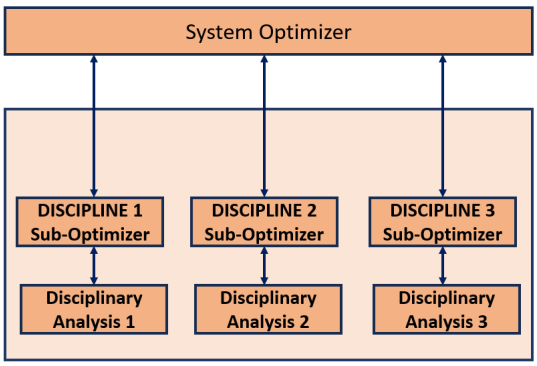

Figure 1.9: Simple scheme of CO and BLISS

the other hand, the basic approach of the BLISS architecture involves the search within the design space through the use of a sequence of linear approximations of the original design problem. Such approximations are driven by user-chosen bounds on the design variable steps, preventing the design point from moving too far away and compromising the accuracy of the approximations. Unlike CO, the BLISS formulates all objective and constraint functions as a linear approximations that are centered on the initial design, calculated at each iteration using the coupled sensitivity information. In order to solve the system sub-problem and prevent the violation of discipline constraints due to variations in shared design variables, the post-optimal derived information is crucial. This knowledge captures the variation of the optimized discipline constraints in response to the variations in the system design variables. However, the considerable cost associated with the computation of these post-optimal derivatives is the main disadvantage of the BLISS architecture.

1.2 The optimization methodology developed

Several tools have been proposed in the literature for the *MDO* of aircraft, which are usually supposed to process the entire optimization, including also the optimization algorithm. Generally, due to the high computational burden a common approach is to use the surrogate models or databases in order to limit this effort. In the present PhD activity, a tool for the model generation and for the simulation of structural, aerodynamic and control laws behaviours is developed and integrated in the optimization process, in order to explore the preliminary design of aircrafts (see Chapter 2 for more details on the modelling part). Specifically, this tool is able to consider the variation of the aircraft geometry during the optimization process through a re-meshing mechanism and automatically perform high-fidelity analysis for the current aircraft configuration without the use of surrogate models. In order to correctly perform the multidisciplinary design optimization, it is essential for the process being able to modify and tune all the relevant design parameters. During the preliminary design, the design variables that significantly influence the disciplines involved in optimization are going to be considered. For this purpose, the model used in the optimization process is expected to carry out the entire analyses associated to the structural, aerodynamic, and the control law disciplines, taking into account adequately for the variation in the key design parameters. Considering some variations in the structural characteristics, such as thickness and area of the structural elements, it could be quite easy to handle such variables directly in a finite element model. In fact, currently commercial FEA codes can execute the structural optimization (e.g., MSC.Nastran®'s solver 200),

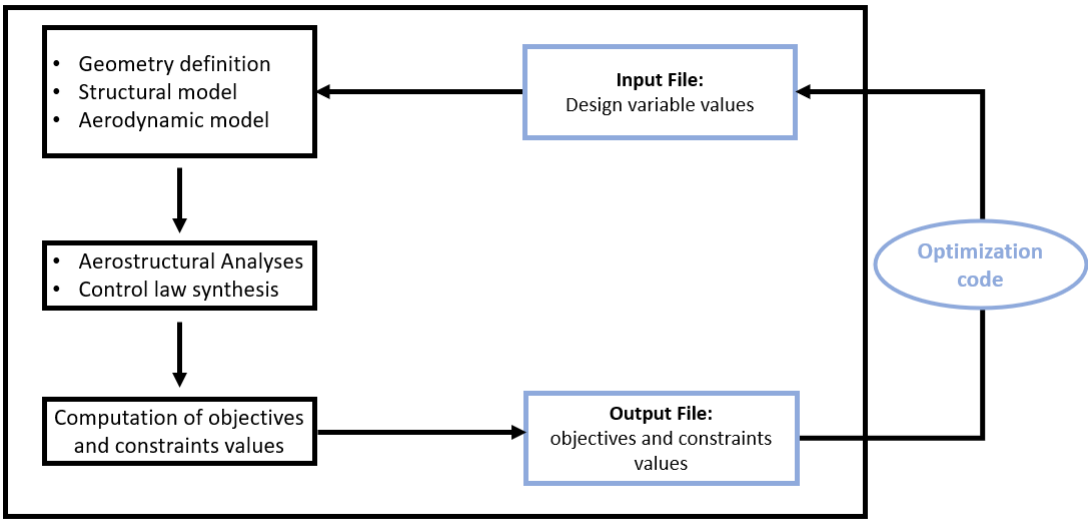

Figure 1.10: The aeroservoelastic model interaction with the optimization algorithm

allowing the user to tune element properties to optimize a particular structural objective subject to specific structural constraints, but they cannot change the model during the optimization. For these issues, the aero-structural control tool has been developed as part of the present PhD activity, based on the requirements of automation and modeling. This tool is capable of handling the entire structural, aeroelastic and control analyses, starting from the generation of the structural finite element model and the aerodynamic model, up to the evaluation of aerostructural performance. In the present work, for each design of the optimization, the aerodynamic and structural numerical models and the control law synthesis are generated. The Figure 1.10 shows the flowchart of the implemented algorithm, which aims to provide the system optimization process with the values of the objectives and constraints as a result of the design variable choice. First, the model geometry is computed using the values of the fixed parameters and the choice of the design variables. The structural and aerodynamic meshes are generated for the current geometry and, as a consequence, the input files (i.e., MSC.Nastran® input files) are produced for that design. In addition, the aerodynamic model based on the analytical functions is also defined in order to use it for the dynamic aeroelastic analyses, which are too slow if solved through MSC.Nastran® solver (see Sect. 2.3 for more details). Next, the tool developed runs all the structural and aeroelastic analyses and tunes the control law for the specific design. More specifically, the results of the analyses requiring the use of a FEM solver is read through the use of read codes for the MSC.Nastran® outputs files. Finally, the objectives and constraints values are computed for each design and are processed by the optimization code. Therefore, the optimization procedure proposed is capable of taking into account the changes of the aircraft geometry during the optimization process due to a re-meshing mechanism of the aircraft geometry, which allows to analyze the current design through a real representation and to perform high-fidelity simulations. The algorithm can exchange input design variables and output constraint and objective values with the optimization code through interchange files. The optimization process presented requires the interaction of all the disciplines involved through the use of their inputs and outputs, specifically this interaction is handled directly by the developed tool. In addition, the definition of the control law model necessarily requires an internal optimization

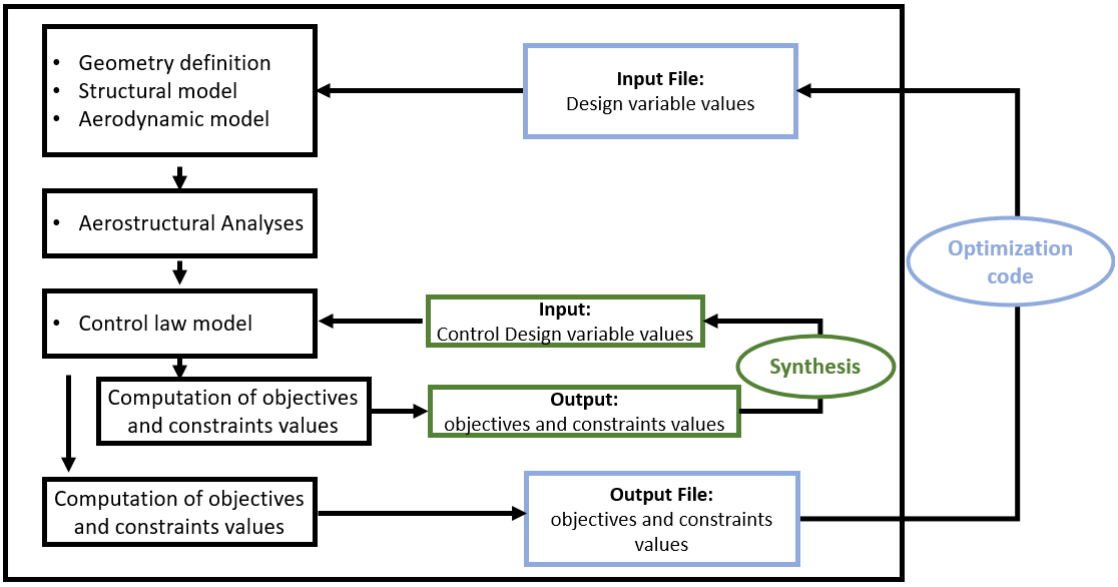

Figure 1.11: The aeroservoelastic model with the control law internal optimization and with the external optimization process

loop, specific for each design. For this purpose, an internal optimization process for the control law is incorporated, so it is associated with objective, design variables and constraints specific for the controller synthesis (see Fig. 1.11). The optimization of the controller is tailored to each design, and the initialization values are unique for each design. This optimization is unlocked as required, specifically when addressing dynamic instabilities or reaching maximum loads.

1.2.1 Discipline analyses performed and disciplinary influence of the design variables

To comprehensively assess the interdisciplinary dynamics of projects throughout the optimization process, the different disciplines engaged in the project are presented which share and exchange information with each other. Specifically, the evaluation of the goals and the constraints of the different disciplines are calculated sequentially, taking into account the previously calculated information. As previously mentioned, the optimizer selects a particular value for the design variables, upon which the structural model, aerodynamic model and control law model are generated. Hence the disciplinary analyses conducted are associated to the models:

- **Aircraft Structural Model (ASM)**
  First, the overall *structural weight estimation* of the aircraft and its mass center are calculated using the weight generator included in MSC.Nastran® . This method includes all masses, both the structural and the non-structural masses, defined in the FE model from the FEM model generator. Moreover, this discipline receives as input the loads calculated through the trim, maneuver and gust response analyses and calculates *the maximum stress* on the structure, on which a constraint on the maximum value eligible is placed, associated with the chosen material and a certain factor of safety. Hence, the outputs of the structural model, i.e., the maximum stresses, depend on the analyses performed using the dynamic model and the aeroelastic model, which are going to be specialized for the critical points of the flight envelope.

- **Aircraft Dynamic Model (ADM)**
  Taking into account the dynamic model of the aircraft, the static stability of the aircraft is verified and the characteristics of the rigid dynamics of the aircraft are checked, requiring a minimum value of damping. Selected static analyses are performed in order to simulate specific flight points on the flight envelope through the use of the Nastran® solver 144, to evaluate the static displacements, loads, and trim angles including the following:

  - *Trim condition* for a given flight condition, in which the tail surface is used to balance the forces. Constraints are applied on the maximum values of the angle of attack and the tail angle required for trimming the aircraft.
  - *Maneuver condition* for a given flight condition. The elevator surface is used to maneuver, in which the aircraft is subjected to a $2.5g$ down gravity load. Constraints are applied on the maximum values of the angle of attack and the angle of elevator required for maneuvering the aircraft. In addition, to be in accordance with the safety specifications for maximum loads in maneuvering, an additional analysis of maneuvering with ailerons symmetrically unlocked in their maximum rotation is added. On such analysis the *Maneuver Load Alleviation (MLA)* specifications are taken into account through constraints on the maximum load in maneuvering with the unlocked ailerons.
  - *Aileron response* check for given flight conditions. It is required to have a certain capability of rolling the aircraft for low speed flight conditions, while for higher flight speed conditions it is required to always have a certain ability to roll, never entering into the aileron reversal condition.

- **Aircraft Aeroealstic Model (AAM)**
  The aerodynamic model based on the indicial functions and the aircraft structural model are considered for the *dynamic stability check* and the *gust response*. The decision of not using the Nastran® solver for these analyses is associated to the computational time (for more information see the Chapt. 2.3). In fact the use of the analytical model provides a good approximation of stability and gust response with computational times reduced by 95% compared to the FEM solver. Constraints on the flutter speed of the system with no controller are applied. In addition, other constraints related to the maximum loads achieved in the gust response are imposed.

- **Aircraft Control Law Model (ACM)**
  A fixed controller structure is considered to fit well within the particular specifications for stability and load reduction during the gust. Such a structure is tuned specifically for each design, based on the need to have *Active Flutter Suppression (AFS)* or *Gust Load Alleviation (GLA)*. Specifically, the structure is tuned through an internal optimization process, enabled as needed by the design, initialized independently from other designs, in which the design variables are the controller characteristics.

- **Aircraft Performance Model**
  Finally, taking into account all the previous information, the aircraft performance model estimates the required targets, evaluating the performance of the aircraft.

		Wing	Tail	Aileron
Structural	Skin panels	root thickness	root thickness	⟍
		thickness ratios	thickness ratios	⟍
	Spars	root web thickness	root web thickness	⟍
		thickness ratios	thickness ratios	⟍
		root cap area	root cap area	⟍
		cap area ratios	cap area ratios	⟍
	Ribs	number	number	⟍
		root thickness	root thickness	⟍
		thickness ratios	thickness ratios	⟍
Aerodynamic	Angles	sweep	⟍	⟍
	Length	root chord	root chord	chord
		taper ratio	taper ratio	⟍
		span	span	span
	Position	⟍	⟍	position
Control	Filters	⟍	⟍	coefficients
	PID	⟍	⟍	PI

Table 1.1: Design Variables

It should be emphasized that the proposed methodology optimizes the aircraft model by focusing exclusively on longitudinal dynamics, as noted by the analyses performed, since this is sufficiently determinative for the design phase under consideration.

Since the optimization problem involves objectives and constraints sensitive to the structural, aerodynamic and control variables, in order to allow the optimizer to modify the design, 49 design variables are chosen, classified considering their disciplinary influence (see Tab. 1.1). More specifically, the design variables choice is conducted considering all the disciplines involved in the optimization problem and the analyses to be performed. The design variables are chosen in order to generate a wide design space and, to evaluate a very different airframe designs by exploring it. The design variables selected involve the variables associated with the wing, the tail surfaces, the aileron, and the elevator surfaces. While the aileron dimensions are design variables of the process, the elevator dimensions are defined by a fixed percentage relative to the tail dimensions, that vary during the optimization. Is worth pointing out that there are actually some other variables in the

problem, representing the nonstructural masses, these are not directly chosen by the optimizer, but depend on the size chosen for the surfaces. For example, the larger the size of the aileron the greater the masses representing the actuators in the model.

The optimization methodology calculates the sizing of the wing, the tail and the control surfaces, while considering the structure and the mass of the fuselage, the engines and the stowed fuel as fixed.

1.2.2 Disciplinary analysis specialization and imposition of constraints

The previously mentioned analyses are here specialized to account for the most critical flight and dimensional conditions for the aircraft. For this reason, two flight envelopes are considered for each design, one for the aircraft configuration with full wing tanks (*Maximum Take Off Weight (MTOW)* configuration) and one for the aircraft configuration with empty wing tanks (*Maximum Zero Fuel Weight (MZFW)* configuration). The Figure 1.12 shows the approach used to choose the critical points in the flight envelope. From the regulatory reference, a reference flight envelope with the maximum value of the load factor imposed as $n = 2.5$, with the maximum value of the angle of attack α_{max}, and with the minimum dynamic pressure for the stall without devices q_{Ds} is taken into account (in black in the Fig. 1.12(a)). By assumption it is considered that the loads do not vary excessively with the value of the Mach value. Each design of the optimization process is described by two flight envelopes, namely *MTOW* and *MZFW* (in blue in the Fig. 1.12(a)), with flight characteristic dynamic pressures, whose most representative values are the dynamic pressure at the flight altitude and cruise speed and the dynamic pressure at the flight altitude and dive speed (the flight altitude is imposed to be $h = 12000m$). The outputs of the aircraft structural model, i.e., the maximum stresses, depend on the analyses performed with the aircraft dynamic and aeroelastic model, which will be specialized here for the critical points of the flight envelope, and which depend on both the weight estimation (performed by the structural model) and the definition of the aerodynamic surfaces. Starting with the analyses carried out using the aircraft dynamic model, it can be observed that the critical flight envelope for these kind of analyses is the one associated with the *MTOW* condition (shown in orange in Fig. 1.12(b)). Therefore, the total mass of the aircraft model is considered for such analyses. Moreover, the previously described analyses are now considered in the reference flight envelope, i.e., the trim analysis (at $n = 1$), the maneuver analysis with and without *MLA* (at $n = 2.5$), and the aileron response (at $n = 1$). For each of these points, the specific design must meet the controllability constraints of the aircraft, as well as fit the maximum load specifications. Instead, the analyses carried out on the aeroelastic model of the aircraft are now considered, whose critical issues are associated with the model with the wing tanks emptied, i.e., the case *MZFW* in green in Fig. 1.12(b). In the velocity range limited by the values of $0.6U_c$ and U_D, where U_c is the cruise speed and U_D is the dive speed, for constant null altitude $h = 0$, the aeroelastic stability check of the aircraft is carried out (green region in Fig. 1.12(b)). Finally, the gust response analysis is carried out again in the case of empty tanks at $n = 1$ and $h = 0m$. The aeroelastic analyses define the analysis conditions of the aircraft control model, in fact the analyses associated with *AFS* are going to be done using the same conditions for which the aeroelastic stability check is done, while the *GLA* analysis, in the same way, is done at the same conditions for which the gust is evaluated (see the purple boxes in Fig. 1.12(b)).

Having described in detail all the analyses conducted, it is now possible to describe the con-

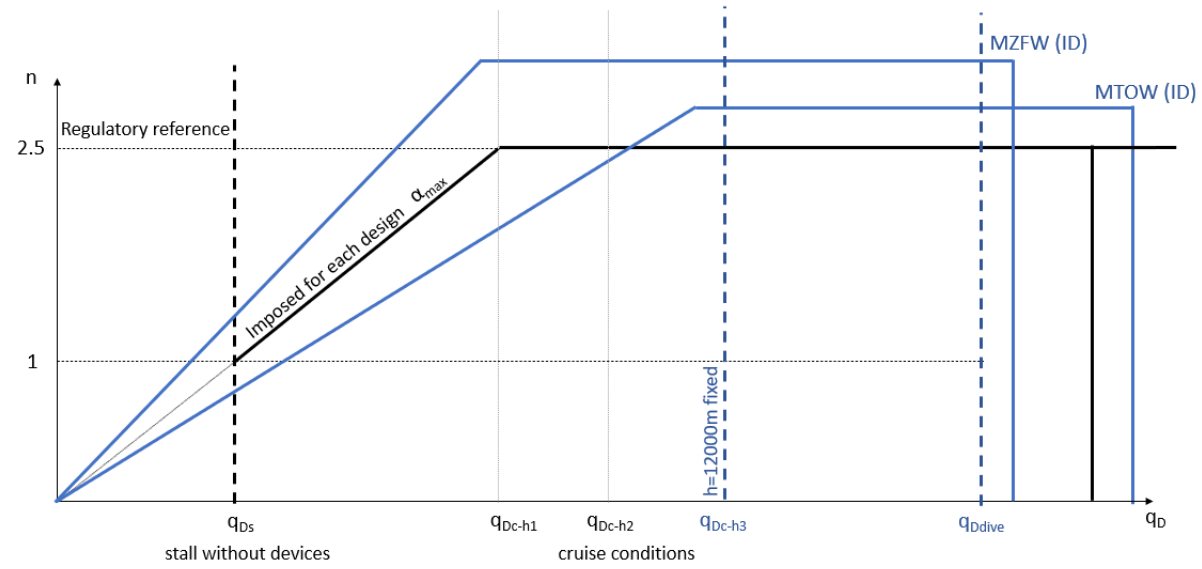

(a) Reference, *MTOW* and *MZFW*

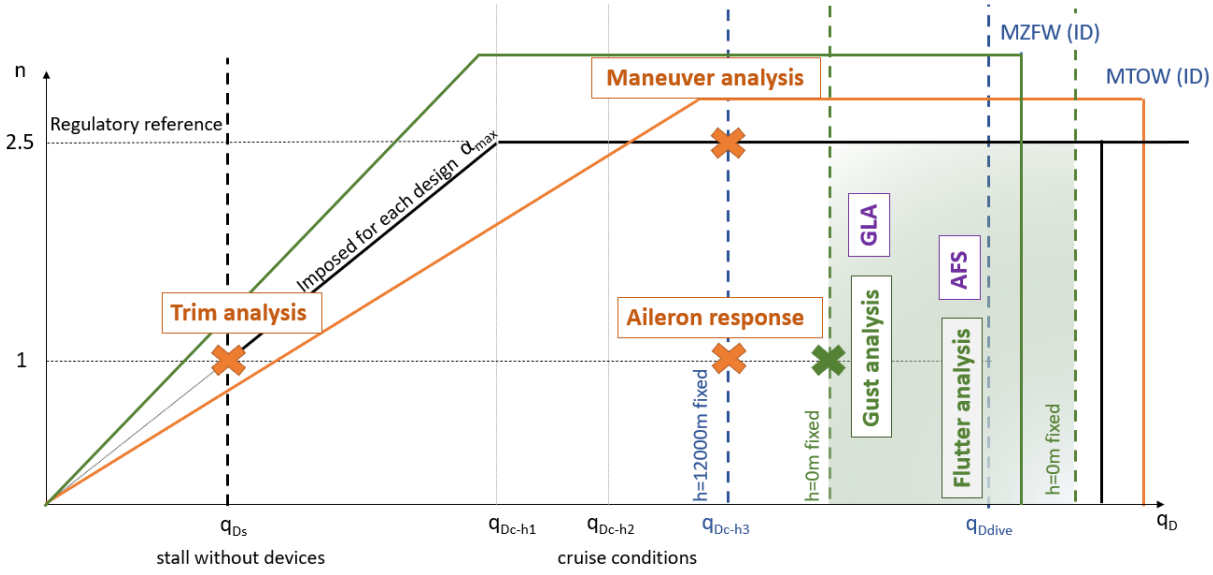

(b) Critical points

Figure 1.12: Critical points in the flight envelope for each design in the optimization process

straints of the proposed methodology. In particular, the disciplinary categorization of these constraints is addressed, as illustrated in Table 1.2. Structural constraints are imposed on the maximum loads identified in the static trim and maneuvering analyses, as well as on the maximum loads determined in the dynamic gust analyses. Additional aerodynamic constraints also come into play, which include limitations on characteristic angles in the static analyses (to also constrain the value of $C_{L_{max}}$), conditions that prevent aileron reversal, and constraints on the flutter speed. Next, constraints on control surface geometry and controller synthesis are applied. For example, constraints on the roll time t_r and controllability derivative for the elevator $C_{m_{\delta_e}}$ fall in the geometry category, while the other constraints relates to the restrictions on the flutter speed and on the maximum loads during the gust using the controller fall in the controller synthesis category.

The mathematical formulation of the problem could be summarized as

$$\begin{aligned}
\sigma_{max}(\mathbf{x}) &\leq \sigma_a \\
\alpha_{trim}(\mathbf{x}) &\leq \alpha_{max} \\
\delta_{t_{trim}}(\mathbf{x}) &\leq \delta_{t_{max}} \\
\delta_{e_{trim}}(\mathbf{x}) &\leq \delta_{e_{max}} \\
U_r(\mathbf{x}) &\geq \bar{U}_r \\
U_f^{OL}(\mathbf{x}) &\geq \bar{U}_f^{OL} \\
U_f^{CL}(\mathbf{x}) &\geq \bar{U}_f^{CL} \\
C_{m_{\delta_e}} &\geq \bar{C}_{m_{\delta_e}} \\
t_r &\leq \bar{t}_r
\end{aligned} \tag{1.4}$$

where the right-hand side of each inequality represents the limit value chosen by the user. These imposed limit values are going to be used to scaled the constrained variables, in order to ensure that the optimizer treats all constraints uniformly, regardless of their original magnitudes.

1.2.3 Objectives to be optimized

The world of aviation mobility is at the forefront of innovation and evolution. Currently, the growth of this market is associated with several factors, as explained in Ref. [71] (see Fig. 1.13). The constant requirement for efficiency has driven the aviation industry to a phase where reducing flight times, improving speed performance and reducing the environmental impact are imperative. With the increasing interconnection and globalization of societies, the need for fast, reliable and time-efficient air travel has never been more pronounced.

In this context of industrial growth accounting for efficiency and environmental impact, the optimization methodology proposed in this PhD activity is focuses its objectives on aircraft performance during cruise phases. The first objective to be maximized is the flight speed in cruise conditions U_c, as this allows for shorter flight times, a feature that could be attractive to potential customers. The second objective to be maximized is the mileage range R, while keeping the amount of fuel used constant, which could be considered as another attractive aspect for potential customers.

$$\underset{\mathbf{x}}{maximize}: \quad \Psi(\mathbf{x}) = [U_c(\mathbf{x}), R(\mathbf{x})] \tag{1.5}$$

	Discipline Description		
Constraint	Structural	Aeroelastic	Control
TRIM	Von Mises σ_{max}	Attack Angle α_{trim} Balance Angle $\delta_{t_{trim}}$	
MANEUVER	Von Mises $\sigma_{max_{MLA}}$	Attack Angle α_{trim} Elevator Angle $\delta_{e_{trim}}$	Static Controllability $C_{m_{\delta_e}}$
AILERON RESPONSE	Von Mises σ_{max}	Reversal speed U_r	Rolling time t_r
AEROELASTIC STABILITY		Flutter speed without controller U_f^{OL}	
GUST RESPONSE	Von Mises σ_{max}		
ACTIVE FLUTTER SUPPRESSION			Flutter speed with controller U_f^{CL}
GUST LOAD ALLEVIATION			Von Mises $\sigma_{max_{GLA}}$

Table 1.2: Disciplinary Constraints

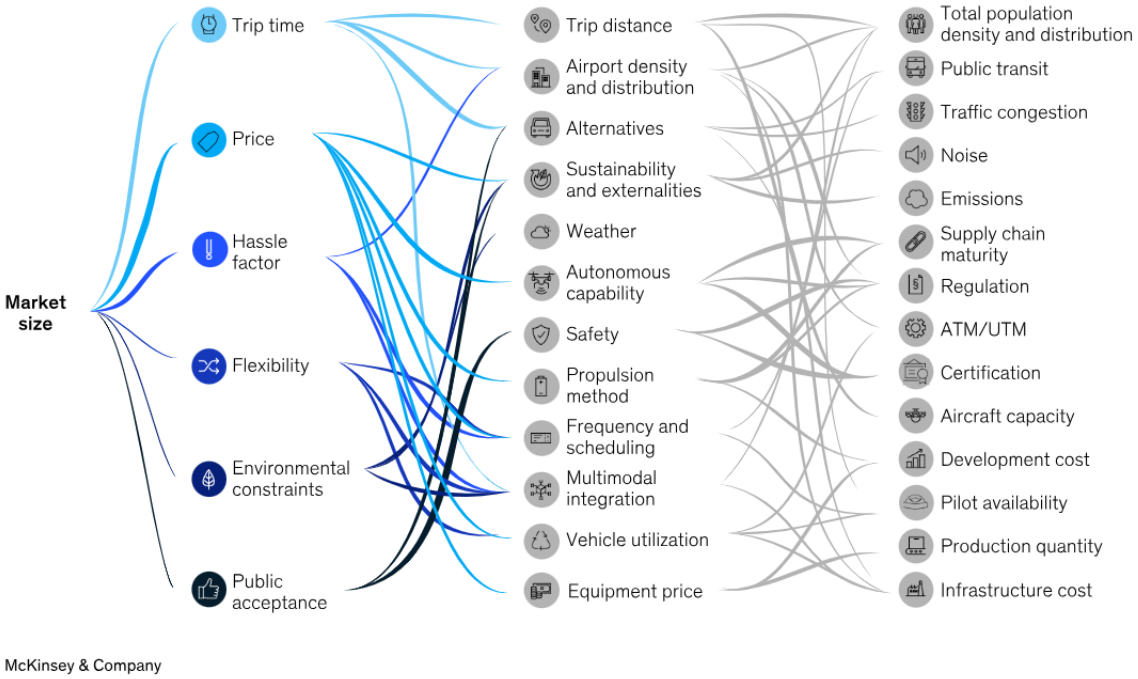

Figure 1.13: Growth of the air market depend on numerous inter-related factors Ref. [71]

However, these objectives are both computed for each design in the maximum lift-to-drag ratio flight condition, considered as the cruise condition.

The optimization of the aircraft model proposed involves the optimization of the wing and the tail surfaces. For the definition of the aircraft performance to be maximized, it is necessary to define some explanatory variables of the aerodynamic model taking into account both surfaces, such as the positions of the aerodynamic centers of the two surfaces and the value of the Equivalent Aspect Ratio AR_e. Taking into account the lift contribution from the half wing L_w and the half tail L_t, the aerodynamic centers of the two surfaces are calculated

$$\begin{aligned} x_w &= \frac{\int_0^{b_w/2} l_w(\eta)\, x(\eta)\, d\eta}{L_w} \\ x_t &= \frac{\int_0^{b_t/2} l_t(\eta)\, x(\eta)\, d\eta}{L_t} \end{aligned} \tag{1.6}$$

in which $b_w/2$ and $b_t/2$ are the semi-span of the wing and the tail. For calculating the AR_e, are used the equation of Drag (see Fig. 1.14),

$$D = D_0 + \underbrace{q_D S_w \frac{C_{L_w}^2}{\pi AR_w e} + q_D S_t \frac{C_{L_t}^2}{\pi AR_t e}}_{D_i} \tag{1.7}$$

in which D_0 is the shape drag, D_i is the induced drag q_D is the dynamic pressure, e is the Oswald factor assumed to be $e = 0.8$, S is the surface, AR is the aspect ratio and C_L is the lift coefficient of the specific surface, denoted with $_w$ for the wing and $_t$ for the tail; and the equations of Lift and

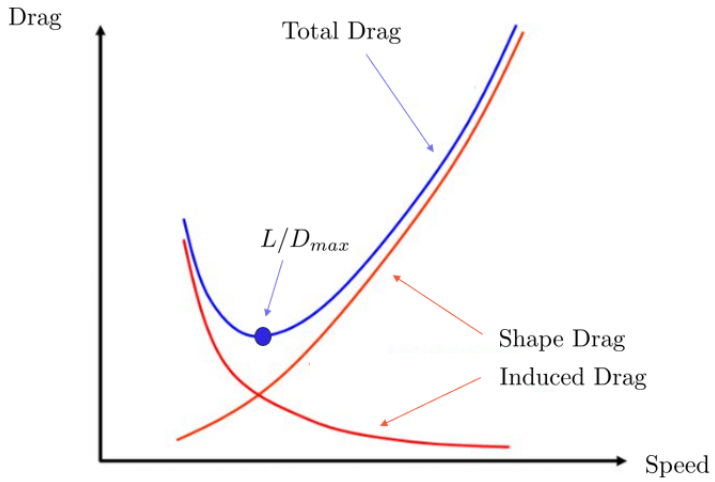

Figure 1.14: Drag contributions: how to maximize the lift-to-drag ratio

Moment around the aircraft mass center

$$\begin{cases} C_{L_w} + C_{L_t}\frac{S_t}{S_w} = C_L \\ C_{L_w}(x_w - x_G) + C_{L_t}(x_t - x_G)\frac{S_t}{S_w} = 0 \end{cases} \tag{1.8}$$

in which x_G is the position of the aircraft mass center. Starting from these equations, the value of the AR_e is calculated (see App. A.2 for more details), namely

$$\begin{aligned} D &= D_0 + \underbrace{\frac{q_D S_w}{\pi AR_e e} C_L^2}_{D_i} \\ \frac{1}{\pi AR_e e} &= \frac{\beta_1^2}{\pi AR_w e} + \frac{\beta_2^2}{\pi AR_t e}\frac{S_t}{S_w} \end{aligned} \tag{1.9}$$

in which

$$\begin{aligned} \frac{1}{\beta_1} &= 1 - \left(\frac{x_w - x_G}{x_t - x_G}\right) \\ \beta_2 &= -\beta_1\left(\frac{x_w - x_G}{x_t - x_G}\right)\frac{S_w}{S_t} \end{aligned} \tag{1.10}$$

At this point, the maximum lift-to-drag ratio flight condition can be defined for each design. Demanding the maximum lift-to-drag ratio L/D is equivalent to finding the minimum of the inverse ratio D/W, in the level flight condition in which the lift is equal to the weight $L = W$. The equation to solve is

$$\frac{\partial}{\partial W}\left(\frac{D}{W}\right) = 0 \tag{1.11}$$

Taking into account the value of the lift coefficient in the level flight condition

$$C_L^2 = \frac{W^2}{q_D^2 S_w^2} \tag{1.12}$$

the drag-to-weight ratio is

$$\left(\frac{D}{W}\right) = \frac{D_0}{W} + \frac{1}{\pi\, AR_e\, e}\frac{W}{q_D S_W} \tag{1.13}$$

and from the equation

$$\frac{\partial}{\partial W}\left(\frac{D}{W}\right) = -\frac{D_0}{W^2} + \frac{1}{\pi\, AR_e\, e}\frac{1}{q_D S_W} = 0 \tag{1.14}$$

is possible to find the optimum weight value, the optimum value of the drag, and finally the optimum value of lift-to-drag ratio, whose value depends on the Equivalent Aspect Ratio, the Oswald factor and the shape drag coefficient C_{D_0}.

$$\begin{aligned} W_{opt}^2 &= \pi\, q_D\, AR_e\, e\, S_w\, D_0 \\ D_{opt} &= 2D_0 \\ \left(\frac{L}{D}\right)_{max} \rightarrow \left(\frac{W}{D}\right)_{opt} &= \sqrt{\frac{\pi\, AR_e\, e}{4C_{D_0}}} \end{aligned} \tag{1.15}$$

For the aircraft shape drag coefficient see Sect. 2.3.5. Finally, for this flight condition the objective function U_c is calculated

$$U_c = \sqrt{\frac{2W_{opt}}{\rho S_w}\sqrt{\frac{1}{\pi\, AR_e\, e\, C_{D_0}}}} \tag{1.16}$$

In addition, it is worth mentioning that for this calculation, a certain percentage of the fuel used for takeoff is considered in the mass calculation, since the aircraft is in the cruise condition. The second objective, the aircraft range, is calculated by using the Breguet formula for jet aircraft for performance at constant speed and lift coefficient C_L, Ref. [72]

$$R = \frac{U_c}{SFCJ}\,\frac{C_L}{C_D}\, ln\frac{W}{W - W_f} \tag{1.17}$$

in which the $SFCJ$ is the thrust-specific fuel consumption, while W is the weight of the aircraft at the take off and W_f is the weight of the fuel stowed. By looking at the formulations of the two objective functions just outlined, it is possible to identify a correlation with the most frequently addressed objective functions in the literature, such as the weight minimization and the lift-to-drag ratio maximization. The request to maximize the aircraft range in the optimum performance conditions implicitly implies the need to maximize the lift-to-drag ratio. In contrast, the request to maximize the flight speed induces a change in the opposite direction of the lift-to-drag ratio. By requiring simultaneously the maximization of both objectives, i.e., cruise speed and the mileage range, the need to minimize aircraft weight is essentially emphasized. This intricate relationship between the proposed objectives and the traditional considerations of weight and lift-to-drag ratio

underscores the complex interconnection and sensitivity of design decisions in aviation. The tool assessment performs the objective function analysis with a specific approach. The structural weight is estimated with the highest accuracy, through high-fidelity evaluation. On the other hand, the aerodynamic lift-to-drag ratio and the mileage range are calculated using the empirical models. It should be noted that the high-fidelity aerodynamic analysis would require the integration of a computational fluid dynamics code into the optimization process. However, such analyses require significantly more computational time than high-fidelity structural analyses. In the framework of an early phase of the optimization process, with the goal of evaluating as many designs as possible, it has been chosen not to include a high-fidelity aerodynamic code. Nevertheless, the level of precision employed to estimate the two objectives allows us to consider the main coupling between them. At this preliminary stage, the focus is on modeling the interdisciplinary contrasts between the objectives, rather than obtaining the exact values of the output parameters. Finally, a crucial aspect is highlighted regarding a key performance parameter – specifically, the fuel consumption over time, interpreted as the change in weight over time. By employing Brequet's formulation once more (Ref. [72]), the rate of change of the aircraft weight is calculated considering the *Thrust-specific fuel consumption (TSFC)* and a steady level flight (for which the thrust is equal to the drag $T = D$, and the weight is equal to the lift $L = W$)

$$\frac{dW}{dt} = TSFC\,T = TSFC\,D = TSFC\frac{W}{L/D} \tag{1.18}$$

Typically, the goal is to minimize this quantity, which is inherently linked to both weight and lift-to-drag ratio. Achieving this objective involves designing for maximum lift-to-drag ratio and minimum weight.

1.2.4 Validation process of the proposed methodogoly

In order to validate the proposed optimization methodology, a process involving three optimizations with an increasing number of constraints involved is proposed. The constraints involved reflect the use of different disciplines, they are incorporated into the optimization in a gradually increasing way up to represent the complete problem previously proposed. The ranges of variation of the design variables, the optimization objectives and the initial starting population are kept fixed. However, the nature of the disciplines involved is the only thing that is changed during the validation process, in order to check how the different discipline involved interact with each other and how the best solutions change during the three different optimizations process. The three proposed optimizations can be summarized as follows:

- **The Aeroelastostatic Optimization (AESO)**
  This optimization involves the use of only the static constraints in the optimization. Therefore, structural, aeroelastic, and control constraints are included only for static analyses as the aeroelastic trim, the maneuver, and the aileron response analyses. In addition, the stability of the aircraft on rigid dynamics is required.

- **The Aeroelastic Optimization (AEO)**
  This optimization involves the use of static and dynamic constraints in the optimization. Thus in addition to the previously used static constraints, additional structural and aeroelastic con-

			Discipline Description		
		Constraint	Structural	Aeroelastic	Control
AESO / AEO / ASEO	STATIC	TRIM	$\sigma_{max} \leq \bar{\sigma}$	$\alpha_{trim} \leq \alpha_{max_1}$ $\delta_{t_{trim}} \leq \delta_{t_{max}}$	
		MANEUVER	$\sigma_{max_{MLA}} \leq \bar{\sigma}$	$\alpha_{trim} \leq \alpha_{max_2}$ $\delta_{e_{trim}} \leq \delta_{e_{max}}$	$C_{m_{\delta_e}} \geq \bar{C}_{m_{\delta_e}}$
		AILERON RESPONSE	$\sigma_{max} \leq \bar{\sigma}$	$U_r \geq \bar{U}_r$	$t_r \leq \bar{t}_r$
	DYNAMIC	AEROELASTIC STABILITY (RIGID)		$U_f^{OL} \geq 1.1U_D$	
		GUST RESPONSE	$\sigma_{max} \leq \bar{\sigma}$		
		AEROELASTIC STABILITY		$U_f^{OL} \geq 1.1U_D$ $U_f^{OL} \geq U_D$	
	CONTROL	ACTIVE FLUTTER SUPPRESSION			$U_f^{CL} \geq 1.1U_D$
		GUST LOAD ALLEVIATION			$\sigma_{max_{GLA}} \leq \bar{\sigma}$

Table 1.3: Disciplinary Constraints involved in the validation process of the optimization methodology

straints are applied for the aeroelastic stability and the gust response analyses. No controller is used for possible unstable conditions or excessive stress due to the gust input. Since the controller is not active, it is essential that the aircraft be stable up to $U_f^{OL} \geq 1.1U_D$ (U_D is the dive speed)

- **The Aeroservoelastic Optimization (ASEO)**
  This optimization involves the use of static, dynamic and control constraints in the optimization. So it involves the complete proposed methodology. In addition to the constraints used in the previous optimization, the controller optimization for the reduction of loads due to the gust input and for the aeroelastic stability are included. With the controller active, it is possible to lighten the constraint on the aircraft stability in open loop case ($U_f^{OL} \geq U_D$) and insert an additional constraint on stability in closed loop ($U_f^{CL} \geq 1.1U_D$)

The constraints involved in the three optimizations are shown in Tab. 1.3 in detail.

The process of optimizing the aeroservoelastic model with a sequential disciplinary approach as described previously is shown with more details in Fig. 1.15. A key consideration when implementing *MDO* is how disciplinary analysis models, approximate models and optimisation software are

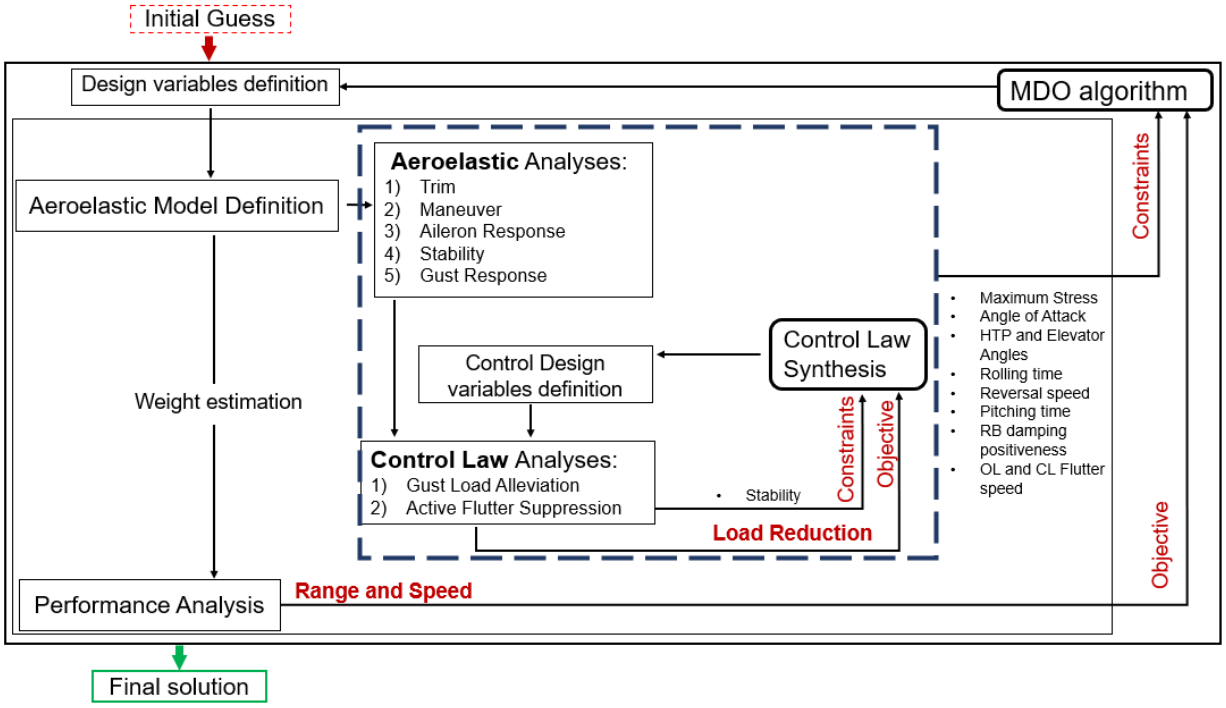

Figure 1.15: The optimization process of the aeroservoelastic model: sequential disciplinary behavior

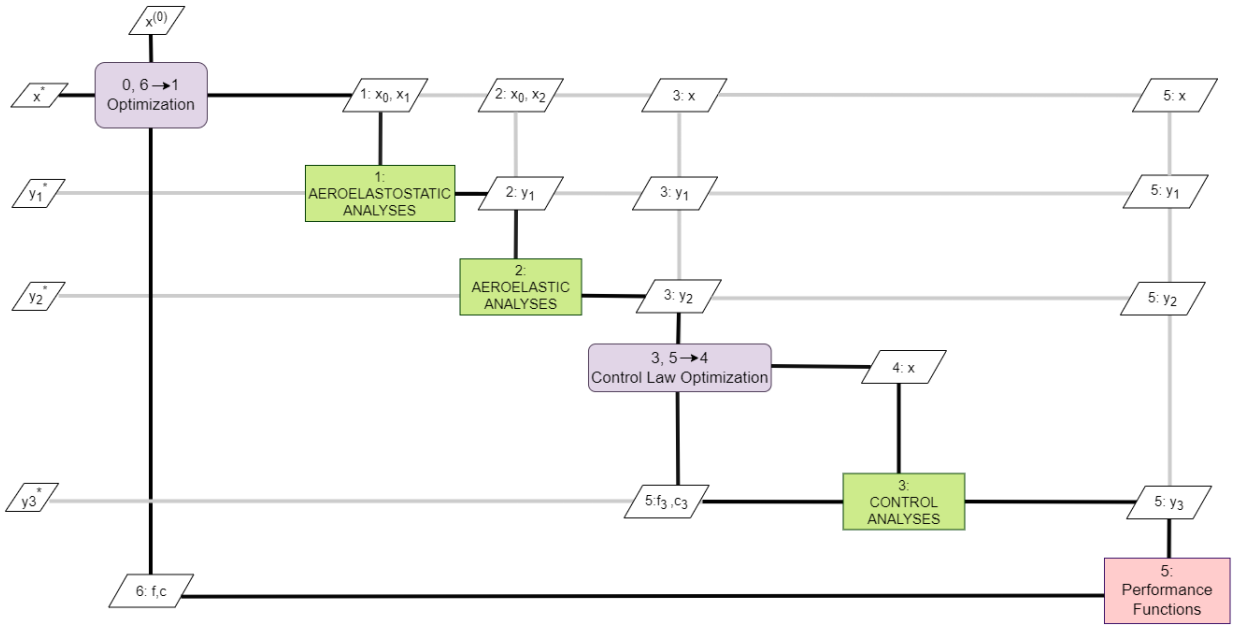

Figure 1.16: The optimization architecture

organised with problem formulation for optimal design. This combination of problem formulation and organisational strategy, referred to as the *MDO* architecture, defines both the coupling between the different models and the solution to the overall optimisation problem (Ref. [65]). The overall architecture proposed in this thesis is represented by the *Extended Design Structure Matrix (XDSM)* diagram in Fig. 1.16. As the name suggests, the *XDSM* is based on a common systems engineering diagram used to visualise interconnections between complex system components (Refs. [73, 74]). *XDSM*s are designed to communicate both data dependencies and process flows between computing components of an architecture. More specifically, the components of the diagram are made up of the analyses to be carried out, while the interface between the components is made up of the data to be exchanged. Components are placed on the main diagonal of a matrix, while interfaces are placed off the diagonal, so that inputs to a component are in the same column and outputs in the same row. In the case of Figure 1.16, the external input consists of the design variables $\mathbf{x}$ and an initial hypothesis of the system $\mathbf{x}^{(0)}$. Each discipline analysis computes its own set of output variables $\mathbf{y}$, which are passed to the other discipline analyses and may depend on all or only some of the design variables. The thick grey lines are used to show the flow of data between the components, while the black lines are used to show the flow of the diagram. In addition, one of the components of the diagram is an internal optimisation process associated with the control law and the calculation of its objective functions and constraints. The analysis to calculate the system's constraints and objectives is the final component of the diagram. At the end of the optimisation process, therefore, the best design is obtained, characterised by its design variables $\mathbf{x}^*$ and by the values of its output variables $\mathbf{y}^*$.

Chapter 2

Aeroservoelastic modelling

In the search for the optimal and innovative designs during the optimization process, the balance between accuracy and computational efficiency is a critical consideration. In this regard, the use of a simplified aeroservoelastic model provides a good balance between the rapid exploration of the goal space and the good descriptive accuracy of the physical problem. This chapter presents the tool developed in the present doctoral activity for the aeroservoelastic model generation and the simulation of structural and aerodynamic behaviours used in the optimization process, presenting its characteristics and its validation. It is a powerful tool capable of describing aerodynamics, structural and control system dynamics in an efficient framework for optimization usable in the preliminary design phases. First, the integrated modeling of aeroelasticity and flight dynamics is described. Subsequently, the creation of the global finite element model for the aircraft, the development of the aerodynamic model, and the formulation of the control system model are sequentially presented. The aim of this chapter is to describe the aeroservoelastic model used in the optimisation process, presenting the positive aspects of using a simplified model, such as speed of performance calculation, and the negative aspects, such as limitation to preliminary design.

2.1 Integrated modelling of aeroelasticity and flight dynamics

The present section provides the integrated modelling of aeroelasticity and flight dynamics based on the formulation presented in Ref. [75]. The current modelling requires the rigid body degrees of freedom to be associated with a set of practical mean axes (PMAs) and the linearized structural dynamics to be described as a combination of unconstrained aircraft mode shapes in the PMAs coordinate system. Specifically, the PMAs origin corresponds to the instantaneous center of mass of the aircraft, and the principal axes orientation remains constant in the deformed configuration (see Fig. 2.1). The inertial coupling illustration is simplified by description of linearized structural dynamics in terms of unconstrained aircraft mode shapes in the PMAs coordinate system. Fully-coupled equations of rigid-body and structural dynamics of flexible aircraft can be obtained from the weak formulation (virtual work principle) of the Cauchy equation (Ref. [75])

$$\iiint_{\mathcal{V}} \rho \mathbf{a} \cdot \delta \mathbf{u} \, \mathrm{d}\mathcal{V} = \iiint_{\mathcal{V}} \rho \mathbf{f} \cdot \delta \mathbf{u} \, \mathrm{d}\mathcal{V} + \oiint_{\mathcal{S}} \mathbf{t} \cdot \delta \mathbf{u} \, \mathrm{d}\mathcal{S} - \iiint_{\mathcal{V}} \mathbf{T} : \delta \mathbf{E} \, \mathrm{d}\mathcal{V} \tag{2.1}$$

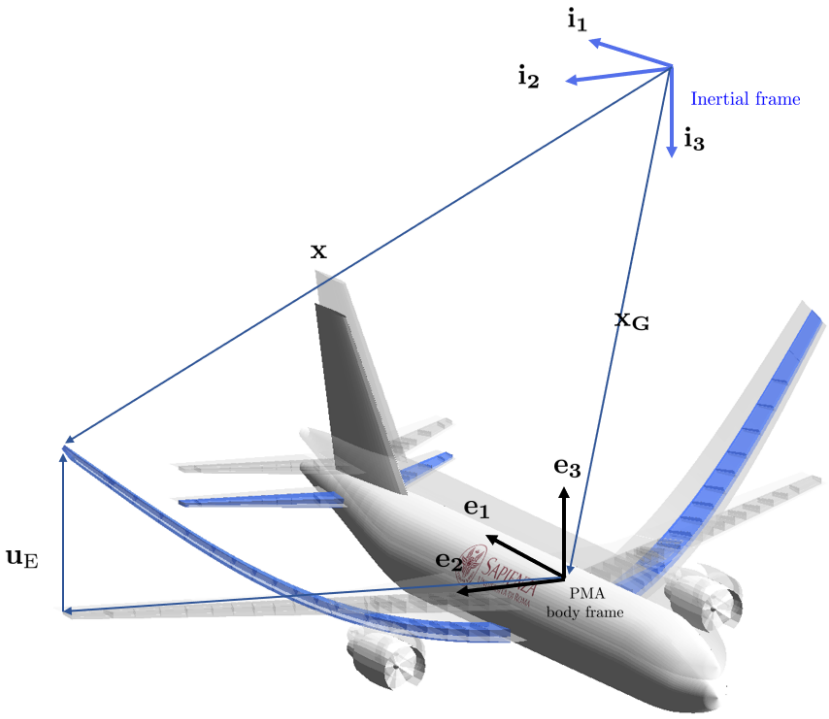

Figure 2.1: Coordinate systems to describe the unconstrained aircraft motion: the set of practical mean axes **e** and the set of inertial axes **i**

In Eq. (2.1) $\mathcal{V}$ is the aircraft material volume, $\mathcal{S}$ is the aircraft material surface, $\mathbf{a}$ is the local acceleration field, $\mathbf{f}$ and $\mathbf{t}$ are, respectively, the acting forces per unit volume and area, $\mathbf{T}$ is the stress tensor, $\delta\mathbf{E}$ is the virtual strain increment tensor, and $\delta\mathbf{u}$ is the virtual displacement. The linearized virtual displacement for elastic continuous structures is given by

$$\delta\mathbf{u} \approx \delta\mathbf{x}_{\mathsf{G}} + \delta\boldsymbol{\theta} \times (\mathbf{x} - \mathbf{x}_{\mathsf{G}}) + \sum_{n=1}^{\infty} \delta q_n \boldsymbol{\phi}_n \tag{2.2}$$

where $\delta\mathbf{x}_{\mathsf{G}} = \delta x_{\mathsf{G}}\,\mathbf{i}_1 + \delta y_{\mathsf{G}}\,\mathbf{i}_2 + \delta z_{\mathsf{G}}\,\mathbf{i}_3$, $\delta\boldsymbol{\theta} = \delta\theta_1\,\mathbf{e}_1 + \delta\theta_2\,\mathbf{e}_2 + \delta\theta_3\,\mathbf{e}_3$, and δq_n are arbitrary virtual translations, rotations, and variations of the modal coordinates, respectively. It is worth remarking that the virtual displacement has been approximated for the case in which the displacement due to rigid-body rotation does not take into account the deformed configuration. From the present choice of the reference axes and the arbitrariness of the virtual displacement (2.2) one obtains

$$\begin{aligned} m\frac{\mathrm{d}\mathbf{v}_{\mathsf{G}}}{\mathrm{d}t} &= \mathbf{f}_T \\ \frac{\mathrm{d}\mathbf{h}_{\mathsf{G}}}{\mathrm{d}t} &= \mathbf{m}_G \\ m_n\ddot{q}_n + k_n q_n &= f_n \end{aligned} \tag{2.3}$$

where $\mathbf{v}_{\mathsf{G}}$ is the center of mass velocity, $\mathbf{h}_{\mathsf{G}}$ the angular momentum, m the total mass, $\mathbf{f}_T$ and $\mathbf{m}_G$ the total force and moment, respectively, q_n denotes the n-th modal coordinate (which, together with the n-th elastic mode shape of the unconstrained aircraft $\boldsymbol{\phi}_n$, allows to write the elastic displacement of a generic point as $\mathbf{u}_{\mathsf{E}} = \sum_{n=1}^{\infty} q_n\boldsymbol{\phi}_n$) and m_n, k_n, and f_n the n-th modal mass, stiffness and external force, respectively. The equations of motion in Eq. 2.3 are then recast with respect to a body frame

of reference and linearized around a level flight aeroelastic trim condition:

$$\begin{aligned} m\frac{\mathrm{d}\mathbf{v}_{\mathsf{G}}}{\mathrm{d}t} = m\dot{\mathbf{v}}_{\mathsf{G}} + \boldsymbol{\omega}\times\mathbf{v}_G \approx m\Delta\dot{\mathbf{v}}_{\mathsf{G}} - \mathbf{v}_{\mathsf{G}_e}\times\Delta\boldsymbol{\omega} = \Delta\mathbf{f}_T \\ \frac{\mathrm{d}\mathbf{h}_{\mathsf{G}}}{\mathrm{d}t} = \frac{\mathrm{d}\mathbf{J}\boldsymbol{\omega}}{\mathrm{d}t} + \boldsymbol{\omega}\times\mathbf{J}\boldsymbol{\omega} \approx \mathbf{J}\Delta\dot{\boldsymbol{\omega}} = \Delta\mathbf{m}_G \\ m_n\Delta\ddot{q}_n + k_n\Delta q_n = \Delta f_n \end{aligned} \tag{2.4}$$

where $\mathbf{J}$ is the inertia tensor and $\boldsymbol{\omega}$ is the angular velocity. As a consequence of the approximation in Eq. 2.2 the inertial coupling terms are in here neglected. More specifically, the total force and moment and the external forces are

$$\begin{aligned} \mathbf{f}_T &= \oint_S p\mathbf{n}\,dS + \int_V \rho g\,dV \\ \mathbf{m}_G &= \oint_S p\mathbf{n}\times(\mathbf{x}-\mathbf{x}_{\mathsf{G}})\,dS \\ f_n &= \oint_S p\mathbf{n}\cdot\boldsymbol{\phi}_n\,dS \end{aligned} \tag{2.5}$$

2.1.1 State-Space form of the aeroelastic model

The linearized equations are here recast in the second order matrix form. The perturbation vectors are expressed through their components in the PMA reference system

$$\begin{aligned} \Delta\mathsf{v}_{\mathsf{G}} &= \{\Delta u,\,\Delta v,\,\Delta w\}^{\mathsf{T}} \\ \Delta\boldsymbol{\omega} &= \{\Delta p,\,\Delta q,\,\Delta r\}^{\mathsf{T}} \\ \Delta\mathbf{f}_T &= \Delta\mathbf{f}_A + \Delta\mathbf{f}_W = \{\Delta X,\,\Delta Y,\,\Delta Z\}^{\mathsf{T}} \\ \Delta\mathbf{m}_G &= \{\Delta L,\,\Delta M,\,\Delta N\}^{\mathsf{T}} \end{aligned} \tag{2.6}$$

where $\Delta\mathbf{f}_A$ and $\Delta\mathbf{f}_W$ are the perturbed aerodynamic and weight forces. The system Eqn. 2.3 can be recast in the second-order compact form as

$$\mathsf{M}_e\begin{Bmatrix}\Delta\dot{\mathsf{v}}_{\mathsf{G}}\\ \Delta\dot{\boldsymbol{\omega}}\\ \Delta\ddot{\mathsf{q}}\end{Bmatrix} + \mathsf{D}_e\begin{Bmatrix}\Delta\mathsf{v}_{\mathsf{G}}\\ \Delta\boldsymbol{\omega}\\ \Delta\dot{\mathsf{q}}\end{Bmatrix} + \mathsf{K}_e\begin{Bmatrix}\Delta\mathsf{x}^{\mathsf{B}}_{\mathsf{G}}\\ \Delta\theta\\ \Delta\mathsf{q}\end{Bmatrix} = \begin{Bmatrix}\Delta\mathbf{f}_T\\ \Delta\mathbf{m}_G\\ \Delta f_n\end{Bmatrix} \tag{2.7}$$

where

$$\begin{aligned} \Delta\mathsf{x}^{\mathsf{B}}_{\mathsf{G}} &= \left\{\Delta x^{\mathsf{B}}_{\mathsf{G}},\,\Delta y^{\mathsf{B}}_{\mathsf{G}},\,\Delta z^{\mathsf{B}}_{\mathsf{G}},\right\}^{\mathsf{T}} \\ \Delta\theta &= \{\Delta\theta_1,\,\Delta\theta_2,\,\Delta\theta_3\}^{\mathsf{T}} \end{aligned} \tag{2.8}$$

are the perturbation vectors of the center of mass position expressed in the PMA and of the rigid-body rotation about the PMA, respectively. In the present formulation, the variables associated to a second order dynamics are listed in the following vector:

$$\Delta\eta^{\mathsf{T}} = \left\{\Delta\mathsf{x}^{\mathsf{T}}_{\mathsf{G}}, \Delta\Theta^{\mathsf{T}}, \Delta\mathsf{q}^{\mathsf{T}}\right\} \tag{2.9}$$

where the perturbation vectors of the center of mass coordinates in inertial frame of reference, Euler angles and modal coordinates are

$$\begin{aligned} \Delta \mathsf{x}_{\mathsf{G}} &= \{\Delta x_{\mathsf{G}}, \Delta y_{\mathsf{G}}, \Delta z_{\mathsf{G}}\}^{\mathsf{T}} \\ \Delta \Theta &= \{\Delta\phi, \Delta\theta, \Delta\psi\}^{\mathsf{T}} \\ \Delta \mathsf{q} &= \{\Delta q_1, \ldots, \Delta q_{N_e}\}^{\mathsf{T}} \end{aligned} \tag{2.10}$$

and N_e is the number of considered elastic mode shapes. Since the equations of motion of the aircraft are expressed in a non inertial frame of reference, the following vector is defined

$$\Delta\nu^{\mathsf{T}} = \left\{\Delta \mathsf{v}_{\mathsf{G}}^{\mathsf{T}}, \Delta\boldsymbol{\omega}^{\mathsf{T}}, \Delta\dot{\mathsf{q}}^{\mathsf{T}}\right\} \tag{2.11}$$

Taking into account the relationship $\dot{\mathsf{x}}_{\mathsf{G}} = \mathsf{R}_{\Theta}\mathsf{v}_{\mathsf{G}}$ (with R_{Θ} a rotational matrix dependent on Euler angles) can be linearized in order to have $\Delta\dot{\mathsf{x}}_{\mathsf{G}} = \Delta\mathsf{v}_{\mathsf{G}} - \mathsf{v}_{\mathsf{G}_e} \times \Delta\Theta$, the linearized relation between $\Delta\eta$ and $\Delta\nu$ is expressed as

$$\Delta\dot{\eta} = \Delta\nu + \mathsf{T}_1^*\Delta\eta \tag{2.12}$$

where

$$\mathsf{T}_1^* = \begin{bmatrix} 0 & -\hat{\mathsf{V}}_{\mathsf{G}_e} & 0 \\ 0 & 0 & 0 \\ 0 & 0 & 0 \end{bmatrix} \;,\; \hat{\mathsf{V}}_{\mathsf{G}_e} = \begin{bmatrix} 0 & 0 & 0 \\ 0 & 0 & -U_\infty \\ 0 & U_\infty & 0 \end{bmatrix} \tag{2.13}$$

allows to highlight the link between the variables expressed in the PMAs and those defined in the inertial reference system (being T_1^* a square matrix with dimension $(6+N_e)$). The aeroelastic model can be expressed in the Laplace domain as follows

$$\begin{aligned} (s\mathsf{M} + \mathsf{D})\,\Delta\tilde{\nu} + \mathsf{K}\,\Delta\tilde{\eta} &= q_D\,\mathsf{C}_w\,\Delta\tilde{\mathsf{r}}_w + q_D\,\mathsf{C}_t\,\Delta\tilde{\mathsf{r}}_t \\ (s + \mathsf{P}_w)\Delta\tilde{\mathsf{r}}_w &= (\mathsf{F}_{0w} + s\mathsf{F}_{1w}) \\ (s + \mathsf{P}_t)\Delta\tilde{\mathsf{r}}_t &= (\mathsf{F}_{0t} + s\mathsf{F}_{1t}) \end{aligned} \tag{2.14}$$

where

$$\begin{aligned} \mathsf{M} &:= \mathsf{M}_e - q_D\left(\frac{b}{U_\infty}\right)^2\mathsf{A}_2 \\ \mathsf{D} &:= \mathsf{D}_e - q_D\,\frac{b}{U_\infty}\,(\mathsf{A}_1 - \mathsf{A}_1^D) \\ \mathsf{K} &:= \mathsf{K}_e - q_D\mathsf{A}_0 + \mathsf{K}_{\mathsf{W}} \end{aligned} \tag{2.15}$$

are the overall mass, damping and stiffness matrices, respectively. As an additional stiffness term, K_{W} is the projection of the weight force on the aircraft body reference, under the assumption of small perturbation with respect to the trimmed configuration. The matrices A_0, A_1, A_2, C, P, F_0 and F_1 come from the aerodynamic model (see Chapter 2.3). The matrix A_1^D is a correction matrix applied on the generalized aerodynamic matrix in order to account for perturbation of the

aerodynamic loads given by the longitudinal motion of the aircraft (see Subs. 2.3.4 for more details). The linearized system is here rewrite in the state-space form in time-domain in terms of the state vector x, expressed as follows

$$\mathsf{x}^{\mathsf{T}} = \left\{ \Delta\eta^{\mathsf{T}}, \Delta\nu^{\mathsf{T}}, \Delta\mathsf{r}_w^{\mathsf{T}}, \Delta\mathsf{r}_t^{\mathsf{T}} \right\} \tag{2.16}$$

Finally the global integrated and linearized system can be recast as $\dot{\mathsf{x}} = \mathsf{A}\mathsf{x}$ in which the state-space matrix is

$$\mathsf{A} = \begin{bmatrix} \mathsf{T}^* & \mathsf{I} & 0 & 0 \\ -\mathsf{M}^{-1}\mathsf{K} & -\mathsf{M}^{-1}\mathsf{D} & q_D\mathsf{M}^{-1}\mathsf{C}_w & q_D\mathsf{M}^{-1}\mathsf{C}_t \\ \mathsf{F}_{0_w}\frac{U_\infty}{b} & \mathsf{F}_{1_w} & -\mathsf{P}_w\frac{U_\infty}{b} & 0 \\ \mathsf{F}_{0_t}\frac{U_\infty}{b} & \mathsf{F}_{1_t} & 0 & -\mathsf{P}_t\frac{U_\infty}{b} \end{bmatrix} \tag{2.17}$$

where b is the half mean aerodynamic chord of the wing. To complete the formulation it is possible to consider the presence of the controls inputs associated to the control surfaces present on the aircraft and the presence of an external input due to the atmospheric gust. Hence, the linearized system can be recast as

$$\dot{\mathsf{x}} = \mathsf{A}\mathsf{x} + \mathsf{B}_g\mathsf{u}_g + \mathsf{B}_H\mathsf{u}_H \tag{2.18}$$

where the u_g and u_H are the input vectors, namely the gust velocity components and their derivative and the pilot requests applied to the control surfaces, respectively. The input matrix for the gust response and the control input (B_g and B_H) are described in Eqn. 2.23 and Eqn. 2.25.

Input matrix for Gust Response

The possible input to which the aeroelastic system can be subjected is the atmospheric gust. Understanding and mitigating the effects of gusts is crucial for ensuring not only the safety of flight but also optimizing the overall efficiency and performance of the aircraft. A good representation of the gust profile is given by the 1-cosine gust shape function

$$\begin{cases} \mathsf{w} = 0.5\,\mathsf{w}_a \left\{ 1 - \cos\left[\frac{2\pi}{T_g}\left(t - t_0\right) \right] \right\} & \text{if} \quad t_0 < t < T_g + t_0 \\ \mathsf{w} = 0 & \text{if} \quad t < t_0 \end{cases} \tag{2.19}$$

where the gust penetration and the gust period are

$$\begin{aligned} S_g &= \frac{U_\infty}{f} \\ T_g &= \frac{S_g}{U_\infty} \end{aligned} \tag{2.20}$$

Is worth to note that the gust penetration S_g is chosen according to the frequency f of the aeroelastic mode to be excited. According to the EASA regulations (CS 25.341 Ref. [76]) the maximum design gust velocity must be at the sea level

$$\mathsf{w}_a = 17.07\left(\frac{S_g}{212.28}\right)^{1/6} \tag{2.21}$$

Furthermore, no flight profile alleviation factor are considered. The gust input is defined as

$$\mathsf{u}_g^{\mathsf{T}} = \left\{ \mathsf{w}_w^{\mathsf{T}}, \dot{\mathsf{w}}_w^{\mathsf{T}}, \mathsf{w}_t^{\mathsf{T}}, \dot{\mathsf{w}}_t^{\mathsf{T}} \right\} \tag{2.22}$$

in which the input gust on the tail w_t is the time-shifted input gust on the wing, with a delay equal to $t_d = \Delta x / U_\infty$, with Δx equal to the distance between the pressure centers of the two aerodynamic surfaces. Finally the input gust matrix is

$$\mathsf{B}_g = \begin{bmatrix} 0 & 0 & 0 & 0 \\ -q_D \frac{b}{U_\infty} \mathsf{M}^{-1} \mathsf{A}_{1_w}^{(1,3)} & -q_D \left(\frac{b}{U_\infty} \right)^2 \mathsf{M}^{-1} \mathsf{A}_{2_w}^{(1,3)} & -q_D \frac{b}{U_\infty} \mathsf{M}^{-1} \mathsf{A}_{1_t}^{(1,3)} & -q_D \left(\frac{b}{U_\infty} \right)^2 \mathsf{M}^{-1} \mathsf{A}_{2_t}^{(1,3)} \\ -\mathsf{F}_{1w}^{(1,3)} & 0 & 0 & 0 \\ 0 & 0 & -\mathsf{F}_{1t}^{(1,3)} & 0 \end{bmatrix} \tag{2.23}$$

where the superscript $^{(1,3)}$ indicates the extraction of the first three columns of the relevant matrix.

Input matrix for Controls Response

The equilibrium in flight dynamics comes from the complex interaction between aerodynamics and the control systems, where the input matrix for the aircraft controls takes a central role in modeling this interaction. The perturbation vector of the control surfaces rotation is

$$\Delta\delta = \{\Delta\delta_a, \Delta\delta_e, \Delta\delta_r\}^{\mathsf{T}} \tag{2.24}$$

with $\Delta\delta_a$,$\Delta\delta_e$, and $\Delta\delta_r$ associate respectively to the aileron, elevator and rudder surfaces. The imposed control input to the aeroelastic system is $\mathsf{u}_H^{\mathsf{T}} = \left\{ \Delta\delta, \Delta\dot{\delta} \right\}^{\mathsf{T}}$. Considering only the quasi-steady aerodynamics given by the imposition of the control surface rotations, the controls input matrix is

$$\mathsf{B}_H = \begin{bmatrix} 0 & 0 \\ -q_D \mathsf{M}^{-1} \mathsf{A}_0^c & -q_D \left(\frac{b}{U_\infty} \right) \mathsf{M}^{-1} \mathsf{A}_1^c \\ 0 & 0 \\ 0 & 0 \end{bmatrix} \tag{2.25}$$

in which the components of the aerodynamic matrices A_1^c and A_0^c are calculated using the Theodorsen model, taking the rotation of the control surfaces and the modified strip theory.

2.2 Generation of aircraft global finite element models

In the field of structural analysis, creating a reliable and efficient finite element model is the key to accurate predictions. This section describes the *Finite Element Model (FEM)* generator used in the optimization process, an indispensable resource for analyzing and optimizing structures in a virtual environment. The *FEM* generator creates the input file to run the structural analysis in MSC-

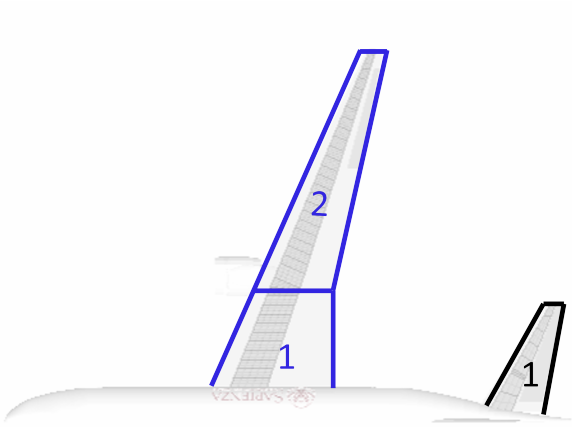

Figure 2.2: Planform of a wing and a tail that can be built

Structural components	Finite Element type
Skin - Ribs - Spar Webs	Shell element (QUAD4)
Spar Caps	Bar Element (BAR)
Fuselage - Engines - Fuel - Payload non-structural masses - Control systems	Concentrated mass (CONM2) and RBE2 or RBE3 links

Table 2.1: Elements used for building the structural *FEM*

NASTRAN® solver Ref. [77]. The approach employed in this finite element model formulation involves the representation of the primary structure by finite elements that reflect the predominant structural contribution of the component. The number of grids is kept at acceptable levels by avoiding the inclusion of irrelevant details for the analyses; moreover, this number is constant for each design within the optimization. Another important issue concerns the homogeneity of simulations across the different disciplines involved in multidisciplinary optimization. In fact, too much detailed analysis of one discipline over the others could compromise the balance in the design process. With these issues considered, a *FEM* generator is developed to create basic but complete structural and aerodynamic models for an aircraft while maintaining a uniform level of fidelity across both disciplines. The *FEM* generator takes a parametric approach to building geometry in aircraft designs. It can handle structural and aerodynamic variables for building the aircraft models, including components such as the wing, horizontal tail, and control surfaces. More details on the model creation are provided in the following subsections.

2.2.1 Aircraft parametrization and models

The optimization process aims to establish the dimensions of the wing, tail, and control surfaces. While choosing the type of mission to be performed, some parameters are inevitably set. Consequently, the design decision is to define the fuselage as represented only by a characteristic mass and a rigid body. To simplify the geometric representation, the wing is divided into two sections, driven by the kink position (as shown in the Figure 2.2), while the tail geometry requires no further sub-

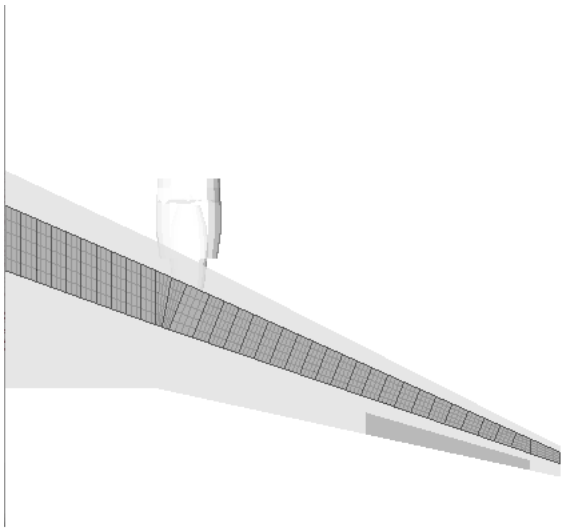

Figure 2.3: Wing Planform Example

division. First, the geometry in plan is created for each section, using the span and chord lengths, along with the sweep and the taper ratio as input parameters. Special points at leading and trailing edges, as well as at the quarter and half chords of the interfaces, are identified for proper location of masses. An example of the wing planform, with the integration of the structural wing box in the lifting surface, is shown in Fig. 2.3. Having the plan shape for each section of the wing and the tail surfaces, the box structure can be constructed considering all the structural parameters. The Figure 2.4 shows an example of the structural box definition from the plan form, in which some parameters such as heights, widths and positions are fixed as percentages of the aerodynamic variable of the chord. In detail, the aerodynamic surface is positioned in the centerline of the structural box. As evident, the shape of the structural box does not exactly match the shape of a specific aerodynamic airfoil. This discrepancy is intentional, maintaining fidelity to the model's level of accuracy. It is a design choice that is sufficient for the overall description of the model. The structural properties (thickness and area of the spars) are defined for each respective section. The wing and tail box structures are completely modeled by using uni- and bi-dimensional finite elements (see Tab. 2.1). The one-dimensional longitudinal elements are designed to provide their structural contribution for axial and bending loads, therefore the spar caps are modeled using beam elements, while the skins and the spar webs are modeled using shell elements (CBAR and CQUAD4 in MSC.Nastran®, respectively). Each element has its own properties that define, for example, the cross-sections of the beams and the thickness of the shell, as well as the materials used. These properties can vary along the span through an appropriate linear variation laws, that could be defined for each section of the wing and tail surfaces. Once the structure material is fixed, the design variable that confers this variation in properties is the variation in the thickness Δt or in the area of the spar ΔA_s.

Finally, the ribs, whose main role is to maintain the cross-sectional shape and transfer loads from the skin to the internal structure, also have properties that can vary along the span according to the same appropriate linear variation laws. In detail, the positioning of the ribs is not random, but is designed to manage the positioning of the control surface, which requires the presence of at least two ribs at its beginning and end position. Furthermore, in the case of the wing, a fixed

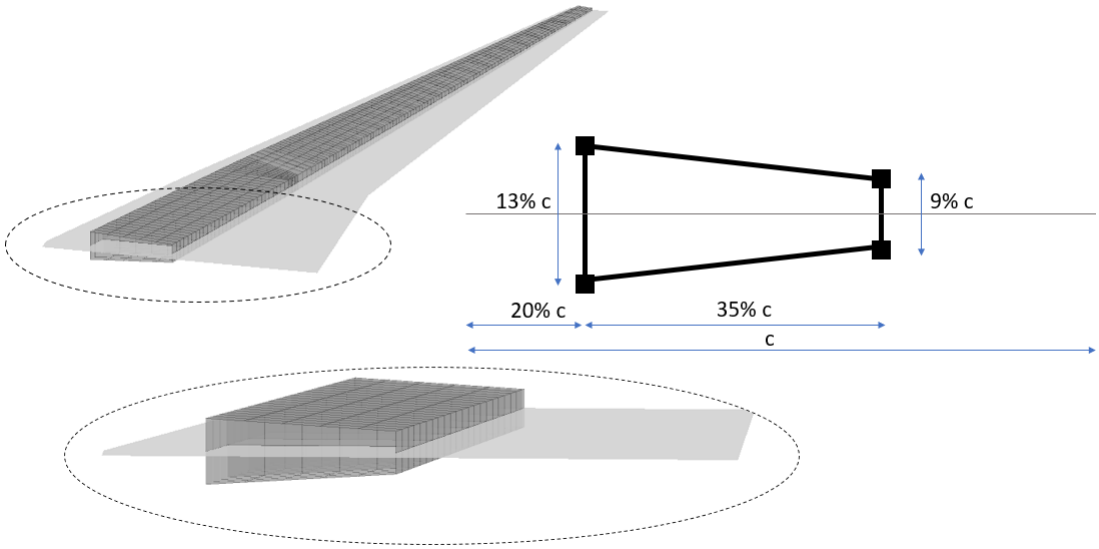

Figure 2.4: Wing box definition according to the plan form

number of ribs are placed in the kink area. The methodology chosen for the placement of the ribs, involves, in addition to the presence of three ribs at the kink and two at the beginning and end of the control surface, maximizing the distance between the ribs. Given the total number of ribs to insert n_{ribs} and the semi-span of the surface l, the maximum distance at which the ribs can be placed is Δy_{max}. Since two ribs must necessarily be placed on the control surface, the distance between the beginning and the end positions of the control surface $l_{c_2} - l_{c_1}$ is considered and the maximum number of ribs that can be placed in that area n_{ribs_c} is calculated (see Fig. 2.5). In the same way, the ribs to be distributed on the preceding and following span parts respect to the control surface are calculated (n_{ribs_1} and n_{ribs_2}, respectively)

$$\begin{aligned} \Delta y_{max} &= \frac{l}{n_{ribs}} \\ n_{ribs_c} &= \lfloor \frac{l_{c_2} - l_{c_1}}{\Delta y_{max}} \rfloor \\ n_{ribs_1} &= \lfloor \frac{l_{c_1}}{\Delta y_{max}} \rfloor \\ n_{ribs_2} &= \lfloor \frac{l - l_{c_2}}{\Delta y_{max}} \rfloor \end{aligned} \tag{2.26}$$

Some corrections are made afterward in order to achieve exactly the number of ribs requested by the user. An example of two different requirements for the number of ribs is shown in Figure 2.6. Instead, the Figure 2.7 highlights how the same number of ribs can be positioned in different ways depending on the position of the control surface.

The proper placement of the ribs is of critical importance, especially regarding the placement of the concentrated masses representing the fuel. Depending on the specifications of a given mission and the amount of fuel to be stored, this mass is distributed along the wing according to the following criteria. The 35% of the fuel is allocated in the central tank of the wing, considering its extension into the fuselage. The remaining part is divided between the inner and outer tanks of the wing (see

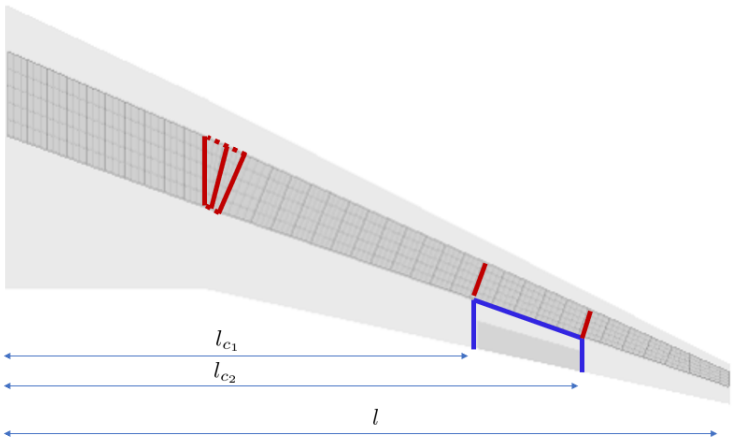

Figure 2.5: References for the ribs placement

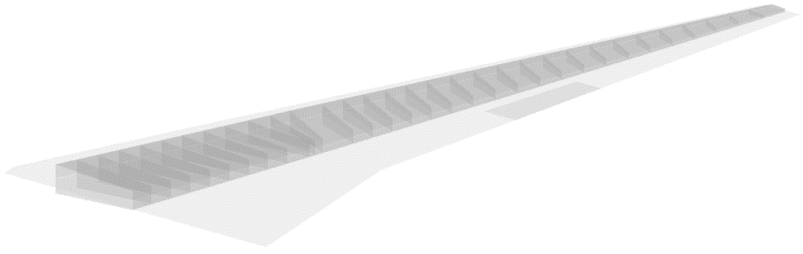

(a) $n_{ribs} = 31$

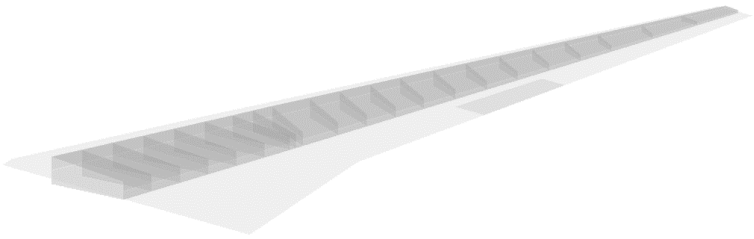

(b) $n_{ribs} = 20$

Figure 2.6: Example of two different rib number requests and their corresponding spacing

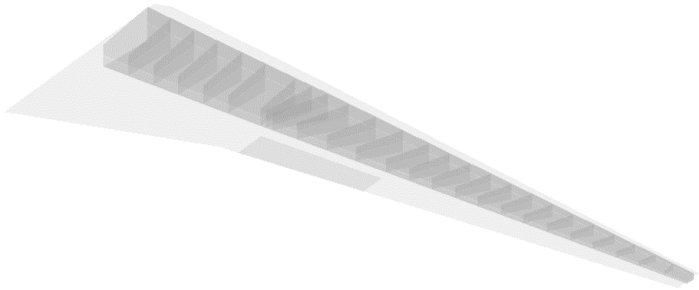

(a) $n_{ribs} = 24$ and aileron placement at 30% of the span

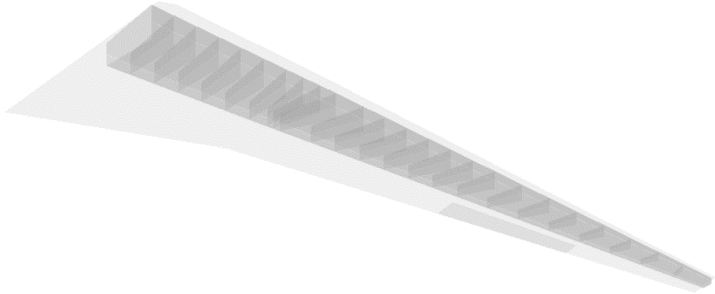

(b) $n_{ribs} = 24$ and aileron placement at 60% of the span

Figure 2.7: Example of two different aileron position requests and the corresponding ribs spacing

Fig. 2.8). The fuel is represented by concentrated masses (CONM2) placed in the centerline area between two ribs, connected to them by RBE3 elements. The distance between the ribs involved defines a volume, and knowing the density of the fuel, it is possible to calculate the amount of mass that can be contained in the tanks bounded by the ribs. The engine is also represented by a concentrated mass, located at the kink and connected to the lower part of the wing box by rigid links (RBE3) at the ribs (see Fig. 2.9).

Additional concentrated masses representing the masses of the actuators of the controllers are inserted into the model. In addition, it is also relevant to consider all other non-structural masses, which could be defined as secondary masses, and their inertial loads (Ref. [78]). These secondary masses include the fixed and the movable parts of the leading and trailing edges. Usually the value of the representative mass of these components is calculated through predetermined weight functionals (Ref. [78]), which return the mass relying on the corresponding surface area. Good accuracy of the weight functionals is very important, because the secondary masses contribute significantly to the total weight of the body (according to Ref. [78] for the wing it is approximately $30 - 40\%$). In this work, the parametric weight functionals are not used; instead, a simplification of the problem is considered, consistent with the level of structural accuracy of the model. Through MSC.Nastran® weight estimator is known the total weight of the aircraft, approximately the wing weight is assumed to be about 33% of the total weight. Note the approximation of the wing weight, it is possible to calculate the amount of the secondary mass to be included (30% of the wing mass) and divide it up along the span at the leading edge (7.5%) to the trailing edge (15%) and the remaining portion (the miscellaneous) at the center of the wing box (see Fig. 2.10 for more details on the

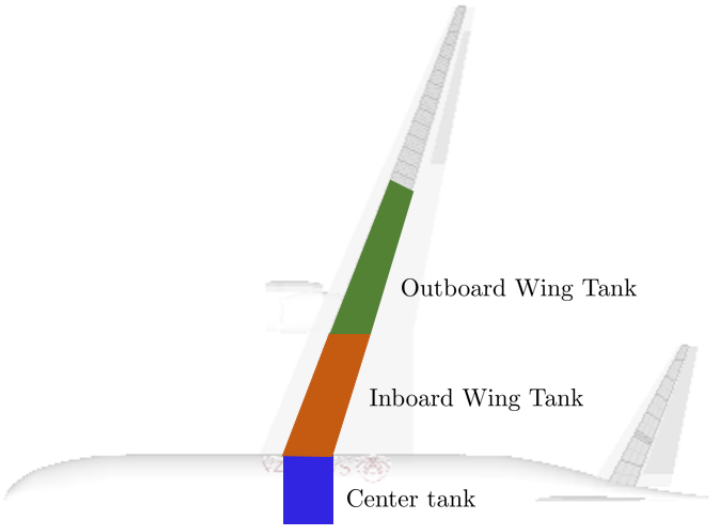

Figure 2.8: Fuel Tank locations

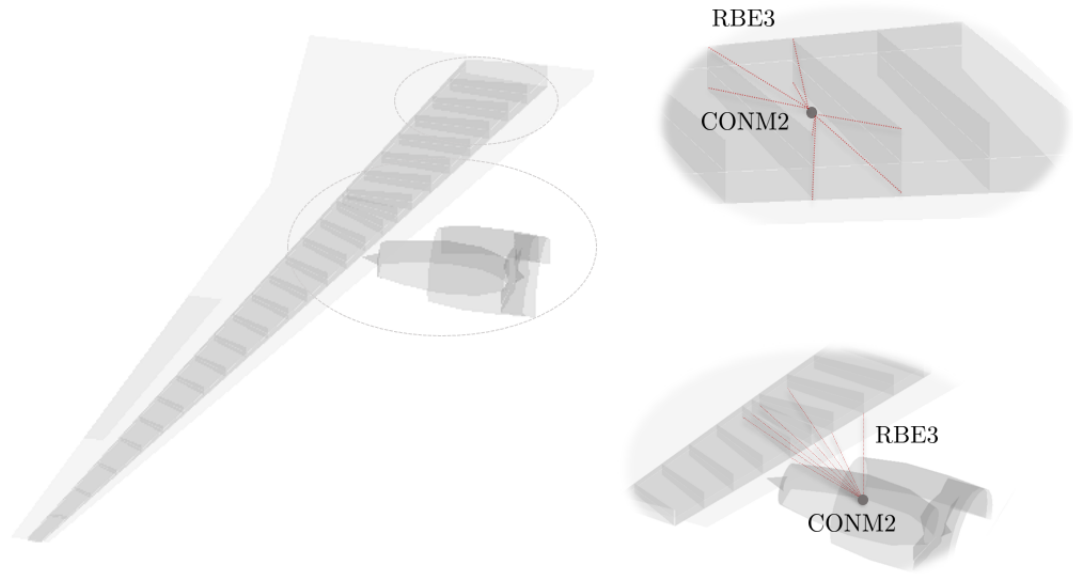

Figure 2.9: RBE3 links between the concentrated masses and the wing box

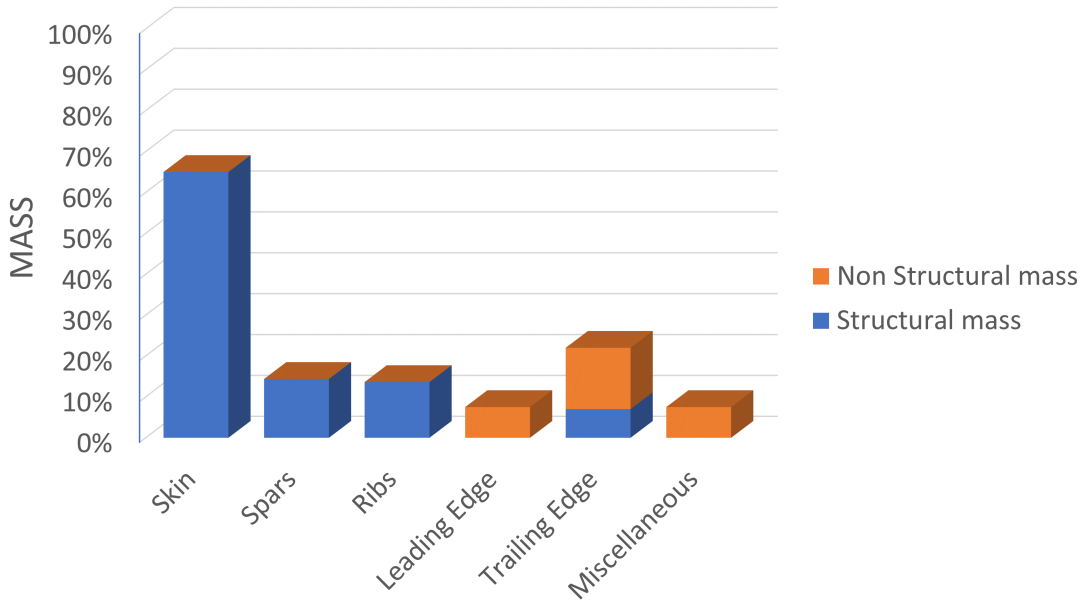

Figure 2.10: Mass percentages of the structural and non-structural component of the wing mass.

representative mass percentages of the wing, and Fig. 2.11 for the placement of the non-structural masses). Inevitably, the presence of these additional masses in the model generates the possibility of concentrated loads in some areas of the structure. To achieve the most uniform load distribution on the structure, RBE3 type links are inserted between the ribs and the earlier and later portions of the structure. For this purpose, a generic reference line, discretized with some reference points, is considered and is positioned in the center of the structural box. Each point belonging to this reference line is used to connect portions of the structure as shown in Fig. 2.12.

Finally, the definition of the fuselage is addressed, which is represented by a rigid body with a characteristic mass. However, there is no *FEM* model for it. The fuselage mass (CONM2) is connected to the wing and tail by rigid RBE2 links. The fuselage mass, which is known depending on the aircraft type, along with the mass of the payload to be transported, is considered. In the case of designs with different shapes and weights for wing and tail, a change in the center of gravity position inevitably occurs for each design. In the opposite, in the context of this work, keeping the position of the mass center constant relative to the length of the fuselage is important in order to compare the designs during the optimization process. For this purpose, the placement of the fuselage and payload masses is chosen to ensure that the center of gravity always remains in the same position respect to the fuselage length. It is emphasized that the fuselage length is unchanged, as is the position of the wing and tail, and no consideration is given to any effect of fuselage flexibility. The decision on the location of the center of gravity is given to the user. However, in this specific context, the center of gravity arrangement is chosen to be as critical as possible, i.e., at 30% of the *Mean Aerodynamic Chord (MAC)* in the aircraft configuration with the full tanks (for more details on criticality, see the Ref. [79]).

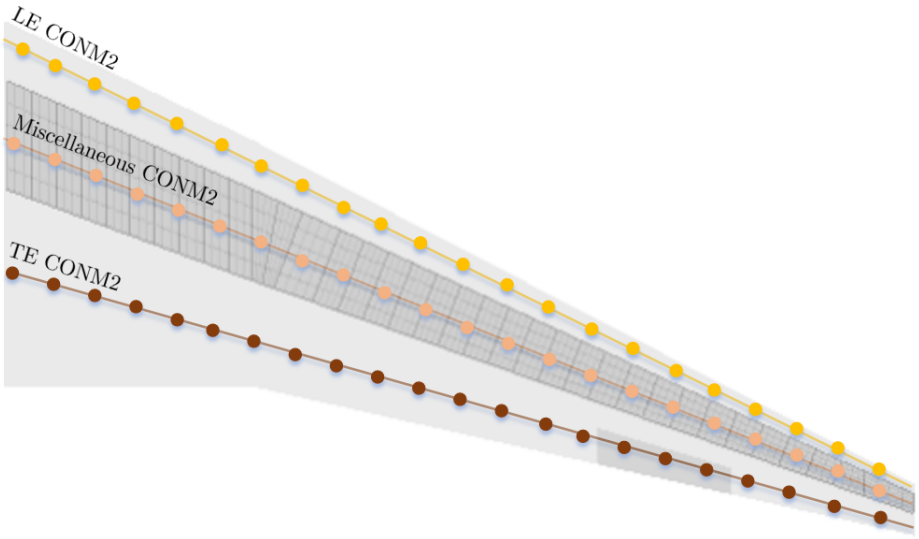

Figure 2.11: Non-structural mass locations on wing

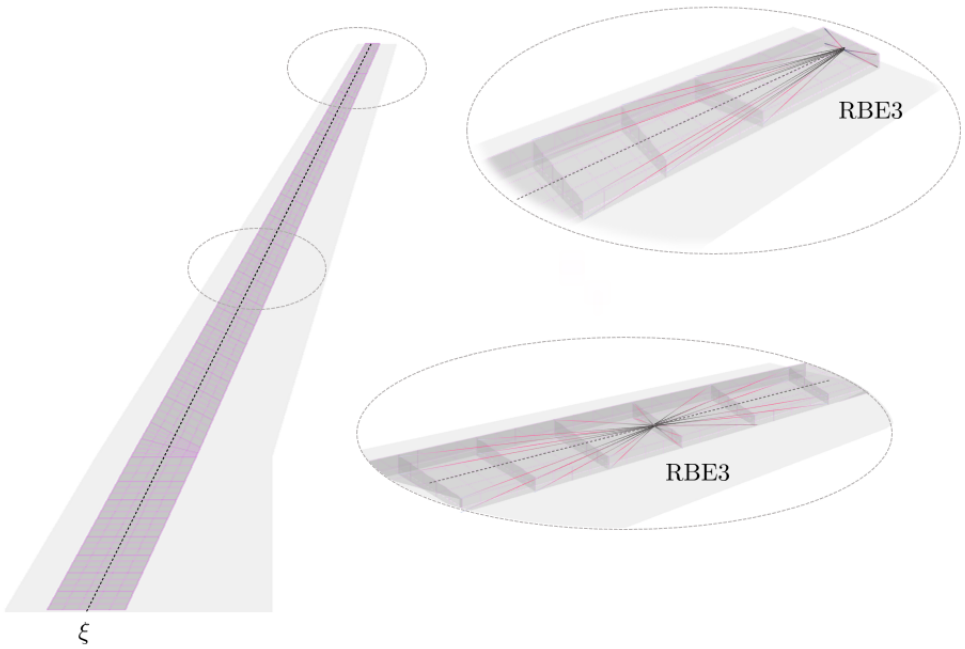

Figure 2.12: Reference line and RBE3 links

Aerodynamic panel models

The model generator has the capability to create the aerodynamic panel models for the MSC.Nastran® aeroelastic solvers, based on the Doublet-Lattice (CAERO1) or Strip Theory using the Theodorsen aerodynamic model (CAERO4). The Nastran aerodynamic model is designed for use in aero-structural coupling and includes the wing and tail lift surfaces. In particular, it is used to analyze the aircraft's dynamic behavior, including the trim and maneuvering analyses, as well as it is also applied for the verification of the aircraft's aeroelastic model. The lift panels are build following the geometry of the planform for each section. A fixed percentage of the tail is allocated to the elevator, modeled as an aerodynamic control surface and used during maneuvering, while the entire tail surface is used as a control surface for the aircraft trim. In contrast, the aileron control surface is modeled according to design variables, including the percentage of surface area and position on the wing. The aerodynamic discretization can be specified in the input file, allowing the user to select the appropriate number of grids for analysis and avoid an excessive number of degrees of freedom. As a general rule, each aerodynamic panel is divided into a mesh with a variable number of boxes in the two directions, maintaining an aspect ratio of less than three. This mesh must respect the rule $\delta x \leq 0.1V/f$, where V is the minimum velocity of flight and f is the maximum frequency, especially for dynamic aero-structural coupling analyses. This ensures the correct description of unsteady motion in the flow direction, by ensuring that chordal boxes per wavelength at the maximum frequency are described by at least 10 panels. The wavelength mentioned represents the distance traveled by a particle at the free-flow velocity during an oscillation period T.

The aero-structural coupling is performed using spline elements that transfer the forces and the displacements between the section panels and the structural sections. In order to obtain a model that transfers forces and displacements properly between the two meshes, the structural and the aerodynamic one, a surface spline (SPLINE1) is chosen instead of a line spline (SPLINE2). Finally, to improve the accuracy in transferring the informations between the structural mesh and the aerodynamic mesh, a fishbone model is used. A number of sections along the span of the surface are chosen, and for each section three structural grids are considered, one at the center line of the box (CE), one at the leading edge (LE) and one at the trailing edge (TE). The same positions are considered for the aerodynamic mesh. These specific locations are chosen for the exchange of the information between the two meshes. So, these are the points chosen for the definition of the surface spline (SPLINE1) and thus for the connection between the two meshes. More specifically, in order to have a smooth transition of information to the structure, the three structural nodes are connected through the RBE3 links (see Fig. 2.13).

Finally, for the post-process evaluations of the static aeroelasticity, monitoring points are also included on the structure. These are basically post-processing operators that allow the monitoring of the key results in an analysis beyond what is available in the standard data retrieval. The MONPNT1 entry is used, it provides the loads integrated at a user-defined point in a chosen coordinate system, and its output is calculated in a user-defined output coordinate system. Therefore, the nodes to be monitored (the nodes at the root of the specific surface or the nodes along the full span) on the structural or aerodynamic model whose loads are to be integrated are chosen. This provides the output of the applied load for the specified set of nodes.

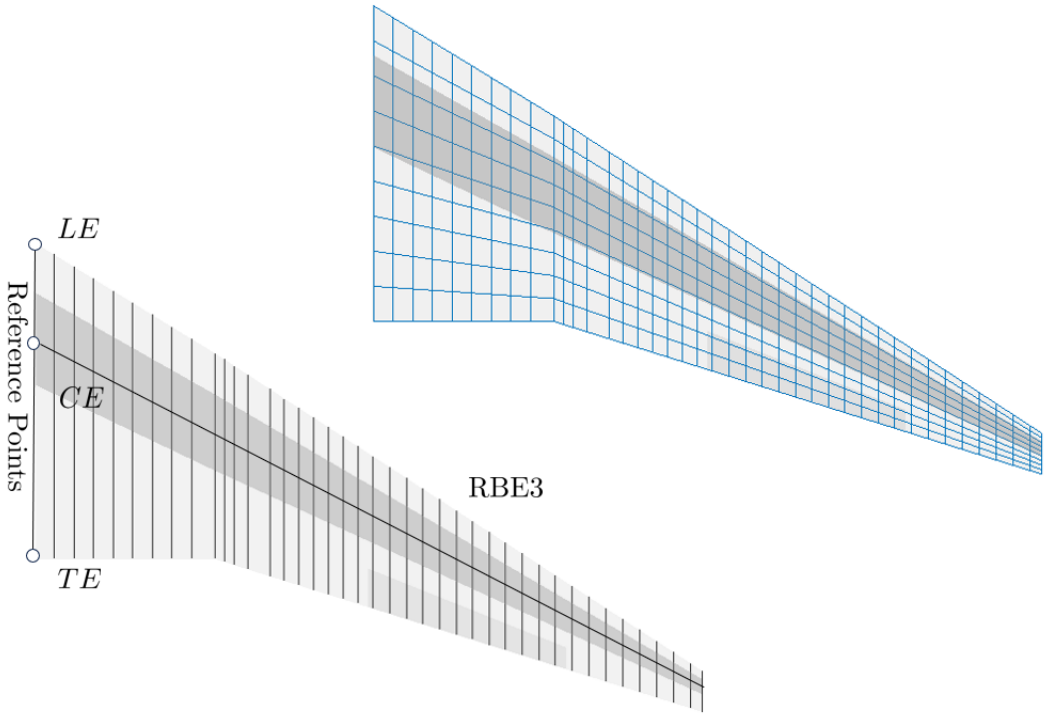

Figure 2.13: Fishbone model on the wing

Benchmark configuration

A reference configuration of the aircraft is defined in this section in order to use it for the validation of the proposed Reduced Order Models; in addition, it serves as a key reference point for the optimization efforts since it is designed as an initial guess. Therefore, the set of the design parameters, including wing geometry, control surface dimensions, and aerodynamic characteristics are defined for this design. This initial guess is based on a balanced mixture of stability and performance, providing a starting point for the optimization.

Taking into account the reference configuration, the optimization algorithms can iteratively refine these parameters, with the goal of improving specific performance metrics while maintaining the overall stability and efficiency of the aircraft. The benchmark configuration is explained in Tab. 2.6, in which the aircraft performance features and the geometrical definition are summarized. This design has the performance characteristics typical of a short-range configuration. Furthermore, to ensure a comprehensive reference, particularly for the subsequent validation of the aerodynamic model, the modal shapes of the benchmark aircraft in the *MZFW* configuration (the specific case examined in the dynamic analyses) are presented in Fig. 2.14. In detail, it is possible to see how the presence of the engine, and in particular its mass, affects the modal shapes, as can be seen in Figs. 2.14(b) and 2.14(g).

	DESIGN FEATURES	
AIRCRAFT	Cruise Mach M_∞	0.78
	Range R	$6950Km$
	Lift-to-Drag ratio $\bar{E}$	19.3
	Weight W	$70e3Kg$
	Equivalent Aspect Ratio AR_e	7.76

Table 2.2: Performance parameters

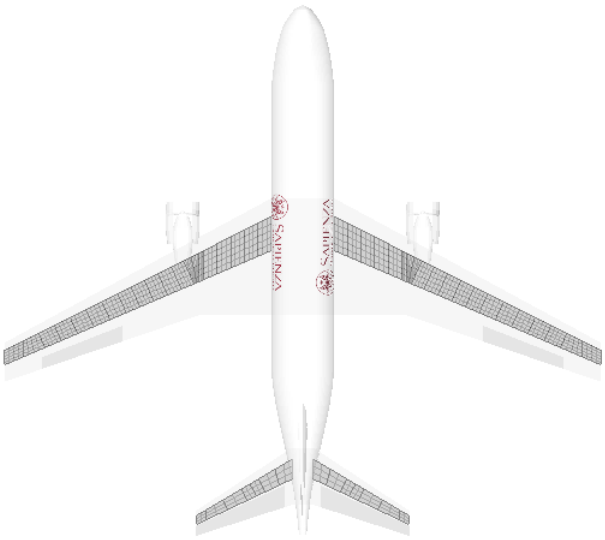

	DESIGN FEATURES	
WING	Surface S_w	$150m^2$
	Taper ratio λ_w	0.42
	Span l_w	$34.14m$
	Sweep angle Λ	$24.95°$

Table 2.3: Wing parameters

	DESIGN FEATURES	
TAIL	Surface S_t	$32.24m$
	Taper ratio λ_t	0.44
	Span l_t	$12.26m$
	Sweep angle Λ_t	$27.96°$

Table 2.4: Tail parameters

	DESIGN FEATURES	
AILERON	Position $p = \%l_w/2$	81%
	Surface S_a	$8.22m^2$

Table 2.5: Aileron parameters

Table 2.6: Short Range Benchmark configuration

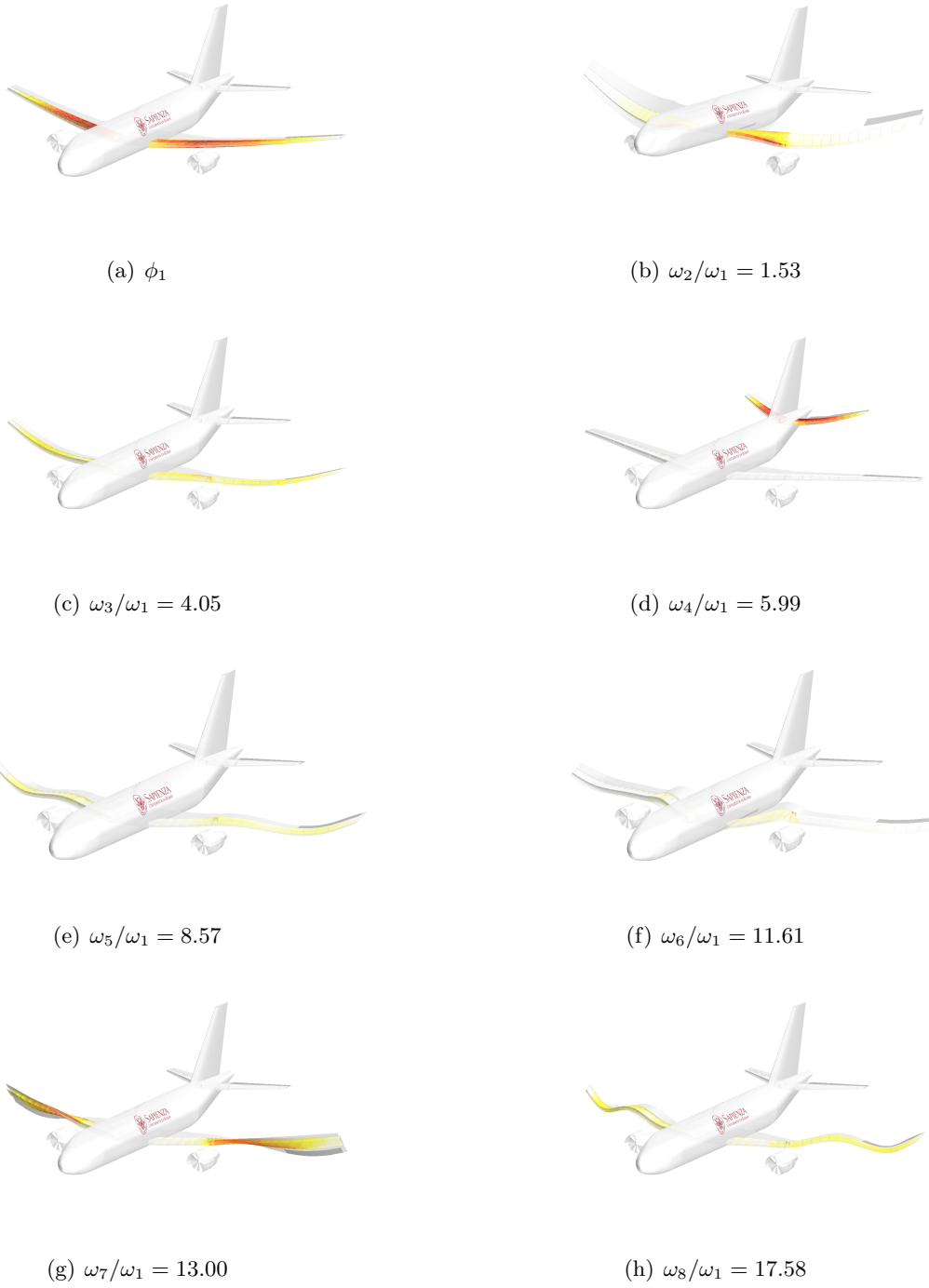

(a) ϕ_1

(b) $\omega_2/\omega_1 = 1.53$

(c) $\omega_3/\omega_1 = 4.05$

(d) $\omega_4/\omega_1 = 5.99$

(e) $\omega_5/\omega_1 = 8.57$

(f) $\omega_6/\omega_1 = 11.61$

(g) $\omega_7/\omega_1 = 13.00$

(h) $\omega_8/\omega_1 = 17.58$

Figure 2.14: Mode shapes of benchmark configuration with their natural frequencies (*MZFW* case).

2.3 Aerodynamic modelling based on non-standard strip theory

The solution of aeroelastic problems requires accurate modeling of non-stationary aerodynamics. To solve time-dependent problems, such as flutter suppression and gust alleviation, and frequency-dependent problems, such as flutter instability, it is necessary to formulate the aerodynamic problem in the frequency and time domain. A formulation for unstable aerodynamics at subsonic velocities using indicial functions is presented and used in this thesis, in order to solve aeroealstic response and flutter analyses. This section presents the description of the aerodynamic reduced order model used in the optimization. First an overview of the aerodynamic problem based on indicial functions is presented, then the definition of the aerodynamic forces and the formulation of the *Reduced-Order Model (ROM)* are described, and finally the comparisons between the results of the gust response and the instability analyses obtained with the analytical model and with the finite element model (using the double lattice method for the aerodynamic description) are presented.

2.3.1 Overview of the aerodynamic problem set up using indicial functions

In the study of transient flows, two types of wing motion are of particular interest - harmonically oscillating wing profiles and wing profiles that undergo sudden changes in the angle of attack. To predict the aerodynamic load due to small arbitrary movements of an airfoil in subsonic flight regime, the only fully workable way is to use the Fourier integral superposition of the theoretical results for simple harmonic oscillations. To avoid the difficulties of convergence, indicial-admittance are defined for the important degrees of freedom of the airfoil. Specifically, the lift and moment functions of an airfoil that undergoes a sudden change in angle of attack are often called indicial lift and moment functions. Generally the concept of indicial functions (see Refs. [80–85]) is used to determine the unsteady aerodynamic forces of a two-dimensional lifting surface at different airspeed ranges (including compressible subsonic and supersonic speeds). More specifically, it is known that given the indicial functions, the lift and the aerodynamic moment due to any change in the angle of attack and/or the inflow velocity (in the time or frequency domain), can be calculated using the Duhamel superposition principle (see Ref. [80]). Moreover, the use of indicial functions takes a number of advantages; it's a more accurate approach for describing aerodynamic characteristics than the usual methods (such as the lifting line formulation); it allows obtaining air loads on an aircraft subjected to arbitrary movements; it allows a unified form of aerodynamics at different flight speed regimes; and eventually, expressions of indicial functions can be deduced through various approaches, as computational fluid dynamics or experimental findings (see Refs. [83, 86]). Furthermore, indicial analytical models of aerodynamics provide a good approximation of stability and response problems, allowing solutions to be obtained at lower cost and in less computational time than using *FEM* solvers, admitting a certain margin of error.

For compressible flow, several works have been concerned with finding the best analytical expression of indicial functions (see Refs. [80, 81, 87, 88]). For a certain range of velocities, the circulation around the profile can be well defined according to the values tabulated in Ref. [80, 89–91]. The case of a two-dimensional lifting surface is considered, includeing both the plunging and pitching degrees of freedom. In addiction, the presence of small angles of attack is assumed, which means that for subsonic flows the linearized version of the velocity potential equation can be used (Refs. [92, 93]). The generic form of the indicial function is dependent on the Mach value (M_∞) and on

the dimensionless time ($\tau = \frac{U_\infty t}{b}$, for which b is the semi-chord length of the airfoil) or reduced frequency ($k = \frac{\omega b}{U_\infty}$)

$$\begin{aligned} \phi(\tau, M_\infty) &= b_0 + b_1 e^{-\beta_1 \tau} + b_2 e^{-\beta_2 \tau} + b_3 e^{-\beta_3 \tau} \\ \phi(k, M_\infty) &= \frac{b_0}{ik} + \frac{b_1}{ik + \beta_1} + \frac{b_2}{ik + \beta_2} + \frac{b_3}{ik + \beta_3} \end{aligned} \tag{2.27}$$

The indicial functions for the plunging and pitching degrees of freedom are obtained following the formulation of Mazelsky and Drischler, Ref. [89, 90], and are summerized in Tab. 2.7. In detail, the lift and the aerodynamic moment are calculated at the quarter-chord considering as an inputs the downwash w and the pitch q at three-quarter-chord.

In a fluid with finite sound velocity, the non-circulatory flow pattern is not immediately affected by changes in the boundary conditions. The non-circulatory lift and aerodynamic moment do not depend instantaneously on the accelerations and the speeds of the aerodynamic surface, but depend to their time history, therefore additional mass term and division of aerodynamics into circulatory and no-circulatory parts are meaningless. Infact, in the incompressible case the non-circulatory loads become infinite at the beginning of the impulsive motion, but in the compressible case this singularity vanishes. Therefore, the circulation around the profile in the compressible flow requires two indicial admittance functions, one for vertical translation and one for the pitching velocity, to replace the single Wagner function. Finally, it is important to note that for the incompressible case (represented in the table by the Wagner function), a correction is necessary to add the non-circulatory aerodynamics part. The trends of the ϕ functions in dimensionless time are shown in Fig. 2.15 as a comparison of indicial lift and moment functions due to a sudden change in downwash and pitching velocity for an airfoil rotation about three-quarter-chord point for several Mach numbers.

$Indicial function$	M_∞	b_0	b_1	b_2	b_3	β_1	β_2	β_3
ϕ_w	0	1	−0.165	−0.335	0	0.0455	0.3	0
	0.5	1.155	−0.406	−0.249	0.773	0.0754	0.372	1.89
	0.6	1.25	−0.452	−0.63	0.893	0.0646	0.481	0.958
	0.7	1.4	−0.5096	−0.567	0.5866	0.0536	0.357	0.902
ϕ_q	0	0	0	0	0	0	0	0
	0.5	0	0	−2.68	2.362	0	4.08	4.9
	0.6	0	0	0	−0.2653	0	0	1.345
	0.7	0	−0.083	−0.293	0.149	0.8	1.565	2.44
ϕ_{Mw}	0	0	0	0	0	0	0	0
	0.5	0	0.0557	−1	0.6263	2.555	3.308	6.09
	0.6	0	−0.1	−1.502	1.336	1.035	4.04	5.022
	0.7	0	−0.2425	0.084	−0.069	0.974	0.668	0.438
ϕ_{Mq}	0	0	0	0	0	0	0	0
	0.5	−0.0721	−0.248	0.522	−0.2879	1.562	2.348	6.605
	0.6	−0.0781	−0.077	0.38	−0.2469	0.551	2.117	4.138
	0.7	−0.0875	−0.00998	0.1079	−0.0292	0.1865	1.141	4.04

Table 2.7: Coefficients for approximating the indicial lift and moment at the quarter-chord considering as inputs the downwash w and the pitch q at three-quarter-chord.

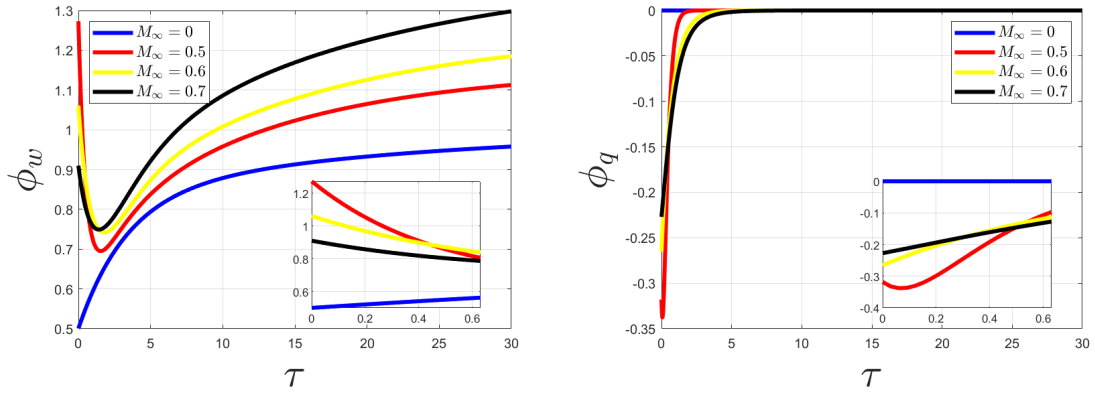

(a) $\phi_w(\tau)$

(b) $\phi_q(\tau)$

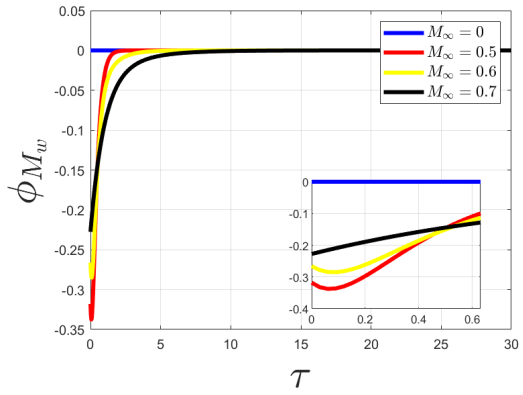

(c) $\phi_{M_w}(\tau)$

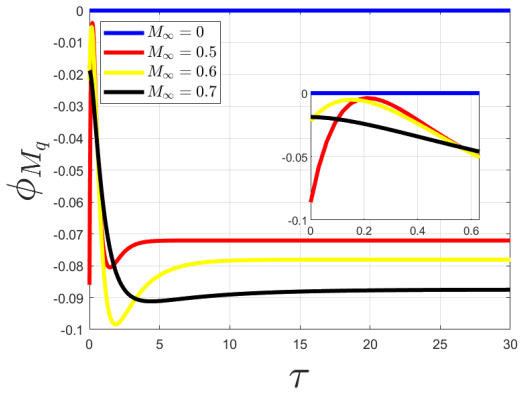

(d) $\phi_{M_q}(\tau)$

Figure 2.15: Comparison of indicial lift and moment functions due to a sudden change in downwash and pitching velocity for several Mach numbers

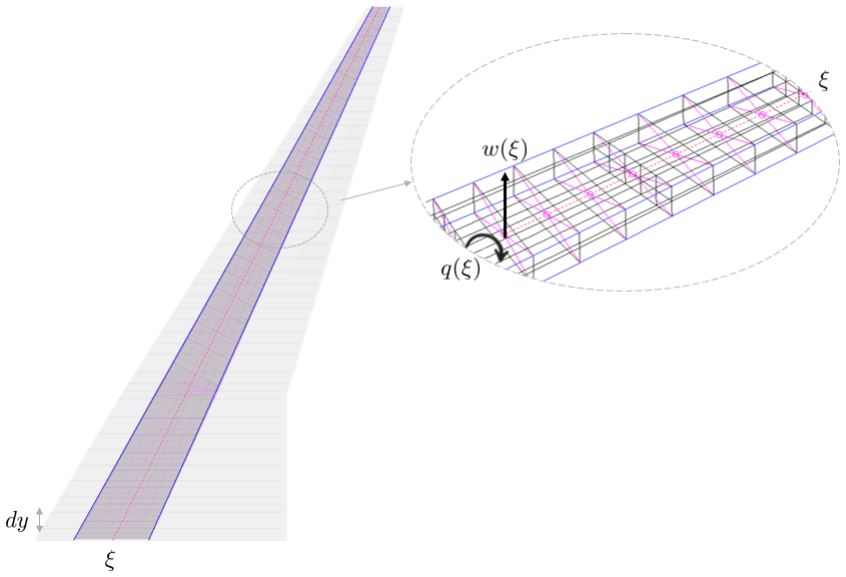

Figure 2.16: Downwash $w(\xi)$ and the pitch velocity $q(\xi)$ of the reference points

2.3.2 Definition of the aerodynamics forces for incompressible and compressible flow

The objective of this section is to define the aerodynamic forces $\mathbf{f}_{\mathsf{T}}$ and $\mathbf{m}_{\mathsf{G}}$ of the wing and tail surfaces. For this purpose, a generic reference line, discretized with some reference points (see Fig. 2.16), is considered for each aerodynamic surface, and is positioned in the center of the structural box. Recalling the definition of the inertial reference defined in the previous chapter, another reference system $\mathbf{a}$ is taken into account for calculating the reference line movements. Specifically, the $\mathbf{a}_1$ axis lies on the wind axis, $\mathbf{a}_3$ is defined as normal to the aerodynamic surface, and $\mathbf{a}_2$ is generated consequently. More specifically, the integrated aerodynamic forces $\mathbf{f}_{\mathsf{T}}$ and $\mathbf{m}_{\mathsf{G}}$ are computed as

$$\begin{aligned} \mathbf{f}_T &= \sum_{s=1}^{S} \int_0^{l_n} L(\xi)\,\mathbf{a}_3\,d\xi + m\mathbf{g} \\ \mathbf{m}_G &= \sum_{s=1}^{S} \int_0^{l_n} \Big(L(\xi)\,\mathbf{a}_3 \times (\mathbf{x} - \mathbf{x}_G) + M(\xi)\,\mathbf{a}_2 \Big)\,d\xi \\ f_n &= \sum_{s=1}^{S} \int_0^{l_n} \Big(L(\xi)\,\mathbf{a}_3 \cdot \boldsymbol{\phi}^n + M(\xi)\,\mathbf{a}_2 \cdot \boldsymbol{\varphi}^n \Big)\,d\xi \end{aligned} \tag{2.28}$$

in which S is the number of aerodynamic surfaces involved, and l_n is the aerodynamic span of each aerodynamic surface. The aerodynamic forces of each strip (with length dy and half aerodynamic chord $b(\xi) = \frac{c(\xi)}{2}$) are expressed in the frequency domain (using the reduced frequency $k^\star := \frac{\omega\, c(\xi)}{U_\infty}$) as function of the rotational and translational speeds at the reference line, namely $\tilde{w}(\xi)$ and $\tilde{q}(\xi)$

$$\begin{Bmatrix} \tilde{w}(\xi) \\ \tilde{q}(\xi) \end{Bmatrix} = \begin{Bmatrix} \mathbf{a}_3 \cdot \tilde{\mathbf{v}}_{\mathsf{G}} - \mathbf{a}_2 \cdot (\mathbf{x}(\xi) - \mathbf{x}_G) \times \tilde{\boldsymbol{\omega}} \\ \mathbf{a}_2 \cdot \boldsymbol{\omega} \end{Bmatrix} + \sum_{n=1}^{\infty} \begin{Bmatrix} -j\omega\, \boldsymbol{\phi}^n(\xi) \cdot \mathbf{a}_3 + U_\infty \boldsymbol{\varphi}^n(\xi) \cdot \mathbf{a}_2 \\ j\omega\, \boldsymbol{\varphi}^n(\xi) \cdot \mathbf{a}_2 \end{Bmatrix} \tilde{q}_n \tag{2.29}$$

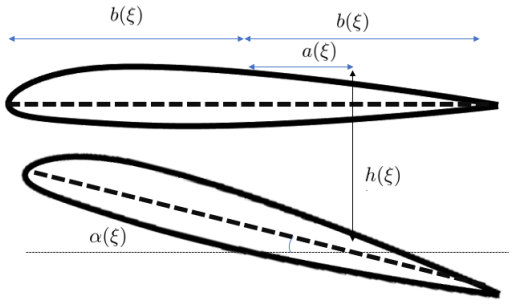

Figure 2.17: Airfoil performing vertical translation and pitching at three quarter point of the chord.

$$\begin{Bmatrix} \tilde{L}(\xi) \\ \\ \tilde{M}(\xi) \end{Bmatrix} = C_{l_\alpha}(\xi)\, q_D \mathsf{S}_1(\xi) \mathsf{T}_1(\xi)\, ik^\star \Phi(k^\star, M_\infty) \mathsf{T}_2(\xi) \begin{Bmatrix} \tilde{w}(\xi)/U_\infty \\ \\ 2b(\xi)\tilde{q}(\xi)/U_\infty \end{Bmatrix} \tag{2.30}$$

More specifically, the $C_{l_\alpha}(\xi)$ represents the lift coefficient of the specific section ξ computed using the lifting line theory (see the Subsection 2.3.3), q_D is the dynamic pressure, the matrix $\mathsf{S}_1(\xi)$ dimensions the problem, while T_1 and T_2 are reference system change matrices (recall that the functions ϕ return aerodynamic forces at the quarter chord point given downwash and pitch velocity at three-quarter chord point). These matrices are defined as follows

$$\mathsf{S}_1 = \begin{bmatrix} 2b(\xi) & 0 \\ 0 & 4b^2(\xi) \end{bmatrix} \tag{2.31}$$

$$\mathsf{T}_1 = \begin{bmatrix} 1 & 0 \\ \frac{1}{2}(a(\xi) + \frac{1}{2}) & 1 \end{bmatrix} \qquad \mathsf{T}_2 = \begin{bmatrix} 1 & \frac{1}{2}(a(\xi) - \frac{1}{2}) \\ 0 & 1 \end{bmatrix} \tag{2.32}$$

in which $b(\xi)$ represents the half aerodynamic chord of the airfoil, while $a(\xi)$ represents the distance between the ξ position and the mean chord point (see Fig. 2.17). The matrix $ik^\star\Phi(k^\star)$ collects the indicial functions in the domain of the reduced frequency $k^\star$ (due to downwash and pitch rate at three quarter point of the aerodynamic chord and give the aerodynamic forces at the quarter aerodynamic chord point)

$$ik^\star \Phi(k^\star, M_\infty) = ik^\star \begin{bmatrix} \phi_w(k^\star, M_\infty) & \phi_q(k^\star, M_\infty) \\ \phi_{M_w}(k^\star, M_\infty) & \phi_{M_q}(k^\star, M_\infty) \end{bmatrix} \tag{2.33}$$

Note carefully that the indicial functions shown above represent only the circulatory aerodynamics. As already mentioned, the indicial definition for the incompressible case (see Tab. 2.7) fits the Wagner's definition, and for this reason it can easily be related to the Theodorsen function $C(k^\star)$. Therefore, the indicial function in the incompressible case is rewritten, taking into account also the

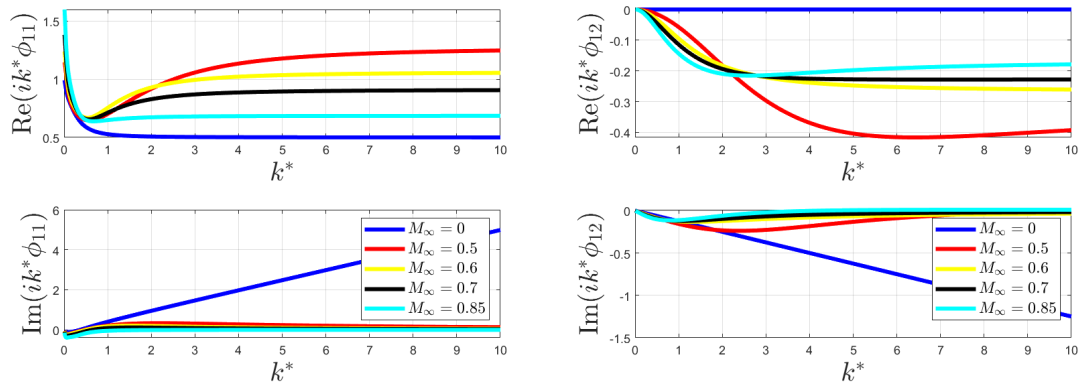

(a) $ik^\star\phi_{11}$

(b) $ik^\star\phi_{12}$

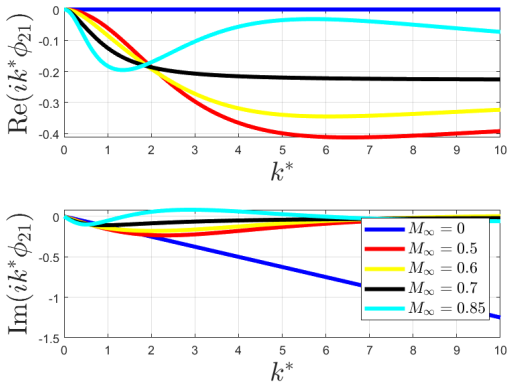

(c) $ik^\star\phi_{21}$

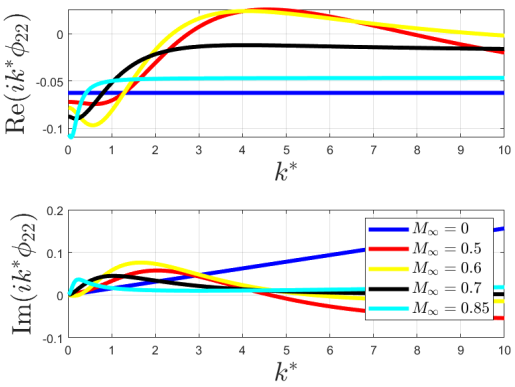

(d) $ik^\star\phi_{22}$

Figure 2.18: Comparison of the $ik^\star\Phi$ components used in the aerodynamic model for several Mach numbers

non-circulatory part.

$$ik^\star\Phi(k^\star, M_\infty = 0) = \underbrace{\begin{bmatrix} 0 & 0 \\ 0 & -\frac{1}{16} \end{bmatrix}}_{\mathsf{B}_0} + ik^\star \underbrace{\begin{bmatrix} \frac{1}{2} & -\frac{1}{8} \\ -\frac{1}{8} & \frac{1}{64} \end{bmatrix}}_{\mathsf{B}_1} + ik^\star \underbrace{\begin{bmatrix} \phi_w(k^\star, M_\infty = 0) & \phi_q(k^\star, M_\infty = 0) \\ \phi_{M_w}(k^\star, M_\infty = 0) & \phi_{M_q}(k^\star, M_\infty = 0) \end{bmatrix}}_{\begin{bmatrix} C(k^\star) & 0 \\ 0 & 0 \end{bmatrix}} \tag{2.34}$$

Therefore, the non-circulatory part is rewritten in the same reference system as the circulatory part through an additional term of stiffness and damping (note that in the final equations, where the translational and the rotational displacements are imposed, these matrices define terms of damping and mass, respectively). The figures 2.18 show the real and imaginary part of the matrix $ik^\star\Phi(k^\star, M_\infty)$ components, taking into account also the functions for $M_\infty = 0.85$, whose values are calculated from the reference data using the extrapolation method.

Generally, the aerodynamic chord does not remain constant along the wingspan, so the aerodynamic forces in each section will be dependent on a different reduced frequency $k^\star$. This dependence is not computationally convenient, so a rewriting of the aerodynamic forces based on reduced frequency scaling is used. In this regard, the taper ratio $\gamma(\xi) := \frac{c(\xi)}{\bar{c}}$ and the average reduced frequency

$k := \frac{\omega \bar{c}}{U_\infty}$ are introduced, considering the mean value of the aerodynamic chord $\bar{c}$. The reduced frequency $k^\star$ and the aerodynamic matrix are rewritten as follows

$$k^\star := \frac{\omega c(\xi)}{U_\infty} = \underbrace{\frac{\omega \bar{c}}{U_\infty}}_{k} \underbrace{\frac{c(\xi)}{\bar{c}}}_{\gamma} \tag{2.35}$$

$$\Phi(k^\star, M_\infty) = \Phi(k, M_\infty, \gamma(\xi)) \tag{2.36}$$

In order to speed up the computation, a frequency-scaled aerodynamic matrix database has been created as a function of the taper ratio $\gamma(\xi)$ and the Mach numbers M_∞ with the fixed structure

$$ik\,\Phi(k, M_\infty, \gamma) \approx \bar{\mathsf{B}}_0(M_\infty, \gamma) + ik\,\bar{\mathsf{B}}_1(M_\infty, \gamma) + \sum_{n=2}^{N_a+1} \frac{\bar{\mathsf{B}}_n(M_\infty, \gamma)}{(ik) + \beta_n} \tag{2.37}$$

in which, for each components of the $ik\,\Phi(k, M_\infty, \gamma(\xi))$ matrix the number N_a and values β_n of the aerodynamic poles are fixed.

The interpolation results of the four indicial functions are shown below in Figs. 2.19, 2.20, 2.21, 2.22 by the coefficients $\bar{b}$. The new form of the generic indicial function is written using the $\bar{b}$ coefficients considering five aerodynamic poles

$$ik\,\phi(k, M_\infty, \gamma) \quad = \quad \bar{b}_0(M_\infty, \gamma) + ik\,\bar{b}_1(M_\infty, \gamma) + \sum_{n=2}^{6} \frac{\bar{b}_n(M_\infty, \gamma)}{ik + \beta_n} \tag{2.38}$$

with $\beta_2 = 0.05$, $\beta_3 = 0.3$, $\beta_4 = 0.8$, $\beta_5 = 1.6$ and $\beta_6 = 6.4$. An example of the indicial functions interpolation over Mach is shown below (Fig. 2.23); in order to define the matrix components, for $M_\infty = 0.65$ and unit γ the new formulation is used (see Eqn. 2.38), while for the cases at $M_\infty = 0.7$ and $M_\infty = 0.6$ the values in Tab. 2.7 are used. The same reference case, i.e., $M_\infty = 0.65$ with the new formulation and $M_\infty = 0.6$ and $M_\infty = 0.7$ with the tabulated formulation, is drawn again in Fig. 2.24 by including also the scaling of the reduced frequency through $\gamma = 1.3$. In detail, the components of the new formulation depend on the reduced frequency k while the components of the tabulated formulation depend on the scaled reduced frequency $\frac{k}{\gamma}$.

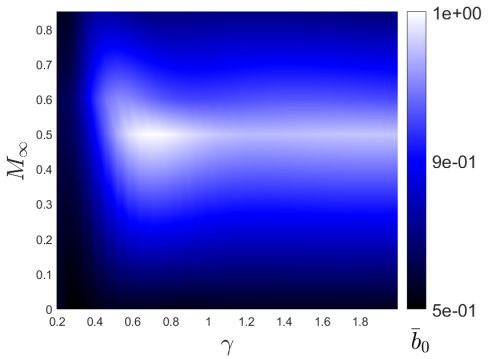

(a) Coefficients $\bar{b}_0$

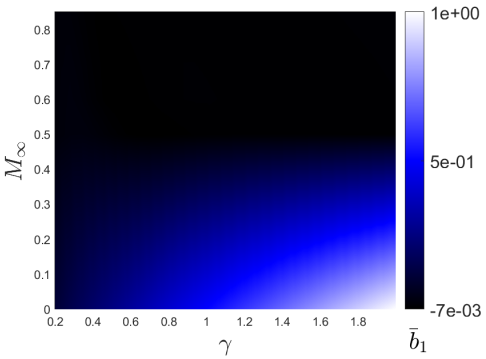

(b) Coefficients $\bar{b}_1$

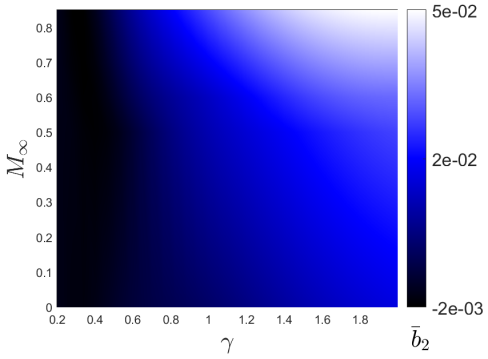

(c) Coefficients $\bar{b}_2$ with $\beta_2 = 0.05$

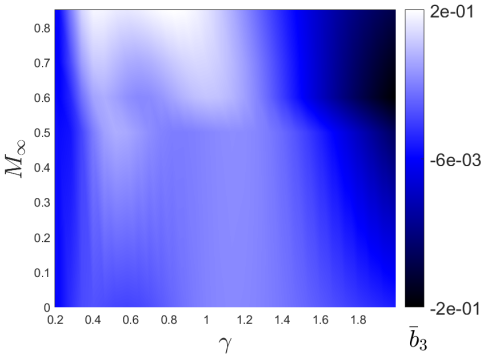

(d) Coefficients $\bar{b}_3$ with $\beta_3 = 0.3$

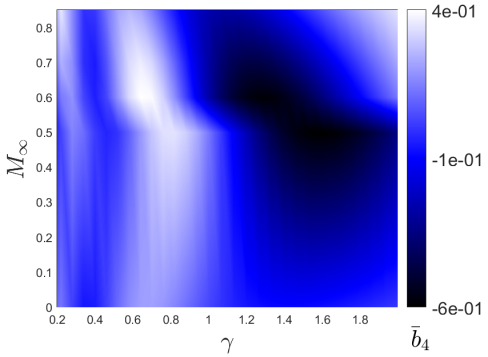

(e) Coefficients $\bar{b}_4$ with $\beta_4 = 0.8$

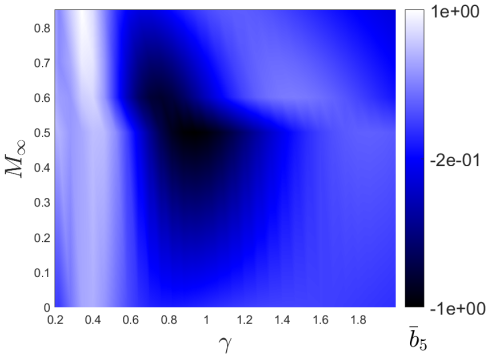

(f) Coefficients $\bar{b}_5$ with $\beta_5 = 1.6$

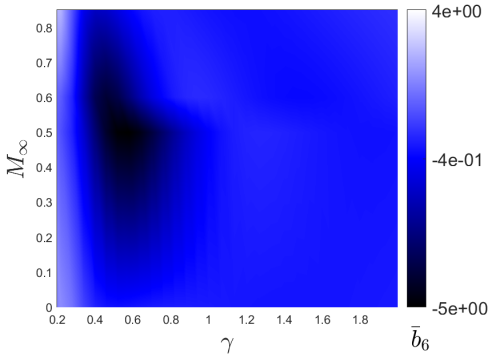

(g) Coefficients $\bar{b}_6$ with $\beta_6 = 6.4$

Figure 2.19: Interpolated coefficients $\bar{b}$ for the lift indicial function ϕ_w (Eqn. 2.38)

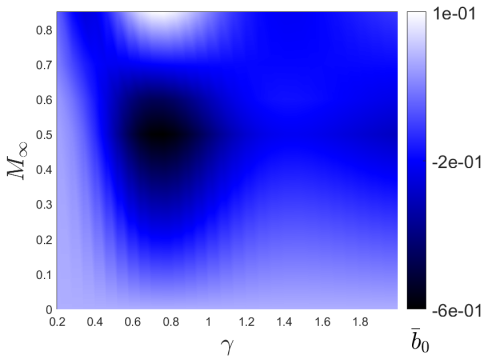

(a) Coefficients $\bar{b}_0$

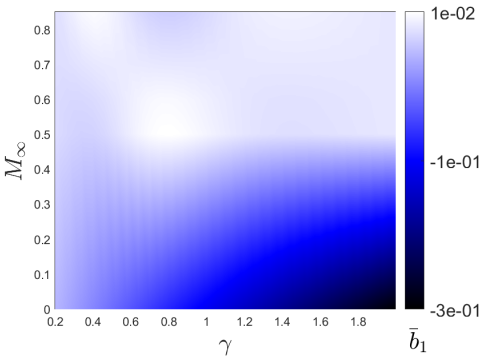

(b) Coefficients $\bar{b}_1$

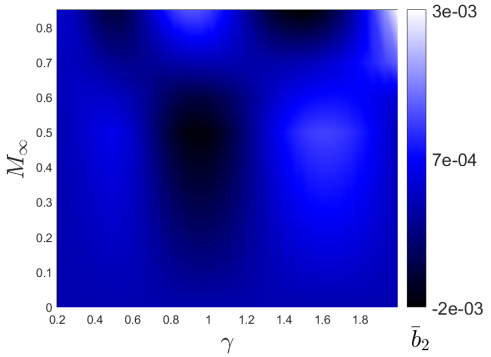

(c) Coefficients $\bar{b}_2$ with $\beta_2 = 0.05$

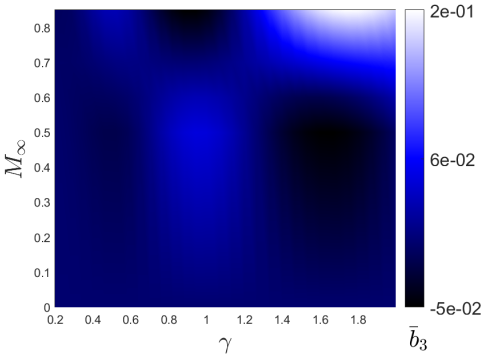

(d) Coefficients $\bar{b}_3$ with $\beta_3 = 0.3$

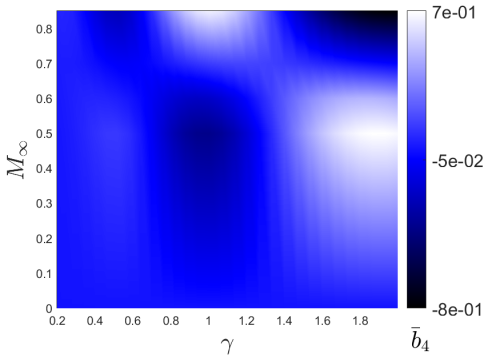

(e) Coefficients $\bar{b}_4$ with $\beta_4 = 0.8$

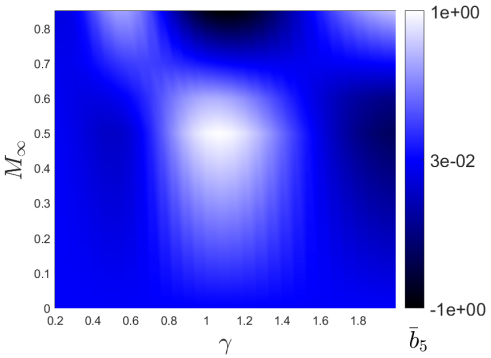

(f) Coefficients $\bar{b}_5$ with $\beta_5 = 1.6$

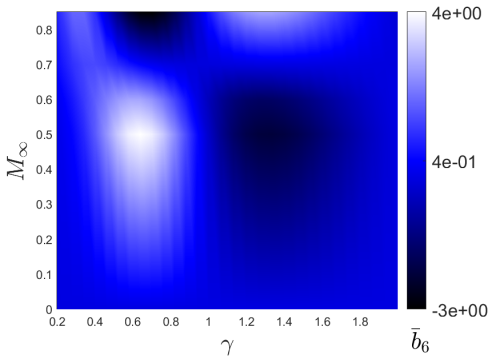

(g) Coefficients $\bar{b}_6$ with $\beta_6 = 6.4$

Figure 2.20: Interpolated coefficients $\bar{b}$ for the lift indicial function ϕ_{M_w} (Eqn. 2.38)

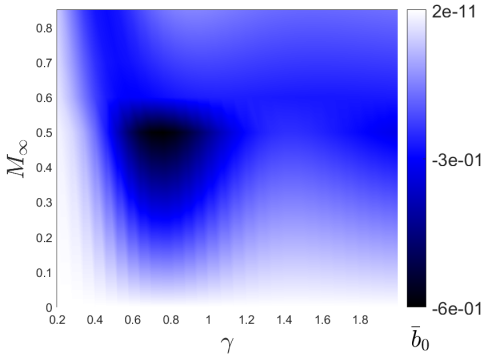

(a) Coefficients $\bar{b}_0$

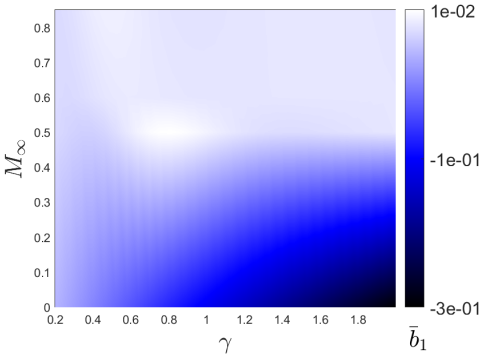

(b) Coefficients $\bar{b}_1$

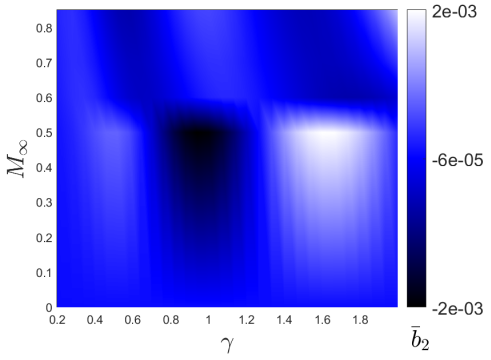

(c) Coefficients $\bar{b}_2$ with $\beta_2 = 0.05$

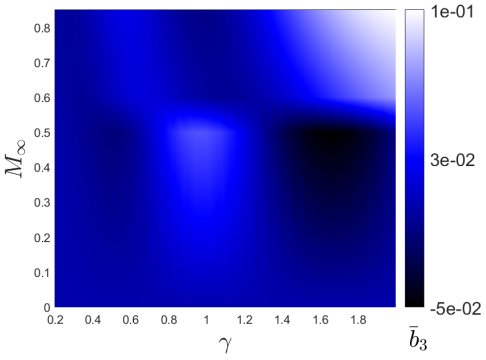

(d) Coefficients $\bar{b}_3$ with $\beta_3 = 0.3$

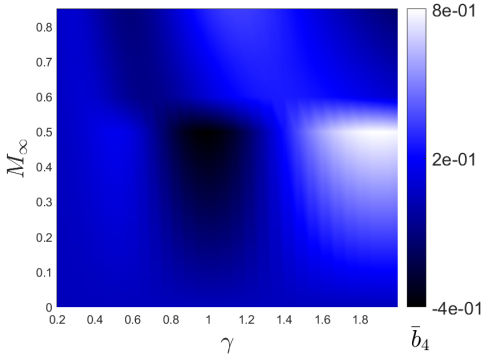

(e) Coefficients $\bar{b}_4$ with $\beta_4 = 0.8$

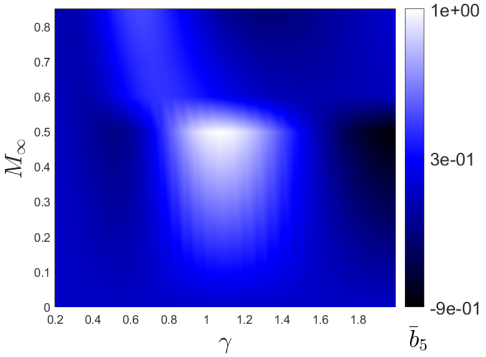

(f) Coefficients $\bar{b}_5$ with $\beta_5 = 1.6$

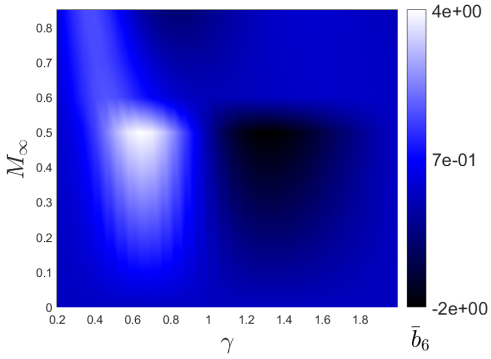

(g) Coefficients $\bar{b}_6$ with $\beta_6 = 6.4$

Figure 2.21: Interpolated coefficients $\bar{b}$ for the lift indicial function ϕ_q (Eqn. 2.38)

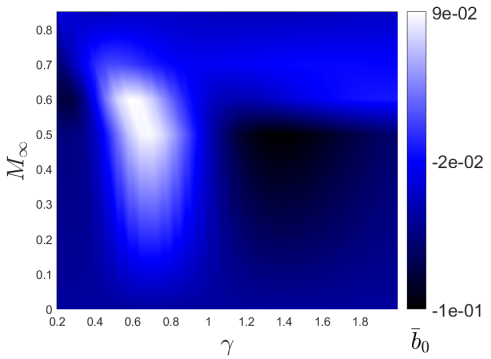

(a) Coefficients $\bar{b}_0$

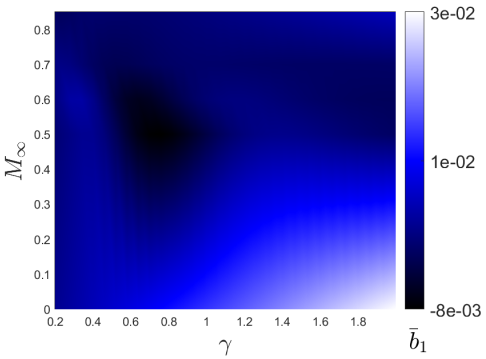

(b) Coefficients $\bar{b}_1$

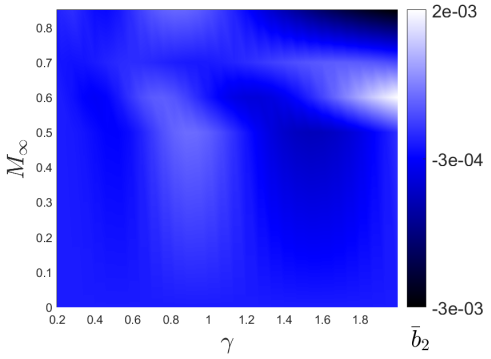

(c) Coefficients $\bar{b}_2$ with $\beta_2 = 0.05$

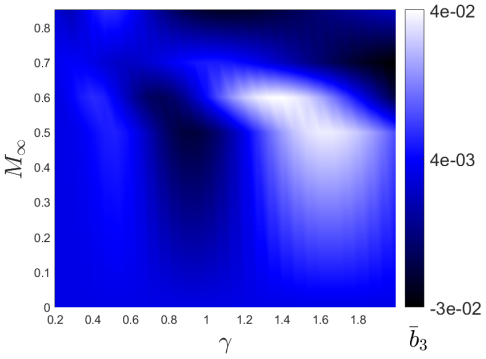

(d) Coefficients $\bar{b}_3$ with $\beta_3 = 0.3$

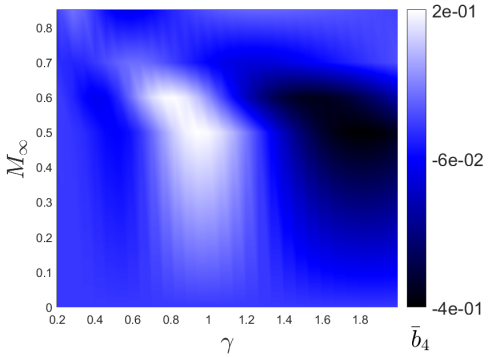

(e) Coefficients $\bar{b}_4$ with $\beta_4 = 0.8$

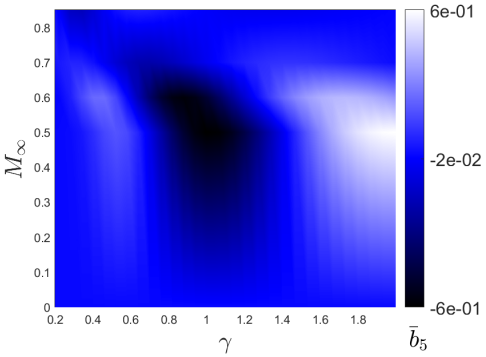

(f) Coefficients $\bar{b}_5$ with $\beta_5 = 1.6$

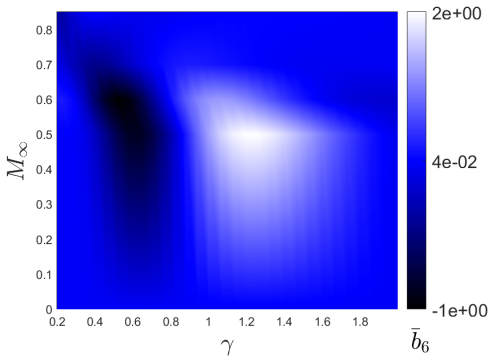

(g) Coefficients $\bar{b}_6$ with $\beta_6 = 6.4$

Figure 2.22: Interpolated coefficients $\bar{b}$ for the lift indicial function ϕ_{M_q} (Eqn. 2.38)

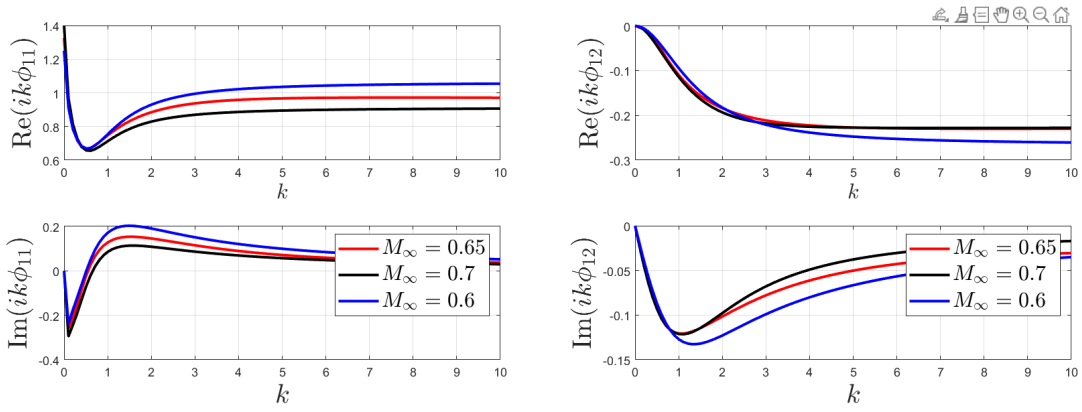

(a) $ik\phi_{11}$ (b) $ik\phi_{12}$

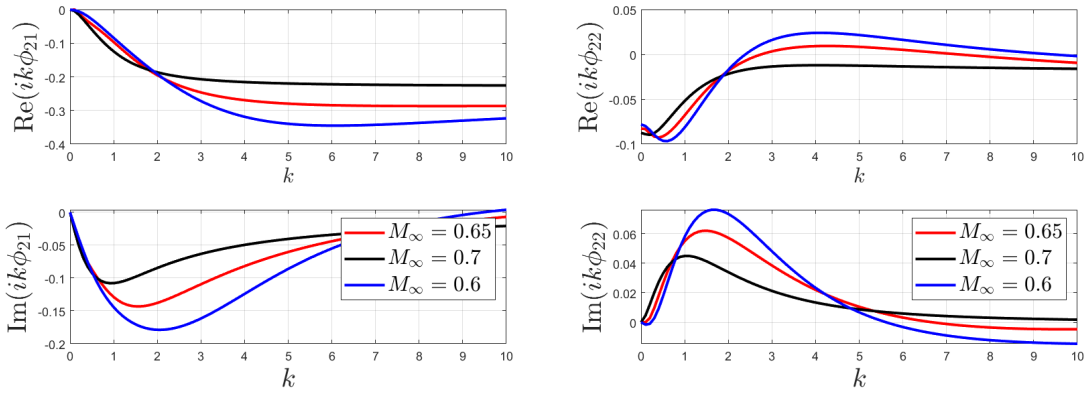

(c) $ik\phi_{21}$ (d) $ik\phi_{22}$

Figure 2.23: Comparison of the $ik\Phi$ components between the interpolation case ($M_\infty = 0.65$, $\gamma = 1$) and the tabulated components (Tab. 2.7, $M_\infty = 0.7$ and $M_\infty = 0.6$)

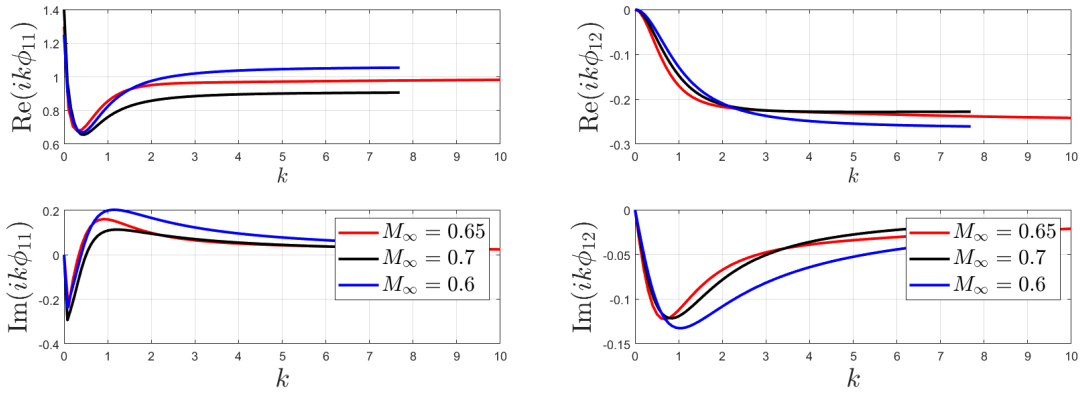

(a) $ik\phi_{11}$ (b) $ik\phi_{12}$

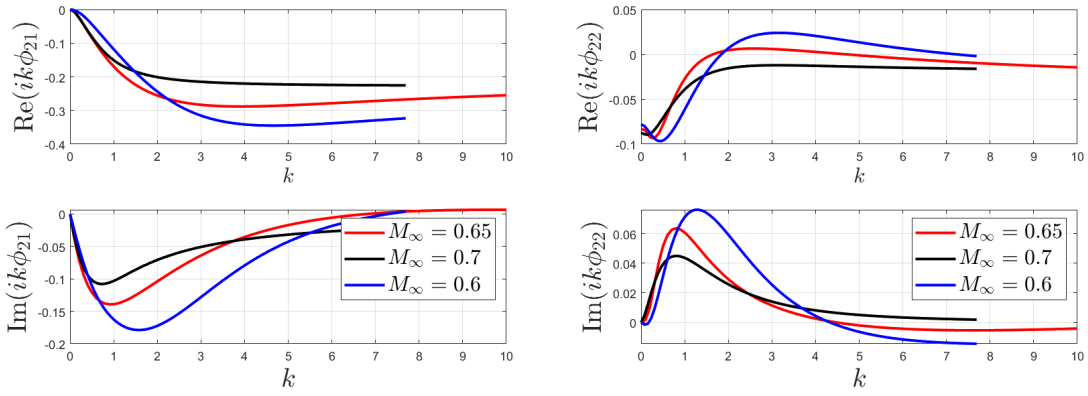

(c) $ik\phi_{21}$ (d) $ik\phi_{22}$

Figure 2.24: Comparison of the $ik\Phi$ components between the interpolation case ($M_\infty = 0.65$, $\gamma = 1.3$), and the tabulated components (Tab. 2.7, $M_\infty = 0.7$ and $M_\infty = 0.6$) with the scaled reduced frequency.

2.3.3 Lift coefficient definition based on the lifting line theory

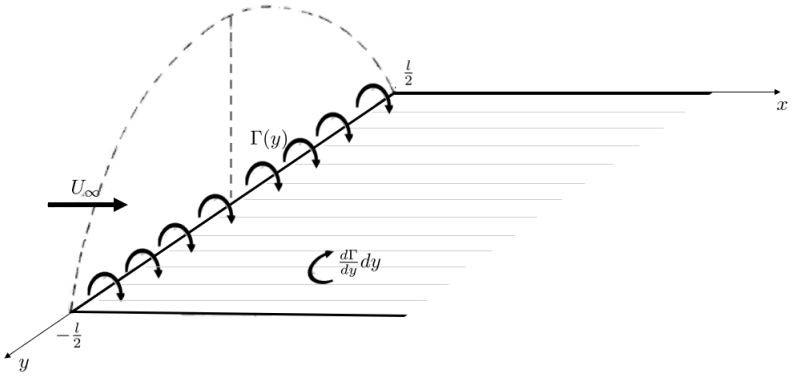

Figure 2.25: Spanwise distribution of circulation Γ around the finite span wing and an effect of finite span on downwash velocity w

For a finite three-dimensional wing, the lift of each section is strongly influenced by the lift of the neighboring sections. In order to account for this influence, the lifting line theory is considered (see Refs. [92, 94, 95]), which provides the linear lift distribution along the direction of the wingspan. Following the Prandtl-Lanchester theory, the total circulation Γ around the aerodynamic surface is described by a continuous variation $\Gamma(y)$ along the wingspan to which corresponds a continuous release of vortex filaments downstream of the wing. Each semi-infinite vorticity filament released at the y-position downstream of the wing corresponds to a change in vorticity $d\Gamma = \frac{d\Gamma}{dy}dy$, which by assumption is constant according to x (see Fig. 2.25). The vortex filament at the y-point of the lifting line produces an elementary contribution of the induced velocity at each point of the line. Specifically, at position y of the lifting line, the induced velocity contribution due to the semi-infinite vortex filament at y^* is

$$w(y) = \frac{1}{4\pi}\int_{-\frac{l}{2}}^{\frac{l}{2}} \frac{\frac{d\Gamma}{dy}dy^*}{y - y^*} \tag{2.39}$$

Since the lift of each section is given by

$$L(y) \quad = \quad -\rho U_\infty \Gamma(y) = q_D\, 2b(y)\, 2\pi(\alpha - \alpha_i) \tag{2.40}$$

in which the induced angle of incidence is equal to

$$\alpha_i(y) \quad = \quad -\frac{w(y)}{U_\infty} \tag{2.41}$$

it is possible to rewrite the lift equation considering the dependence of circulation on α

$$L(y) \quad = \quad q_D\, 2b(y)\, 2\pi(\, 1 - \frac{d\alpha_i}{d\alpha}(y)\,)\alpha \tag{2.42}$$

Therefore the lift coefficient of each section of the aerodynamic surface can be derived calculating $2\pi(\, 1 - \frac{d\alpha_i}{d\alpha}(y)\,)$ through the use of Fourier series for representing the circulation Γ (see App. A.1

for more details).

2.3.4 Aerodynamic Reduced Order Model based on indicial lift and moment functions

This section presents the aerodynamics Reduced Order Model used during the optimization to perform stability and response analyses. Having calculated the coefficients of the aerodynamic matrices for each section of the aerodynamic surfaces (see Eqn. 2.30) the aerodynamic problem is rewritten as a function of plunging and pitching displacements (h and α) :

$$\begin{Bmatrix} \tilde{L}(\xi) \\ \\ \tilde{M}(\xi) \end{Bmatrix} = C_{l_\alpha}(\xi)\, q_D \mathsf{S}_1(\xi)\mathsf{T}_1(\xi) \Big(\bar{\mathsf{B}}_0(M_\infty,\gamma)+ik\,\bar{\mathsf{B}}_1(M_\infty,\gamma)+\sum_{n=2}^{N_a+1}\frac{\bar{\mathsf{B}}_n(M_\infty,\gamma)}{ik+\beta_n}\Big)\mathsf{T}_2(\xi) \begin{Bmatrix} \tilde{w}(\xi)/U_\infty \\ \\ 2b(\xi)\tilde{q}(\xi)/U_\infty \end{Bmatrix} \tag{2.43}$$

$$\begin{aligned} \begin{Bmatrix} \tilde{w}(\xi)/U_\infty \\ \\ 2b(\xi)\tilde{q}(\xi)/U_\infty \end{Bmatrix} &= \Big(ik\,\gamma\,\mathsf{D}_1(\xi)+\mathsf{D}_0\Big)\begin{Bmatrix}\tilde{h}(\xi)\\ \tilde{\alpha}(\xi)\end{Bmatrix} \\ &= \Big(ik\,\gamma\begin{bmatrix}\frac{1}{b(\xi)} & 0\\ 0 & 2\end{bmatrix}+\begin{bmatrix}0 & 1\\ 0 & 0\end{bmatrix}\Big)\begin{Bmatrix}\tilde{h}(\xi)\\ \tilde{\alpha}(\xi)\end{Bmatrix} \end{aligned} \tag{2.44}$$

The following aerodynamic matrices for the section at ξ station are introduced

$$\begin{aligned} \bar{\mathsf{A}}_0 &= C_{l_\alpha}\mathsf{S}_1\mathsf{T}_1\bar{\mathsf{B}}_0\,\mathsf{T}_2\mathsf{D}_0 \\ \bar{\mathsf{A}}_1 &= C_{l_\alpha}\Big(\mathsf{S}_1\mathsf{T}_1\bar{\mathsf{B}}_0\,\mathsf{T}_2\mathsf{D}_1\gamma+\mathsf{S}_1\mathsf{T}_1\bar{\mathsf{B}}_1\,\mathsf{T}_2\mathsf{D}_0\Big) \\ \bar{\mathsf{A}}_2 &= C_{l_\alpha}\mathsf{S}_1\mathsf{T}_1\bar{\mathsf{B}}_1\,\mathsf{T}_2\mathsf{D}_1\gamma \\ \bar{\mathsf{F}}_{0n} &= C_{l_\alpha}\mathsf{S}_1\mathsf{T}_1\bar{\mathsf{B}}_n\,\mathsf{T}_2\mathsf{D}_0 \\ \bar{\mathsf{F}}_{1n} &= C_{l_\alpha}\mathsf{S}_1\mathsf{T}_1\bar{\mathsf{B}}_n\,\mathsf{T}_2\mathsf{D}_1\gamma \end{aligned} \tag{2.45}$$

and are integrated along the span using the formulation of Eqn. 2.28, taking into account the structural modal shapes taken through the use of the elastic line. It is important to note that in the case in which the aerodynamic forces are calculated with the rigid modal shapes of the aircraft, the matrix D_0 undergoes a modification and is assumed to be a matrix of zeros. In this way, the total aerodynamic stiffness matrix will have no contribution associated with the rigid modes. The matrices with the $\bar{}$ symbol are used to indicate the section aerodynamic forces while the matrices without the $\bar{}$ symbol are used to indicate the total forces of the aerodynamic surface. The total aerodynamic forces vector e is finally given by the aerodynamic forces of the wing and the tail surfaces

$$\begin{aligned} \mathsf{e} &= q_D\;\mathsf{E}(k,M_\infty,\gamma)\;\eta \\ &= q_D\Big[\mathsf{A}_{0_w}+ik\mathsf{A}_{1_w}-k^2\mathsf{A}_{2_w}+\mathsf{C}_w\Big(ik+\mathsf{P}_w\Big)^{-1}\Big(\mathsf{F}_{0_w}+ik\mathsf{F}_{1_w}\Big) \\ &\quad +\mathsf{A}_{0_t}+ik\frac{\bar{c}_t}{\bar{c}_w}\mathsf{A}_{1_t}-k^2\Big(\frac{\bar{c}_t}{\bar{c}_w}\Big)^2\mathsf{A}_{2_t}+\mathsf{C}_t\Big(ik\frac{\bar{c}_t}{\bar{c}_w}+\mathsf{P}_t\Big)^{-1}\Big(\mathsf{F}_{0_t}+ik\frac{\bar{c}_t}{\bar{c}_w}\mathsf{F}_{1_t}\Big)\Big]\eta \end{aligned} \tag{2.46}$$

The matrices P_w and P_t are introduced to collect the aerodynamic poles chosen for the wing and tail, as well as the matrices F_0 and F_1 collect the stiffness and damping aerodynamic contributions associated to the added aerodynamic states. Moreover, the reduced frequency used for the tail must be rescaled with the size of the wing by using the ratio $\frac{\bar{c}_t}{\bar{c}_w}$.

The aerodynamic forces is finally rewritten in order to include also the longitudinal aerodynamic force distributions, the friction drag distribution and the induced drag contributions through the A_1^D matrix

$$\begin{aligned}
\mathsf{e} &= q_D\Big(\mathsf{A}_0 + ik(\mathsf{A}_1 + \mathsf{A}_1^D) - k^2\mathsf{A}_2\Big)\eta + \mathsf{C}_w\mathsf{r}_w + \mathsf{C}_t\mathsf{r}_t \\
\mathsf{r}_w &= \Big(ik + \mathsf{P}_w\Big)^{-1}\Big(\mathsf{F}_{0w} + ik\mathsf{F}_{1w}\Big)\eta \\
\mathsf{r}_t &= \Big(ik + \mathsf{P}_t\Big)^{-1}\Big(\mathsf{F}_{0t} + ik\mathsf{F}_{1t}\Big)\eta
\end{aligned} \tag{2.47}$$

in which the matrices are defined as

$$\begin{aligned}
\mathsf{A}_0 &= \mathsf{A}_{0_w} + \mathsf{A}_{0_t} \\
\mathsf{A}_1 &= \mathsf{A}_{1_w} + \frac{\bar{c}_t}{\bar{c}_w}\mathsf{A}_{1_t} \\
\mathsf{A}_2 &= \mathsf{A}_{2_w} + \Big(\frac{\bar{c}_t}{\bar{c}_w}\Big)^2\mathsf{A}_{2_t} \\
\mathsf{P}_t &= \frac{\bar{c}_w}{\bar{c}_t}\mathsf{P}_t \\
\mathsf{F}_{0_t} &= \frac{\bar{c}_w}{\bar{c}_t}\mathsf{F}_{0_t} \\
\mathsf{A}_1^D &= S\begin{bmatrix} -2C_{D_e}/\bar{c}_w & 0 & -C_{D_\alpha}/\bar{c}_w & 0 & \dots & 0 \\ 0 & 0 & & & & 0 \\ \vdots & & \ddots & & & \vdots \\ 0 & & & & & 0 \end{bmatrix}
\end{aligned} \tag{2.48}$$

In order to account the aerodynamic load perturbation due to the aircraft longitudinal motion, the A_1^D makes a correction to the GAF matrix, according to Ref. [75]. In fact, the aerodynamic drag is defined as

$$D = D_0 + D_i = \frac{1}{2}\rho U_\infty^2 S\left(C_{D_0} + C_{D_\alpha}\alpha\right) \tag{2.49}$$

in which D_0 is the shape drag contribution, while D_i is the induced drag contribution (see Subs. 2.3.5 for more details). The equilibrium value is

$$D_e = \frac{1}{2}\rho U_\infty^2 S\left(C_{D_0} + C_{D_\alpha}\alpha_e\right) = \frac{1}{2}\rho U_\infty^2 S\, C_{D_e} \tag{2.50}$$

A perturbation on the angle of attack of the airplane and its forward speeds define a perturbation of the aerodynamic drag

$$\Delta D = \frac{\partial D}{\partial u}\Big|_{D=D_e}\Delta u + \frac{\partial D}{\partial \alpha}\Big|_{D=D_e}\Delta\alpha \tag{2.51}$$

in which the two derivatives ca be evaluated as

$$\begin{aligned}\frac{\partial D}{\partial u}\Big|_{D=D_e} &= \rho U_\infty S C_{D_e} = \frac{2q_D S}{U_\infty} C_{D_e} \\ \frac{\partial D}{\partial w}\Big|_{D=D_e} &= \frac{1}{U_\infty}\frac{\partial D}{\partial \alpha}\Big|_{D=D_e} = \frac{1}{2}\rho U_\infty S C_{D_\alpha} = \frac{q_D S}{U_\infty} C_{D_\alpha}\end{aligned} \tag{2.52}$$

Therefore, finally the perturbation of the aerodynamic loads caused by the two preceeding terms is

$$f_D = q_D \frac{b}{U_\infty} \mathsf{A}_1^D \begin{Bmatrix} \Delta x \\ \Delta\theta \end{Bmatrix}$$

2.3.5 Drag modelling

The aerodynamic drag is computed considering the contribution of the aircraft shape drag D_0, due to the wet surface of the aircraft, and the contribution of the induced drag D_i associated with the total lift coefficient and the equivalent aspect ratio AR_e of the aircraft (for more details see App. A.2).

$$D = D_0 + D_i = q_D S_w C_{D_0} + q_D S_w \frac{C_{L_w}^2}{\pi A R_w e} + q_D S_t \frac{C_{L_t}^2}{\pi A R_t e} = q_D S_w C_{D_0} + \frac{1}{\pi A R_e e} C_L^2 \tag{2.53}$$

The friction drag coefficient C_{D_0} due to the total wet area of the aircraft is given by the contribution of the wing, the tail and the fuselage friction coefficients, denoted with C_f

$$C_{D_0} = C_{f_w} + C_{f_t}\frac{S_t}{S_w} + C_{f_f}\frac{S_f}{S_w} \tag{2.54}$$

considering their wet surfaces S_w, S_t and S_f. In order to calculate the friction coefficient of each part of the aircraft the Reynolds number, which is the ratio between inertial force and viscous force, is calculated (the Reynolds number have a significant influence value on the equivalent skin-friction coefficient Ref.[96])

$$Re_x = \frac{S_{wet}}{l}\frac{U}{\nu} \tag{2.55}$$

in which a reference length S_{wet}/l, the air speed and the air kinematic viscosity ν are considered. The friction coefficient is finally calculated as (Ref. [97])

$$C_f = 0.00258 + 0.00102\, e^{-6.2810^{-9} Re_x} + 0.00295\, e^{-2.0110^{-8} Re_x} \tag{2.56}$$

2.4 Comparison against NASTRAN solver

The validation of the developed aeroelastic model is here described by comparing stability and response analyses performed with the analytical model and with the finite element model. The benchmark aircraft model used is defined geometrically in the 2.2.1 section. The model *MZFW* case is chosen because this configuration provides the most critical performance for both stability and gust response. In the interests of outline the results of the stability and gust analyses, two aeroelastic models are considered. The first model is the analytical and it is represented by the

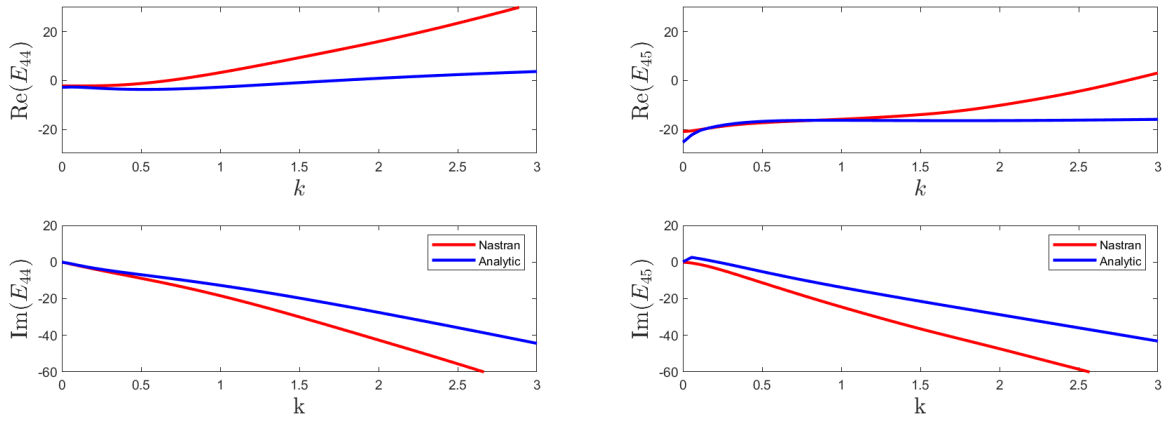

(a) E_{44}

(b) E_{45}

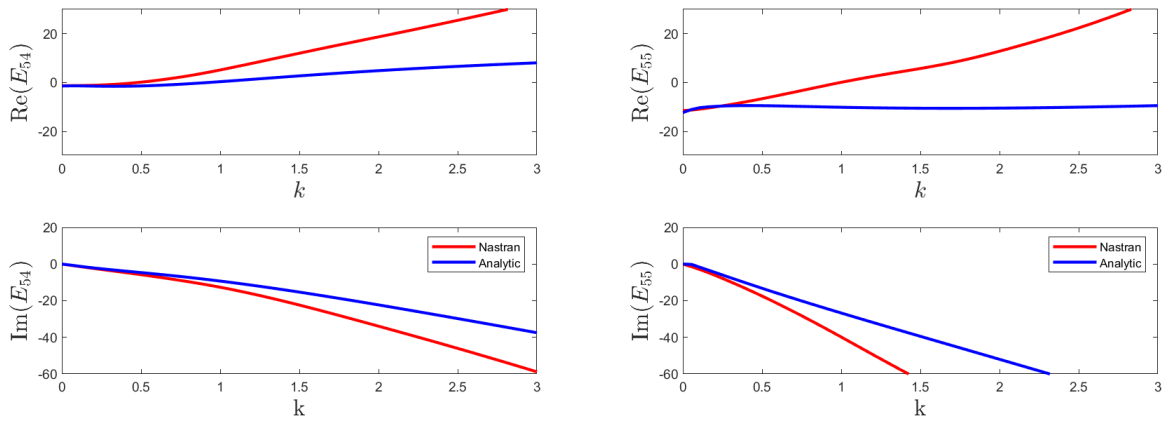

(c) E_{54}

(d) E_{55}

Figure 2.26: E components comparison for $M_\infty = 0.7$ and $\rho = 1.22\frac{Kg}{m^3}$

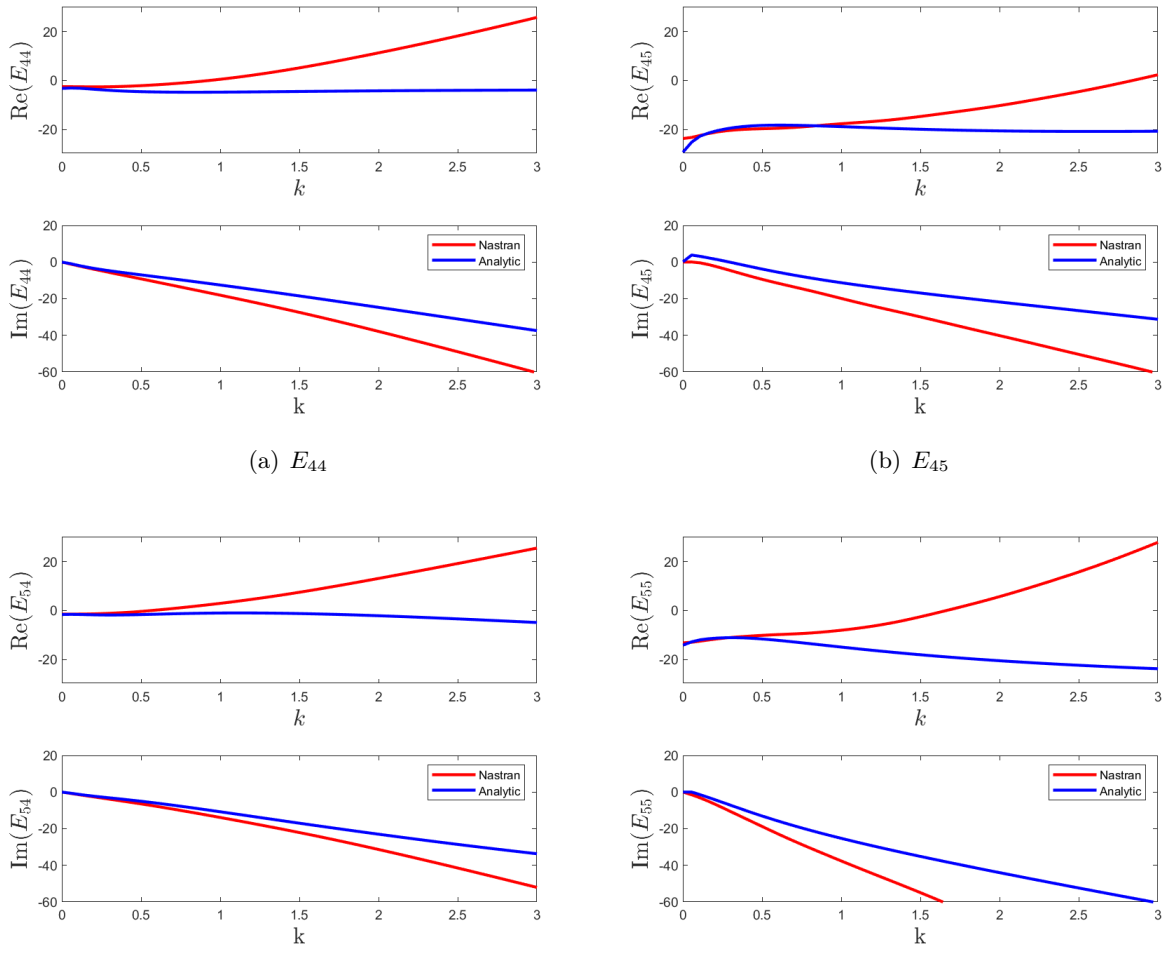

(a) E_{44} (b) E_{45}

(c) E_{54} (d) E_{55}

Figure 2.27: E components comparison for $M_\infty = 0.85$ and $\rho = 1.22 \frac{Kg}{m^3}$

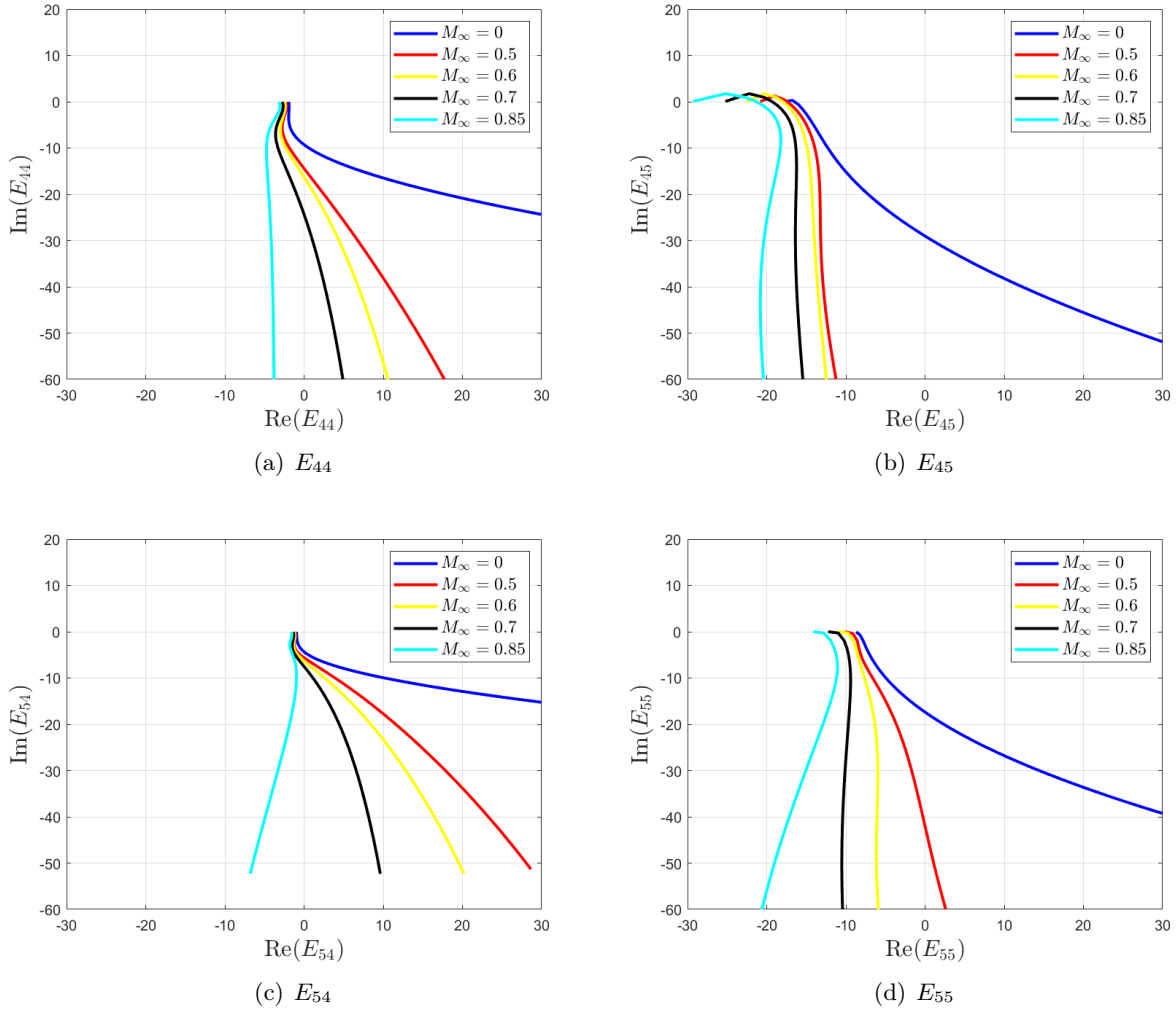

(a) E_{44} (b) E_{45}

(c) E_{54} (d) E_{55}

Figure 2.28: E components comparison for several Mach numbers and $\rho = 1.22\frac{Kg}{m^3}$

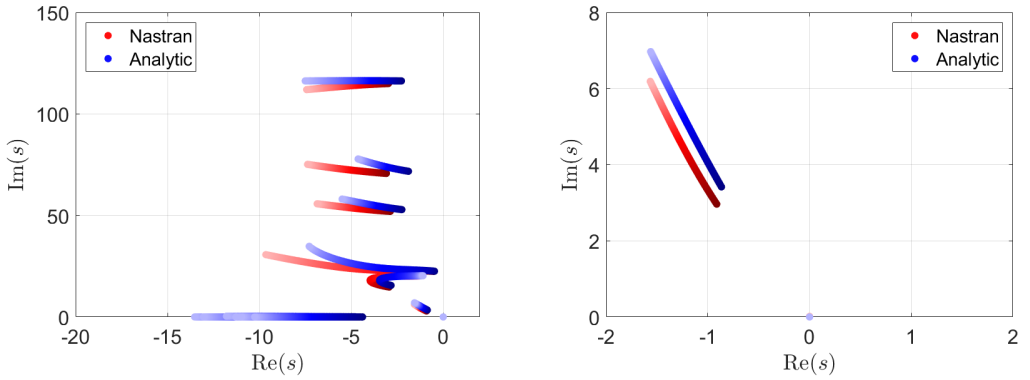

(a) Root locus of the aeroealstic system (b) Root locus for rigid body modes

Figure 2.29: Root locus comparison between the analytical ad *FEM* model ($M_\infty = 0.7$ and $\rho = 1.22\frac{Kg}{m^3}$).

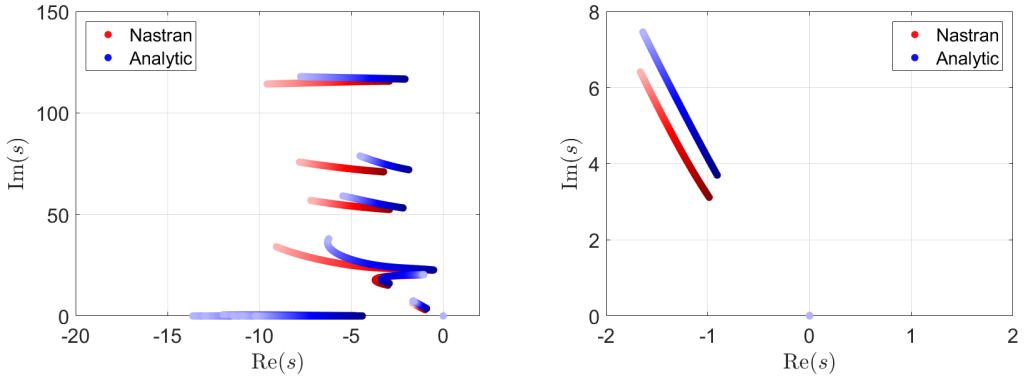

(a) Root locus of the aeroealstic system

(b) Root locus for rigid body modes

Figure 2.30: Root locus comparison between the analytical ad *FEM* model ($M_\infty = 0.85$ and $\rho = 1.22\frac{Kg}{m^3}$).

state matrix A (Eqn. 2.17) and by the gust input matrix B (Eqn. 2.23) . Whereas the second one is a *FEM* model in which the aerodynamics is defined by the Double Lattice Method and in which the analyses are conducted through MSC-NASTRAN® solver Ref. [77].

The aeroelastic stability problem is performed computing the eigenvalues s varying the free stream velocity U_∞ (from 170 m/s up to 400 m/s), varying the Mach number and keeping fixed the air density to $\rho = 1.22\frac{Kg}{m^3}$. For the model validation, the first comparison is given considering the components of the generalized aerodynamic forces matrix E. Specifically, the components of the E matrix associated with the first bending and first torsional modes of the wing are considered (respectively Fig. 2.14(a) and Fig. 2.14(b)). The results are presented for two cases of Mach number, namely $M_\infty = 0.7$ in Fig. 2.26 and $M_\infty = 0.85$ in Fig 2.27. The Figures present the components of the E matrix in blue for the analytic case and in red for the *FEM* model and demonstrate how the analytic model represents a good approximation of the *FEM* model. Moreover, in order to illustrate how the components of the E matrix vary as a function of the Mach number for the same aircraft configuration, the same components of the E matrix previously displayed are presented using the analytical model as function of the number of Mach in Fig. 2.28. Finally, the results obtained through the two models are presented using the stability scenario. The cases at $M_\infty = 0.7$ (Fig. 2.29) and $M_\infty = 0.85$ (Fig. 2.30) are again shown, comparing the root locus obtained from *FEM* and analytical analysis, in red and blue, respectively. For both models the aeroelastic system is stable in the required speed range, and in addition, the aeroelastic scenario given by the two models is quite similar. Therefore, concluding the validation part associated with the aeroelastic stability, all the previous comparisons show that the analytical model is a good approximation of the *FEM* model. During the optimisation process, it is clear that both models could be used. The *FEM* model is much more accurate and can therefore be used in an industrial setting, although it is very time consuming and expensive, while the approximation model, although it has a certain margin of error, allows a good approximation at a very low time and expense. Choosing the latter is not only related to reduced time and computational cost, but also to the robustness of the formulation, since the aerodynamics is directly expressed in time by using indexed functions. Furthermore, it has been verified that the approximate model used is always more conservative than the FEM model, almost always keeping us within safety margins.

As a second validation of the aeroelastic model, the results of the gust response analyses, defined

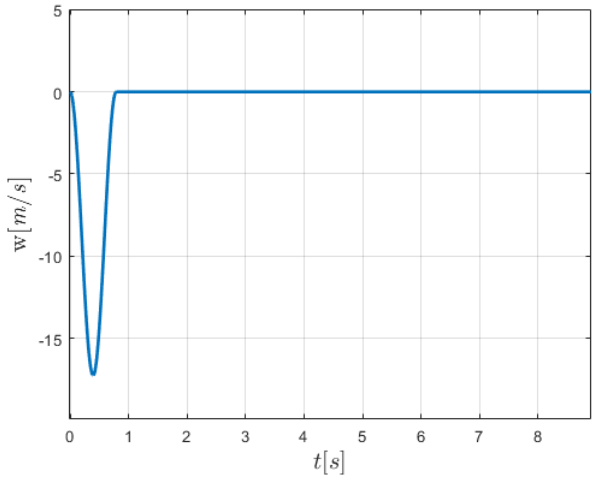

Figure 2.31: Vertical gust imposed as input

in Subs. 2.1.1, are presented. The only input imposed on the system is a gust profile, a good representation of which is given by 1-*cosine* gust shape function, displayed in Fig. 2.31. The gust is assumed to be vertical, with the maximum amplitude equal to $18m/s$. The response analysis is carried out varying the Mach number and keeping fixed the air density to $\rho = 1.22\frac{Kg}{m^3}$. The results related to the gust input at $M_\infty = 0.7$ and $M_\infty = 0.85$ are presented in Fig. 2.32 and Fig. 2.33, where the time evolution of the elastic modal coordinates due to the gust input are shown (representing the motion of a structure in terms of its natural modes and providing a useful means for reconstructing the displacements of the structure). The elastic modal coordinates due to the gust input are presented in red for the *FEM* model and in blue for the analytical model. Comparing all elastic modal coordinates in time due to the gust input, it is seen that the largest deformation component is associated with the first elastic mode shape (reminding that modes are dimensionless at unit displacement). More specifically, the second peak in the Figures 2.32(a) and 2.33(a) represents the maximum deformation associated with the maximum stress on the structure. The maximum stress associated to the maximum deformation calculated using the analytical model is equal to the 90% of the *FEM* maximum stress for the case at $M_\infty = 0.7$, while is equal to the 87% for the case at $M_\infty = 0.85$. This result is justified since the analytical maximum peak of the q_1 coordinate is lower than the peak obtained with the *FEM* model. Instead, looking at the q_2 coordinate, the maximum peak of the analytical model is greater than the peak of the *FEM* model. Therefore, it is found that the maximum load to which the spars are subjected in the engine zone (where the maximum deformation occurs) is in the analytical model equal to the 113% of the value obtained with the *FEM* model for $M_\infty = 0.7$, and equal to the 115% for $M_\infty = 0.85$.

As the results associated with the aeroelastic stability and the gust response demonstrate, the analytical aeroealstic model developed turns out to be a good approximation of the *FEM* aeroelastic model with a limited margin of error. More specifically, the analytical model always turns out to be more conservative compared with the finite element model, which allows us a greater confidence in using this model. In addition, an important advantage of using the analytical stability and response analyses instead of the finite element analyses is in the reduction of computational cost and time. In fact, the analytical aeroelastic stability analysis takes $2.5s$ while *FEM* analysis takes $49s$, whereas the analytical gust response takes $12.2s$ while *FEM* analysis takes $122.4s$.

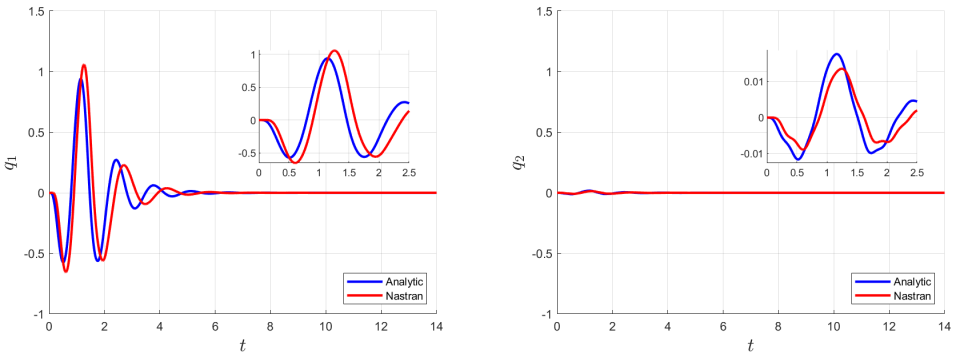

(a) q_1

(b) q_2

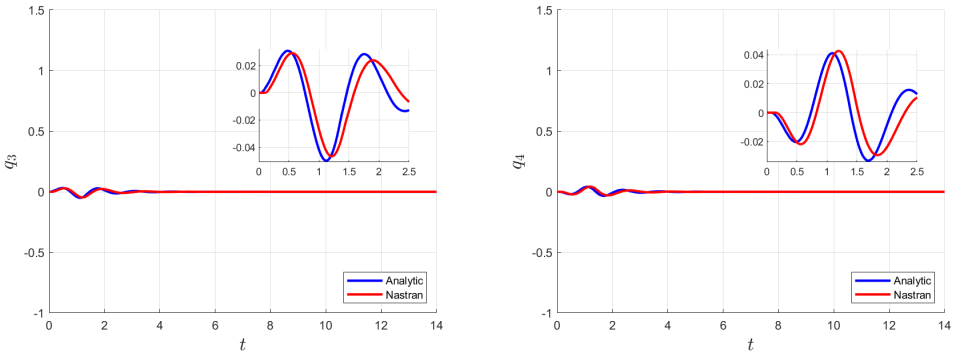

(c) q_3

(d) q_4

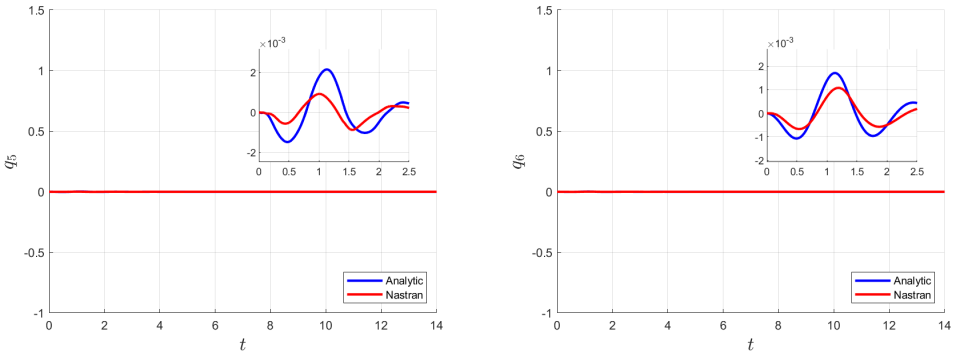

(e) q_5

(f) q_6

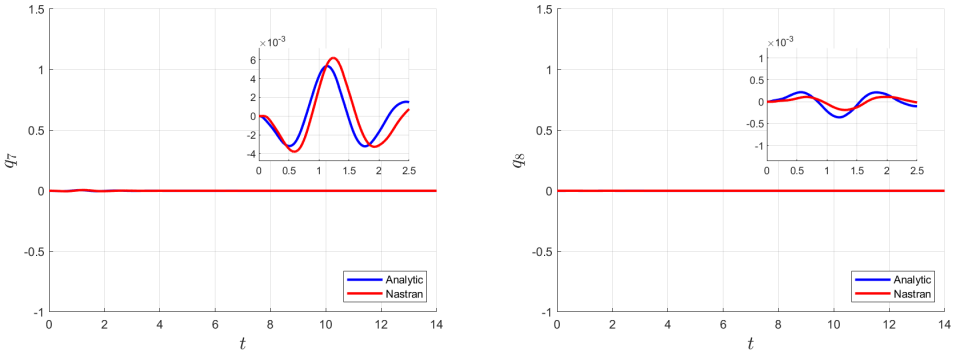

(g) q_7

(h) q_8

Figure 2.32: Elastic modal coordinates due to the gust input ($M_\infty = 0.7$ and $\rho = 1.22\frac{Kg}{m^3}$)

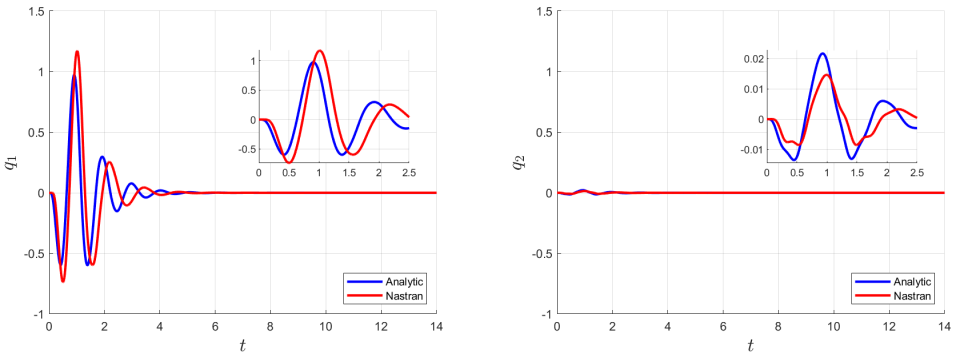

(a) q_1

(b) q_2

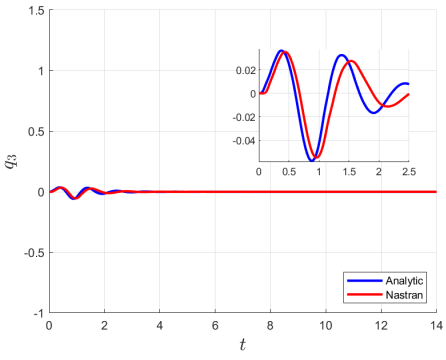

(c) q_3

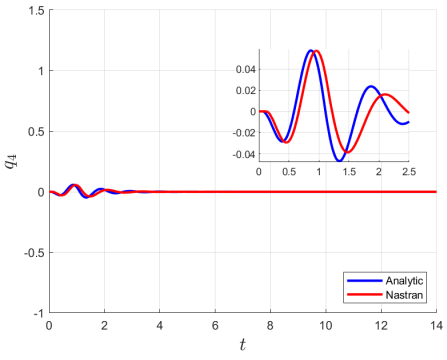

(d) q_4

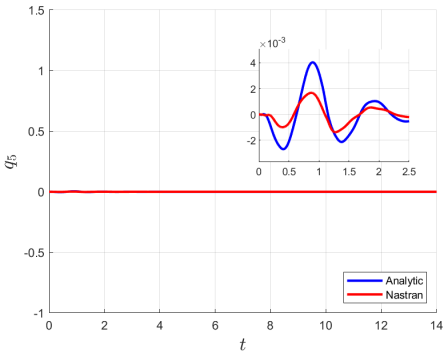

(e) q_5

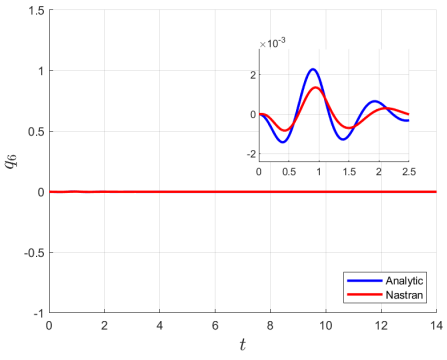

(f) q_6

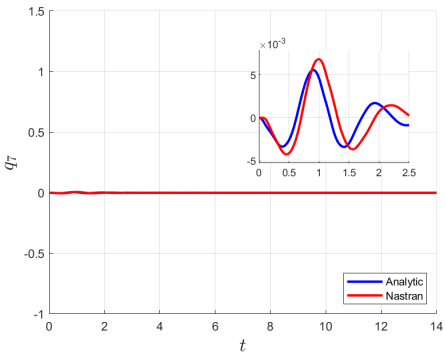

(g) q_7

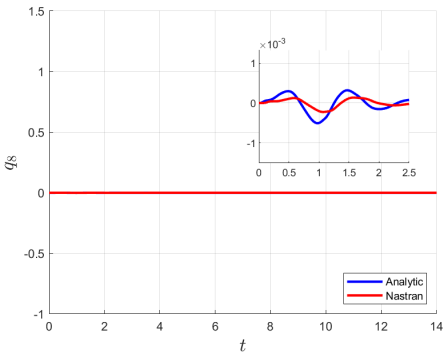

(h) q_8

Figure 2.33: Elastic modal coordinates due to the gust input ($M_\infty = 0.85$ and $\rho = 1.22\frac{Kg}{m^3}$)

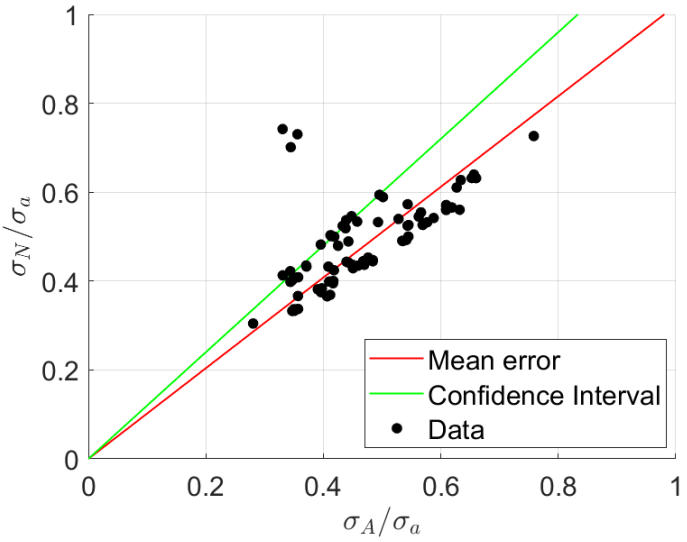

Figure 2.34: Comparisons on gust response data (*FEM* and Analytical model) among a given population

Considering and acknowledging the limitations of the analytical model concerning the calculation of the maximum load reached as a result of the external gust input, now the aim is minimizing this error. A population consisting of 85 different individuals is examined and the aircraft stability is observed. In the case of stable cruise flight, the gust response and the maximum load values achieved are observed. For all designs, two analysis using the analytical model and the *FEM* by applying the same gust are considered. The objective is to define the mean squared error and a confidence interval. The maximum loads obtained with MSC.Nastran®σ_N and the analytical model σ_A are compared, normalized with the maximum allowable value for the structure σ_a (see Fig. 2.34). It is noted that the mean error obtained is approximately 2% in favor of the load obtained with MSC.Nastran®. Additionally, the root mean square value is considered and the confidence interval equal to the mean error plus 2 times the standard deviation is calculated to account for and correct the majority of the calculated data.

Therefore, in order to correct the analytical limit in the calculation of dynamic loads, it is considered an increased input of 20% compared to that provided by EASA specifications Ref. [76], aiming to achieve a more accurate load.

2.5 Control law modelling

In cases where some designs derived from the optimization process fail to meet the constraints associated with the dynamic stability and the dynamic loads, the integration of a controller model is recommended. The primary objective of this controller is to actively suppress flutter and reduce the dynamic loads induced by the gust inputs if such intervention becomes necessary.

There are several approaches to translating the stabilization and the load reduction goals into quantitative criteria for the controller synthesis. A crucial first consideration concerns models: the use of unstable models, as demonstrated in Ref. [98], produces a stabilization criterion that helps to achieve the design goals. Requiring stability over multiple models, as noted in Refs. [99, 100], results in a closed-loop robustness criterion that aligns with the previously defined goals. Moreover,

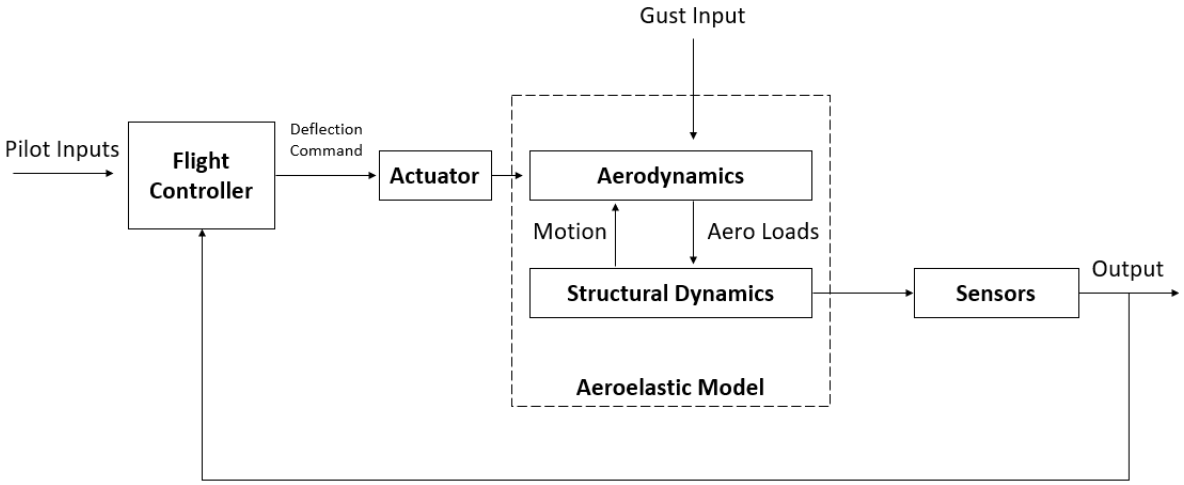

Figure 2.35: The Aeroservoelastic Model

during the synthesis, it may be necessary to attenuate the transfer function based on *LQG* Ref.[101] or H_∞ criteria Ref. [98]. In fact, near the instability, the peak of the open-loop transfer function associated with the flutter mode increases, and enforcing its attenuation in closed loop leads to damping and stability.

The structure of the proposed controller adopts an H_∞ approach (Refs. [102]), and its synthesis is achieved through an internal optimization process, using *systune* command in Matlab ® Ref. [103]. Specifically, *systune* is a powerful and flexible tool for tuning complex control systems, with a focus on stability, performance, and compatibility with complex simulation environments. In addition, it enables multi-variable tune ups, where several control parameters are adjusted simultaneously, and automates the tune up process, reducing the time needed to reach the optimum solution compared to manual tune ups or other less automated processes. This procedure has the disadvantage of designing a full order controller, therefore requiring a reduction of control order. Promising results for fixed-order controllers have been presented in Refs. [104–106]. More in details, active control can be used to avoid flutter while ensuring stability and maneuverability at the same time. Indeed, the inclusion of control laws for *AFS* and *GLA*, in particular, in the early stages of aircraft design improves the aircraft's performance (Ref. [107, 108]).

The integrated structural and control design is an optimization problem that requires a multidisciplinary approach also known as *co-design*, Refs. [109–111]. Perez and al. [112] have applied a similar methodology to optimize payload weight while maintaining structural flexibility. Using a similar design approach, Ref. [113] sized an aircraft vertical tail along with propeller electrical actuator bandwidth, and lateral control laws. Moreover, the co-design method was used by Deneul [114] to size the control surfaces of a blended-wing-body aircraft while meeting the requirements of flying quality. The challenge in integrated design arises from the lack of a Multidisciplinary Optimization method that considers the coupled nature of the control design and the aeroelastic design.

2.5.1 Aeroservoelastic Model and Control Architecture

The representative scheme of the aeroservoelastic model used in the optimization process is summarized in Figure 2.35. The aeroelastic model is subject to the pilot's external inputs (i.e. a request for rotation of the control surfaces) and environmental conditions, such as gusts. On-board sensor readings detect the aircraft dynamics and the flight conditions throughout the mission. The inertial measurement sensors, installed in the wings and fuselage, help to distinguish the rigid body motion and the flexible deflection of the aircraft structure. No delays or disturbances are added to the sensor units. The sensor readings come from the structural dynamics, selected specific points on the structural model. The g-set of accelerations are expressed

$$\mathsf{x}_g(t) = \mathbf{\Phi}_{gh}\mathsf{x}_h(t) \tag{2.57}$$

from the displacement in generalized coordinates using a multiplication by the modal matrix. Recovery of accelerations is then simple by selecting the point in the set g at which the quantity needs to be calculated and taking the time derivatives as required. The sensor readings are the outputs of the system, while pilot commands for the control surface deflections are the inputs.

Through a linearization, the dynamics of the aeroservoelastic system can be represented by the state-space system form (considering the Eqn. 2.18)

$$\begin{aligned} \dot{\mathsf{x}} &= \mathsf{A}\mathsf{x} + \mathsf{B}_g\mathsf{u}_g + \mathsf{B}_H\mathsf{u}_H \\ \mathsf{y} &= \mathsf{C}\mathsf{x} + \mathsf{D}_g\mathsf{u}_g + \mathsf{D}_H\mathsf{u}_H \end{aligned} \tag{2.58}$$

The state-space system correlates the input vectors, (u_g and u_H, namely the gust velocity components and their derivative and the pilot requests applied to the control surfaces, respectively) and the state vector x (defined in 2.1), in which y is the output vector of the sensor measurements. More specifically, these are the equations of the *Open Loop (OL)* system and are used to design control laws for the flutter controller and load alleviation. A more accurate description of the model used is given by the Simulink® (Ref. [115]) model in Fig. 2.36. The aeroelastic state space system specifically receives as input the command from the pilot and the gust. The dynamics of the actuator are modelled with a second order low pass filter, and additionally, the system incorporates the input saturation to consider the physical limit of the control surface rotation.

The control path of the controller consists of a second-order filter and a *Proportional–integral controller (PI)* controller as well as a band-pass filter to suppress high and low frequency instabilities

$$N(s) = \frac{a_1 s^2 + b_1 s + c_1}{a_2 s^2 + b_2 s + c_2} \tag{2.59}$$

$$F(s) = \frac{b_3 s + c_3}{a_4 s^2 + b_4 s + c_4} \tag{2.60}$$

The measured outputs are processed in the input-output blending box to improve the observability and controllability of the system, with the goal of maximizing efficiency.

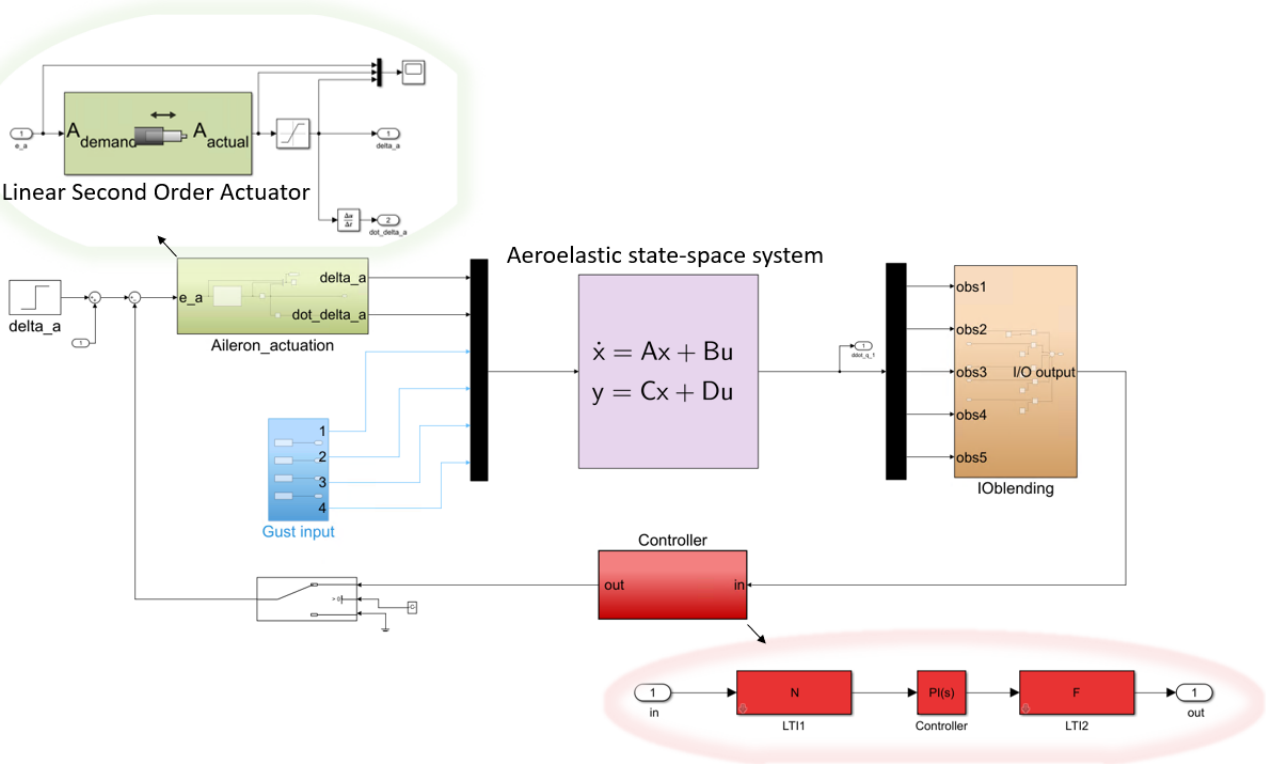

Figure 2.36: Model used for the control law synthesis

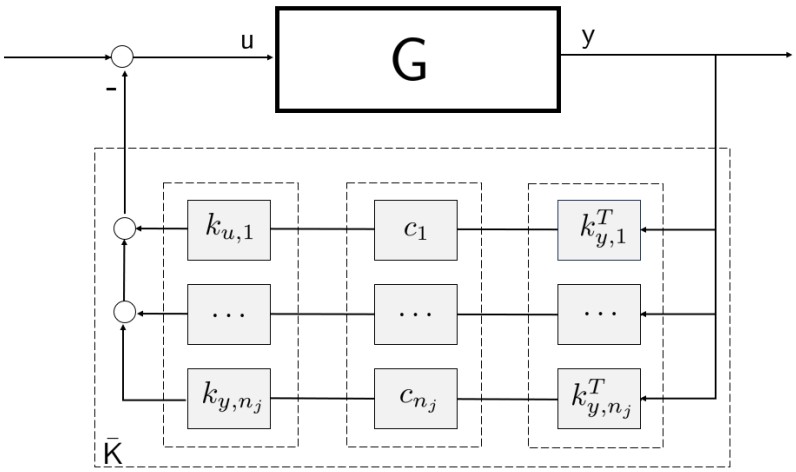

Figure 2.37: Closed-loop interconnection of the state-space model of the aeroelastic system with the controller

2.5.2 Optimal Blending approach for the Aeroealastic Mode control

Although there are various criteria for choosing the most suitable inputs and outputs, in order to improve the observability or the controllability of the system, in this section an attempt is made to align the criterion as closely as possible with the specific *AFS* synthesis problem under consideration. In order to maximize the observability and the controllability of the flutter mode, the *Inputs/Outputs Blending* technique is used (Ref. [116–118]). Specifiaclly, it consists in selecting a proper linear combination of the inputs and of the outputs to transforms the *Multi-Inputs,Multi-Outputs (MIMO)* controller synthesis into a *Single-Input,Single-Output (SISO)* problem to control an isolated mode, i.e. the flutter mode. Specifically, the method involves the isolation of the mode to be controlled through a combination of blending inputs and outputs. The corresponding vectors associated with the inputs and outputs blending, referred to $k_{u,n_j} \in \mathbb{R}^{n_u}$ and $k_{y,n_j} \in \mathbb{R}^{n_y}$, respectively, depend on the characteristics of the mode to be controlled and can be considered as directional filters. This approach ensures a robust response to frequency variations, since the blending vectors are not affected by the natural frequency of the mode. The *Closed Loop (CL)* interconnection is shown in Fig.2.37, where n_j modes are subject to be controlled, and the overall controller could be defined as

$$\bar{\mathsf{K}} = \mathsf{k}_u \begin{bmatrix} c_1 & 0 & \dots & 0 \\ 0 & c_2 & \dots & 0 \\ \vdots & \vdots & & \vdots \\ 0 & 0 & \dots & c_{n_j} \end{bmatrix} \mathsf{k}_y^T \tag{2.61}$$

where c_{n_j} are the *SISO* controllers, and the vectors $\mathsf{k}_u = [k_{u,1}, \dots, k_{u,n_j}]$ and $\mathsf{k}_y = [k_{y,1}, \dots, k_{y,n_j}]$ summerize the input and output blending vectors. It is worth remembering that while *SISO* controllers are frequency dependent (e.g. *PI* or filters) the inputs and outputs blending vectors are composed by real values.

Since the flutter dynamics depends largely on the effective airspeed, a great improvement in the performance of the controllers is achieved by taking this flight parameter into account during the programming of the blending vectors. However, it has been shown that constant blending vectors are indeed quite sufficient to stabilize the flutter modes within a considered flight envelope (Ref. [116]). Taking into account the state-space model of the aeroelastic system G in modal form, for which the matrix A is diagonal, is possible to isolate the second-order model G_f (associated to the mode of interest represented by two conjugate poles) from the rest of the dynamics G_s

$$\mathsf{G}(s) = \mathsf{G}_s(s) + \mathsf{G}_f(s) \tag{2.62}$$

The objective is to find the components of the input/output blending vectors that maximize the H_2 norm of the transfer function associated with the mode of interest

$$\max_{\substack{\|\mathsf{k}_u\|_2=1 \\ \|\mathsf{k}_y\|_2=1}} \frac{\|\mathsf{k}_y^T \mathsf{G}_f \mathsf{k}_u\|_2}{\|\mathsf{G}_f\|_2} \tag{2.63}$$

As explained in Ref. [117], in the case in which G_f is a stable second-order transfer function, the

optimization problem can be rewritten as

$$\begin{aligned} \underset{\phi\in[0;\pi]}{max} \quad & \|\mathsf{F}(\phi)\|_2 \\ \mathsf{F}(\phi) \quad = \quad & \mathrm{Re}(\mathsf{G}_f(j\omega_n))cos\phi + \mathrm{Im}(\mathsf{G}_f(j\omega_n))sin\phi \end{aligned} \tag{2.64}$$

where ω_n is the natural frequency of G_f and Re and Im represent the real and imaginary parts of the complex number. For several values of ϕ in the range from 0 to π, the matrix $\mathsf{F}(\phi)$ can be calculated easily, and for each value of ϕ a *Singular Value Decomposition (SVD)* is performed, resulting in its norm 2. Specifically, if the value of ϕ that maximizes this norm is considered, the vectors k_y and k_u correspond to the left and right unit vectors associated with the highest singular value, respectively. However, it is worth noting that the norm H_2 becomes infinite when the mode of interest is unstable, as in our case. To overcome this problem, the authors of Ref. [117] suggest a solution in which the real part of the unstable poles is simply mirrored and then the algorithm described in Ref. [119] is applied.

In the specific case of this thesis work, the input/output blending methodology is implemented in the specific case of *AFS*, considering the accelerations of the wing structure in specific points as measurements and the rotation of the aileron control surface as input. The methodology is applied for a given range of unsteady velocities for which the controller synthesis is performed.

2.5.3 Synthesis criterion

Once the structural and aeroelastic analyses are completed, the process of control optimization begins. The feedback loops are built with blocks of fixed structure. The synthesis of the control laws is implemented using *systune* command in Matlab ® in which the robust control toolbox works as a black box that return the controller performances and the optimal control law. Indeed, the control design variables, such as the filters coefficients and the *PI* variables, are internal local variables that are updated by the optimization algorithm while maintaining the overall order of the filter.

The feedback loop used for *AFS* and *GLA* is the same and it is initialized by means of three sequential blocks in which the first block is a notch filter centered on the structural bending frequency of the wing, the second block is a *PI* and the third block is a band-pass filter. The controller is responsible for stabilizing the aeroelastic system up to a certain speed ($1.1U_D$, where U_D is the dive speed) and reducing the gust load, using the aileron surface. Therefore, the velocity range for which the *AFS* controller is optimized is reduced to $[U^f_{OL}, 1.1U_D]$ with U^f_{OL} the open loop flutter speed, whereas the *GLA* controller is optimized for the cruise conditions. A stability constraint is always imposed to ensure the stability of the *CL* system, while the prescribed target focus on the controller function's weight, that must be limited. Generally, for given specifications, the system is considered stable over a given speed range if all poles are to the left of the complex plane, requiring no specific pole damping values. More specifically, constraint on the actuation power are introduced by limiting the frequency domain response of the controller. Additionally, in instances where load reduction is requested during a gust, there is an additional request for limit the gain of the gust transfer function. This transfer function takes the gust acceleration as input and provides the measured acceleration as output. The gain constraint enforce a design requirement of disturbance rejection across a particular input/output pair, by constraining the gain to be less than 1. The

	DESIGN FEATURES	
AIRCRAFT	Cruise Mach M_∞	0.86
	Range R	$5170Km$
	Lift-to-Drag ratio $\bar{E}$	14.87
	Weight W	$67e3Kg$
	Equivalent Aspect Ratio AR_e	6.2

Table 2.8: Performance parameters

	DESIGN FEATURES	
WING	Surface S_w	$115.2m^2$
	Taper ratio λ_w	0.32
	Span l_w	$25.4m$
	Sweep angle Λ	26.9°

Table 2.9: Wing parameters

	DESIGN FEATURES	
AILERON	Position $p = \%l_w/2$	80%
	Surface S_a	$6.5m^2$

Table 2.10: Aileron parameters

Table 2.11: Application case: *AFS*

control optimization strategy is summarized in the following:

$$\begin{cases} f^c_{obj_1}(\mathbf{x}^*_s, \mathbf{x}_c) = min_{\mathbf{x}_c} min\bar{\sigma}\left(\frac{T_{u_g \to \ddot{q}_1}}{W_{u_g \to \ddot{q}_1}}\right) & for \quad GLA \\ f^c_{obj_2}(\mathbf{x}^*_s, \mathbf{x}_c) = min_{\mathbf{x}_c} min\bar{\sigma}\left(\frac{C_{in \to out}}{W_{in \to out}}\right) \\ s.t.\ g^c_i(\mathbf{x}^*_s, \mathbf{x}_c) \leq 0 \end{cases} \tag{2.65}$$

$$g^c_1 \quad = \quad \lambda_i \in D \qquad \forall U \in [U^f_{OL}, 1.1U_D] \tag{2.66}$$

where $\bar{\sigma}$ is the highest singular value, $T_{u_g} \to \ddot{q}_1$ and $C_{in} \to C_{out}$ indicate the gust and the controller transfer function, λ_i are the poles of the *CL* system, W are used to indicate the weight function, $\mathbf{x}^*_s$ are the fixed structural variables, and $\mathbf{x}_c$ are the control design variables. Finally, from the optimization of the design variables of the control system, the maximum load achieved during the gust and the unsteady velocity U^f_{CL} of the *CL* aeroservoelastic model are computed.

Application case of *AFS* and *GLA*

Two examples of application cases of *AFS* and *GLA* are shown here. First, an unstable aircraft configuration is considered, which instead satisfies all other structural and aerodynamic constraints. The performance and geometric characteristics of this aircraft are shown in Tab. 2.11. The stability scenario of the present reference aircraft is illustrated in Fig. 2.38, in which the zoom of the pole going unstable is shown. Specifically, the speed of instability is equal to U_D, and the request to the control system optimizer is to stabilize the system from U_D down to $1.1U_D$. The optimizer uses 5 initial designs as starting points, including the first initialization previously described and the remaining random ones, to fit within the stability constraint of the *CL* system. Spending 2 minutes on controller optimization, *systune* succeeds in constraining the poles of the *CL* system while staying

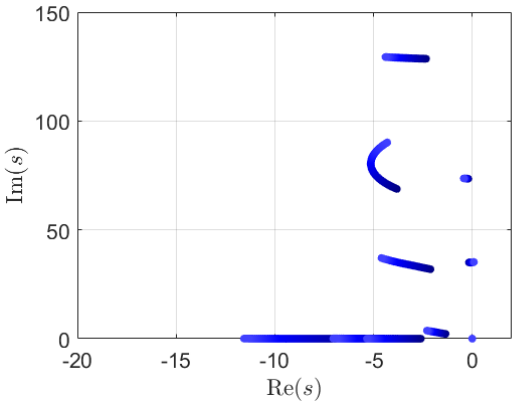

(a) Root locus of the aeroelastic system

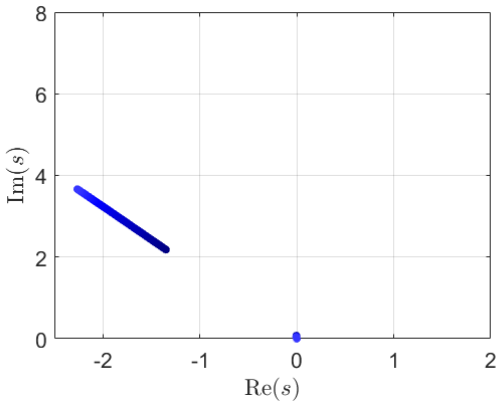

(b) Root locus for rigid body modes

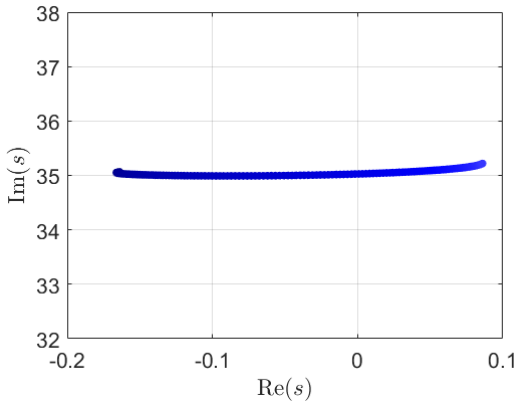

(c) Root locus for the flutter mode

Figure 2.38: Stability scenario

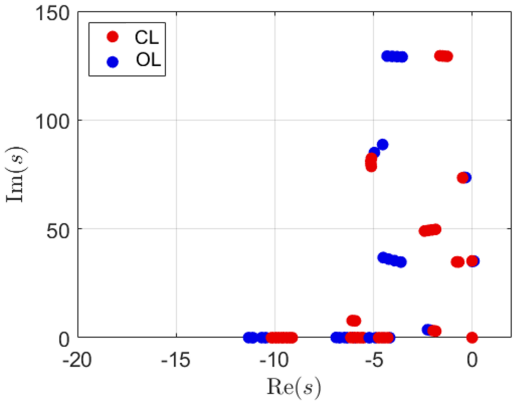

(a) Root locus of the aeroelastic systems

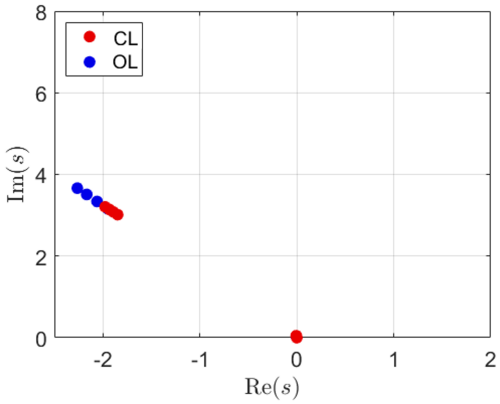

(b) Root locus for rigid body modes

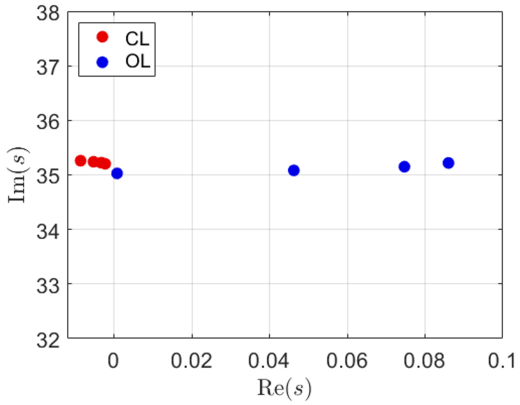

(c) Root locus for the flutter mode

Figure 2.39: Stability scenario: : *OL* and *CL* case

within the limits of the weight functions of the controller. The comparison of the system poles in *OL* and *CL* cases are shown in Fig. 2.39. Due to the blending process applied to input and output, along with the utilization of filters, it becomes apparent that the remaining stable poles of the aeroelastic system experience a partial shift rather than a large one. Highlighting the significance, it is crucial to underscore that the synthesis of the controller is conducted within a restricted set of flight speeds within the unsteady range.

The second application example is the case of load reduction in the presence of a gust as input. Therefore, a standard aircraft is taken into account that require the *GLA* controller component to damp the influence of gust-induced excitation on the elastic modes of the wing. Its performance and geometric characteristics are shown in the Tab. 2.15. More specifically, a gust designed to excite the short-period frequency of the specified aircraft is applied, meeting the EASA Ref. [76] specifications for the maximum allowable value for the applied gust input. The figure Ref.2.41(a) presents the instant in which the wing load reaches its maximum value. The load at this time is 1.2 times the maximum allowable value, equivalent to the yield value with a safety factor of 1.5. Specifically, the depicted scenario is derived through the following process: the load represents a dynamic load, and its maximum value is considered. This dynamic load is the cumulative result of static loads during trimmed flight (empty wing condition), and dynamic loads induced by gusts. To mitigate the dynamic load, the aileron is used, whose time-varying rotation allows it to remain within the

	DESIGN FEATURES	
AIRCRAFT	Cruise Mach M_∞	0.75
	Range R	$6283Km$
	Lift-to-Drag ratio $\bar{E}$	18.12
	Weight W	$72e3Kg$
	Equivalent Aspect Ratio AR_e	7.44

Table 2.12: Performance parameters

	DESIGN FEATURES	
WING	Surface S_w	$159.1m^2$
	Taper ratio λ_w	0.19
	Span l_w	$34.4m$
	Sweep angle Λ	26.29°

Table 2.13: Wing parameters

	DESIGN FEATURES	
AILERON	Position $p = \%l_w/2$	73%
	Surface S_a	$7.1m^2$

Table 2.14: Aileron parameters

Table 2.15: Application case: *GLA*

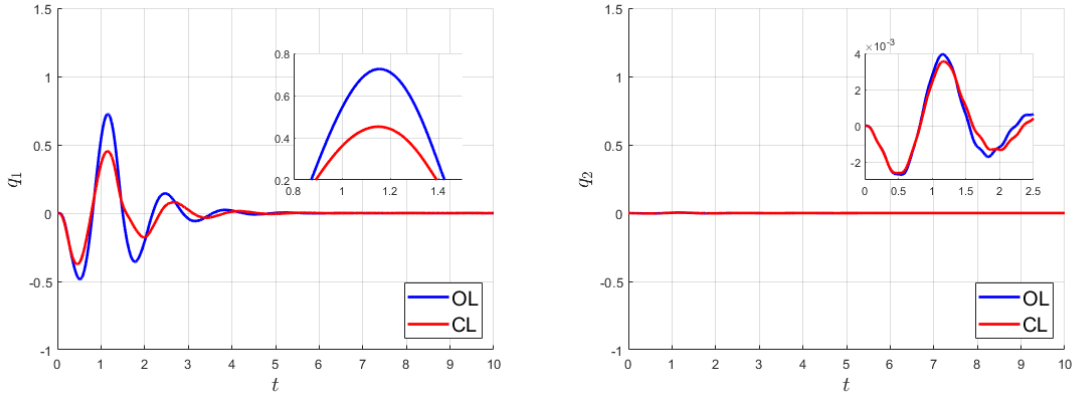

(a) q_1 (b) q_2

Figure 2.40: Elastic modal coordinates due to the gust input: OL and CL cases

structural limits set for the maximum allowable load. For control law synthesis, again the optimizer uses 5 initial designs as starting points, including the first initialization and the remaining random ones, to meet the stability constraints and the frequency reduction gain of the transfer function between the gust input and the accelerations measured on the wing.

The outcomes achieved through the controller optimizer are presented below. First, the response of the *CL* system to the applied gust is evaluated, considering the optimized structure of the controller. Notably, a comparison of the excited elastic coordinates in *CL* and *OL* scenarios is provided to highlight the reduction achieved in the closed-loop case (see Fig. 2.40). In addition, it is reconsidered the specific moment when the worst load occurs (see Fig. 2.41(b)), which reaches 80% of the maximum allowable load. This load is determined by combining the static load from previous analysis with the dynamic load induced by gusts, accounting for the aileron's rotational influence over time.

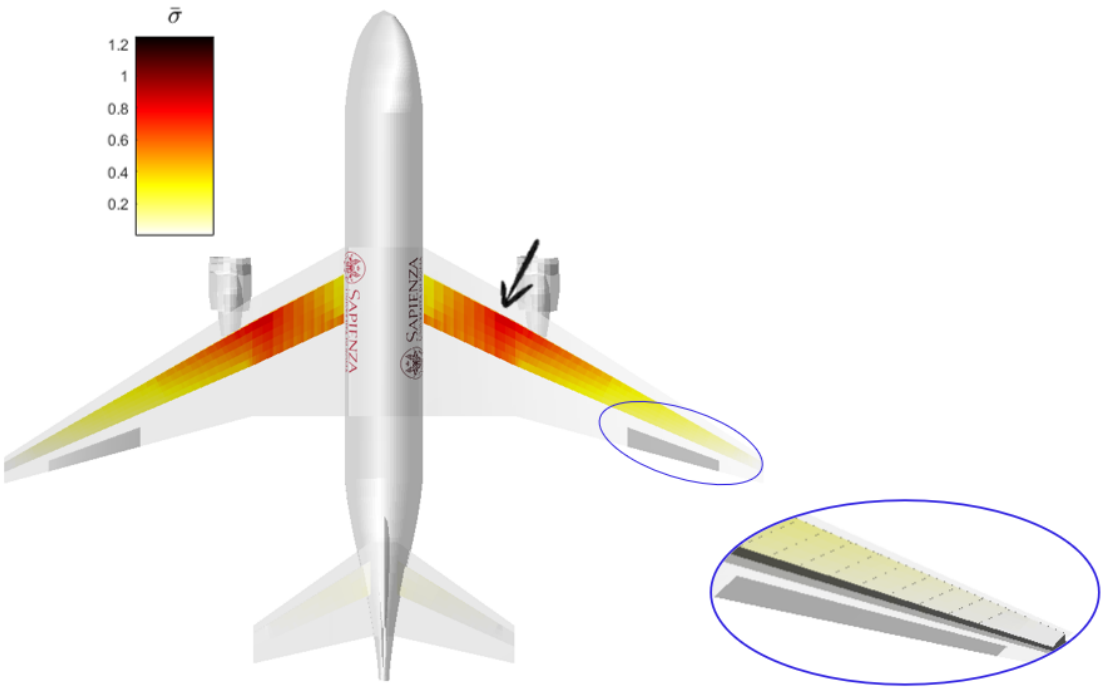

(a) OL case: Maximum Load $\bar{\sigma} = 1.2$

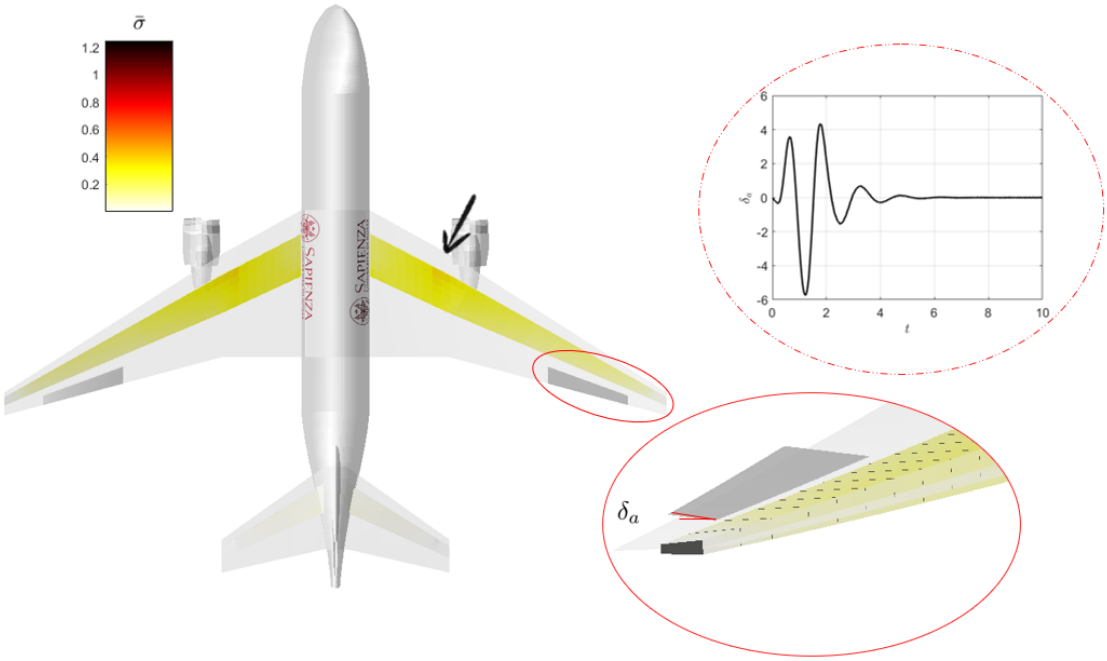

(b) CL case: Maximum Load $\bar{\sigma} = 0.8$

Figure 2.41: Maximum Load on Wing: OL and CL cases

Chapter 3

Application cases

The objective of this chapter is to establish the Pareto frontier for a Multi-Objective Optimization (*MOO*) problem concerning a short-range aircraft, comprising the fuselage, tail, wing and controllers. This includes comprehensive structural analyses (statics and dynamics), aerodynamic analyses (steady and unsteady), flight mechanics analyses, and aircraft performance evaluations. The optimization process involves maximizing the cruise speed and the mileage range while maintaining a constant amount of stowed fuel, considering structural, aerodynamic, and control constraints.

In this application, the discipline behaviors and the resulting output parameters are determined using the developed tool throughout the optimization process. Both high and low fidelity analyses are incorporated to assess the disciplinary performance. In particular, the high-fidelity analyses exploit the Finite Element analyzer (MSC.Nastran® solver Ref. [77]) for structural simulations, while directly implemented analytical models are used to evaluate key aerodynamic, aeroelastic, and performance objectives. To evaluate the Pareto frontier for the problem *MOO*, a genetic algorithm is used starting from an initial population, as in Ref. [120]. The methodology outlined in the Sect. 1.2 is initially validated through a step-by-step approach. The main objective is to examine the interaction between the disciplines involved and to understand how they affect the Pareto front and the best designs. The steps involve the progressive inclusion of the disciplines involved. Therefore, it starts with the Aeroelastostatic optimization, continues with the Aeroelastic optimization, and finally arrives at the overall Aeroservoelastic methodology. In conclusion, the calculation times of the three proposed optimizations are shown.

3.1 The application case

As an actual application, a short range transport aircraft (the baseline is shown in Fig. 3.1) is considered for the research optimization activities. The standard configuration aircraft is intended for a subsonic cruise ($M_\infty = 0.78$), it is sized for a 170 passenger payload and for a mission range of about $6950\,Km$. In this aircraft design, the wing, tail (and consequently the elevator), and aileron are sized, taking into account a predetermined fuselage mass of $18000\,Kg$, specific engine types with a mass of $6700\,Kg$, a given payload, with a mass of $11250\,Kg$ and mass of fuel stowed equal to $18000\,Kg$.

The optimization is directed toward maximizing flight speed and mileage range, considering structural, aeroelastic, and controller model-associated constraints. Significantly, the design focuses

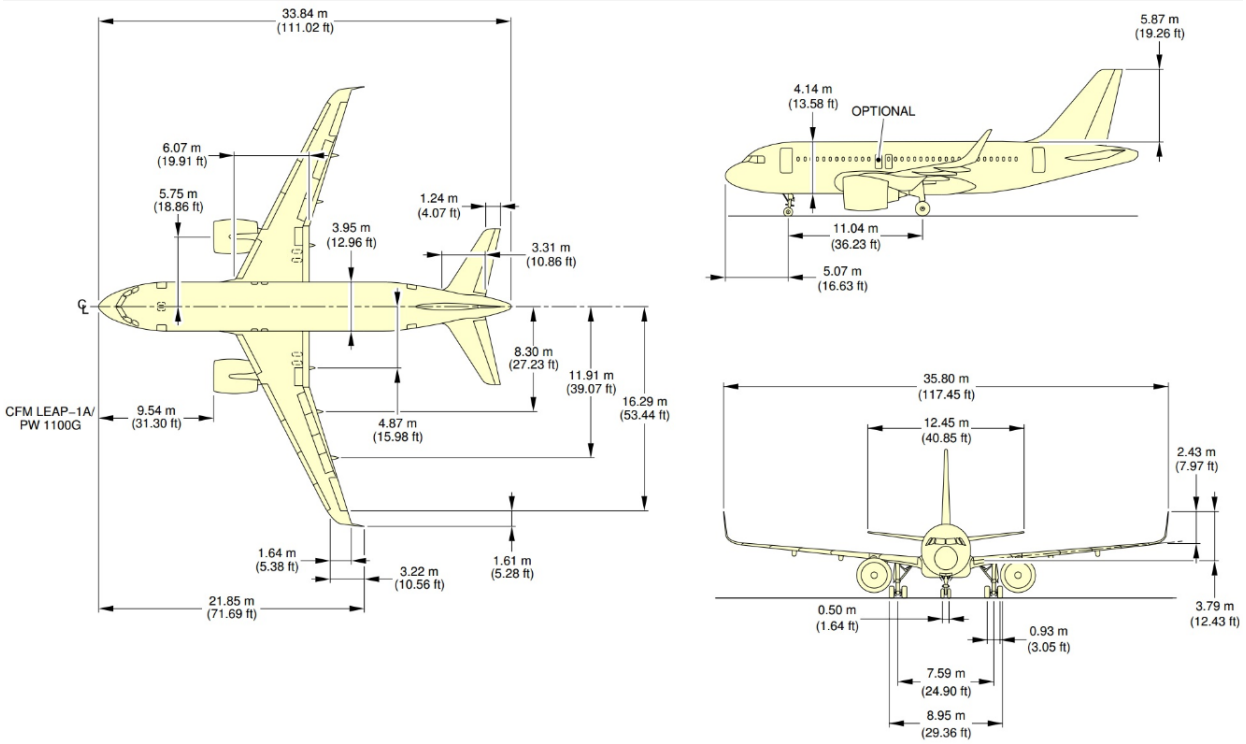

Figure 3.1: Baseline of the short range aircraft design proposed for optimization activities (Ref. [121])

exclusively on the longitudinal degrees of freedom of the aircraft. Specifically, the problem design variables are 49, and in order to prevent unfeasible solutions with excessive or unrealistic values of the design variables is necessary fix the minimum and the maximum permissible values of each design variable. Together, the lower and upper bounds create a well-defined design space within which the optimization algorithms can search the optimal solutions (see Tabs. 3.1, 3.2, and 3.3, unless otherwise specified, the structure has identical properties on both the leading edge and trailing edge). The optimizations utilize dimensionless design variables within their feasible ranges to enhance numerical stability. Dimensionless variables exhibit more consistent value ranges, mitigating issues associated with scale disparities that might hinder or complicate optimization convergence. The starting design, taken as the initial guess, is the reference design shown in Sect. 2.2.1, whose design variables values are given in Tabs. 3.1, 3.2, and 3.3). More specifically, this reference aircraft model is used to adimensionalize the performance variables of the optimized designs. This allows for a direct comparison of the optimized aircraft's performance against the reference value.

$$\begin{aligned}
\bar{R} &= R/R_{IG} \qquad R_{IG} = 6950\,Km \\
\bar{E} &= E/E_{IG_{max}} \qquad E_{IG_{max}} = 19.3 \qquad \textit{with} \qquad E = L/D \\
\bar{W} &= W/W_{IG} \qquad m_{IG} = 70e3\,Kg \\
d\bar{W}/dt &= \frac{dW/dt}{(dW/dt)_{IG}} \qquad (dW/dt)_{IG} = TSFC\frac{W_{IG}}{E_{IG_{max}}} \\
M_\infty &= U_c/a(h = 12000m)
\end{aligned} \tag{3.1}$$

Therefore, in this section, when addressing the objectives for maximization, we will consistently refer to dimensionless values. The range objective will be based on the value scaled with the initial guess attempt, whereas the speed objective will be denoted by the Mach of flight calculated across

all fixed-altitude designs at 12.000 meters. In the optimization process, following the selection of these design variables, the developed tool defines the geometric sizing and tailors the analyses to be specific for the sizing cases, as described earlier (see Sect. 1.2). In the Finite Element Model analysis, the wing and tail components of each design are described using the same isotropic material (see Tab. 3.4). Furthermore, to facilitate the comparison of configurations with the same mass center position, the payload mass is repositioned for each set of chosen design variables. Similarly in this instance, the reference mass center position corresponds to that of the reference aircraft, located at its 0.25 *MAC*.

The methodology outlined in the Sect.1.2 is here validated through a step-by-step approach, including an higher and higher numbers of disciplines involved in the optimization process. The results of the three proposed optimizations are presented here. Specifically, these optimizations differ in their treatment of static, dynamic, and control constraints during the optimization process. Initially, the results of Aeroelastostatic optimization, which consider only static constraints, are presented. Subsequently, the Aeroelastic optimization results, which incorporate both static and dynamic constraints, are shown. Finally, the results of the Aeroservoelastic optimization are displayed, encompassing all proposed constraints, including static, dynamic, and control constraints. It's important to note that all constraints introduced in the optimization process are scaled relative to the maximum or minimum permissible values. This scaling ensures that the optimizer treats all constraints uniformly, regardless of their original magnitudes. By doing so, the optimizer assigns equal importance to each constraint, facilitating a balanced optimization process and preventing any single constraint from dominating the outcome.

Each optimization employs the same initial starting population (*DOE*), which is computed using the *ULH* algorithm (Ref. [13]) and comprises 450 individuals. The optimization process spans 50 generations using the Genetic Algorithm (*Simple GA* Driver) in *OpenMDAO* (Ref.[28, 29]), utilizing mutation and crossover parameters set at 0.01 and 0.1, respectively. After evaluating the best optimization designs on the Pareto front, calculated using the *Simple GA* driver, these are used as starting points for a subsequent optimization aimed solely at improving the Pareto front. This optimization phase employed the $NSGA-II$ Driver in *OpenMDAO* using 10 generations, a genetic algorithm whose main feature is to improve the optimal designs through accurate evaluation of their constrained variables. Finally, in order to compare the proposed optimizers, the *SLSQP* algorithm in *OpenMDAO* is used for further optimization only on some designs on the Pareto front. This algorithm asks to go back to the definition of a single objective function, and makes sure that the final best design is placed in a minimal zone of the objectives space.

3.2 Aeroelastostatic Optimization (AESO)

This optimization involves the use of only the static constraints (the number of constraints applied is equal to 27). More specifically, the structural, aeroelastic, and control constraints are included only for the static analyses (aeroelastic trim, the maneuver, and the aileron response analyses, see Tab. 1.3 for more details). In addition, the stability of the aircraft on rigid dynamics is required.

Initially, the objective space obtained using the *Simple GA* Driver (with the calculation of 50 generations) is presented in Fig.3.2, in which only the feasible designs are presented and the goals are focused on maximizing both the cruise flight speed M_∞ and the adimensionalized mileage range $\bar{R}$.

	DESIGN VARIABLE		LOWER BOUND	UPPER BOUND	INITIAL GUESS
WING	Skin panels	root thickness	$0.001m$	$0.025m$	$0.021m$
	Spars	root web thickness	$0.001m$	$0.02m$	$LE : 0.016m$ $TE : 0.016m$
		root cap area	$0.0004m^2$	$0.005m^2$	$LE : 0.003m^2$ $TE : 0.003m^2$
		cap area ratios	$\Delta A_{s_1} = 0.2$ $\Delta A_{s_2} = 0.1$	$\Delta A_{s_1} = 0.65$ $\Delta A_{s_2} = 0.5$	0.6 0.4
	Ribs	number	20	40	25
		root thickness	$0.004m$	$0.02m$	$0.012m$
	Variation along span	thikness ratios	$\Delta t_1 = 0.2$ $\Delta t_2 = 0.1$	$\Delta t_1 = 0.65$ $\Delta t_2 = 0.5$	0.6 0.3
	Angles	sweep	$0°$	$34°$	$24.95°$
	Length	root chord	$3.5m$	$8m$	$6.5m$
		taper ratio	$\lambda_1 = 0.6$ $\lambda_2 = 0.1$	$\lambda_1 = 1$ $\lambda_2 = 0.7$	0.85 0.5
		span	$24m$	$50m$	$34.14m$

Table 3.1: Design Variables Range for the Wing

	DESIGN VARIABLE		LOWER BOUND	UPPER BOUND	INITIAL GUESS
AILERON	Length	% of wing chord	15%	35%	25%
		% of wing span	15%	40%	30%
	Position	% along wing span	35%	80%	66%

Table 3.2: Design Variables Range for the Aileron

	DESIGN VARIABLE		LOWER BOUND	UPPER BOUND	INITIAL GUESS
TAIL	Skin panels	root thickness	$0.0005m$	$0.02m$	$0.013m$
	Spars	root web thickness	$0.0005m$	$0.02m$	$0.0078m$
		root cap area	$0.0003m^2$	$0.005m^2$	$0.003m^2$
		cap area ratios	$\Delta A_{s_1} = 0.1$	$\Delta A_{s_1} = 0.5$	0.21
	Ribs	number	5	20	7
		root thickness	$0.0005m$	$0.015m$	$0.01m$
	Variation along span	thikness ratios	$\Delta t_1 = 0.2$	$\Delta t_1 = 0.6$	0.32
	Length	root chord	$2m$	$5m$	$3.65m$
		taper ratio	$\lambda_1 = 0.25$	$\lambda_1 = 0.9$	0.44
		span	$6m$	$16m$	$12.26m$

Table 3.3: Design Variables Range for the Tail

Material characteristics	Value
Strengh modulus E	72.9 GPa
Density ρ	2810 Kg/m^3
Poisson ν	0.33
Ultimate Stress σ_U	600 MPa
Yield Stress σ_Y	520 MPa

Table 3.4: Characteristics of the chosen material

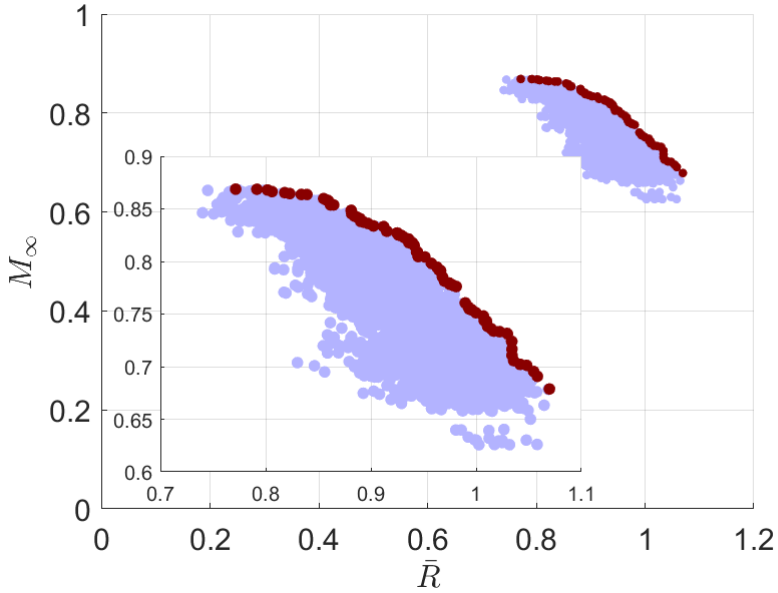

Figure 3.2: Objective space of the Aeroelastostatic Optimization: Pareto Front

The optimal designs in the Pareto front, representing the best among all feasible designs (depicted in lilac in the figure), are highlighted in burgundy.

The objectives space includes precious information about the feasible designs. In particular, the goal of maximizing both the adimensionalized mileage range and flight speed in cruise conditions is equivalent to minimizing design weight, as illustrated in Fig. 3.3(a). The approach to the Pareto front in the figure corresponds to a decrease in dimensionless weight, which means greater design efficiency. On the other hand, the scaled lift-to-drag ratio of the feasible designs changes a lot along the Pareto front, as shown in Fig. 3.3(b). In fact, designs with lower cruising speeds and with the ability to travel longer distances are those with better lift-to-drag ratio, which means greater design aerodynamic efficiency and greater equivalent aspect ratio. As the third performance parameter, the trend of fuel consumption within the target space is examined. Improving this parameter, minimizing it, involves concurrently minimizing the weight and maximizing the lift-to-drag ratio. As illustrated in Figure 3.4, designs exhibiting the lowest fuel consumption are located within the objective region characterized by a low cruise speed and an high mileage range. This occurrence come from the improvement in the weight parameter as designs move towards the Pareto front, and the major improvement in optimal lift-to-drag ratios in the low-speed and high-range domain. It is important to note that the mileage range calculated during the optimization is determined by considering the use of the entire stowed fuel mass. When examining the fuel consumption of the Pareto front projects for mileage range values different from their specified maximum range, a trend emerges: projects with lower cruising speeds generally have lower fuel consumption than those with higher speeds. The Figure 3.5 illustrates this trend of fuel consumption for selected mileage range values, such as 25%, 50% and 75% of the reference value ($R_{ref} = R_{IG}$). In contrast, the set of projects representing the 100% of fuel mass utilization serves as the Pareto benchmark, including various mileage ranges, moving from $R = 77\%R_{ref}$ to $R = 107\%R_{ref}$.

The presented results derived from an optimization conducted using the *OpenMDAO Simple GA* driver over 50 generations. In order to examine and potentially refine the best-performing designs

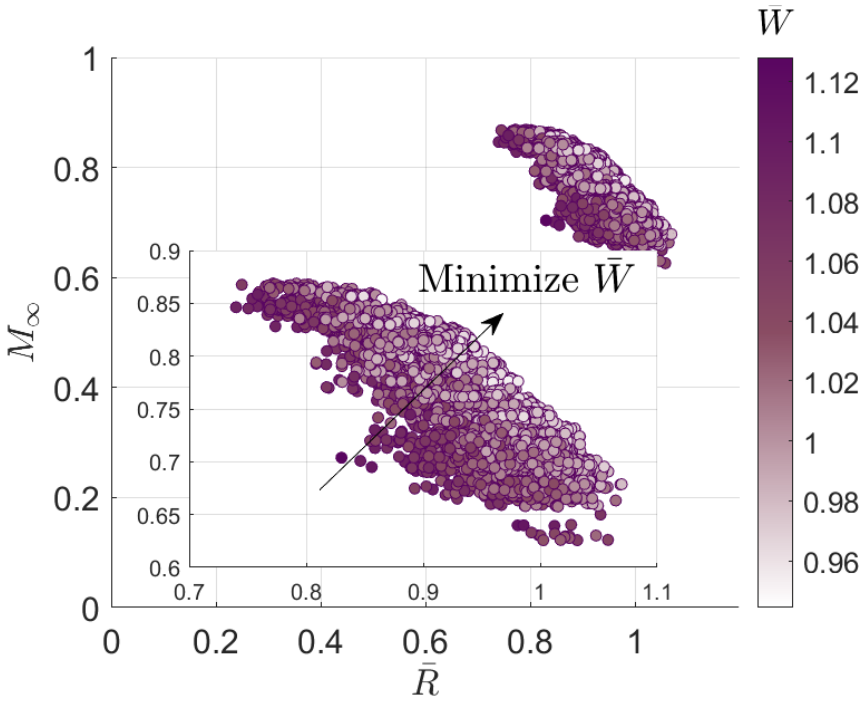

(a) Weight estimation: $\bar{W} = W/W_{IG}$

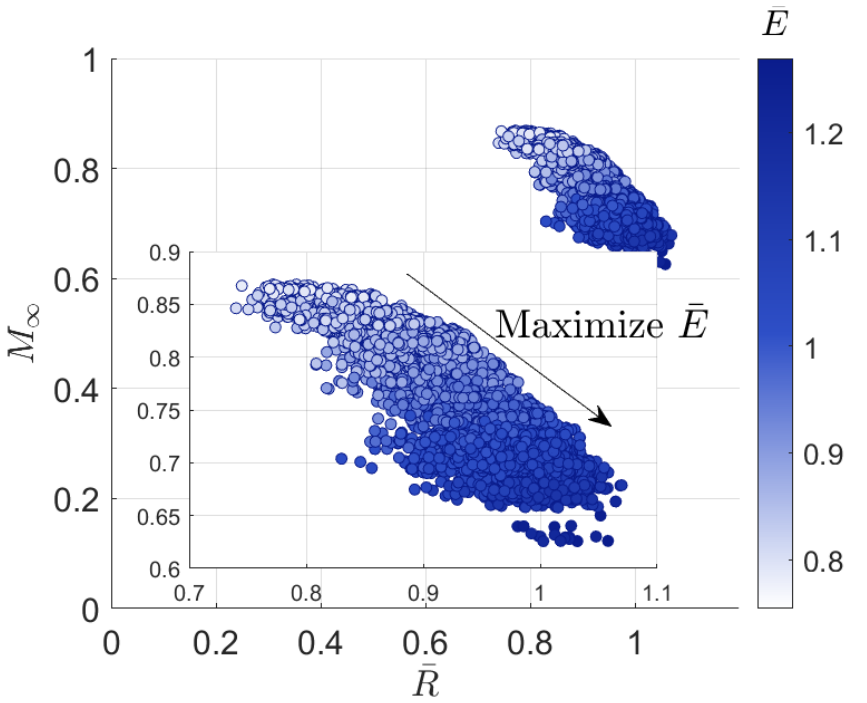

(b) Lift-to-Drag estimation: $\bar{E} = E/E_{IG}$

Figure 3.3: Objective space of the Aeroelastostatic Optimization: feasible designs and their performance

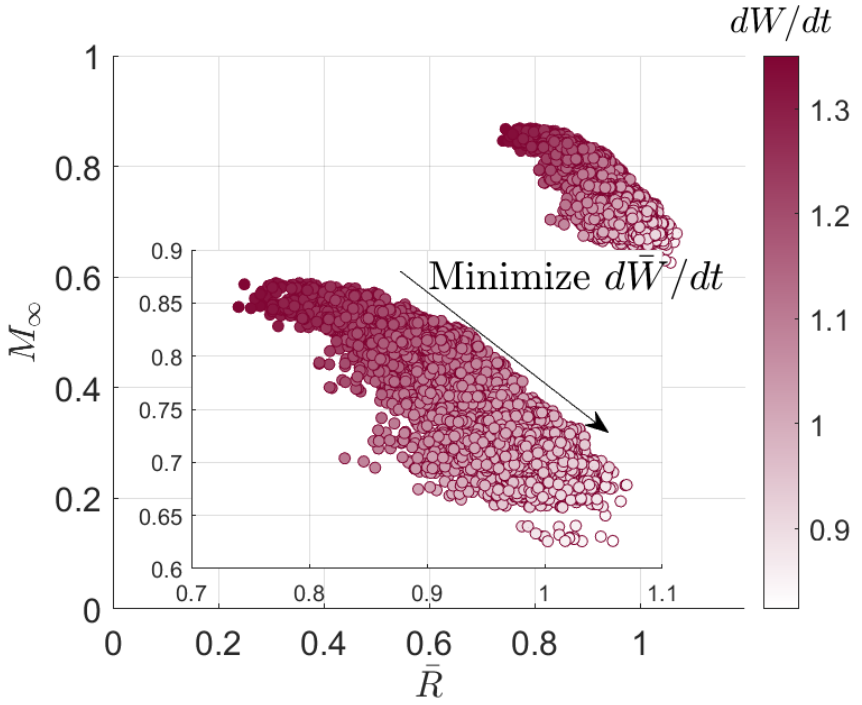

Figure 3.4: Objective space of the Aeroelastostatic Optimization: Fuel consumption estimation $d\bar{W}/dt = (dW/dt)/(dW/dt)_{IG}$

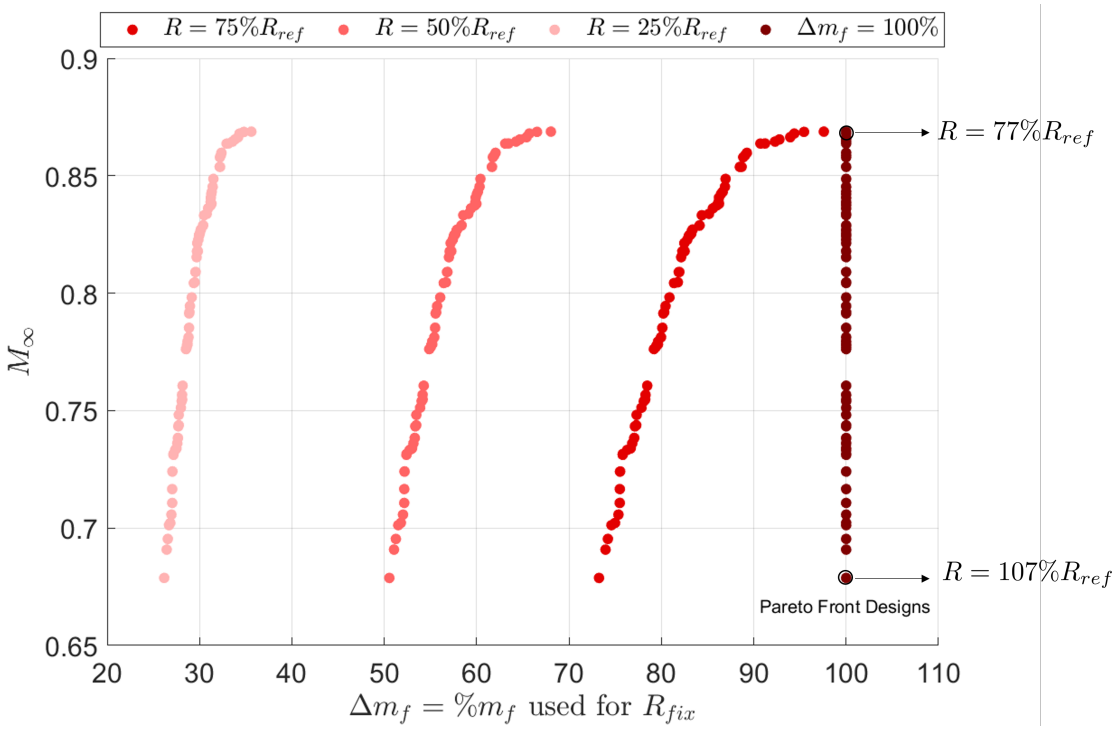

Figure 3.5: Fuel Consumption of Aeroelastostatic Optimization Pareto Front Designs for different Fixed Mileage Range

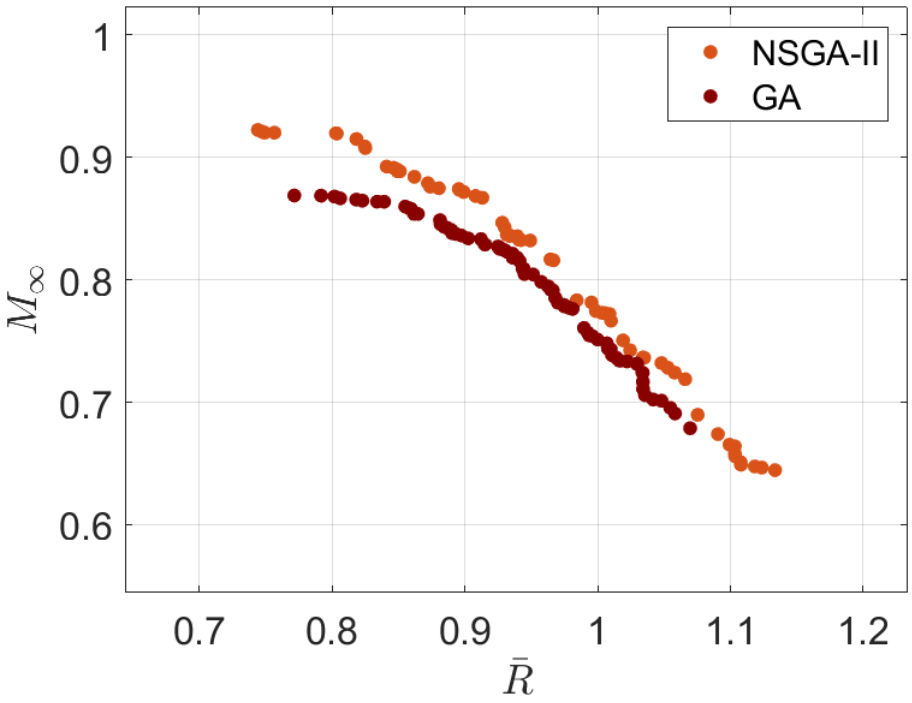

Figure 3.6: Comparison of the Pareto front obtained with $Simple\,GA$ Driver and with $NSGA-II$ Driver: Aeroelastostatic Optimization

from the Pareto front, a subsequent optimization stage is undertaken. The refinement is carried out through a second optimization process subsequent to the one conducted with the $Simple\,GA$ driver, using the $NSGA-II$ algorithm and performing an additional computation of 10 generations. The comparison between the two Pareto fronts obtained with $Simple\,GA$ driver and $NSGA-II$ is illustrated in Figure 3.6. It's worth noting that employing an algorithm specifically designed to enhance the Pareto front significantly boosts performance, as evidenced by the advancements observed in the forward region. Unfortunately, due to constraints associated with the aeroservoelastic model used, it is not possible to consider Pareto front segments corresponding to flight Mach numbers above 0.9 and below 0.65. This is because at such high and low flight speeds, aircraft would deploy devices that are not currently modeled or considered in the present analyses.

In order to investigate the sizing of the tail, wing and ailerons, and to determine which analyses have the most significant impact during the optimization process, characteristic points are selected on the Pareto front, considering the limitation mentioned earlier. Four designs are selected: one at maximum flight speed and minimum mileage distance traveled, the second at minimum flight speed and maximum mileage distance traveled, and the third and fourth at average positions. The selection of these four designs on the Pareto front is depicted in Figure 3.7, where the color parameter represents the Equivalent Aspect ratio. This illustrates the significant diversity among the designs along the Pareto front. Obviously, this parameter changes along the Pareto front and increases toward the design area with low flight speed and high kilometer range, mirroring what has been said about the lift-to-drag ratio value. Therefore, to understand the sizing and then to compare the results obtained from the different optimizations, four reference designs are chosen, named for the Aeroelastostatic Optimization as A, B, C and D designs. After selecting a number

of designs from the Pareto front, the $SLSQP$ algorithm is used to further optimise them, it is an optimization method that combines the Sequential Least Squares (SLS) method with Sequential Quadratic Programming (SQP). The goal is to ensure that these designs are actually placed at the bottom of the optimisation hole. To do this, it is necessary to switch from the bi-objective to the mono-objective perspective. Given the placement of each design in the objectives space, the angular coefficient of the line passing through the origin and the specific design is given. Using this information, a new objective function is defined as a weighted combination of the previous objective functions, considering the individual angular coefficient. This approach directs the now single-objective, gradient-based optimizer to improve the design as if it is moving in the space of the two objectives along the diagonal defined by that angular coefficient. During this process, both objective functions are simultaneously optimized with appropriate weights. In this way, designs on the Pareto Front are improved and are described below. The comparison among all characteristics of the Pareto Front designs obtained from the Aeroelastostatic optimization is shown in Tab. 3.5, in which the geometry variables and the performance parameters are shown for the four design. It is worth noting that the performance parameters are scaled using the baseline values of the starting point, which has a flight Mach number of 0.78 and Range equal to $6950Km$. Specifically, among the best four designs chosen the value of the cruise Mach M_∞ changes from 0.892 to 0.649, as the scaled range $\bar{R}$ changes from 84% to 111.4% of the reference value. The values of the performance parameters such as the lift-to-drag ratio, the scaled weight and the equivalent aspect ratio changes accordingly to the previous description on the Pareto front. More specifically, all designs on the Pareto front achieve a weight below the reference weight $70e3Kg$ by a maximum of 6% (design B) and a minimum of 1% (design D). Given the range of designs across the Pareto front, with the equivalent aspect ratio varying from 5.96 to 12.41 (the reference value being 7.76), it is inevitable that this variability extends to the aerodynamic efficiency of the aircraft, specifically the L/D ratio. Comparatively, its dimensionless value, with a reference of 19.3, changes along the Pareto front from 74.7% to 123%.

Regarding the geometry of the four selected designs (see Fig. 3.8 for more details), it is evident that there are notable changes in the wing surface area (from a value of $105.36\,m^2$ for the Design A to $164.29\,m^2$ for the Design D), particularly concerning the variations in the wing span values (from a value of $24.96\,m$ for the Design A to $45.46\,m$ for the Design D), in the aerodynamic wing chord and taper ratio. Since the reference aircraft designs chosen fly at various speeds, it's natural that the sweep angle for the wings differs accordingly. Indeed, there's a range of variation observed, spanning from 30.73° to 17.12° for the sweep angle. In addition, changes in tail surface area occur, which are closely related to changes in wing surface area. When the wing surface area expands from model A to model D, the tail surface area (from $24.03\,m^2$ to $35.5\,m^2$) and tail span length (from $8.53\,m$ to $12.16\,m$) also undergoes an increase. Finally, the aileron position and area are also important and vary for the four designs chosen. In fact as it can be seen from the figures 3.8 the optimizer chooses the aileron position and area according to the wing surface area that is available to it. Typically, with longer wings, aileron placement is limited to avoid control reversal. This explains why the aileron positioning of designs C and D results in more inboard than that of designs A and B.

Furthermore, considering the structural characteristics of the wing, Figure 3.9 presents the adimensionalized characteristic values of skin panel thicknesses ($\bar{t}_{UD}$), root web thicknesses ($\bar{t}_{LE}$ and $\bar{t}_{TE}$), ribs thicknesses ($\bar{t}_R$), cap area of spars ($\bar{A}_{LE}$ and $\bar{A}_{TE}$) at root, together with their variations

	DESIGN FEATURES	DESIGN A	DESIGN B	DESIGN C	DESIGN D
AIRCRAFT	Cruise Mach M_∞	0.892	0.815	0.736	0.649
	Scaled Range $\bar{R}$	0.841	0.966	1.035	1.114
	Scaled lift-to-drag ratio $\bar{E}$	0.747	0.867	0.983	1.23
	Scaled Weight $\bar{W}$	0.955	0.939	0.947	0.994
	Equivalent Aspect Ratio AR_e	5.96	7.61	8.21	12.41
WING	Surface S_w	105.366 m^2	112.89m^2	146.66 m^2	164.29 m^2
	Taper Ratio λ_w	0.32	0.19	0.135	0.15
	Span l_w	24.96 m	27.91 m	34.68 m	45.46 m
	Sweep angle Λ	30.73°	27.91°	25.46°	17.12°
TAIL	Surface S_t	24.03 m^2	24.03 m^2	29.64 m^2	35.5 m^2
	Taper Ratio λ_t	0.37	0.45	0.28	0.25
	Span l_t	8.53 m	8.75 m	10.18 m	12.16 m
AILERON	Position $p = \%l_w/2$	85.23 %	83.82 %	64.37 %	69.76%
	Surface S_a	3.65 m^2	2.61 m^2	8.09 m^2	5.33 m^2

Table 3.5: Comparison of characteristics of Pareto Front designs obtained from the Aeroelastostatic optimization

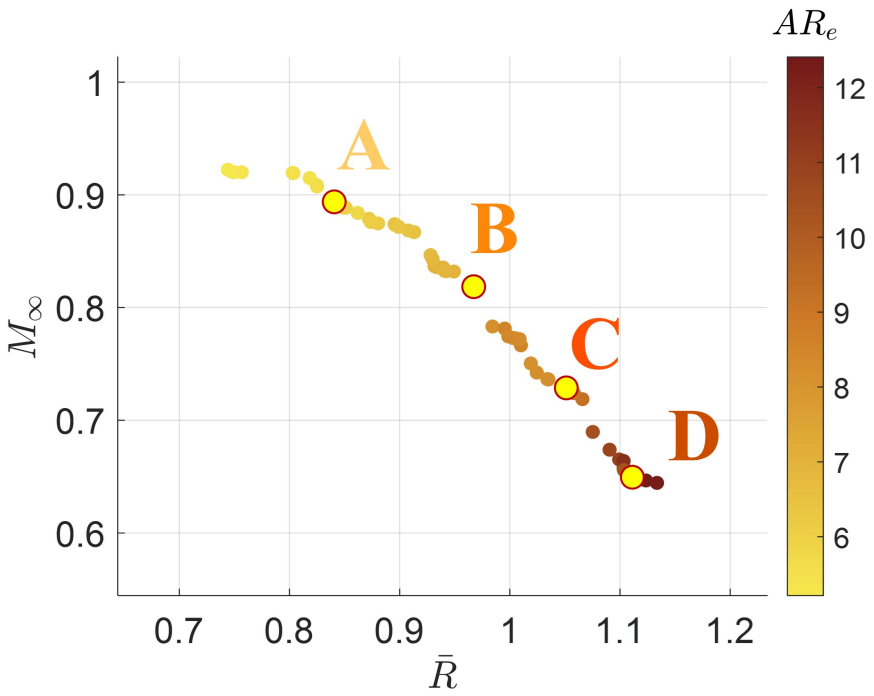

Figure 3.7: Equivalent Aspect Ratio of the Aeroelastostatic Optimization Pareto front, choice of displayed projects

along the span (Δt_1, Δt_2, ΔA_{s_1}, and ΔA_{s_2}, in which the number denotes the design variables variation in the first and second section), for the four selected reference designs. Specifically, the scaling of these variables is done by considering their variance range, defined by their upper bound and lower bound. The choice of these design variables depends on the geometry of the wing, the loads to be supported and the placement of the concentrated non-structural masses. In order to get more information about that, it is necessary to look at the values of the constraints on these four designs (see Figs. 3.10 and Fig. 3.11). More specifically, first our focus is on the loads obtained from the different static analyses conducted for all four designs. Hence, the Figure 3.10 illustrates the peak load held by the wing structure in the different static analyses conducted, including trim, *MLA* maneuver, aileron reversal, and roll. The load values are normalized to maximum allowable value. Specifically, the prevailing load occurs during the maneuver aided by the use of the *MLA* (ailerons rotated symmetrically to lighten the load in static way). In fact, this is the dimensioning constraint for the thicknesses, which are chosen by the optimizer in order to lean on the load constraints in maneuvering. Thus, the structural constraint linked to the maximum load during the maneuver serves as the design limitation for the model thicknesses, which obviously are structural design variables.

Alternatively, examining the aeroelastic constraints depicted in Fig. 3.11, which inherently shape the aerodynamic design variables such as the plan form of the surfaces to be sized, it is observed that the maneuver emerges as a significant dimensioning factor in this scenario as well. Bear in mind that all constraints shown have been dimensionalized with respect to the maximum and/or minimum allowable value. Then, an examination of Fig. 3.11(b) reveals that the angle of attack during a $2.5g$ maneuver remains consistently at the maximum allowable limit across the four selected designs on the Pareto front. However, the rotation of the elevator required for executing such a maneuver varies, ranging from 83% to 69% of the maximum allowable rotation for that control

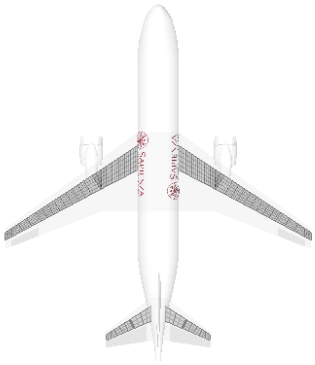

(a) Design: A

(b) Design: B

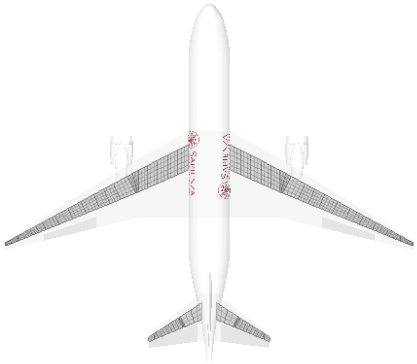

(c) Design: C

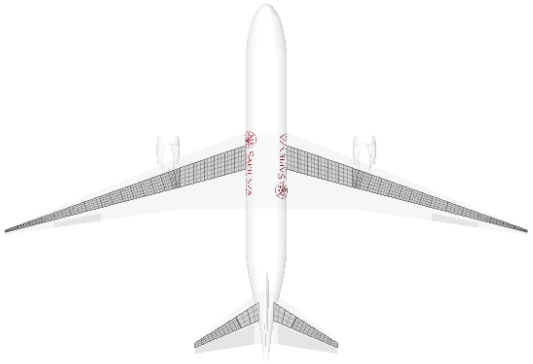

(d) Design: D

Figure 3.8: Best designs among the Pareto Front of the Aeroelastostatic Optimization

surface. The distinguishing factor among designs depicted is the static controllability $C_{m_{\delta_e}}$, which is influenced by tail sizing. In addition, the values of the angle of attack and tail angle required for the aircraft trim are also essential constraints for the wing and tail sizing. In the specifications of the four observed designs, looking at Fig. 3.11(a) shows that the angle of attack required for trimming the aircraft reaches the maximum allowed value in all cases. However, the tail rotation for the same analysis varies between 82% and 98% of the maximum value.

Lastly, the aileron sizing part is discussed, obviously none of the feasible designs shown suffers the aileron reversal condition in the observed speed domain (i.e., from the cruise speed to the dive speed). Examining the time taken by the four aircrafts to roll t_r after applying the same input to the aileron control surface (refer to Fig. 3.11(c)), it's evident that the design featuring the largest aileron surface (design C) accomplishes the maneuver in 82% of the anticipated time limit. Remarkably, even the design with minimal wing span and a small aileron surface (design A) manages to execute the maneuver in nearly the same duration by positioning the aileron as outward as possible. In contrast, the design that maximizes roll time is design D, characterized by maximum wing span, a relatively large aileron surface area, and 69.76% aileron position. The slower response of this design is inevitably linked to the wing type and the influence of its flexibility, which adversely affects aileron effectiveness.

In conclusion, the Aeroelastostatic optimization study conducted under specified static constraints has yielded valuable insights into the design space and performance characteristics of the aircraft configurations considered. Through an in-depth analysis of the results, it is evident that the best identified designs exhibit notable characteristics such as excellent balance of aerodynamic surface sizing and efficient roll response. In particular, it has been seen that wing and tail surface sizing is associated with the presence of the aeroelastic constraint on maneuvering and trim, while aileron sizing is associated with the effectiveness and inversion constraints of the control surface controls. These findings underscore the importance of considering various design parameters and constraints in aircraft optimization to achieve desired performance objectives. In addition, the assessments gained from this study can serve as a valuable basis for the next optimization, in which constraints of a static nature are included in addition to constraints of a dynamic nature. Overall, the results presented contribute to advancing our understanding of aircraft design optimization and have significant implications for the development of more efficient and effective aircraft configurations.

3.3 Aeroelastic Optimization (AEO)

This optimization involves the use of both static and dynamic constraints. Therefore, in addiction to the static constraints, structural and aeroelastic constraints are applied for the aeroelastic stability and the gust response analyses (the number of constraints applied is equal to 43, see Tab. 1.3). The controller is not active, so it is essential that the aircraft be stable up to $U_f^{OL} \geq 1.1 U_D$.

Initially, the objective space is presented in Fig. 3.12, in which only the feasible designs are presented and the goals are focused again on maximizing both the cruise flight speed M_∞ and the adimensionalized mileage range $\bar{R}$. The graph reveals a lower density in the target space than the previous figure 3.2, indicating a correlation with the greater presence of constraints. This inevitably leads to a shift in the target space and alters the position of the Pareto front. The aforementioned results are derived from the computation of 50 generations using the *Simple GA* Driver

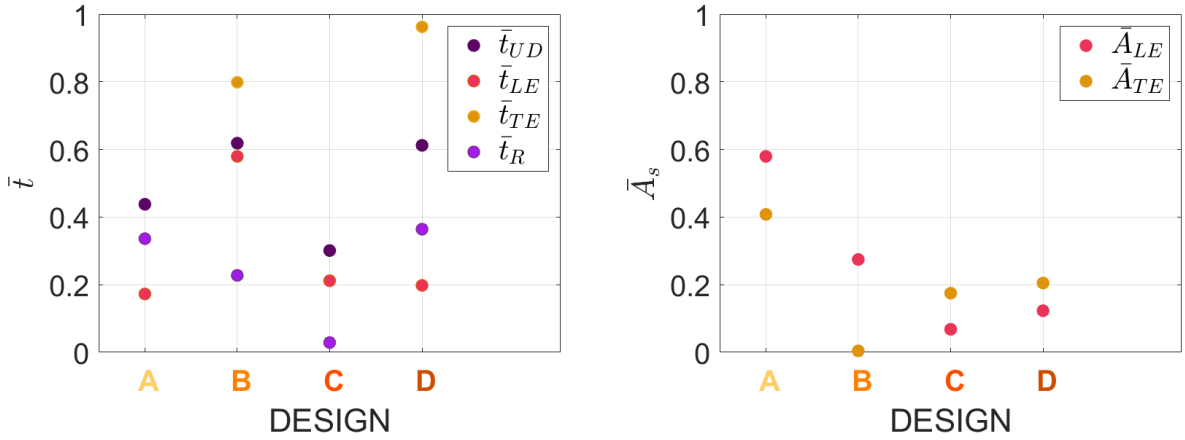

(a) Thickness at root

(b) Cap Area at root

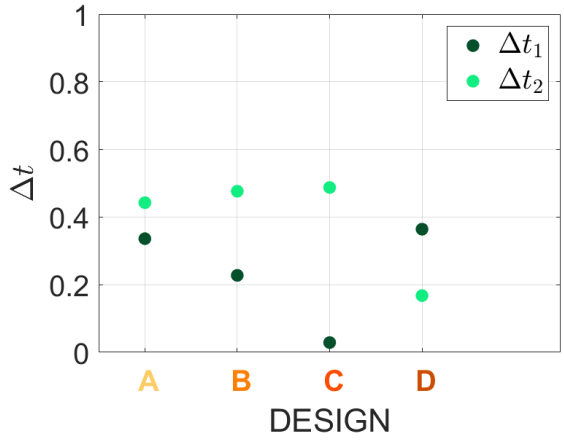

(c) Thickness Ratios

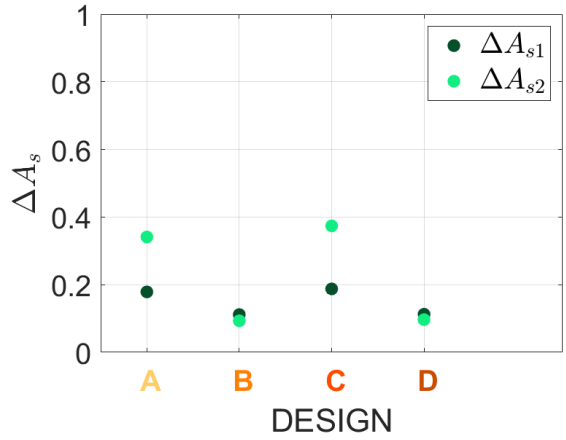

(d) Cap Area Ratios

Figure 3.9: Dimensionless thickness and cap area of the spars at the wing root and and their variation along the span

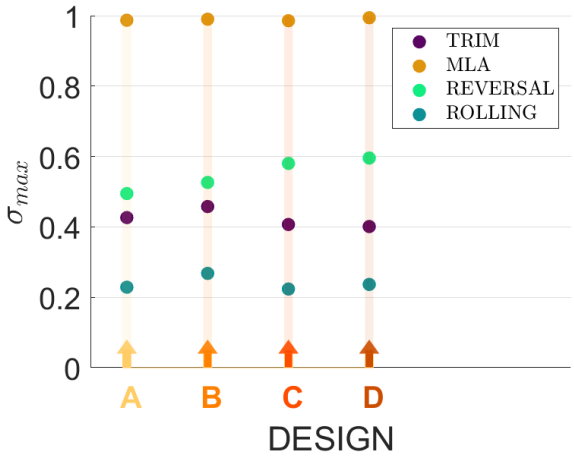

Figure 3.10: Structural constraint (σ_{max} values on wing) evaluated on the Pareto Front designs of the Aeroelastostatic optimization

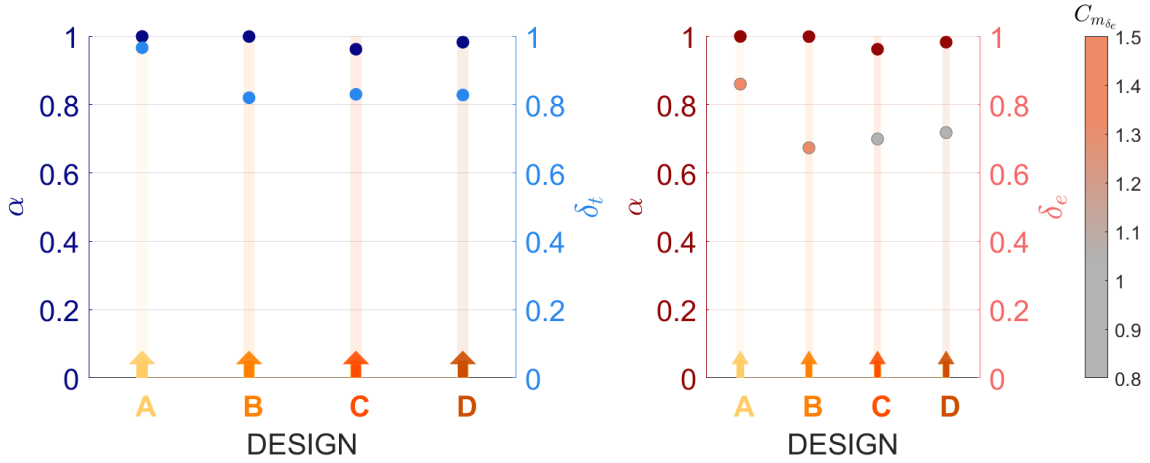

(a) Trim analyses results

(b) Maneuver analyses results

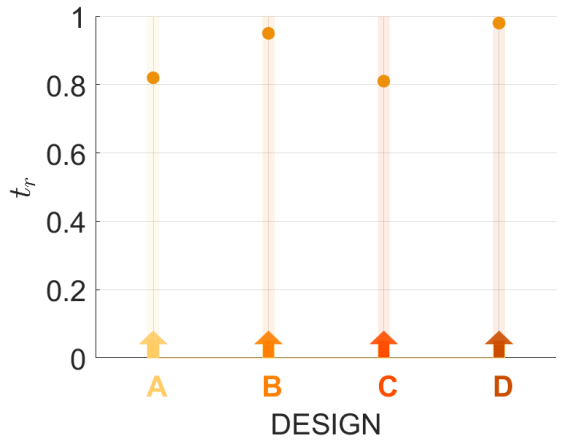

(c) Aileron response results

Figure 3.11: Aeroelastic constraints (α, δ_t, δ_e, $C_{m_{\delta_e}}$, and t_r values) evaluated on the Pareto Front designs of the Aeroelastostatic optimization

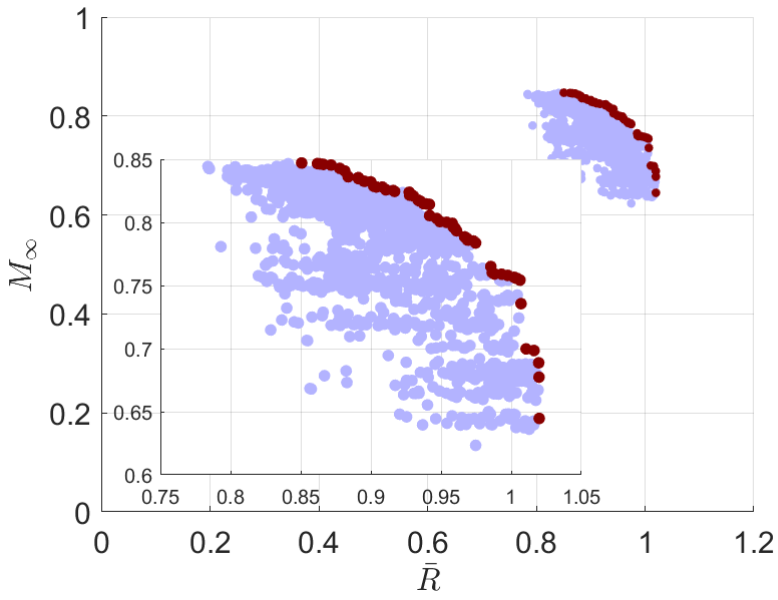

Figure 3.12: Objective space of the Aeroelastic Optimization: Pareto Front

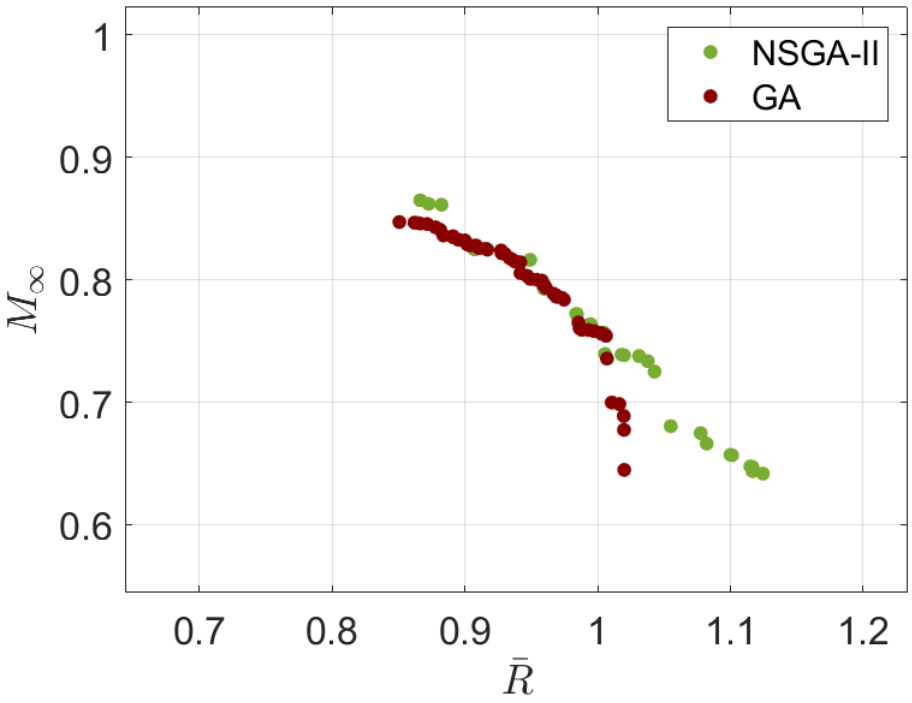

Figure 3.13: Comparison of the Pareto front obtained with *Simple GA* Driver and with $NSGA-II$ Driver: Aeroelastic Optimization

of *OpenMDAO*. Following the previous methodology, a subsequent optimization is performed based on the outcomes obtained with the *Simple GA* driver. In this subsequent optimization, the $NSGA-II$ algorithm is employed, with an evaluation spanning an additional 10 generations. The comparison between the two Pareto fronts of the Aeroelastic optimizations is illustrated in Fig. 3.13. Similar to the previous Aeroelastostatic optimization, employing a secondary optimization with a custom algorithm to improve the designs on the Pareto front leads to superior performance characteristics. In fact, the Pareto front obtained with $NSGA-II$ driver has better performance than the one obtained with *Simple GA* driver. However, it is crucial to recognize the constraints of the model. Projects with excessively high or low optimum speeds cannot be considered feasible, stressing the importance of considering the limitations of the model during the evaluation process.

In order to understand the different interaction of the involved disciplines in terms of constraints, a preliminary comparison is proposed regarding the best performance achieved by the two optimizations, the Aeroelastostatic and the Aeroelastic. The Figure 3.14 illustrates the comparison of the two obtained Pareto fronts. From this, it can be observed that the performance achieved by the Aeroelastic optimization (in green in the figure) is inferior to that obtained by the Aeroelastostatic optimization (in orange in the figure). This is because, in addition to the static constraints (which are the only ones applied in the Aeroelastostatic optimization), dynamic constraints such as aeroelastic stability and maximum load on the structure downstream of a gust application are also included. The application of additional constraints limits the objective space and inevitably results in a Pareto front with worse performance. Therefore, the best designs obtained from the Aeroelastic optimization exhibit inferior performance compared to those obtained with the Aeroelastostatic optimization, with the exception of two regions on the Pareto front where the optimal performances

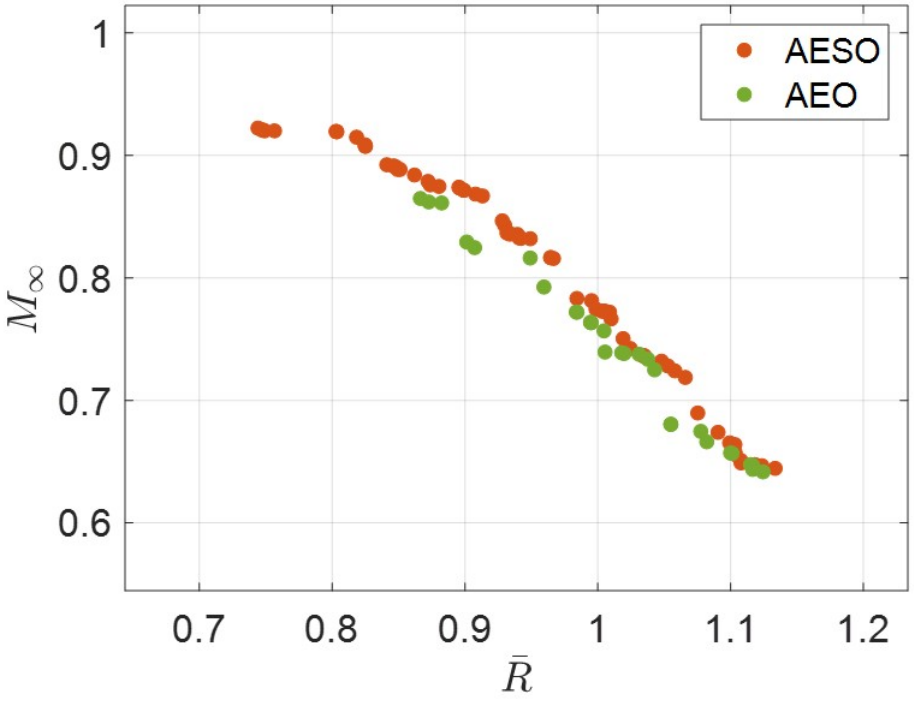

Figure 3.14: Pareto Front comparison: Aeroelastostatic Optimization (AESO) and Aeroelastic (AEO) Optimization

achieved by the two optimization problems are similar. At the end of this section, a specific comparison will be presented among the designs that achieve these similar performances, aiming to further understand the interaction process of constrained variables associated with different disciplines.

Obviously, the trends of performance variables such as weight, lift to drag and fuel consumption in the target space are similar to those shown above and therefore not reported. Once again, four Pareto front designs, as E, F, G and H designs, are improved through $SLSQP$ optimisation, using the same approach as described above, and they are examined to facilitate comparison of optimal designs both among themselves and in relation to those derived from the Aeroelastostatic optimization. The Figure 3.15 shows the target space related to the equivalent aspect ratio, in which the positioning of the chosen reference projects on the Pareto front is shown. As before, the geometric features of these designs and their plan forms are shown in Tab. 3.6 and Fig. 3.16.

Let's consider the performance obtained for the best designs, remembering that all performance variables have been scaled using the baseline values of the starting point. Specifically, the value of the cruise Mach M_∞ changes from 0.862 to 0.647, as the scaled range $\bar{R}$ changes from 87.2% to 111% of the reference value. Comparing these performance parameters, namely the best performance speed and the maximum range achieved using all available fuel, obtained from both Aeroelastostatic and Aeroelastic optimizations, it is observed that in the high Mach flight region, the best performances are more disparate compared to those at lower Mach flight, which is already evident from the Pareto comparison. All designs on the front Pareto achieve a reduction in weight compared to the reference of $70e3Kg$ by a maximum of 5% (design F) and a minimum of 1% (design E and H). So, remembering the previous results, the maximum weight reduction obtained on the Aeroelastic Pareto front is 1% lower than the maximum obtained on the Aeroelastostatic Pareto front. The

equivalent aspect ratio varies from 6.64 to 12.45 (reference value being 7.76), as well as the scaled aerodynamic efficiency of the aircraft, specifically the scaled L/D ratio varies from 80.9% to 123.3%.

Observing thoroughly the geometries of the four designs on the Pareto front, it can be seen that again there is an increase in the aerodynamic surface area of the wing, from a value of $113.26\,m^2$ for design E to a value of $163.76\,m^2$ for design H, and in the wing span, from a value of $27.36\,m$ for design E to a value of $45.45\,m$ for design H. When examining the most extreme designs on the Pareto front, denoted as A and D for the Aeroelastatic scenario and E and H for the Aeroelastic scenario, respectively, it becomes evident that the designs are different, particularly at high flight Mach numbers. Acknowledging the necessity to optimize performance across varying flight velocities, it's apparent that, as previously observed, the sweep angle of the wing adjusts accordingly. As the flight speed diminishes, this angle decreases as well, transitioning from a value of 29.93° for the E design to 17.22° for the H design. Moreover, changes in tail surface area occur, the wing surface area expands from model E to model H, as well as the tail surface area (from $23.62m^2$ to $37.13m^2$) and tail span length (from $8.86m$ to $12.16m$) also undergoes an increase. Finally, taking into account the Fig. 3.16 the aileron position and its area are selected by the optimizer according to the wing surface area that is available to it. Longer wings allow a greater occurrence of the control reversal condition and a reduction in aileron effectiveness, so the optimizer may place the aileron in an outermost position in the case of designs with shorter wing lengths (such as designs E and F), while placing the aileron more inwardly for designs with longer wing lengths (such as design H).

In addition, the structural characteristics of the wing are again considered, and these are shown in Figure 3.17, with the dimensionless characteristic values of the thicknesses of the skin panels ($\bar{t}_{UD}$), the thicknesses of the root web ($\bar{t}_{LE}$ and $\bar{t}_{TE}$), the thicknesses of the ribs ($\bar{t}_R$), the cap area of the stringers ($\bar{A}_{LE}$ and $\bar{A}_{TE}$) at the root, with their variations along the span (Δt_1, Δt_2, ΔA_{s_1} and ΔA_{s_2}, where the number always indicates the variation of the design variables in the first and second sections), for the four selected reference designs. As described above, the choice of these design variables depends on the geometry of the wing, the loads to be supported and the placement of the non-structural concentrated masses. In order to obtain further information on this, it is also necessary to examine the constraints values for these four projects (see Figures 3.18 and 3.19).

In particular, primarily the focus is on the loads obtained from the different static and dynamic analyses conducted for all four projects. Thus, the Figure 3.18 illustrates the peak load held by the wing structure in the different static analyses conducted, including trim, *MLA* maneuver, aileron reversal and roll, and during the dynamic analyses conducted, including different types of gust inputs (the figure shows only the maximum case evaluated between the different gust analyses). Specifically, the predominant load occurs during gusts, making this the primary constraint for thickness sizing. The optimizer selects thicknesses based on the maximum allowable load. Consequently, the structural constraint linked to the maximum load during gusts acts as the design threshold for thicknesses. It's worth noting that in the Aeroelastostatic optimization, the sizing constraint for thicknesses is the maneuver with *MLA*. This implies that the Pareto achievement obtained only with static constraints becomes unattainable when dynamic constraints, such as maximum gust loads, are introduced. These gust loads further restrict the objective space. Obviously, the target space is not only limited by the gust constraint added in the Aeroelastic Optimization, but also by the constraint imposed on the stability of the aeroelastic system, which is not shown for the four reference designs because all of them have a higher flutter velocity than the allowable limit and fall

	DESIGN FEATURES	DESIGN E	DESIGN F	DESIGN G	DESIGN H
AIRCRAFT	Cruise Mach M_∞	0.862	0.826	0.733	0.647
	Scaled Range $\bar{R}$	0.872	0.949	1.037	1.11
	Scaled lift-to-drag ratio $\bar{E}$	0.809	0.864	1.022	1.233
	Scaled Weight $\bar{W}$	0.985	0.951	0.966	0.989
	Equivalent Aspect Ratio AR_e	6.64	7.27	8.14	12.45
WING	Surface S_w	113.26 m^2	118.65 m^2	140.58 m^2	163.76 m^2
	Taper Ratio λ_w	0.29	0.16	0.17	0.09
	Span l_w	27.36 m	29.34 m	35.82 m	45.45 m
	Sweep angle Λ	29.93°	27.78°	23.74°	17.22°
TAIL	Surface S_t	23.62 m^2	26.73 m^2	25.46 m^2	37.13 m^2
	Taper Ratio λ_t	0.35	0.58	0.45	0.25
	Span l_t	8.86 m	9.3 m	9.63 m	12.16 m
AILERON	Position $p = \%l_w/2$	68.02 %	77.15 %	68.31 %	60.9 %
	Surface S_a	7.54 m^2	4.22 m^2	4.73 m^2	5.67 m^2

Table 3.6: Comparison of characteristics of Pareto Front designs obtained from the Aeroelastic optimization

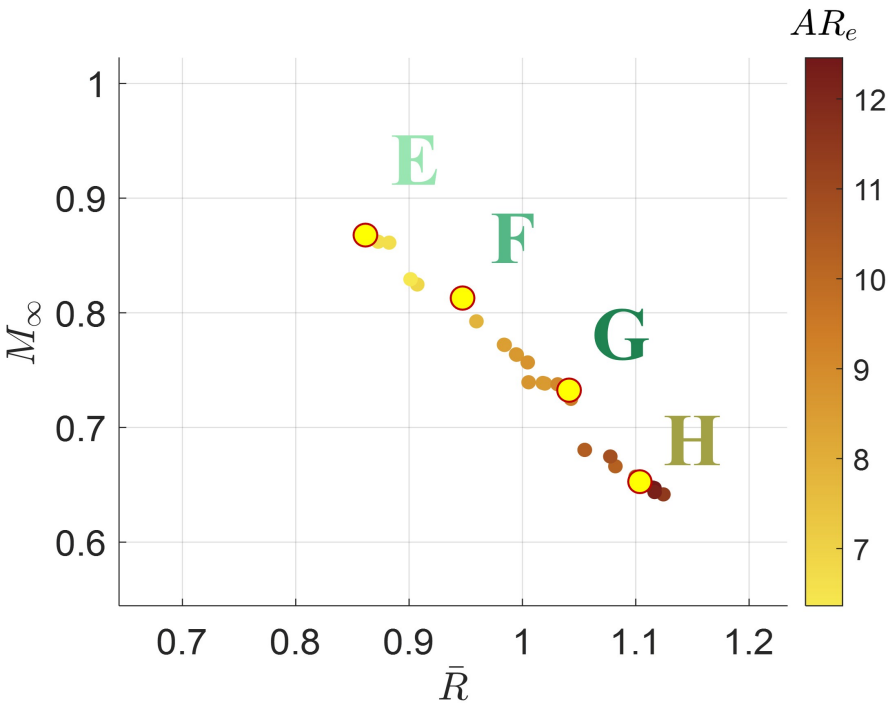

Figure 3.15: Equivalent Aspect Ratio of the Aeroelastic Optimization Pareto front, choice of displayed projects

exactly within the flight safety criteria. Therefore, the structural constraints associated with the maximum load during the gust size the model thicknesses. In contrast, looking at the constraints of an aeroelastic nature in Fig. 3.19, it can be seen that also in this optimization the sizing of the wing and tail surfaces is associated with the dimensioning constraints of maneuver and trim. In fact, the angle of attack during a 2.5g maneuver remains consistently at the maximum allowable limit across the four selected designs on the Pareto front (see Fig. 3.19(b)), while the elevator rotation required for such maneuver varies from 58% to 83% of the maximum allowable rotation for that control surface, with different values of static controllability $C_{m_{\delta_e}}$. On the other hand, looking at Fig. 3.19(a), it shows that the angle of attack required for trimming the aircraft reaches the maximum allowed value in all cases, while the tail rotation for the same analysis varies between 70% and 99% of the maximum allowable value. Finally, the aileron sizing and the characteristic constraint i.e., roll time are observed (see Fig. 3.19(c)), remembering that for each design the minimum speed is set for the negative condition of control reversal. When comparing the roll response time of the four designs to the same imposition of aileron rotation, it's evident that design F exhibits the slowest response (100% of the maximum limit value), while design E exhibits the fastest response (72% of the maximum limit value). Bear in mind that each design has different aileron position and surface areas and different wing areas, this inevitably reflects on aileron response. Moreover, another important parameter to consider is the taper ratio of the wing, as the higher this value, the less area will be available to aileron placement in the outermost area of the wing, in fact in the F design, the aileron is placed at the 77% of the wing and its area is very small $4.22m^2$.

In comparing the two optimization approaches, the Aeroelastostatic and Aeroelastic, where the first considers only static constraints and the second includes both static and dynamic constraints, a notable observation emerges. While examining the Pareto fronts, it becomes apparent that they

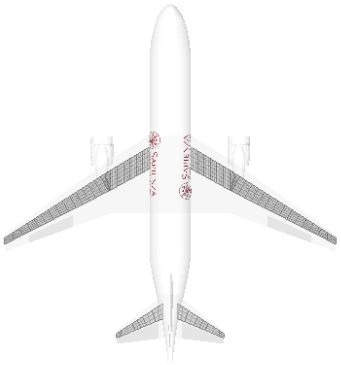

(a) Design: E

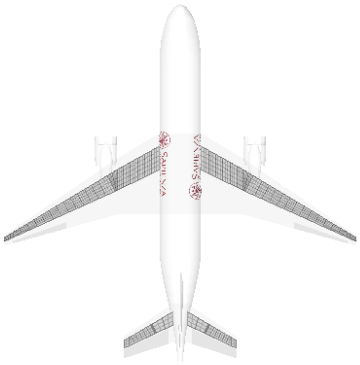

(b) Design: F

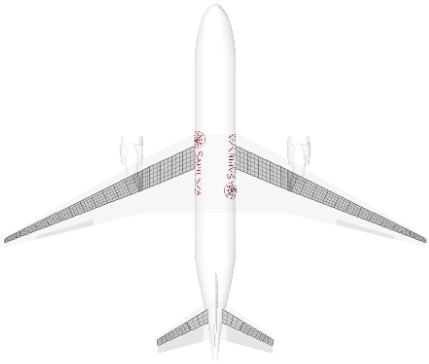

(c) Design: G

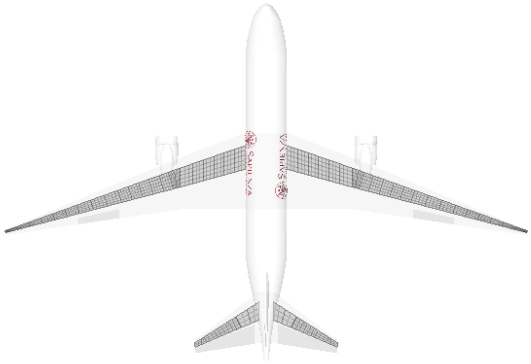

(d) Design: H

Figure 3.16: Best designs among the Pareto Front of the Aeroelastic Optimization

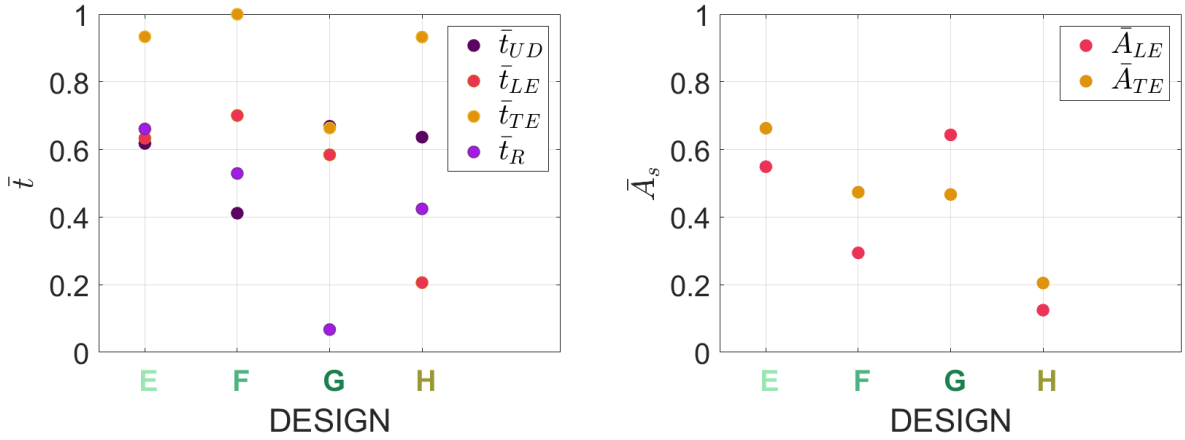

(a) Thickness at root

(b) Cap Area at root

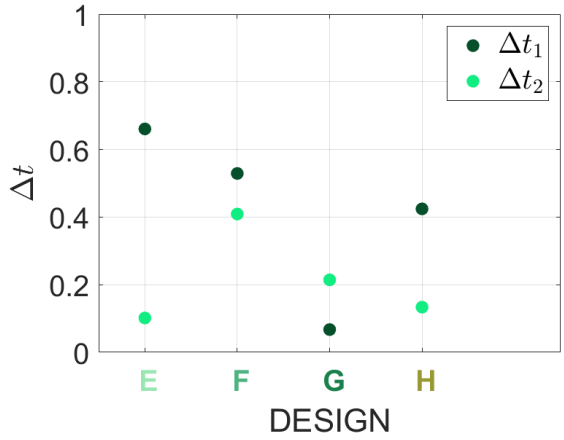

(c) Thickness Ratios

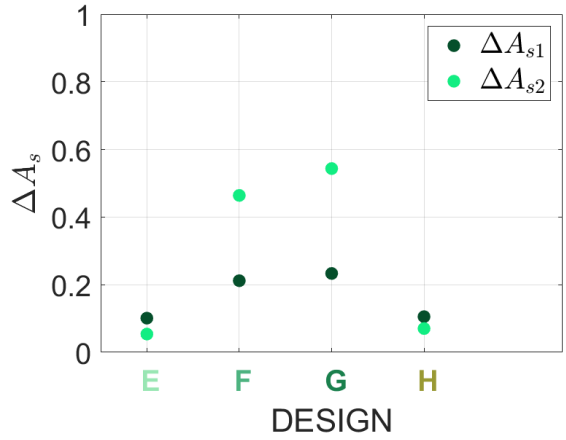

(d) Cap Area Ratios

Figure 3.17: Dimensionless thickness and cap area of the spars at the wing root and and their variation along the span

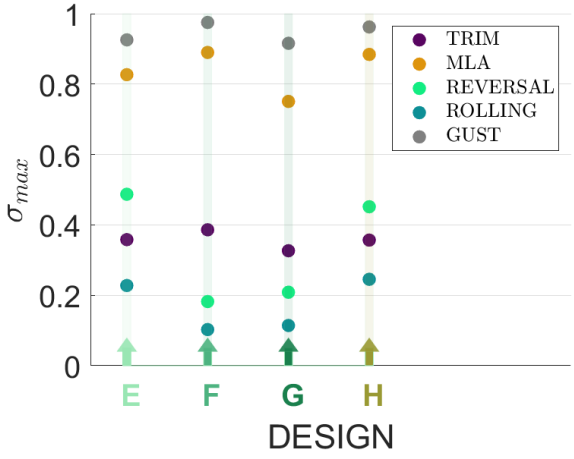

Figure 3.18: Structural constraint (σ_{max} values on wing) evaluated on the Pareto Front designs of the Aeroelastic optimization

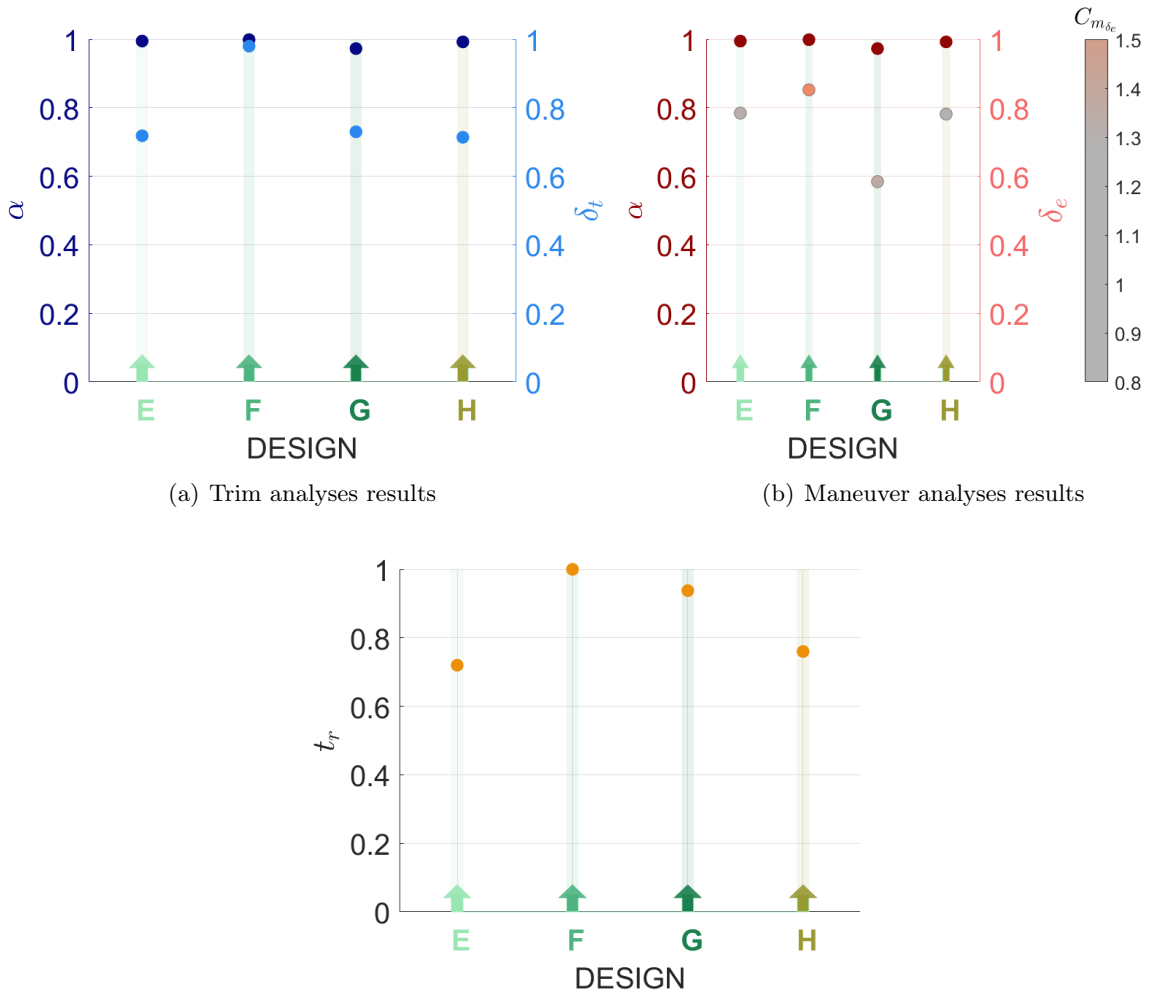

(a) Trim analyses results

(b) Maneuver analyses results

(c) Aileron response results

Figure 3.19: Aeroelastic constraints (α, δ_t, δ_e, $C_{m_{\delta_e}}$ and t_r values) evaluated on the Pareto Front designs of the Aeroelastic optimization

achieve similar performance within a specific region, i.e the region at cruise Mach M_∞ equal to 0.73 and the adimensionalized mileage range $\bar{R}$ equal to 1.03. In this specific region, let now consider two designs that represent the optimization outcomes, namely design C and design G. These designs achieve similar performance, however, upon closer examination of the designs themselves, differences emerge, particularly in the shape of the wing (see Tab. 3.5 and Tab. 3.6 for more details). This discrepancy underscores the varied interactions and influences of different disciplines in shaping the optimal design solutions. Despite reaching a similar zone of best performance, the designs produced by each approach reflect distinct responses to the combined effects of static and dynamic constraints, highlighting the multidisciplinary nature of the optimization process proposed.

In summary, the aerelastic optimization process has yielded valuable insights into the intricate interplay between various disciplines involved in aircraft design. By showing the performance metrics, constraints, and optimal designs resulting from this approach, the importance of considering multiple disciplines and their interactions during the design process have been underscored. Moreover, comparison of these results with those obtained from optimization with fewer constraints has revealed a key phenomenon: as the number of active constraints increases, the design space becomes more constrained, potentially leading to suboptimal performance. This highlights the need for an in-depth understanding of how different disciplines interact and influence optimal design outcomes.

3.4 Aeroservoelastic Optimization (ASEO)

This section presents the results of the Aeroservoelastic optimization, encompassing the integration of disciplinary constraints from structural, aerodynamic, and control domains. The final optimization incorporates controller presence, enabling relaxation of certain constraints. Specifically, controller synthesis for Active Flutter Suppression and Gust Load Alleviation alleviates the aeroelastic stability and the maximum load constraints during gust conditions. With the controller active, stability requirements are adjusted, notably with flutter speed constraints being eased within a designated speed range where controller benefits can be utilized, the constraints applied are

$$\begin{aligned} U_f^{OL} &\geq U_D \\ U_f^{CL} &\geq 1.1U_D \end{aligned} \tag{3.2}$$

However, complete removal of open-loop stability constraints isn't feasible for flight safety. Additionally, the controller aids in load alleviation during gust encounters, with load calculations potentially performed directly with an active controller, further relieving this constraint. Thus, the additional dynamics constraints inherent in aeroelastic optimization are also incorporated here but mitigated by the controller's presence.

Similar to the previous optimizations, the objective space in Fig. 3.20 obtained with the *SimpleGA* Driver of *OpenMDAO* and the calculation of 50 generations is shown, in which only the feasible designs are presented and the goals are focused again on maximizing both the cruise flight speed M_∞ and the adimensionalized mileage range $\bar{R}$. Following the previous methodology, a subsequent optimization using the $NSGA-II$ algorithm is employed, with an evaluation spanning an additional 10 generations; the comparison between the two Pareto fronts of the Aeroservoelastic optimizations is illustrated in Fig.3.21. Similarly to the previous optimizations, employing a sec-

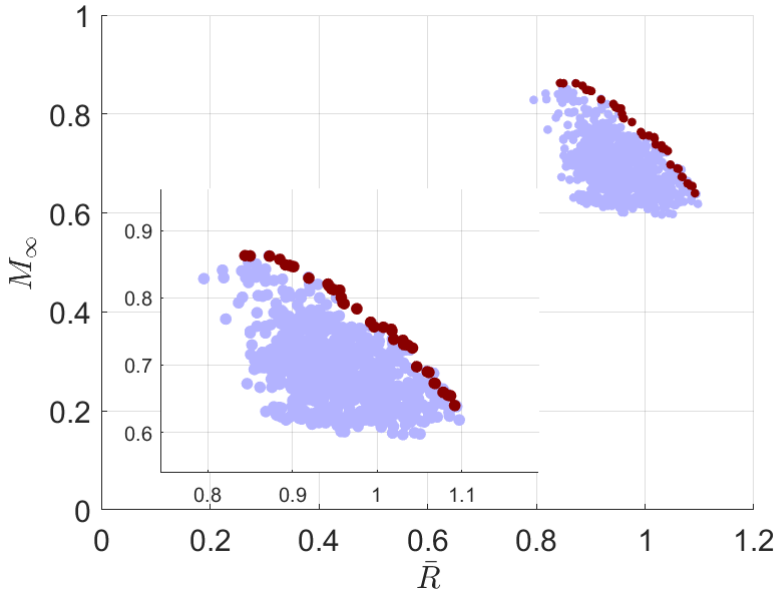

Figure 3.20: Objective space of the Aeroservoelastic Optimization: Pareto Front

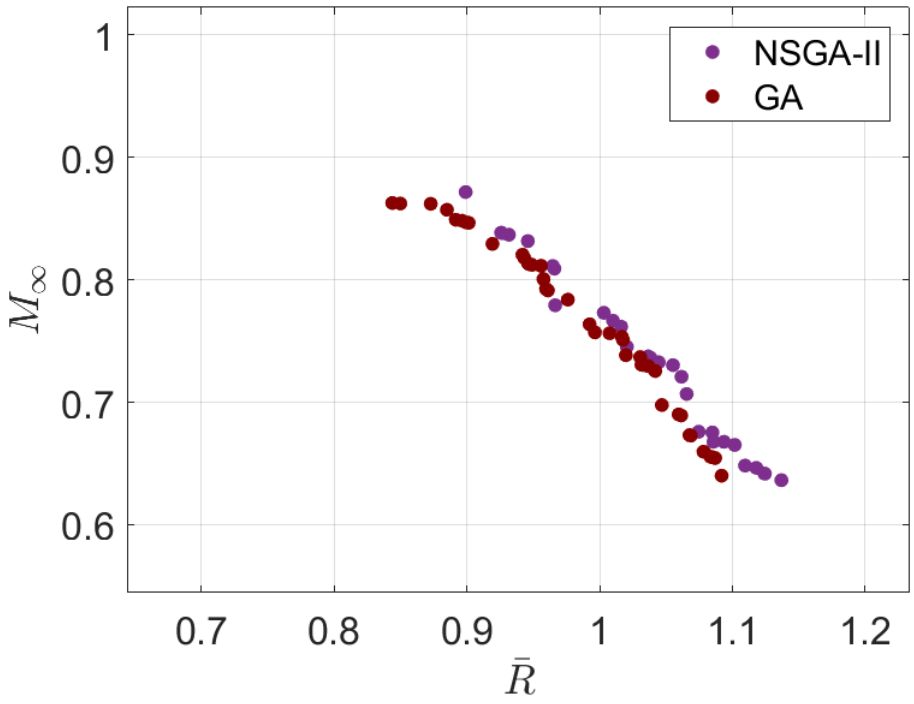

Figure 3.21: Comparison of the Pareto front obtained with *Simple GA* Driver and with $NSGA-II$ Driver: Aeroservoelastic Optimization

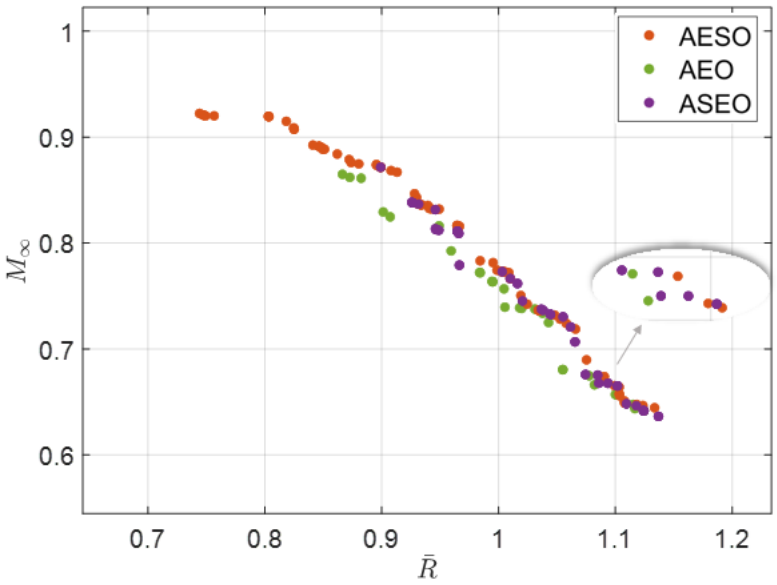

Figure 3.22: Pareto Front comparison: Aeroelastostatic Optimization (AESO), Aeroelastic (AEO) Optimization, and Aeroservoelastic Optimization (AESO)

ondary optimization utilizing a custom algorithm to refine designs on the Pareto front results in enhanced performance attributes. Indeed, the Pareto front attained with the $NSGA-II$ driver exhibits superior performance compared to that achieved with the *Simple GA* driver. Nevertheless, it's imperative to acknowledge the constraints inherent in the model. As seen above, projects with too high or low optimal velocities cannot be considered feasible, underscoring the importance of taking model limitations into account during the evaluation phase. To comprehend the varying interactions among the involved disciplines in terms of constraints, a preliminary comparison is suggested regarding the optimal performance achieved by the three optimizations: the Aeroelastostatic, the Aeroelastic, and the Aeroservoelastic in Fig. 3.22. The initial comparison between the optimal designs achieved through the Aeroelastostatic and the Aeroelastic optimization revealed that superior performance are attained in the first case. It is evident that the inclusion of the dynamic constraints with static constraints limited the target space, resulting in inferior performance. Naturally, in aircraft sizing, dynamic constraints are indispensable for ensuring the flight safety. Upon closer examination of the comparison involving the optimal designs from all three optimizations, it becomes apparent that the presence of a controller in the Aeroservoelastic optimization (depicted in lilac in the figure) enables the retrieval of the excellent performance observed in the Aeroelastostatic optimization (depicted in orange) in certain areas. Additionally, in other regions, it facilitates an intermediate placement between the Aeroelastostatic Pareto (in orange) and the Aeroelastic Pareto (in green). Such recovery in terms of goal space is obviously related to the possibility of alleviating dynamic constraints and ensure the aeroelastic stability through the use of controller.

Clearly, the performance trends of variables such as weight, lift-to-drag ratio, and fuel consumption in the target space follow similar patterns to those previously depicted and thus are not reiterated here. Once again, four Pareto front designs are improved through $SLSQP$ optimisation and are examined -designated as I, L, M, and N-to facilitate the comparison of optimal designs both amongst themselves and in relation to those derived from the Aeroelastostatic and the Aeroelastic

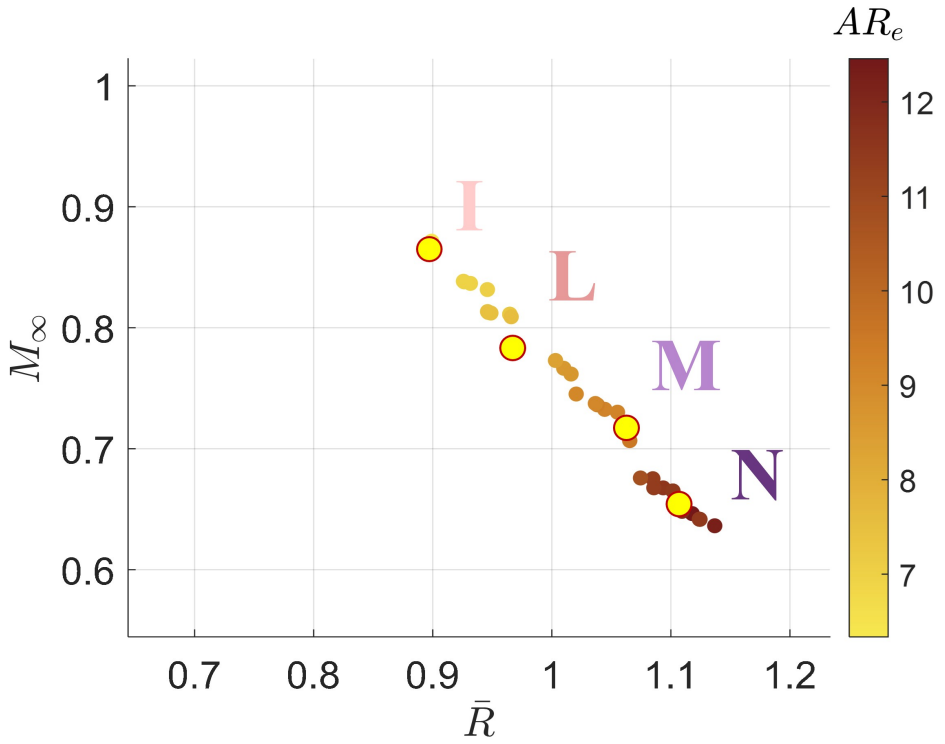

Figure 3.23: Equivalent Aspect Ratio of the Aeroservoelastic Optimization Pareto front, choice of displayed projects

optimization. The Figure 3.23 illustrates the target space related to the equivalent aspect ratio, highlighting the positioning of selected reference projects on the Pareto front. As in previous analyses, the geometric attributes and plan forms of these designs are detailed in Table 3.7 and in the Figure 3.24, respectively.

Let's examine also for this optimization the performance achieved by the best designs, bearing in mind that all performance metrics have been normalized using the baseline values from the initial point. Specifically, the cruise Mach number M_∞ varies from 0.872 to 0.642, corresponding to a scaled range $\bar{R}$ change from 89.9% to 112.4% of the reference value. Comparing these performance indicators —namely, the optimal speed and the maximum range achieved using all available fuel— across the Aeroelastostatic, the Aeroelastic and the Aeroservoelastic optimizations, it becomes evident that the performance gap between the first two optimizations diminishes when the controller is incorporated. All designs on the Pareto front achieve a weight reduction relative to the reference of 70e3 Kg, ranging from a maximum of 5% (design M) to a minimum of 3% (designs L and N). Thus, recalling previous findings, the minimum weight reduction on the Aeroservoelastic Pareto front is 2% greater than that achieved on the Aeroelastostatic and Aeroelastic Pareto front. The equivalent aspect ratio ranges from 6.34 to 11.45 (with the reference value being 7.76), while the scaled aerodynamic efficiency of the aircraft, specifically the scaled lift-to-drag ratio (L/D), varies from 78.5% to 122.7%. Upon close examination of the geometries of the four designs on the Pareto front, there's a noticeable increase in the aerodynamic surface area of the wing, from 108.31 m^2 for design I to 177.84 m^2 for design N, as well as in the wing span, from 26.16 m for design I to 45.13 m for design N. Recognizing the need to optimize performance across various flight velocities, it's observed that, as previously noted, the sweep angle of the wing adjusts accordingly. As flight

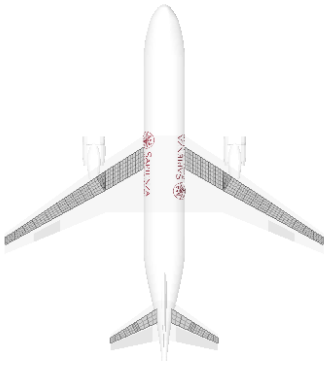

(a) Design: I

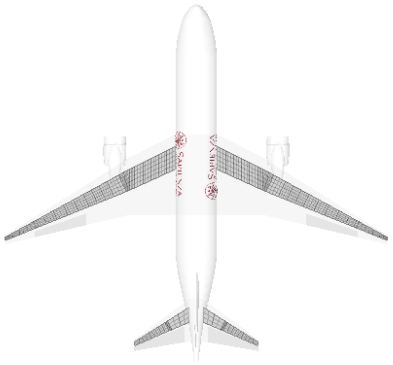

(b) Design: L

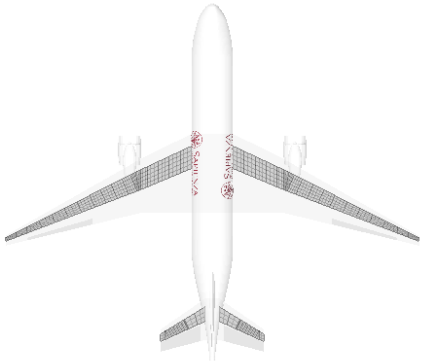

(c) Design: M

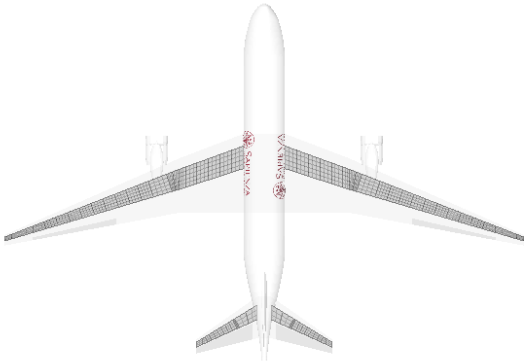

(d) Design: N

Figure 3.24: Best designs among the Pareto Front of the Aeroservoelastic Optimization

	DESIGN FEATURES	DESIGN I	DESIGN L	DESIGN M	DESIGN N
AIRCRAFT	Cruise Mach M_∞	0.872	0.779	0.737	0.642
	Scaled Range $\bar{R}$	0.899	0.967	1.037	1.124
	Scaled lift-to-drag ratio $\bar{E}$	0.785	0.931	1.006	1.227
	Scaled Weight $\bar{W}$	0.948	0.972	0.956	0.976
	Equivalent Aspect Ratio AR_e	6.34	8.01	9.02	11.45
WING	Surface S_w	108.31 m^2	130.24 m^2	137.20 m^2	177.84 m^2
	Taper Ratio λ_w	0.35	0.14	0.16	0.17
	Span l_w	26.16 m	32.19 m	35.17 m	45.13 m
	Sweep angle Λ	31.13°	25.46°	23.86°	18.88°
TAIL	Surface S_t	23.56 m^2	25.46 m^2	25.5 m^2	30.51 m^2
	Taper Ratio λ_t	0.4	0.26	0.53	0.33
	Span l_t	8.86 m	11.7 m	8.47 m	11.57 m
AILERON	Position $p = \%l_w/2$	69.65 %	67.5 %	70.74 %	70.7 %
	Surface S_a	4.49 m^2	8.03 m^2	4.98 m^2	6.66 m^2

Table 3.7: Comparison of characteristics of Pareto Front designs obtained from the Aeroservoelastic optimization

speed decreases, this angle also decreases, transitioning from 31.13° for design I to 18.88° for design N. Moreover, changes in tail surface area occur, with both the wing surface area and tail surface area expanding from model I to model N, alongside an increase in tail span length. Finally, considering Figure 3.24, the optimizer selects the aileron position and its area based on the available wing surface area. Longer wings allow for a greater occurrence of the control reversal condition and a reduction in aileron effectiveness. Looking closely at the design depictions, it's apparent that the optimizer positions the aileron as outwardly as feasible, thereby reducing its chord to mitigate the impact of decreased aileron effectiveness.

Furthermore, the structural attributes of the wing are re-evaluated, as illustrated in Figure 3.25, showcasing dimensionless characteristic values of various components such as skin panel thicknesses ($\bar{t}_{UD}$), root web thicknesses ($\bar{t}_{LE}$ and $\bar{t}_{TE}$), rib thicknesses ($\bar{t}_R$), and the cap area of the stringers ($\bar{A}_{LE}$ and $\bar{A}_{TE}$) at the root, along with their variations across the span (Δt_1, Δt_2, ΔA_{s_1}, and ΔA_{s_2}, where the numbers denote variations in design variables for the first and second sections) for the four reference designs selected. As previously mentioned, the selection of these design variables is contingent upon wing geometry, the static and dynamic loads, and the placement of the non-structural concentrated masses. To gain deeper insights into this aspect, it is imperative to scrutinize the constraint values for these four projects as well (refer to Figures 3.26 and 3.27). In particular, the primary focus lies on the loads derived from various static and dynamic analyses conducted for all four projects. It's crucial to highlight that, if deemed necessary (such as when the gust loads in open loop are excessively high), the control path switches to the activate state, enabling the controller synthesis and load calculations during gusts with the controller activated. Figure 3.26 illustrates the peak loads on the wing structure during the different static analyses, encompassing trim, *MLA* maneuver, aileron reversal, and roll, as well as during dynamic analyses involving different types of gust inputs (with the figure showcasing only the maximum case evaluated among the various gust analyses). Notably, the predominant loads manifest during gusts and/or maneuvers, thereby constituting the primary constraints for thickness sizing. The optimizer selects thicknesses based on the maximum allowable load, thereby establishing the structural constraint associated with maximum load during gusts and maneuvers as the design threshold for thicknesses. It's notable that in the Aeroelastostatic optimization, the primary sizing constraint for thicknesses is the maneuver with *MLA*, while in the Aeroelastic optimization, it's the gust. However, in the Aeroservoelastic optimization, both become sizing constraints due to the utilization of the Aileron controls. This indicates that achieving the Pareto frontier solely based on static constraints becomes not as far when the dynamic constraints, such as maximum gust loads, are introduced and alleviated using the controller, because these gust loads impose less restriction on the objective space. It's important to recognize that the target space isn't solely confined by the added gust constraint but also by the constraint imposed on the stability of the aeroelastic system. This stability constraint is illustrated for the four reference designs in Fig. 3.27(d), where all designs exhibit a higher scaled flutter velocity in the closed-loop case than the allowable limit, aligning precisely with flight safety criteria. In addition, the use of the controller makes it possible to re-obtain designs obtained within the Aeroelastostatic target space that would otherwise not be feasible due to stability problems, as had been shown in the Aeroelastic optimization.

In contrast, examining the aeroelastic constraints depicted in Fig. 3.27, it's apparent that in this optimization as well, the sizing of wing and tail surfaces is dictated by dimensioning constraints

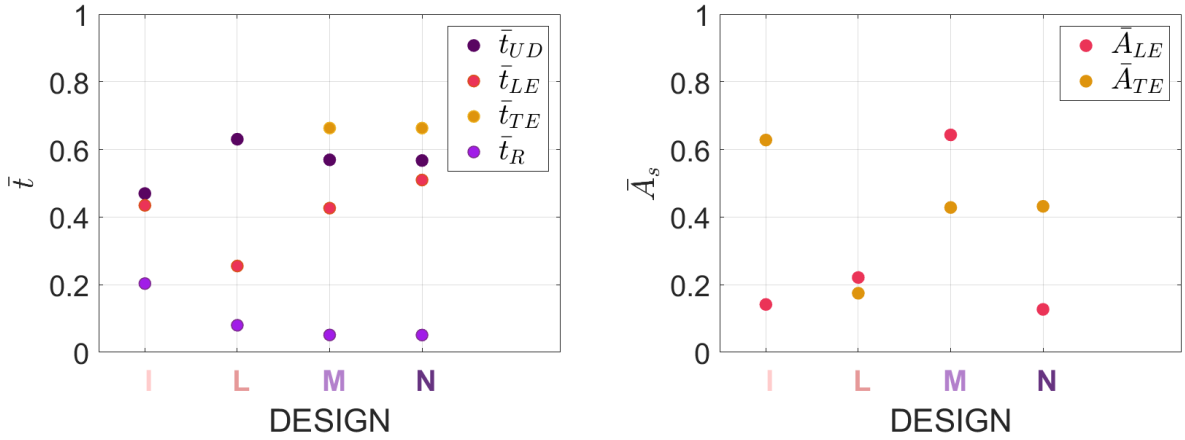

(a) Thickness at root

(b) Cap Area at root

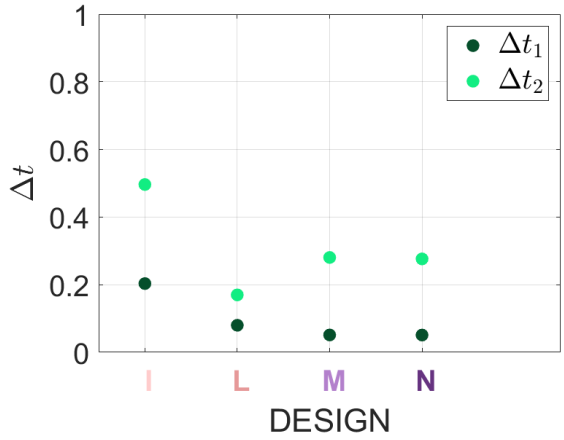

(c) Thickness Ratios

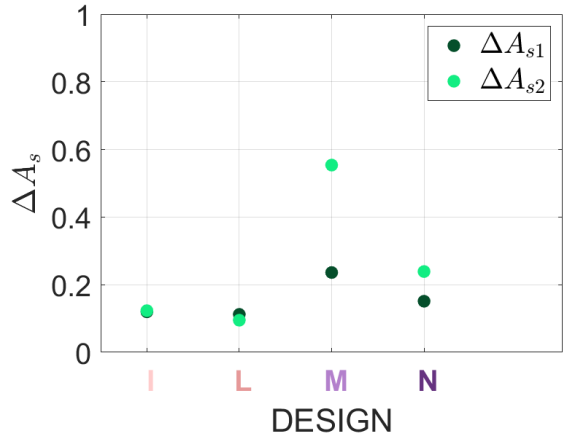

(d) Cap Area Ratios

Figure 3.25: Dimensionless thickness and cap area of the spars at the wing root and and their variation along the span

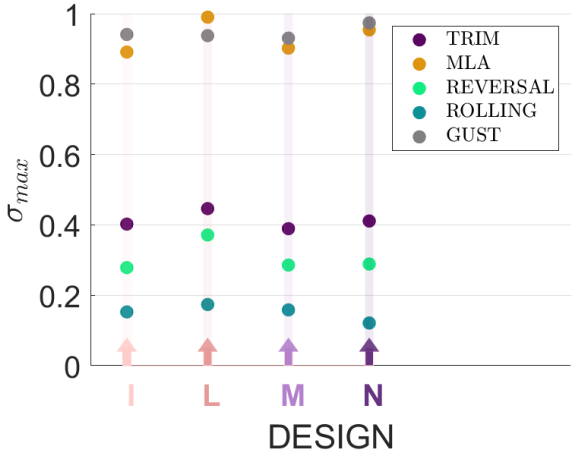

Figure 3.26: Structural constraint (σ_{max} values on wing) evaluated on the Pareto Front designs of the Aeroelastic optimization

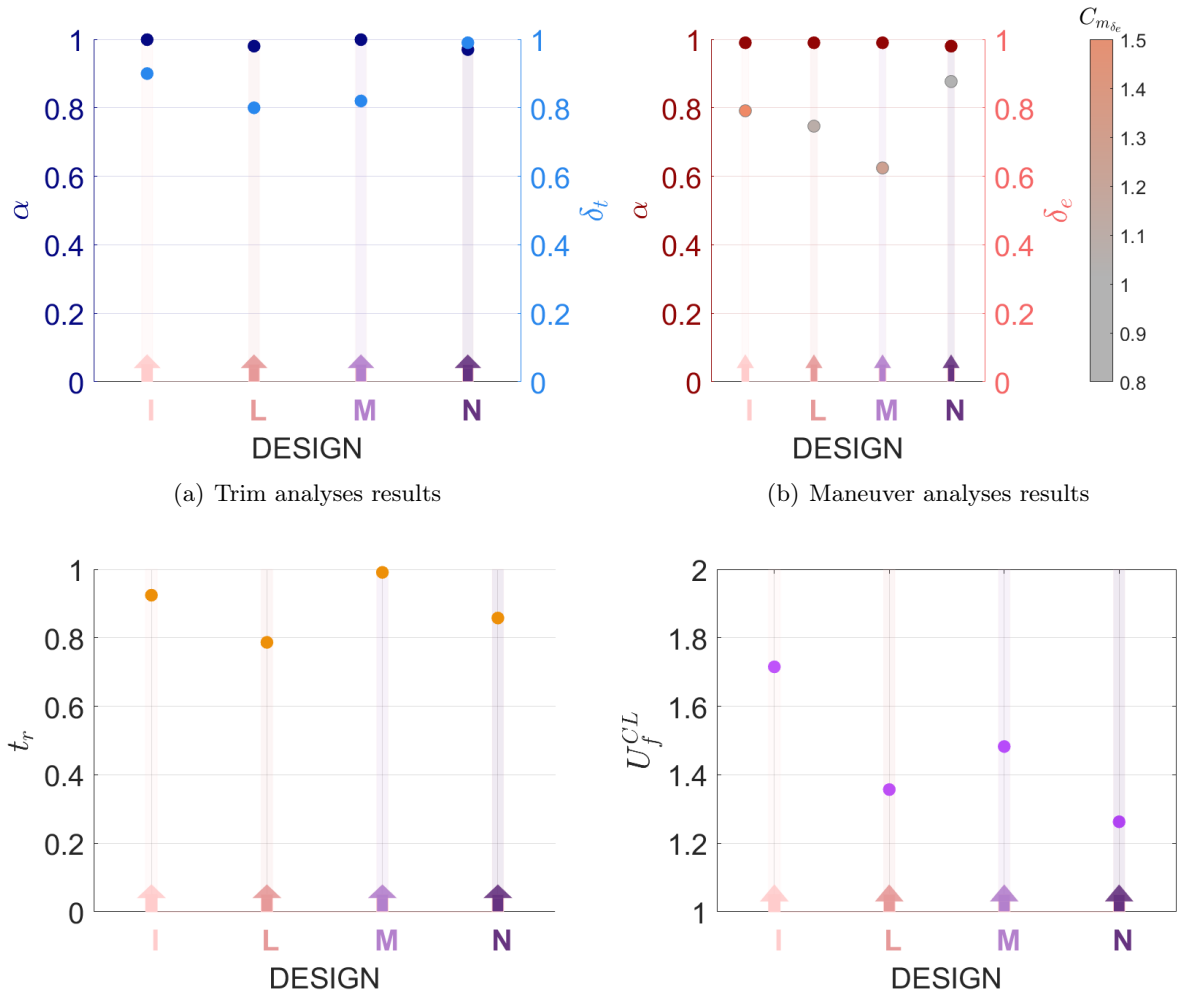

(a) Trim analyses results

(b) Maneuver analyses results

(c) Aileron response results

(d) Stability results

Figure 3.27: Aeroservoelastic constraints (α, δ_t, δ_e, $C_{m_{\delta_e}}$, t_r and U_f^{CL} values) evaluated on the Pareto Front designs of the Aeroelastic optimization

Optimization	Iter	Time	CPU	f	N
AESO	27000	$23h$	© AMD Ryzen 9 7950X	4.5 GHz	8
AEO	27000	$32h$	© AMD Ryzen 9 7950X	4.5 GHz	8
ASEO	27000	$45h$	© AMD Ryzen 9 7950X	4.5 GHz	8

Table 3.8: MDO computational cost

related to maneuver and trim. During a 2.5g maneuver, the angle of attack remains consistently at the maximum allowable limit across the four selected designs on the Pareto front (as shown in Fig. 3.27(b)). However, the elevator rotation required for such a maneuver varies from 62% to 90% of the maximum allowable rotation for that control surface, exhibiting different values of static controllability ($C_{m_{\delta_e}}$). On the other hand, examining Fig. 3.27(a), it's evident that the angle of attack needed for trimming the aircraft reaches the maximum allowed value in all cases. Meanwhile, the tail rotation for the same analysis varies between 80% and 99% of the maximum allowable value.

Lastly, attention is directed towards the sizing of ailerons and a key characteristic constraint, namely the roll time (refer to Fig. 3.27(c)). Upon comparing the roll response time of the four designs under the same aileron rotation requirement, it's evident that design M demonstrates the slowest response (at 100% of the maximum limit value), whereas design L displays the fastest response (at 79% of the maximum limit value). Design L, characterized by the fastest roll response, features a larger aileron area positioned towards the outer section along the wing span. Conversely, design M possesses a smaller aileron area with a more outward positioning along the wing span.

In conclusion, the analysis of the Aeroservoelastic optimization has demonstrated the effectiveness of incorporating all proposed constraints, including static, dynamic and control constraints. The best designs obtained have been compared with those obtained from the previous optimization analyses, showing how the introduction of dynamic constraints has significantly influenced the design process. The inclusion of the control discipline has become critical in determining design sizing because it allows to work with dynamic constraints in a different way. Furthermore, it has been found that the presence of the controller improved the overall performance by enabling the recovery of designs that would otherwise not meet safety criteria in terms of load and stability. These results underscore the importance of carefully considering the interaction between different disciplines and the impact of dynamic constraints in aircraft design.

3.5 MDO computational aspects

In this section, the computational times of the separate optimization processes conducted to refine our design are analyzed. Computational efficiency plays a crucial role in the optimization process, influencing the speed and effectiveness of reaching optimal solutions. Here a Table 3.8 of the time taken by each optimization, showing on the computational efficiency of our methodologies. It is worth noting that, during the optimization, each design corresponds to the definition of a Finite Element Method model, along with the calculation of the analyses required to evaluate the constrained variables. In the context of the initial Aeroelastostatic optimization (AESO), which involves only static analyses, the calculation times are remarkably short. As an example, calculations for 27.000 designs are completed in 23 hours. However, with the inclusion of dynamic constraints in

the Aeroelastic optimization (AEO), such as the aeroelastic stability within a specific velocity ranges and responses to various gust scenarios, the calculation times rise to 32 hours for the same amount of designs. In the final optimization phase, the Aeroservoelastic optimization (ASEO), which also includes controller synthesis to solve designs that exceed load constraints during gusts and have instabilities at specific flight speeds, computation times inevitably increase. For the same number of designs, computation time reaches 45 hours. Obviously, the proposed optimizations have been carried out by the same computer with eight processors available to calculate the same number of designs. The decision to use a Reduced Order Model that describes the aeroservoelastic system to a good approximation has been made specifically to meet computational time constraints. During the preliminary design phase, the goal is to conduct an efficient and rapid exploration of the design space. This goal has been achieved through the use of the developed ROM model.

Conclusion and Future remarks

This PhD thesis is framed in a historic time in which there are new and interesting challenges to the aviation industry, characterized by the emergence of innovative designs aimed at improving aircraft performance and mitigating environmental impact. These imperatives call for a re-evaluation of aircraft sizing from the preliminary design stage, aiming for greater efficiency and an ongoing commitment to environmental sustainability. In order to achieve wise sizing that optimizes aircraft performance while meeting all design constraints, it is essential to adopt a Multi Disciplinary design Optimization approach, in which all relevant disciplines are considered simultaneously and interact with competing goals and constraints, in the search for the optimal design that meets all requirements. The Multidisciplinary Design Optimization (*MDO*) practice stands as a potent methodology in next-generation design research. It enables the exploration of interdisciplinary connections that might remain undiscovered when relying solely on individual disciplines. Nonetheless, the effectiveness of this approach hinges on various factors, including the design space definition, the fidelity of modeling across involved disciplines, the integration of multidisciplinary aspects, and the selection of an appropriate optimization architecture.

This thesis introduces a rapid and effective *MDO* methodology for wing, tail, and aileron sizing applicable in preliminary aircraft design, with specific emphasis on an explicit multi-objective approach incorporating controller optimization, and using reduced-order models for the aeroservoelastic description of aircraft. Therefore, the thesis focuses on two main aspects: aircraft design and optimization. More precisely, this thesis is driven by distinct objectives: first, the development of a robust tool for conducting Aircraft Multi-Disciplinary Design Optimization, leveraging Finite Element Models and Reduced Order Models. Second, it aims to deepen understanding of the intricate interplay among disciplines within the aircraft system. Finally, it attempts to pragmatically apply the developed tool, adapting the analyses to speed up the time and cost associated with the development of new aircraft designs.

In this regard, the use of a simplified aeroservoelastic model provides a good balance between the rapid exploration of the goal space and the good descriptive accuracy of the physical problem. Key components include a structural finite-element model for the wing and tail, simplified models for the fuselage and control surfaces, an analytical aerodynamic model employing modified Strip theory and Theodorsen approximation for compressible flow, and a control law model for aileron usage in Load Alleviation or Active Flutter Suppression. In particular, the aircraft ROM is represented by appropriate engineering models for each discipline involved and is developed as a black box. The aircraft model is equipped with a comprehensive range of functionalities aimed at facilitating thorough analysis and optimization of aircraft design. Firstly, it enables the precise definition of vehicle geometry sizing, tailored to meet specific mission requirements, while also providing an

estimate of the aircraft's Maximum Take Off Weight. This foundational aspect ensures that the aircraft is appropriately sized and configured to fulfill its intended operational objectives. Furthermore, the model incorporates a Finite Element Model, formulated to encompass both structural and aerodynamic considerations of the aircraft. Notably, the model accommodates two distinct aircraft configurations: the Maximum Take Off Weight configuration and the Maximum Zero Fuel Weight configuration, allowing for comprehensive analysis under varying operational scenarios. Additionally, the model provides the creation of an aerodynamic Reduced Order Model, using the analytical indicial functions to provide a simplified but accurate representation of aerodynamic behavior. Through rigorous validation exercises against the finite element model, the efficacy and reliability of this reduced-order approach are confirmed. Moreover, the model integrates perfectly with aeroelasticity and flight dynamics, enabling the simulation of static and dynamic analyses under different flight conditions. By selecting the most challenging scenarios within the flight envelope, the model facilitates a focused examination of sizing output, ensuring robustness across operational parameters. Furthermore, the model incorporates the control law models, including Active Flutter Suppression and Gust Load Alleviation, designed according to specific synthesis criteria. This enables the optimization of aircraft performance and stability under varying environmental and operational conditions. Ultimately, the model enables the calculation of optimal cruise performance parameters, providing valuable insights for the design and operation of next-generation aircraft. With its array of capabilities, the model serves as a good approximation for aeroservoelastic aircraft, offering rapid computation of performance metrics and constrained variables. This makes it highly applicable in the field of early-stage aircraft design, facilitating rapid exploration of the design space.

In pursuit of the second objective of the thesis, namely optimization, instead, the black box representing the aircraft is integrated into the optimization process, along with all the internal interdisciplinary analyses conducted sequentially. This sequential architecture, which includes internal optimization for the control law synthesis, is selected for its effectiveness in managing the complexity of the optimization process. Additionally, considerable attention is devoted to selecting appropriate design variables for the optimization process. These variables are carefully chosen, taking into account their range bounded by lower and upper limits. The aim is to strike a balance between the speed of optimization and the thorough exploration of the solution space, all while ensuring the feasibility of physical realization and manufacturing constraints. In addition, careful consideration is given to all potential constraints to be included in the proposed optimization methodology. This entailed not only incorporating constraints commonly found in academic literature but also integrating constraints typically encountered in industrial optimization during the preliminary design phase. By including a comprehensive range of constraints, the optimization process is tailored to address both theoretical and practical considerations, ensuring its relevance and effectiveness across various application domains. Ultimately, the thesis concludes with the execution of a multi-objective disciplinary optimization for aircraft design. The results obtained from this optimization process are thoroughly reviewed and discussed from multiple perspectives, including those associated with performance and those associated with the constrained sizing. This comprehensive analysis provided valuable insights into the effectiveness and potential applications of the optimization methodology developed as part of this thesis.

The thesis aims to illustrate how the integration of diverse disciplines into an optimization pro-

cess leads to the attainment of specific optimal designs. Additionally, it demonstrates how the sizing decisions are contingent upon prevailing constraints, which may vary with the inclusion of additional disciplines, thus altering the objective space. In order to validate the proposed optimization methodology, a process involving three optimizations with an increasing number of constraints involved is proposed. The constraints involved reflect the use of different disciplines, they are incorporated into the optimization in a gradually increasing way up to represent the complete methodology proposed. The ranges of variation of the design variables, the optimization objectives and the initial starting population are kept fixed. However, the nature of the disciplines involved is the only thing that is changed during the validation process, in order to check how the different discipline involved interact with each other and how the best solutions change during the three different optimizations process. It has been observed that optimizing with solely static constraints yields designs with excellent performance, where sizing constraints come from maneuvering and trim analyses. However, when dynamic constraints are introduced, the objective space becomes more constrained, limiting the achievement of optimal performance levels observed previously. In fact, to the previous dimensioning constraints are added the maximum load during the gust and the demand for aeroealstical stability within a certain speed range as sizing constraints. To address this challenge, the utilization of controllers proves beneficial by alleviating some of these dominant constraints, thereby allowing for the recovery of optimal zones or, at the very least, their partial restoration during optimization.

Hence, the unconventional application of controller optimization during the preliminary design phase has emerged as a valuable tool for achieving optimal designs. This approach, while introducing a modest increase in time and computational resources, yields significant benefits in terms of design quality and performance. By integrating controller optimization early in the design process, aircraft performance and stability could be effectively optimized, leading to more robust and efficient designs.

3.6 Future developments

Numerous pathways for future exploration and advancement emerge in the field of the aeroservoelastic optimization, presenting exciting opportunities for further research and innovation. This section outlines potential directions for future developments, focusing on areas where advances can improve the efficiency, effectiveness, and applicability of aeroservoelastic optimization techniques.

The use of reduced order models within the optimization poses a limitation in terms of the fidelity of the model's descriptive accuracy, often offset by the model's low computational costs and quick processing times. In this regard, with access to more efficient computing resources, there is potential for enhancing the aeroservoelastic model. Starting with the structural finite element model, improvements could involve incorporating the fuselage modeling, which could also be introduced into the optimization problem through additional design variables. Further enhancements to the structural model could entail the inclusion of structural nonlinearities. In addition, weighted use of computational fluid dynamics for the aerodynamic model could be considered, possibly creating data tables based on the known ranges of variation of design variables accessed during optimization to minimize computational time. Moreover, the current model only considers the longitudinal dynamics for sizing, hence the possibility of incorporating lateral-directional dynamics could be explored. In this context, the use of a more comprehensive controller could be considered, validating the handling qualities for longitudinal and lateral dynamics but also considering the safety

considerations addressed in this thesis.

Turning our attention to recent aircraft concepts proposed by the aerospace industry, there is potential to apply the same methodology proposed here to unconventional aircraft configurations. One such example of an unconventional aircraft could be a hydrogen-powered aircraft, where the storage and positioning of fuel would be entirely different from the typical placement in the wings and fuselage. As a consequence, this results in substantial effects to both the static and dynamic stability of the aircraft. In this regard, it is essential to consider constraints such as structural safety and handling qualities to avoid pressure collapse in cryogenic tanks due to tank acceleration as a result of the aircraft's response to gusts. With such a different aircraft configuration, it would be interesting to explore the interaction among the various disciplines involved in the optimization process. This entails observing the constrained variables associated with both static and dynamic analyses and understanding how the design variables are selected for a fully different problem. Additionally, a crucial aspect would be the controller's role, as it must adhere to stricter safety constraints associated with the use of hydrogen as fuel. The complexity of controller management in this scenario, where security considerations are critical, adds another layer of complexity to the optimization process. The second proposed case of an unconventional aircraft is an airplane that uses semi-aeroelastic hinge devices. The semi aeroelastic hinge is an innovative structural component that can be used in aircraft wings to control and mitigate the aerodynamic loads and the structural deformations. It is positioned along the span of the wing, typically near the wingtips, and it serves as a passive control mechanism to influence the aeroelastic behavior of the wing. By allowing controlled bending or twisting of the wing in response to aerodynamic forces, the *Semi Aeroelastic Hinge (SAH)* helps improve aerodynamic performance, and structural integrity of the aircraft. Its strategic placement and design are crucial in optimizing aircraft performance and ensuring safe flight operations. Two configurations must be considered for each aircraft in this case: the design configuration where the *SAH* permits free movement, and a failure scenario, where the *SAH* is locked, making the wingtip rigidly attached to the wing. In terms of design variables determining the dimensions of the *SAH*, two key parameters could be selected: its length, defined as a percentage of the wing span, and the flare angle, which represents the angle between the hinge axis and the direction of the airflow. Therefore, the methodology proposed in this thesis could be applied in this unconventional application scenario as well. It would be interesting to observe the interaction among the involved disciplines and how the sizing process is modified for the specific aircraft considered in this case. Clearly, for these two application cases different from the one developed in the thesis, a rethinking of the design variables will be necessary. Moreover, special attention should be given to the constraints used, aiming to tailor them to the worst-case scenarios within the flight envelope.

Finally, it might be useful to re-evaluate the proposed methodology using alternative objectives to compare designs obtained with the new approach. Instead of focusing on cruise speed and maximum range, an alternative approach could involve setting a fixed flight speed for the aircraft and aiming to maximize its range. This strategy would involve adjusting the flight altitude to optimize aerodynamic efficiency during cruise and adjusting all analyses conducted according to the specific flight altitude, including limitations on maximum flight altitude and the incorporation of additional critical design analyses. Hence, a single-objective optimization could be proposed using the same aeroservoelastic model, in order to compare all configurations obtained.

Bibliography

[1] German Aerospace Center (Deutsches Zentrum für Luft-und Raumfahrt; DLR. Towards zero-emission aviation. URL `https://www.dlr.de/en/latest/news/2021/04/20211215_towards-zero-emission-aviation`.

[2] Robert H Liebeck. Design of the blended wing body subsonic transport. *Journal of aircraft*, 41(1):10–25, 2004.

[3] AIRBUS. Airbus zeroe. `https://www.airbus.com/en/innovation/low-carbon-aviation/hydrogen/zeroe`.

[4] Liaquat Iqbal and John Sullivan. Multidisciplinary design and optimization (mdo) methodology for the aircraft conceptual design. In *50th AIAA Aerospace Sciences Meeting including the New Horizons Forum and Aerospace Exposition*, page 552, 2012.

[5] Anne Gazaix, François Gallard, Vincent Gachelin, Thierry Druot, Stéphane Grihon, Vincent Ambert, Damien Guénot, Rémi Lafage, Charlie Vanaret, Benoit Pauwels, et al. Towards the industrialization of new mdo methodologies and tools for aircraft design. In *18th AIAA/ISSMO Multidisciplinary Analysis and Optimization Conference*, page 3149, 2017.

[6] Satadru Roy, William A Crossley, Kenneth T Moore, Justin S Gray, and Joaquim RRA Martins. Next generation aircraft design considering airline operations and economics. In *2018 AIAA/ASCE/AHS/ASC Structures, Structural Dynamics, and Materials Conference*, page 1647, 2018.

[7] Keizo Takenaka, Kazuhiro Nakahashi, Shigeru Obayashi, and KisaLisa KisaMatsushima. The application of mdo technologies to the design of a high performance small jet aircraft-lessons learned and some practical concerns. In *35th AIAA fluid dynamics conference and exhibit*, page 4797, 2005.

[8] A Lambe and JRRA Martins. A unified description of mdo architectures. In *9th World Congress on Structural and Multidisciplinary Optimization*, 2011.

[9] Robert David Braun. *Collaborative optimization: an architecture for large-scale distributed design*. Stanford University, 1996.

[10] Jaroslaw Sobieszczanski-Sobieski, Jeremy Agte, and Robert Sandusky, Jr. Bi-level integrated system synthesis (bliss). In *7th AIAA/USAF/NASA/ISSMO Symposium on Multidisciplinary Analysis and Optimization*, page 4916, 1998.

[11] Luca Cavagna, Sergio Ricci, and Lorenzo Travaglini. Neocass: an integrated tool for structural sizing, aeroelastic analysis and mdo at conceptual design level. *Progress in Aerospace Sciences*, 47(8):621–635, 2011.

[12] E Goldberg David. Holland john henry. *Genetic algorithms and machine learning*, 1988.

[13] Michael D McKay, Richard J Beckman, and William J Conover. A comparison of three methods for selecting values of input variables in the analysis of output from a computer code. *Technometrics*, 42(1):55–61, 2000.

[14] P Piperni, A DeBlois, and R Henderson. Development of a multilevel multidisciplinary-optimization capability for an industrial environment. *AIAA journal*, 51(10):2335–2352, 2013.

[15] Ernst Kesseler and Marin D Guenov. Advances in collaborative civil aeronautical multidisciplinary design optimization. *(No Title)*, 2010.

[16] Patrick Cassidy, Timothy Gatzke, and Charles Vaporean. Integrating synthesis and simulation for conceptual design. In *46th AIAA Aerospace Sciences Meeting and Exhibit*, page 1443, 2008.

[17] Jeremy Agte, Olivier De Weck, Jaroslaw Sobieszczanski-Sobieski, Paul Arendsen, Alan Morris, and Martin Spieck. Mdo: assessment and direction for advancement—an opinion of one international group. *Structural and Multidisciplinary Optimization*, 40:17–33, 2010.

[18] Katherine Alston, Steven Doyle, Tyler Winter, Hongman Kim, and Scott Ragon. High fidelity multidisciplinary optimization (hfmdo). In *13th AIAA/ISSMO Multidisciplinary Analysis Optimization Conference*, page 9319, 2010.

[19] Mark Drela. Simultaneous optimization of the airframe, powerplant, and operation of transport aircraft. *Hamilton Place, London*, 2010.

[20] Antoine DeBlois and Mohammed Abdo. Multi-fidelity multidisciplinary design optimization of metallic and composite regional and business jets. In *13th AIAA/ISSMO Multidisciplinary Analysis Optimization Conference*, page 9191, 2010.

[21] Nicolas E Antoine and Ilan M Kroo. Framework for aircraft conceptual design and environmental performance studies. *AIAA journal*, 43(10):2100–2109, 2005.

[22] Jacob Markish. *Valuation techniques for commercial aircraft program design.* PhD thesis, Massachusetts Institute of Technology, 2002.

[23] Ryan Peoples and Karen Willcox. Value-based multidisciplinary optimization for commercial aircraft design and business risk assessment. *Journal of aircraft*, 43(4):913–921, 2006.

[24] Joaquim RRA Martins, Juan J Alonso, and James J Reuther. A coupled-adjoint sensitivity analysis method for high-fidelity aero-structural design. *Optimization and Engineering*, 6: 33–62, 2005.

[25] Kasidit Leoviriyakit, Sangho Kim, and Antony Jameson. Aero-structural wing planform optimization using the navier-stokes equations. In *10th AIAA/ISSMO Multidisciplinary Analysis and Optimization Conference*, page 4479, 2004.

[26] Zhoujie Lyu and Joaquim RRA Martins. Aerodynamic design optimization studies of a blended-wing-body aircraft. *Journal of Aircraft*, 51(5):1604–1617, 2014.

[27] David Rodriguez and Peter Sturdza. A rapid geometry engine for preliminary aircraft design. In *44th AIAA Aerospace Sciences Meeting and Exhibit*, page 929, 2006.

[28] Justin S Gray, John T Hwang, Joaquim RRA Martins, Kenneth T Moore, and Bret A Naylor. Openmdao: An open-source framework for multidisciplinary design, analysis, and optimization. *Structural and Multidisciplinary Optimization*, 59:1075–1104, 2019.

[29] Christopher Heath and Justin Gray. Openmdao: framework for flexible multidisciplinary design, analysis and optimization methods. In *53rd AIAA/ASME/ASCE/AHS/ASC Structures, Structural Dynamics and Materials Conference 20th AIAA/ASME/AHS Adaptive Structures Conference 14th AIAA*, page 1673, 2012.

[30] John Hwang and Joaquim RRA Martins. Geomach: geometry-centric mdao of aircraft configurations with high fidelity. In *12th AIAA Aviation Technology, Integration, and Operations (ATIO) Conference and 14th AIAA/ISSMO Multidisciplinary Analysis and Optimization Conference*, page 5605, 2012.

[31] Jaroslaw Sobieszczanski-Sobieski and Raphael T Haftka. Multidisciplinary aerospace design optimization: survey of recent developments. *Structural optimization*, 14:1–23, 1997.

[32] Olivier de Weck, Jeremy Agte, Jaroslaw Sobieszczanski-Sobieski, Paul Arendsen, Alan Morris, and Martin Spieck. State-of-the-art and future trends in multidisciplinary design optimization. In *48th Aiaa/Asme/Asce/Ahs/Asc Structures, Structural Dynamics, and Materials Conference*, page 1905, 2007.

[33] Andrew March and Karen Willcox. Constrained multifidelity optimization using model calibration. *Structural and Multidisciplinary Optimization*, 46:93–109, 2012.

[34] Natalia M Alexandrov, Robert Michael Lewis, Clyde R Gumbert, Lawrence L Green, and Perry A Newman. Approximation and model management in aerodynamic optimization with variable-fidelity models. *Journal of Aircraft*, 38(6):1093–1101, 2001.

[35] Vilfredo Pareto. *Manuale di economia politica: con una introduzione alla scienza sociale*, volume 13. Società editrice libraria, 1919.

[36] Jasbir Singh Arora. *Introduction to optimum design*. Elsevier, 2004.

[37] Salvatore Greco, Jose Figueira, and Matthias Ehrgott. *Multiple criteria decision analysis*, volume 37. Springer, 2016.

[38] Matthias Ehrgott, Alexander Engau, and Margaret M Wiecek. Theory, computation, and practice of multiobjective optimisation. *Annals of Operations Research*, 319(2):1477–1478, 2022.

[39] R Timothy Marler and Jasbir S Arora. Survey of multi-objective optimization methods for engineering. *Structural and multidisciplinary optimization*, 26:369–395, 2004.

[40] Marco Cavazzuti. *Optimization methods: from theory to design scientific and technological aspects in mechanics*. Springer science & business media, 2012.

[41] Jorge Nocedal and Stephen J Wright. *Numerical optimization*. Springer, 1999.

[42] Augustine R Dovi and Gregory A Wrenn. Aircraft design for mission performance using nonlinear multiobjective optimization methods. *Journal of Aircraft*, 27(12):1043–1049, 1990.

[43] Geoffrey Bower and Ilan Kroo. Multi-objective aircraft optimization for minimum cost and emissions over specific route networks. In *The 26th Congress of ICAS and 8th AIAA ATIO*, page 8905, 2008.

[44] Claude Lemaréchal. Cauchy and the gradient method. *Doc Math Extra*, 251(254):10, 2012.

[45] Haskell B Curry. The method of steepest descent for non-linear minimization problems. *Quarterly of Applied Mathematics*, 2(3):258–261, 1944.

[46] David G Luenberger, Yinyu Ye, et al. *Linear and nonlinear programming*, volume 2. Springer, 1984.

[47] Charles George Broyden. The convergence of a class of double-rank minimization algorithms 1. general considerations. *IMA Journal of Applied Mathematics*, 6(1–2):76–90, 1970.

[48] Roger Fletcher. A new approach to variable metric algorithms. *The computer journal*, 13(3): 317–322, 1970.

[49] Donald Goldfarb. A family of variable-metric methods derived by variational means. *Mathematics of computation*, 24(109):23–26, 1970.

[50] David F Shanno. Conditioning of quasi-newton methods for function minimization. *Mathematics of computation*, 24(111):647–656, 1970.

[51] Chang Wook Ahn. *Advances in evolutionary algorithms*. Springer, 2006.

[52] Scott Kirkpatrick, C Daniel Gelatt Jr, and Mario P Vecchi. Optimization by simulated annealing. *science*, 220(4598):671–680, 1983.

[53] SS Rao. Game theory approach for multiobjective structural optimization. *Computers & Structures*, 25(1):119–127, 1987.

[54] Timothy Ward Athan and Panos Y Papalambros. A note on weighted criteria methods for compromise solutions in multi-objective optimization. *Engineering optimization*, 27(2):155–176, 1996.

[55] Franco Mastroddi and Stefania Gemma. Analysis of pareto frontiers for multidisciplinary design optimization of aircraft. *Aerospace Science and Technology*, 28(1):40–55, 2013.

[56] Colin Reeves and Jonathan E Rowe. *Genetic algorithms: principles and perspectives: a guide to GA theory*, volume 20. Springer Science & Business Media, 2002.

[57] John H Holland. *Adaptation in natural and artificial systems: an introductory analysis with applications to biology, control, and artificial intelligence*. MIT press, 1992.

[58] Kaspar Höschel and Vasudevan Lakshminarayanan. Genetic algorithms for lens design: a review. *Journal of Optics*, 48(1):134–144, 2019.

[59] Ronald Aylmer Fisher. Design of experiments. *British Medical Journal*, 1(3923):554, 1936.

[60] Von Neumann. Various techniques used in connection with random digits. *Notes by GE Forsythe*, pages 36–38, 1951.

[61] Il'ya Meerovich Sobol'. On the distribution of points in a cube and the approximate evaluation of integrals. *Zhurnal Vychislitel'noi Matematiki i Matematicheskoi Fiziki*, 7(4):784–802, 1967.

[62] Thomas H Cormen, Charles E Leiserson, Ronald L Rivest, and Clifford Stein. *Introduction to algorithms*. MIT press, 2022.

[63] Frank Yates. The design and analysis of factorial experiments. 1937.

[64] Genichi Taguchi, Subir Chowdhury, and Yuin Wu. Taguchi's quality engineering handbook. 2004.

[65] Joaquim RRA Martins and Andrew B Lambe. Multidisciplinary design optimization: a survey of architectures. *AIAA journal*, 51(9):2049–2075, 2013.

[66] Richard J Balling and Jaroslaw Sobieszczanski-Sobieski. Optimization of coupled systems-a critical overview of approaches. *AIAA journal*, 34(1):6–17, 1996.

[67] Raphael T Haftka, Jaroslaw Sobieszczanski-Sobieski, and Sharon L Padula. On options for interdisciplinary analysis and design optimization. *Structural optimization*, 4:65–74, 1992.

[68] Natalia M Alexandrov, M Yousuff Hussaini, et al. Multidisciplinary design optimization: State of the art. 1997.

[69] Evin J Cramer, John E Dennis, Jr, Paul D Frank, Robert Michael Lewis, and Gregory R Shubin. Problem formulation for multidisciplinary optimization. *SIAM Journal on Optimization*, 4(4):754–776, 1994.

[70] Ilan Kroo. Distributed multidisciplinary design and collaborative optimization. *VKI lecture series on optimization methods & tools for multicriteria/multidisciplinary design*, pages 15–19, 2004.

[71] Mckinsey Company. Short-haul flying redefined: The promise of regional air mobility. URL `https://www.mckinsey.com/industries/aerospace-and-defense/our-insights/short-haul-flying-redefined-the-promise-of-regional-air-mobility`.

[72] Colonel Kip P Nygren and Major Robert R Schulz. Breguet's formulas for aircraft range & endurance an application of integral calculus. In *1996 Annual Conference*, pages 1–90, 1996.

[73] Andrew B Lambe and Joaquim RRA Martins. Extensions to the design structure matrix for the description of multidisciplinary design, analysis, and optimization processes. *Structural and Multidisciplinary Optimization*, 46:273–284, 2012.

[74] Donald V Steward. The design structure system: A method for managing the design of complex systems. *IEEE transactions on Engineering Management*, (3):71–74, 1981.

[75] Francesco Saltari, Cristina Riso, Guido De Matteis, and Franco Mastroddi. Finite-element-based modeling for flight dynamics and aeroelasticity of flexible aircraft. *Journal of Aircraft*, 54(6):2350–2366, 2017.

[76] European Union Aviation Safety Agency. CS-25: Certification Specifications for Large Aeroplanes. `https://www.easa.europa.eu/en/document-library/easy-access-rules/online-publications/easy-access-rules-large-aeroplanes-cs-25?page=15`.

[77] E Albano and WP Rodden. Msc/nastran aeroelastic analysis' user's guide. *MSC Software*, 1994.

[78] Florian Hürlimann, Roland Kelm, Michael Dugas, Kim Oltmann, and Gerald Kress. Mass estimation of transport aircraft wingbox structures with a cad/cae-based multidisciplinary process. *Aerospace Science and Technology*, 15(4):323–333, 2011.

[79] Xavier Jolivet and David Zwegers. Airbus support to incident/accident investigations. URL `https://www.icao.int/sam/documents/2014-aig/16.%20airbus%20presentation_lima_icao_aig_raio.pdf`.

[80] Raymond L Bisplinghoff, Holt Ashley, and Robert L Halfman. *Aeroelasticity*. Courier Corporation, 2013.

[81] JG Leishman. Validation of approximate indicial aerodynamic functions for two-dimensional subsonic flow. *Journal of Aircraft*, 25(10):914–922, 1988.

[82] Murray Tobak. On the use of the indicial-function concept in the analysis of unsteady motions of wings and wing-tail combinations. Technical report, 1954.

[83] PS Brar, R Raul, and RH Scanlan. Numerical calculation of flutter derivatives via indicial functions. *Journal of Fluids and Structures*, 10(4):337–351, 1996.

[84] P Marzocca, L Librescu, Gianfranco Chiocchia, et al. Unsteady aerodynamics in various flight speed regimes for flutter/dynamic response analyses, 18th. In *Titolo volume non avvalorato*. 2000.

[85] Herbert C Nelson and Julian H Berman. Calculations on the forces and moments for an oscillating wing-aileron combination in two-dimensional potential flow at sonic speed. Technical report, 1952.

[86] N GUPTA and K ILIFF. Identification of aerodynamic indicial functions using flight data. In *9th Atmospheric Flight Mechanics Conference*, page 1375, 1982.

[87] AV Balakrishnan. Unsteady aerodynamics-subsonic compressible inviscid case. Technical report, 1999.

[88] Harvard Lomax, Max A Heaslet, and Loma Sluder. The indicial lift and pitching moment for a sinking or pitching two-dimensional wing flying at subsonic or supersonic speeds. Technical report, 1951.

[89] Bernard Mazelsky. Numerical determination of indicial lift of a two-dimensional sinking airfoil at subsonic mach numbers from oscillatory lift coefficients with calculations for mach number 0.7. Technical report, 1951.

[90] Bernard Mazelsky and Joseph A Drischler. Numerical determination of indicial lift and moment functions for a two-dimensional sinking and pitching airfoil at mach numbers 0.5 and 0.6. Technical report, 1952.

[91] Piergiovanni Marzocca, Liviu Librescu, and Gianfranco Chiocchia. Aeroelastic response of a 2-d airfoil in a compressible flow field and exposed to blast loading. *Aerospace science and technology*, 6(4):259–272, 2002.

[92] John D Anderson Jr. Fundamentals of aerodynamics, mcgraw-hill. *New York*, 1991.

[93] Krishnamurty Karamcheti. Principles of ideal-fluid aerodynamics. *(No Title)*, 1966.

[94] Frederick William Lanchester. *Aerodynamics: constituting the first volume of a complete work on aerial flight*. Constable, 1911.

[95] Theodore Von Kármán. *Aerodynamics: selected topics in the light of their historical development*. Courier Corporation, 2004.

[96] Charles E Jobe. Prediction and verification of aerodynamic drag, part i: prediction. *Progress in Astronautics and Aeronautics, edited by CE Eugene*, 98:14–15, 1985.

[97] Gerard WH Van Es. Rapid estimation of the zero-lift drag coefficient of transport aircraft. *Journal of aircraft*, 39(4):597–599, 2002.

[98] Sérgio Waitman and Andrés Marcos. h_∞ control design for active flutter suppression of flexible-wing unmanned aerial vehicle demonstrator. *Journal of Guidance, Control, and Dynamics*, 43(4):656–672, 2020.

[99] Luca Marchetti, Alessandro De Gaspari, Luca Riccobene, Francesco Toffol, Federico Fonte, Sergio Ricci, Paolo Mantegazza, Eli Livne, and Kimberly A Hinson. Active flutter suppression analysis and wind tunnel studies of a commercial transport configuration. In *AIAA Scitech 2020 Forum*, page 1677, 2020.

[100] Sergio Ricci, Francesco Toffol, Alessandro De Gaspari, Luca Marchetti, Federico Fonte, Luca Riccobene, Paolo Mantegazza, John Berg, Eli Livne, and Kristi Morgansen. Wind tunnel system for active flutter suppression research: Overview and insights. *AIAA Journal*, 60(12): 6692–6714, 2022.

[101] Ashish Tewari. Output rate weighted active flutter suppression. In *Guidance, Navigation, and Control Conference and Exhibit*, page 4312, 1999.

[102] Julian Theis, Harald Pfifer, and Peter J Seiler. Robust control design for active flutter suppression. In *AIAA Atmospheric Flight Mechanics Conference*, page 1751, 2016.

[103] Gary Balas, Richard Chiang, Andy Packard, and Michael Safonov. Robust control toolbox user's guide. *The Math Works, Inc., Tech. Rep*, 2007.

[104] Hugo Lhachemi, David Saussie, and Guchuan Zhu. Flutter suppression for a two degree of freedom aeroelastic wing section: a structured h-infinity-based gain-scheduling approach with explicit hidden coupling terms handling. In *AIAA Guidance, Navigation, and Control Conference*, page 1735, 2017.

[105] Filip Svoboda and Martin Hromcik. Active flutter suppression by means of fixed-order h_∞ control: Results for the benchmark active control technology (bact) wing. In *2019 18th European control conference (ECC)*, pages 119–124. IEEE, 2019.

[106] Sérgio Waitman and Andrés Marcos. Active flutter suppression: non-structured and structured h_∞ design. *IFAC-PapersOnLine*, 52(12):146–151, 2019.

[107] Eli Livne. Aircraft active flutter suppression: State of the art and technology maturation needs. *Journal of Aircraft*, 55(1):410–452, 2018.

[108] Eli Livne and Terrence A Weisshaar. Aeroelasticity of nonconventional airplane configurations-past and future. *Journal of aircraft*, 40(6):1047–1065, 2003.

[109] Panos Y Papalambros and Douglass J Wilde. *Principles of optimal design: modeling and computation*. Cambridge university press, 2000.

[110] James T Allison, Tinghao Guo, and Zhi Han. Co-design of an active suspension using simultaneous dynamic optimization. *Journal of Mechanical Design*, 136(8):081003, 2014.

[111] Emmeline Faïsse, Robin Vernay, Fabio Vetrano, Joseph Morlier, and Daniel Alazard. Aeroservoelastic wing sizing using integrated structural and control (co-design) optimization. In *AIAA SCITECH 2022 Forum*, page 2243, 2022.

[112] J Alvaro Perez, Christelle Pittet, Daniel Alazard, and Thomas Loquen. Integrated control/structure design of a large space structure using structured h_∞ control. *IFAC-PapersOnLine*, 49(17):302–307, 2016.

[113] E Nguyen Van, Daniel Alazard, Carsten Döll, and Philippe Pastor. Co-design of aircraft vertical tail and control laws using distributed electric propulsion. *IFAC-PapersOnLine*, 52 (12):514–519, 2019.

[114] Yann Denieul, Joël Bordeneuve, Daniel Alazard, Clément Toussaint, and Gilles Taquin. Multi-control surface optimization for blended wing–body under handling quality constraints. *Journal of Aircraft*, 55(2):638–651, 2018.

[115] Steven T Karris. *Introduction to Simulink with engineering applications*. Orchard Publications, 2006.

[116] Tamás Luspay, Daniel Ossmann, Matthias Wuestenhagen, Dániel Teubl, Tamás Baár, Manuel Pusch, Thiemo M Kier, Sergio Waitman, Andrea Ianelli, Andres Marcos, et al. Flight control design for a highly flexible flutter demonstrator. In *AIAA Scitech 2019 Forum*, page 1817, 2019.

[117] Manuel Pusch, Daniel Ossmann, and Tamás Luspay. Structured control design for a highly flexible flutter demonstrator. *Aerospace*, 6(3):27, 2019.

[118] Hugo Fournier. *Aeroelastic reduced-order modeling and active control of flexible aircraft*. PhD thesis, INSA Lyon, 2023.

[119] Manuel Pusch. Aeroelastic mode control using h2-optimal blends for inputs and outputs. In *2018 AIAA guidance, navigation, and control conference*, page 0618, 2018.

[120] W Stalewski and J Żółtak. Multi-objective and multidisciplinary optimization of wing for small aircraft. In *Proceedings of the CEAS Congress on disc*, pages 1483–1492, 2011.

[121] Skybrary. Skybrary:aircraft types. URL `https://skybrary.aero/aircraft/a19n`.

Appendix A

Appendix

A.1 Lifting line theory

The linear lift distribution depends on the shape of the wing, more specifically on the characteristics of each section, such as aerodynamic chord, camber, and wing twist. The concept of circulation and the Kutta-Joukowski theorem are applied, and the induced vertical velocity can be calculated using the velocity distribution within a vortex (it is related to a change in the effective angle of attack on neighboring sections). The vortex filament at the y-point of the lifting line produces an elementary contribution of the induced velocity at each point of the line. Specifically, at position y of the lifting line, the induced velocity contribution due to the semi-infinite vortex filament at y^* is

$$w(y) = \frac{1}{4\pi} \int_{-\frac{l}{2}}^{\frac{l}{2}} \frac{\frac{d\Gamma}{dy} dy^*}{y - y^*} \tag{A.1}$$

Therefore the angle of induced incidence for any point on the lifting line is

$$\alpha_i(y) \quad = \quad -\frac{w(y)}{U_\infty} = -\frac{1}{4\pi U_\infty} \int_{-\frac{l}{2}}^{\frac{l}{2}} \frac{\frac{d\Gamma}{dy} dy^*}{y - y^*} \tag{A.2}$$

while in the hypothesis of $\alpha_{L=0} = 0$ the lifting coefficient is

$$C_{l_\alpha}(y) \quad = \quad \frac{2\Gamma(y)}{U_\infty 2b(y)} = 2\pi(\alpha - \alpha_i) \tag{A.3}$$

For each section along the span, the Glauert theory is considered for calculating the circulation Γ and the induced velocity (from which the induced incidence is easily derived) through the use of Fourier series. The following transformations are used

$$\begin{aligned} y &= -\frac{l}{2} cos(\theta) \\ y^* &= -\frac{l}{2} cos(\theta^*) \end{aligned} \tag{A.4}$$

The circulation is expressed by Fourier series of sines to satisfy the condition of zero value at the

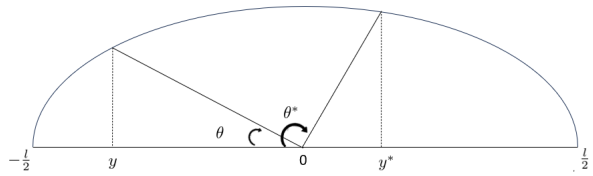

Figure A.1: Transformation of variables defined in Eqn. A.4

wingtips

$$\Gamma(\theta) = 2\,l\,U_\infty \sum_{n=1}^{\infty} A_n\, sin(n\theta) \tag{A.5}$$

from which are obtained

$$\frac{d\Gamma}{d\theta} = 2\,l\,U_\infty \sum_{n=1}^{\infty} n\,A_n\, cos(n\theta) \tag{A.6}$$

$$\alpha_i(\theta^*) = \sum_{n=1}^{\infty} n\,A_n \frac{sin(n\theta^*)}{sin(\theta^*)} \tag{A.7}$$

The section lift coefficient (Eqn. A.3) is rewritten by considering the previous transformations

$$\frac{l}{\pi\, 2b(\theta^*)} \sum_{n=1}^{\infty} A_n\, sin(n\theta^*) + \sum_{n=1}^{\infty} n\,A_n\, \frac{sin(n\theta^*)}{sin(\theta^*)} = \alpha(\theta^*) \tag{A.8}$$

The Fourier series coefficients from the lifting line equation are computed using a finite number of terms, and considering a finite number of sections along the span, with the assumption of symmetrical airfoils. In conclusion, from the calculation of these coefficients, the circulation, the induced velocity and the lift of each section of the aerodynamic surface can be calculated, and therefore the lift coefficients of each sections C_{l_α} can be derived.

A.2 Equivalent Aspect Ratio definition

For calculating the Equivalent Aspect Ratio AR_e, the equations of Drag are used,

$$D = D_0 + D_i = D_0 + q_D S_w \frac{C_{L_w}^2}{\pi AR_w e} + q_D S_t \frac{C_{L_t}^2}{\pi AR_t e} \tag{A.9}$$

in which D_0 and D_i are the shape and the induced drag, q_D is the dynamic pressure, e is the Oswald factor, S is the surface, AR is the aspect ratio and C_L is the lift coefficient of the specific surface, denoted with $_w$ for the wing and $_t$ for the tail; and the equations of Lift and Moment around the

mass center

$$\begin{cases} C_{L_w} + C_{L_t}\frac{S_t}{S_w} = C_L \\ C_{L_w}(x_w - x_G) + C_{L_t}(x_t - x_G)\frac{S_t}{S_w} = 0 \end{cases} \tag{A.10}$$

in which x_G is the position of the mass center. Starting from the Eqns. A.10, the lift coefficient of the tail is calculated

$$C_{L_t} = -C_{L_w}\left(\frac{x_w - x_G}{x_t - x_G}\right)\frac{S_w}{S_t} \tag{A.11}$$

so the the Lift equation can be rewritten as

$$C_{L_w}\left(1 - \frac{x_w - x_G}{x_t - x_G}\right) = C_L \tag{A.12}$$

To summarize the problem, the two lift contributions of the wing and the tail surfaces are

$$\begin{aligned} C_{L_w} &= \beta_1 C_L \\ C_{L_t} &= \beta_2 C_L \end{aligned} \tag{A.13}$$

in which

$$\begin{aligned} \frac{1}{\beta_1} &= 1 - \left(\frac{x_w - x_G}{x_t - x_G}\right) \\ \beta_2 &= -\beta_1\left(\frac{x_w - x_G}{x_t - x_G}\right)\frac{S_w}{S_t} \end{aligned} \tag{A.14}$$

Taking into account the Drag equation (Eqn. A.9), it is possible to rewrite the induced drag as follows

$$\begin{aligned} D_i &= q_D S_w\left(\frac{\beta_1^2}{\pi AR_w e} + \frac{\beta_2^2}{\pi AR_t e}\frac{S_t}{S_w}\right)C_L^2 \\ &= \frac{q_D S_w}{\pi AR_e e}C_L^2 \end{aligned} \tag{A.15}$$

Finally, the Equivalent Aspect Ratio AR_e is defined as

$$\frac{1}{\pi AR_e e} = \frac{\beta_1^2}{\pi AR_w e} + \frac{\beta_2^2}{\pi AR_t e}\frac{S_t}{S_w} \tag{A.16}$$